Simulations of Subsurface Multiphase Flow Including Polymer Flooding in Oil Reservoirs and Infiltration in Vadose Zone

by

Changli Yuan, M. E.

Thesis

Presented to the Faculty of the Graduate School of

The University of Texas at Austin

in Partial Fulfillment

of the Requirements

for the Degree of

Master of Science in Engineering

The University of Texas at Austin

December 2009

Simulations of Subsurface Multiphase Flow Including Polymer Flooding in Oil Reservoirs and Infiltration in Vadose Zone

Approved by
Supervising Committee:

Mary F. Wheeler, Supervisor

Mojdeh Delshad, Co-Supervisor

Dedication

To my beloved family.

Acknowledgements

First and foremost, I would thank my supervisor, Dr. Mary F. Wheeler for her intellectual guidance and support. In particular, I thank her for bringing me into the fascinating fields of numerical analysis and computational sciences.

I wish to express my appreciation to my co-supervisor, Dr. Mojdeh Delshad, for her helpful guidance and suggestions through this research.

I am indebted to Dr. Kees for the collaboration.

I am very thankful to the past and present group members at CSM and the department of PGE for their help and friendship. Particularly, I would like to thank George, Gergina and Connie who have always been warmhearted and helpful during my study here.

December 2009

Abstract

Simulations of Subsurface Multiphase Flow Including Polymer Flooding in Oil Reservoirs and Infiltration in Vadose Zone

Changli Yuan, M.S.E

The University of Texas at Austin, 2009

Supervisors: Mary F. Wheeler

Mojdeh Delshad

With the depletion of oil reserves and increase in oil price, the enhanced oil recovery methods such as polymer flooding to increase oil production from water flooded fields are becoming more attractive. Effective design of these processes is challenging because the polymer chemistry has a strong effect on reaction and fluid rheology, which in turn has a strong effect on fluid transport. We have implemented a well-established polymer model within the Implicit Parallel Accurate Reservoir Simulator (IPARS), which enables parallel simulation of non-Newtonian fluid flow through porous media. The following properties of polymer solution are modeled in this work: 1) polymer adsorption; 2) polymer viscosity as a function of salinity, hardness, polymer concentration, and shear rate; 3) permeability reduction; 4) inaccessible pore volume.

IPARS enables field-scale polymer flooding simulation with its parallel computation capability.

In this thesis, several numerical examples are presented. The result of polymer module is verified by UTCHEM, a three-dimensional chemical flood simulator developed at the University of Texas at Austin. The parallel capability is also tested. The influence of different shear rate calculations is investigated in homogeneous and heterogeneous reservoirs. We observed that the wellbore velocity calculation instead of Darcy velocity reduces the grid effect for coarse mesh. We noted that the injection bottom hole pressure is very sensitive to the shear rate calculation. However, cumulative oil recovery and overall oil saturation appear to not be sensitive to grid and shear rate calculation for same reservoir.

There are two models to model the ground water infiltration in vadose zone. One is Richard's Equation (RE) model. And the other is two-phase flow model. In this work, we compare the two-phase model with an RE model to ascertain, under common scenarios such as infiltration or injection of water into initially dry soils, the similarities and differences in solutions behaviors, the ability of each model to simulate such infiltration processes under realistic scenarios, and to investigate the numerical efficiencies and difficulties which arise in these models. Six different data sets were assembled as benchmark infiltration problems in the unsaturated zone. The comparison shows that two-phase model holds for general porous media and is not limited by several assumptions that must be made for the RE formulation, while RE is applicable only for shallow regions (vadose) that are only several meters in depth and a fully saturated bottom boundary condition must be assumed.

Table of Contents

List of Tables

List of Figures

PART I

SIMULATION OF POLYMER FLOODING IN OIL RESERVOIR

CHAPTER 1

INTRODUCTION

Waterflooding, which was discovered accidently in 1865, found its widespread applications in early 1950s. Waterflooding has been proven to be the simplest and the lowest cost approach to maintain production and increase oil recovery from an oil reservoir. However, these benefits may fall far short of the expectations because of the complexity and the uncertainty of the reservoir, unless concepts and practices are clearly understood and judiciously implemented. Hence, accurate simulation of waterflooding will provide enormous economic benefits for the petroleum industry. Buckley and Leverett first proposed the analytical solution of the one-dimensional Newtonian fluids displacement (Buckley and Leverett, 1942). Douglas *et al.* did pioneer work on numerical calculation of multi-dimensional Newtonian fluids displacement (Douglas *et al.*, 1959). With the availability of high-speed computer, reservoir simulation has blossomed in the past decades and has been utilized extensively to aid in forecasting, planning, execution, and optimization of oil recovery operations. The results of simulation studies are integrated with reservoir economics to maximize the value of the asset.

With the depletion of oil reserves and increase of oil price, enhanced oil recovery (EOR) methods have attracted much attention in recent years. The reason is that the conventional oil recovery (including water flooding) leaves behind much oil in reservoir, often as much as 70%OOIP (original oil in place), due to geological heterogeneity and an unfavorable mobility ratio. There are many types of enhanced oil recovery methods, e.g. thermal, solvent and/or chemical flooding (Lake, 1989). Chemical flooding is an important and widely applied EOR process and includes polymer, surfactant/polymer, alkaline/surfactant/polymer and/or foam flooding. The use of polymers in oil recovery process could be traced back in early 1960s (Pye, 1964; Sandiford, 1964). The purpose of adding polymer into the water is to improve the areal and vertical sweep efficiencies by increasing the aqueous phase viscosity and reducing the aqueous phase permeability. A large number of polymer field tests were reported in the literature during 1960's and 1970's (Sloat, 1969; Jewett, 1970; Agnew, 1972, Chang, 1978). However, the degree of success of those field tests varied. From the mid-1980s, more and more successful polymer flooding field-scale applications were reported worldwide, especially in China (Weiss and Baldwin, 1985; Putz *et al*.; 1988; Christopher *et al*., 1988; Putz and Rivenq, 1992; Du and Guan, 2004; Wang, 2009). Two types of polymers have been used for field applications: polysaccharides and partially hydrolyzed polyacrylamides (HPAM). Recent advances in the polymer technology have increased the limits of polymer flooding to a great extent. Levitt and Pope (2008) have tested polymers with high viscosities even at very high salinities. Their results using Polyacrylamide polymer showed an effective viscosity enhancements at temperature as high as 100°C with the concentration of

calcium below 200 *ppm*. Levitt and Pope (2008) also suggested that for high concentration of calcium at high temperature, sodium metaborate or copolymers such as sodium 2-acrylamide-2-methylpropane sulfate (AMPS) could be used to increase the calcium tolerance.

Mungan *et al*. (1966) studied polymer floods and confirmed that the reduction of water mobility by polymers is due to the increase of the aqueous viscosity and the reduction of the rock permeability. Their study also revealed that the mobility of the polymer solution is affected by many factors, such as polymer concentration, type and molecular weight, water salinity, pH, capillary properties of the rock and type of crude oil. Smith *et al*. (1970) studied the behavior of partially hydrolyzed HPAM solution in porous media. Their key findings include: 1) the adsorption of polymer is much greater on calcium carbonate than that on silica; 2) polymer adsorption increases with salt concentration; 3) the mobility reduction is more pronounced at lower salinity; 4) higher average molecular weight polymer reduces the mobility more effectively and results greater permeability loss. Gogarty *et al*. (1972) conducted the study of viscoelastic effect of polymer solution in porous media. Dawson and Lantz (1972) first reported the inaccessible pore volume phenomenon.

Hirasaki and Pope (1974) analyzed the factors influencing the mobility and the adsorption of polymer solution flowing through porous media. They used the modified Blake-Kozeny model to represent the pseudoplastic behavior of polymer solution. They modeled the dilatant behavior of polymer solution with viscoelastic resistance, which is a function of the Deborah number defined as a ratio of the relaxation time of the fluid to a

characteristic deformation time of the flow field. They formulated a dimensionless pore reduction group to correlate the permeability reduction factor with the polymer, brine, and rock properties. They also used a Langmuir-type isotherm adsorption model to model the adsorption of polymer, which is a function of polymer, brine, and rock properties.

Sorbie *et al*. (1987) conducted an extensive experimental and theoretical study on adsorption, dispersion, inaccessible pore volume, and non-Newtonian behavior of polymer solution. Lake (1989) and Sorbie (1991) reviewed the polymer flooding method and polymer properties, such as adsorption, viscosity, permeability reduction, inaccessible pore volume and degradation, which are essential to the success of polymer flooding.

Huh *et al*. (1990) studied the polymer retention in porous media and observed a frontal delay and prolonged delay in the effluent polymer history data from many coreflood experiments. They explained these features with a polymer retention model, in which the adsorption onto rock contributes to the frontal delay and the mechanical entrapment in pore matrices is responsible for the prolonged delay. Wu (1990) conducted a comprehensive study on non-Newtonian fluid, such as polymer solution, flowing through porous media. He proposed that the apparent viscosity of non-Newtonian fluids for multiphase flow is a function of flow potential gradient and saturation. He suggested an approach to obtain the multiphase flow viscosity from a modified single-phase flow viscosity function by replacing the permeability with an effective permeability followed by multiplying the porosity with saturation to represent an effective pore volume. He

developed analytical solutions for one-dimensional immiscible displacement of power-law and Bingham plastic fluids.

Broseta *et al.* (1995) concluded that the presence of residual oil decreases polymer adsorption/retention in oil-wet porous media, whereas the inverse trend was observed in water-wet porous media. They suggested the reservoir wettability should be taken into account when planning a polymer flood. Many researchers also suggested that polymer flooding might reduce the relative permeability of the water phase (Barreau *et al*., 1999; Zheng *et al*., 2000; Grattoni *et al*., 2004). Recent studies showed that the polymer flooding residual oil saturation is lower than the waterflood residual oil saturation, when polymer flooding is employed right after primary production or at early stages of waterflood (Huh and Pope, 2008).

Choi *et al.* (2009) investigated the influence of the pH on the viscosity, adsorption and inaccessible pore volume of the partially HPAM. They observed: 1) the viscosity of the partially HPAM is higher in high-pH conditions than in low-pH conditions due to the uncoiled molecules; 2) the polymer adsorption increases as pH decreases; 3) the inaccessible pore volume decreases with increasing pH. They proposed a new polymer injection scheme based on their first observation: inject the HPAM solution under acidic conditions. This new process substantially reduces the injection pressure because of the low polymer solution viscosity. The polymer solution viscosity increases with the acid reaction with the formation minerals.

As mentioned above, the flow of the polymer solution in porous media is very complex. This complexity and the uncertainty of the reservoir characterization make the

design and implementation of a robust polymer flooding to be quite challenging. A poorly designed and implemented polymer flooding may even cause a reduction in oil production. Therefore, accurate numerical simulation prior to the field polymer flooding is essential to a successful design and implementation of polymer flooding.

The modeling and simulation of the polymer flooding started in 1960's. Zeito (1968) simulated polymer floods in homogeneous and heterogeneous reservoirs using a three dimensional numerical simulator, wherein only polymer viscosity was modeled as a function of the polymer concentration. Masuda *et al.* (1992) included the viscoelastic effect in their 1D simulation of polymer flooding. Their simulation results showed that the oil recovery of polymer flooding benefits from the viscoelastic effect. Delshad *et al.* (2008) proposed a rheological model for HPAM solution, which correlates the apparent viscosity to the full range of Darcy velocity, including shear-thinning and shear-thickening regimes. Their viscoelastic model was implemented in UTCHEM and successfully history-matched the published coreflood results of Masuda *et al.* (1992). Verma *et al.* (2009) implemented a polymer model into an unstructured gird simulator. They modeled polymer viscosity as a function of polymer concentration, shear rate, multiple salt components and reservoir temperature in both shear thinning and shear thickening regime. They also modeled polymer degradation and retention.

This research implements a well-established polymer model (Delshad *et al*., 2000) into a fully implicit parallel reservoir simulator, the Integrated Parallel Accurate Reservoir Simulator (IPARS), which was developed at the Center for Subsurface Modeling at UT Austin. The following properties of polymer solution were modeled: 1)

polymer adsorption; 2) polymer viscosity as a function of polymer, salt concentrations, and shear rate; 4) inaccessible pore volume. The IPARS framework enables field-scale polymer flooding simulation with its parallel computation capability.

CHAPTER 2

A REVIEW OF IPARS

IPARS is a framework for developing parallel models of subsurface flow and transport through porous media. IPARS enables the high-level specification and composition of simulations, and permits the coupling of different physical and multiscale numerical models in different parts of the domain, while accounting for structural discontinuities due to faults. IPARS currently supports eight physical models, including compositional flow; discretized using mixed finite elements and/or discontinuous Galerkin methods, with implicit or explicit time stepping. It includes linear geomechanics and reactive transport capabilities, as well as the ability to treat optimization and parameter estimation as a second level of parallelism. IPARS is a framework, within which other models can be easily developed. A suite of linear solvers and preconditioners is available to optimize the computation. For more information about IPARS and relevant references, refer to Wheeler (2007). IPARS has a development history of more than 10 years. IPARS can be applied to model water table decline due to overproduction near urban areas, or oil and gas recovery in industrial applications. It has the fundamental functionality of commercial reservoir simulators

In this chapter we review the formulations in IPARS related to two-phase flow (HYDRO model) used for studies in unsaturated zone and species reactive transport (TRCHEM model) used for polymer flood simulations.

2.1 HYDRO MODEL

HYDRO model is a two-phase immiscible (oil/water or air/water) flow module in IPARS. HYDRO model is based on following assumptions

- Reservoir is isothermal;
- Darcy's law applies;
- Oil and water phase are immiscible;
- Oil and water phases are slightly compressible, and fluids densities are functions of pressure only;
- Rock is slightly compressible and immobile.

The mass conservation law for each phase is given by

$$\frac{\partial(\phi N_\alpha)}{\partial t} + \nabla \cdot \rho_\alpha \vec{u}_\alpha = q_\alpha, \qquad \alpha = o,w \tag{2-1}$$

The Darcy's law for multi-phase flow is given by

$$\vec{u}_\alpha = -\vec{\vec{K}} \frac{k_{r\alpha}}{\mu_\alpha} (\nabla P_\alpha - \rho_\alpha g \nabla D), \qquad \alpha = o,w \tag{2-2}$$

Mass concentration is related to saturation by

$$N_\alpha = \rho_\alpha S_\alpha, \qquad \alpha = o,w \tag{2-3}$$

The saturation is constrained by

$$S_o + S_w = 1 \tag{2-4}$$

Capillary pressure is defined as the pressure difference between the wetting phase (water) and the non-wetting phase (oil),

$$P_c(S_w) = P_o - P_w \tag{2-5}$$

Capillary pressure is assumed to be a function of saturation only, which is given by a table in the input file. Once the oil pressure is solved, water pressure can be calculated. The water and oil phase are both slightly compressible. The densities of the two phases are given by

$$\rho_\alpha = \rho_{\alpha,ref} \exp^{[c_\alpha (P_\alpha - P_{\alpha,ref})]}, \qquad \alpha = o,w \tag{2-6}$$

The definitions of variables above are as follows

- N_α = mass of phase α per unit pore volume [lb/ft^3]
- S_α = saturation of phase α [fraction]
- P_α = pressure of phase α [psi]
- ρ_α = density of phase α [lb/ft^3]
- ϕ = porosity [fraction]
- $\vec{u}_\alpha$ = Darcy velocity of phase α [ft/day]
- q_α = source/sink term of phase α [lb/ ft^{3}day]
- μ_α = viscosity of phase α [cp]
- $k_{r\alpha}$ = relative permeability of phase α, a given function of saturation [fraction]
- $\vec{\vec{K}}$ = permeability tensor [md]
- g = gravity magnitude [ft/day^2]
- D = depth of the reservoir [ft]
- P_c = capillary pressure between the wetting phase and the non-wetting phase [psi]
- c_α = compressibility constant of phase α [psi^{-1}]

- $\rho_{\alpha,ref}$ = reference density of phase α at $P_{\alpha,ref}$ [lb/ft^3]
- $P_{\alpha,ref}$ = reference pressure of phase α [psi]

In the HYDRO model, the primary unknowns are oil pressure P_o and oil concentration N_o. Substituting Darcy's law into the mass conservation equation (Eq. 2-1), and using saturation constraint and capillary pressure definition, we obtain the governing flow equation for each phase:

$$\frac{\partial(\phi N_o)}{\partial t} - \nabla \cdot [\rho_o \vec{\vec{K}} \frac{k_{ro}}{\mu_o}(\nabla P_o - \rho_o g \nabla D)] = q_o \tag{2-7}$$

$$\frac{\partial[\phi \rho_w (1 - N_o / \rho_o)]}{\partial t} - \nabla \cdot \{\rho_w \vec{\vec{K}} \frac{k_{rw}}{\mu_w}[\nabla(P_o - P_c) - \rho_w g \nabla D]\} = q_w \tag{2-8}$$

The governing equations are solved over a spatial domain Ω for time t > 0. Initial and boundary conditions are specified to close the system. The governing equations are discretized in space by the expanded mixed finite element method using the lowest order Raviart-Thomas spaces defined over a rectangular grid (Russell and Wheeler, 1983; Arbogast, 1997). The time discretization applied is backward Euler method. The discretization details are outlined in (Peszynska *et al.*, 2002; Wheeler *et al.*, 2009). The nonlinear system of equations arising at each time step is solved fully implicitly by Newton iteration method with a multistage preconditioned GMRES linear solver (Lacroix *et al.*, 2003).

2.2 TRCHEM MODEL

TRCHEM model (Saaf, 1996; Peszynska and Sun, 2001) is a multiphase reactive transport module in IPARS. The goal of the TRCHEM module is to develop an accurate, efficient and relatively general multi-phase reactive transport model for phenomena, which occur in porous media in a number of scientific and engineering applications including chemical, petroleum and environmental engineering. TRCHEM has several options. For example, it can treat multiple flowing phases and multiple stationary phases where the flowing phases can be incompressible or compressible. The solid phase can be either incompressible or be slightly compressible. It can also handle molecular diffusion and physical dispersion. Some general biogeochemistry phenomena such as adsorption, ion-exchange, precipitation, dissolution, bioremediation and radionuclide decay can also be modeled. Three chemical reactions supported are equilibrium controlled, classical mass-action kinetics, and Monod kinetics reactions. Since this module uses an interior-point algorithm to minimize the Gibbs free energy, it handles relatively robust equilibrium controlled reactions, even when stationary phases precipitate or dissolve. The material balance equations for aqueous components are solved by a time splitting algorithm. The concentration of oleic components is calculated from a linear partitioning relationship.

The following assumptions are made in TRCHEM

1. Interphase equilibrium mass transfer between flowing phases is assumed;
2. Rock is not strongly involved in chemical reaction (such as dissolution of the rock by acid);

3. The permeability tensor K and the porosity ϕ are not affected by the reactive transport process;
4. The phase density is assumed to be independent of the concentration of species;
5. The bulk source/sink term due to mass transfer between phases is assumed negligible in the flow equation.

2.2.1 Mass Conservation Law

The mass conservation law is written for species in stationary phase *s* and flowing phases. The mass balance of species *i* in stationary phase *s* is written as

$$\frac{\partial[(1-\phi)c_{is}]}{\partial t} = R_{is}^{I} + R_{is}^{C} + R_{is}^{N} \tag{2-9}$$

where the source terms include contributions from interphase transfer R^I, chemical reactions R^C and radionuclide decay R^N, all functions of the concentrations.

The mass balance of species *i* in flowing phase α is written as

$$\frac{\partial(\phi c_{i\alpha} S_\alpha)}{\partial t} + \nabla\cdot(c_{i\alpha}\vec{u}_\alpha - \phi S_\alpha \vec{\vec{D}}_{i\alpha}\nabla c_{i\alpha}) = R_{i\alpha}^{I} + \phi S_\alpha R_{i\alpha}^{C} + \phi S_\alpha R_{i\alpha}^{N} + q_{i\alpha} \qquad \alpha = w,\ o \tag{2-10}$$

where the diffusion-dispersion tensor $\vec{\vec{D}}_{i\alpha}$ is the sum of the molecular diffusion and the mechanical dispersion. The molecular diffusion $\vec{\vec{D}}_{i\alpha}^{mol}$ and the mechanical dispersion $\vec{\vec{D}}_{i\alpha}^{disp}$ are given by

$$\vec{\vec{D}}_{i\alpha}^{mol} = \frac{d_{i\alpha}^{mol}\vec{\vec{I}}}{\tau_\alpha} \tag{2-11}$$

$$\phi S_\alpha \vec{\vec{D}}_{i\alpha}^{disp} = d_{t,\alpha}|\vec{u}_\alpha|\vec{\vec{I}} + (d_{l,\alpha} - d_{t,\alpha})\frac{\vec{u}_\alpha \vec{u}_\alpha^{T}}{|\vec{u}_\alpha|} \tag{2-12}$$

The definitions of variables are as follows

- c_{is} = concentration of species *i* in stationary phase [lbmol/ft^3]
- $c_{i\alpha}$ = concentration of species in flowing phase α [lbmol/ft^3]
- $R^I_{i\alpha}$ = net mass transfer rate of species *i* into (positive) or out of (negative) phase α [lbmol/ft^3•day]
- $R^C_{i\alpha}$ = net production rate of species *i* in phase α from chemical reactions [lbmol/ft^3•day]
- $R^N_{i\alpha}$ = net production rate of species *i* in phase α from radionuclide decay [lbmol/ft^3•day]
- $d^{mol}_{i\alpha}$ = molecular diffusion coefficient for species *i* in phase α [ft^2/day]
- τ_α = tortuous of porous media [dimensionless]
- $d_{l,\alpha}$ = longitude dispersion coefficient [ft]
- $d_{t,\alpha}$ = transverse dispersion coefficient [ft]

2.2.2 Phase-Summed Transport Equations

Because of the mass balance, the net interphase transfer in the whole system (stationary phases and flowing phases) is zero

$$\sum_\alpha R^I_{i\alpha} + R^A_i = 0 \qquad (2\text{-}13)$$

where R^A_i is the net mass transfer rate of species *i* transferred into (positive) or out of (negative) all stationary phases. To sum over the flowing phases, we assume that the

partitioning of species between flowing phases is linear. The equilibrium linear partitioning constant of species between flowing phases is defined as

$$\Gamma_{i\alpha} = c_{i\alpha} / c_{ir} \tag{2-14}$$

where r is referred to the reference phase, water phase. The equilibrium linear partition coefficient is an input parameter. The equilibrium linear partition coefficient of the reference phase is always 1.

Summing the Eq. (2-10) over all flowing phases and inserting Eq. (2-13), we obtain the phase-summed transport equation for species *i* in the flowing phases

$$\frac{\partial(\phi_i^* c_{iw})}{\partial t} + \nabla \cdot (c_{iw} \vec{u}_i^* - \vec{\vec{D}}_i^* \nabla c_{iw}) = R_i^{TC} + R_i^{TN} - R_i^A + q_i^T \tag{2-15}$$

where the following phase-summed variables are defined for convenience

$$\phi_i^* = \phi(S_w + \Gamma_{io} S_o)$$

$$\vec{u}_i^* = \vec{u}_w + \Gamma_{io} \vec{u}_o$$

$$\vec{\vec{D}}_i^* = \phi(S_w \vec{\vec{D}}_{iw} + S_o \Gamma_{io} \vec{\vec{D}}_{io})$$

$$R_\alpha^{TC} = \phi(S_w R_{iw}^C + S_o R_{io}^C)$$

$$R_\alpha^{TN} = \phi(S_w R_{iw}^N + S_o R_{io}^N)$$

$$q_i^T = q_{iw} + q_{io}$$

Equations (2-15) are solved by a time splitting algorithm, which is presented in the following section.

2.2.3 Time Splitting Algorithm

2.2.3.1 Initial condition

The pressure and saturation are initialized in the HYDRO model. Initially Darcy's velocities for all flowing phases are zero. The initial concentration for each species is given in the input file.

2.2.3.2 Time stepping

In general the time step in the flow model is different from the concentration time step. The flow time step is usually larger than the concentration time step. Given that the solutions of the flow model (pressure, saturations and velocities etc.) are available at t^n and t^{n+1}. The concentrations of all species are available at t^m, and we are computing the concentrations at time t^{m+1}. We assume that $(t^m, t^{m+1}) \subset (t^n, t^{n+1})$. The discretization of Eq. (2-15) in time gives

$$\frac{T_i^{m+1} - T_i^m}{\Delta t} + \nabla \cdot (c_{iw}^m \vec{u}_i^{*,m+1/2} - \vec{\vec{D}}_i^{*,m} \nabla c_{iw}^{m+1}) = R_i^{TC,m+1/2} + R_i^{TN,m+1/2} - R_i^{A,m+1/2} + q_i^{T,m+1/2} \quad (2\text{-}16)$$

where $\Delta t = t^{m+1} - t^m$ and $T_i = \phi_\alpha^* c_{iw}$. ϕ_i^* and $\vec{u}_i^*$ at $t \in (t^m, t^{m+1})$ are evaluated by linear interpolation between t^n and t^{n+1}. The direct solution of Eq. (2-16) is practically impossible to obtain. Therefore, a time-splitting algorithm is used to "independently" solve the advection, diffusion/dispersion, and chemical reaction, which means each subproblem delivers intermediate values of T_i as $\overline{T}_i$, $\hat{T}_i$ and T_i^{m+1}. The individual steps of this algorithm are roughly defined below; more details about this algorithm can be found in (Dawson and Wheeler, 1987; Peszynska and Sun, 2001; Wheeler *et al*., 2009).

2.2.3.3 Advection

The equation solved in advection step is

$$\frac{\partial(\phi_i^* c_{iw})}{\partial t} + \nabla \cdot (c_{iw} \vec{u}_i^*) = q_i^T \tag{2-17}$$

The above equation is solved using the first order Godunov method with upstream weighted concentrations. The upstream scheme eliminates the solution oscillations. Let $T_i^m = \phi_\alpha^{*,m} c_{iw}^m$, where $\overline{T}_i$ is explicitly computed from

$$\frac{\overline{T}_i - T_i^m}{\Delta t} + \nabla \cdot (\vec{u}_i^{*,m+1/2} c_{iw}^m) = q_i^{T,m+1/2} \tag{2-18}$$

The intermediate values of concentrations after the advection step are computed from

$$\bar{c}_{iw} = \overline{T}_i / \phi_i^{*,m+1} \tag{2-19}$$

2.2.3.4 Chemical reaction

For kinetic type chemical reaction, we solve

$$\frac{\partial(\phi_i^* c_{iw})}{\partial t} = R_i^{TC} \tag{2-20}$$

by standard explicit ODE integration. Currently, three schemes are implemented, the forward Euler first-order scheme, second-order Runge-Kutta and fourth-order Runge-Kutta. If the forward-Euler first-order scheme is used, the Eq. (2-20) becomes

$$\frac{\hat{T}_i - \overline{T}_i}{\Delta t} = R_i^{TC,m+1/2} \tag{2-21}$$

The radionuclide decay reaction and the adsorption can be handled as chemical reaction. In this case, Eq. (2-21) becomes

$$\frac{\hat{T}_i - \overline{T}_i}{\Delta t} = R_i^{TC,m+1/2} + R_i^{TN,m+1/2} - R_i^{A,m+1/2} \tag{2-22}$$

2.2.3.5 Diffusion/Dispersion

In diffusion/dispersion step, we solve

$$\frac{\partial(\phi_i^* c_{iw})}{\partial t} - \nabla \cdot (\vec{\vec{D}}_i^* \nabla c_{iw}) = 0 \tag{2-23}$$

implicitly with respect to concentrations by solver. The time discretization of the above equation is given by

$$\frac{T_i^{m+1} - \hat{T}_i}{\Delta t} - \nabla \cdot (\vec{\vec{D}}_i^{*,m} \nabla c_{iw}^{m+1}) = 0 \tag{2-24}$$

2.3 RELATIVE PERMEABILITY MODEL

Relative permeability is a function of water saturation. There are two options to read relative permeability data: 1) table-lookup, and 2) function. A table of relative permeability data over the saturation range of $(S_{rw}, 1 - S_{or})$ is given in the input file; then an array is generated during the initialization, which stores dataset calculated by specified interpolation scheme (linear, spline2, etc.) and extrapolation scheme. The program searches for the corresponding relative permeability for the given saturation during the simulation. By using the table-lookup input, general relative permeability curves can be modeled. Table-lookup is efficient and robust. However, the disadvantage of this option is obvious because when the porous media becomes very heterogeneous, numerous tables may be required corresponding to different rock types. A two phase

Brooks-Corey model (Brooks and Corey, 1964) has been recently implemented in IPARS. The imbibition relative permeability curve for water/oil flow is given by

$$k_{r\alpha} = k_{r\alpha}^{0}(S_{n\alpha})^{n_\alpha} \quad , \qquad \alpha = w,o \tag{2-25}$$

where $k_{r\alpha}^{0}$ is the relative permeability endpoint for phase α, n_α is the relative permeability exponent, and $S_{n\alpha}$ is the normalized phase saturation defined by

$$S_{n\alpha} = \frac{S_\alpha - S_{\alpha r}}{1 - S_{wr} - S_{or}} \qquad \alpha = w,o \tag{2-26}$$

here S_{wr} and S_{or} are residual water and residual oil saturations, respectively.

2.4 WELL MODEL

The well model in IPARS is based on Peaceman well model (Peaceman, 1983). Several options are available for injection and production, i.e. constant volumetric rate or constant bottomhole pressure. A more detailed discussion on well model and available options is given as follows.

- An arbitrary number of wells in any grid block can be added.
- Skin factor (S) and completion intervals can be specified.
- The well type can be changed at anytime during the simulation
- The wells can be in any direction parallel to the axes in Cartesian coordinator system.
- Both constant flow rate constraint and constant bottomhole pressure constraint options are available, the rate and the pressure can be changed at anytime during the simulation.

Due to the similarity between vertical well and horizontal well, here we only show the formulation for vertical wells. The volumetric flow rate for each well block is given by

$$q = q_w + q_o = PI_w(P_{wb,w} - \overline{P}_w) + PI_o(P_{wb,o} - \overline{P}_o) \tag{2-27}$$

where PI_w and PI_o are the productivity index for the water and the oil phases, which is given by

$$PI_\alpha = Gk_{eq}L\frac{k_{r\alpha}}{\mu_\alpha} \quad \alpha = w,\ o \tag{2-28}$$

where L is the length of the open wellbore perforated in the element, and G is dimensionless geometric factor, which is defined as

$$G = \frac{2\pi}{\ln(\frac{r_{eq}}{r_w}) + S} \tag{2-29}$$

P_{wb} is the wellbore pressure, which can be obtained by

$$P_{wb,\alpha} = P_{bh} + \rho_{wb,\alpha}g(D_{wb} - D_{bh}) \quad \alpha = w,\ o \tag{2-30}$$

where P_{bh} is the bottomhole pressure, which may be specified when the well is pressure constraint, $\rho_{wb,\alpha}$ is the average density of the α phase in the wellbore, D_{wb} is the depth of the wellbore, and D_{bh} is the bottom hole depth.

$\overline{P}_\alpha$ is the formation pressure, which is determined by

$$\overline{P}_\alpha = P_\alpha + \rho_\alpha g(D_{wb} - D) \tag{2-31}$$

The equivalent permeability, k_{eq}, is defined as

$$k_{eq} = \sqrt{k_x k_y} \tag{2-32}$$

The equivalent well radius, r_{eq}, is defined as

$$r_{eq} = 0.28 \frac{\left[\left(\frac{k_x}{k_y} \right)^{0.5} \Delta y^2 + \left(\frac{k_y}{k_x} \right)^{0.5} \Delta x^2 \right]^{0.5}}{\left(\frac{k_x}{k_y} \right)^{0.25} + \left(\frac{k_y}{k_x} \right)^{0.25}} \tag{2-33}$$

where Δx, Δy, Δz are gridblock sizes in x, y, and z direction, respectively.

2.5 BOUNDARY CONDITIONS

Two types of boundary conditions have been implemented in HYDRO model: Dirichlet (pressures or concentrations/saturations are prescribed) and Neumann (phase fluxes are prescribed) conditions. The discretization and the implementation details are described in (Peszynska *et al*, 2002). There are six combinations of boundary conditions:

1. Oil pressure, oil concentration;
2. Oil pressure, water saturation
3. Oil pressure, out flow water saturation
4. Oil pressure, water flux
5. Oil pressure, water saturation at a reference depth
6. Oil pressure, outflow water saturation

If no boundary condition is specified, the default boundary is a no-flow boundary.

CHAPTER 3

POLYMER FLOODING SIMULATIONS

Polymer flooding is a common, relative low risk, and inexpensive enhanced oil recovery process, and has been used for many years by the petroleum industry to increase the efficiency of the water floods by increasing volumetric sweep efficiency and by reducing channeling and early water breakthrough. A well-established polymer model (Delshad *et al*., 1996; Delshad *et al*., 2000) has been implemented into Multiphase Reactive Transport Module (TRCHEM) in IPARS. Non-Newtonian polymer viscosity including polymer and electrolyte concentrations effects, polymer adsorption on rock surfaces, effective permeability, and effective pore volume are taken into account.

The polymer model assumptions are:

1. Isothermal conditions;
2. No chemical, mechanical, and biological degradation is modeled;
3. No chemical reactions between polymer and formation, oil, and any other components in the water phase;
4. Polymer exists in water phase only;
5. Water density is not affected by polymer;
6. Adsorbed polymer has no effect on pore volume;
7. Polymer is treated as mono-species without molecular weight distribution, so no chromatographic phenomenon occurs in porous media;
8. The adsorption of polymer on rock surface is assumed to be in equilibrium.

3.1 POLYMER PROPERTIES

3.1.1 Polymer Adsorption

The consumption of polymer in polymer flooding is due to polymer retention in porous media, which prevents polymer from being transported through the porous media. There are three retention mechanisms (Sorbie, 1991): 1) Polymer adsorption onto the rock surface; 2) Polymer mechanically entrapped in narrow pore throats; 3) Polymer hydrodynamically trapped in stagnant zones. The polymer retention depends on polymer type, polymer concentration, molecular weight, degree of hydrolysis (for HPAM), rock type, brine salinity, brine hardness, flow rate, rock permeability, temperature, etc. (Lake, 1989; Sorbie, 1991). In most practical situations, polymer adsorption is the main fundamental mechanism. Therefore, we only consider polymer adsorption as the mechanism of retention in our model.

The polymer adsorption is assumed to be irreversible with polymer concentration and reversible with salt concentration. A Langmuir-type isotherm is used to describe the polymer adsorption onto rock surface (Hirasaki and Pope, 1974). The adsorbed concentration of polymer is a function of polymer concentration, brine salinity, and permeability given by

$$\hat{C}_p = \min\left(C_p, \frac{a_4(C_p - \hat{C}_p)}{1 + b_4(C_p - \hat{C}_p)}\right) \tag{3-1}$$

where C_p is the polymer concentration in water phase, and $\hat{C}_p$ is the adsorbed concentration of polymer. The units of polymer concentration and adsorbed concentration are in *wt%* polymer in the water phase. The minimum in Eq. 3-1 is taken to

guarantee the mass balance. The ratio a_4/b_4 determines the maximum adsorption level and b_4 controls the curvature of the isotherm adsorption curve, as shown in Figure 3.1.

The parameter a_4 is calculated from

$$a_4 = (a_{41} + a_{42}C_{SEP})\left(\frac{k_{ref}}{k}\right)^{-0.5} \tag{3-2}$$

b_4, a_{41}, and a_{42} are input parameters obtained from matching laboratory polymer adsorption data. Here k_{ref} is the reference permeability at which the input adsorption parameters are specified and C_{SEP} is the effective salinity defined as

$$C_{SEP} = \max(C_{anion} + (\beta - 1)C_{d-cation},\ C_{SE1}) \tag{3-3}$$

where C_{anion} and $C_{d-cation}$ are the anion concentration and the divalent cations concentration in the aqueous phase, both in units of *meq/ml*. The influence of divalent ions such as Ca^{2+} and Mg^{2+} on polymer properties is more pronounced than that of monovalent ions (Na^+ and K^+), because of their higher charge and polarisability (Sorbie, 1991). The input parameter β is measured in the laboratory and reflects the influence of divalent cations on the polymer properties compared to monovalent cations. Here $\beta = 1$ indicates the divalent cations have the same influence on polymer properties as monovalent cations; while $\beta > 1$ implies that divalent cations have a stronger influence on the polymer viscosity. C_{SE1} is an input tolerance data.

3.1.2 Polymer Viscosity

The viscosity of the polymer solution is the most important property in polymer flooding. The high viscosity of the polymer solution decreases the water/oil mobility

ratio and increases areal and vertical sweep efficiency. The polymer viscosity is a function of brine salinity, brine hardness, polymer concentration, molecular weight, temperature, and shear rate. Polymer viscosity increases with polymer concentration whereas it decreases with increasing brine salinity. Polymer solutions exhibit non-Newtonian flow behavior, which involves both shearing and elongational flow. At low shear rates, polymer viscosity is independent of shear rate. Most EOR polymers show shear-thinning behavior where viscosity decreases as shear rate increases. Above a critical shear rate, polymer viscosity rises rapidly to a high value (Chauveteau, 1981). This non-Newtonian behavior is shown in Figure 3.2. Currently we can model either the shear thinning or shear thickening viscosity behavior. The elongational viscosity (viscoelasticity) model where both shear thinning and shear thickening occurs is not implemented at this time.

The modified Flory-Hugging equation (Flory, 1953) is used to calculate polymer viscosity at zero shear rate.

$$\mu_p^0 = \mu_w[1 + (A_{P1}C_P + A_{P2}C_P^2 + A_{P3}C_P^3)C_{SEP}^{S_p}] \tag{3-4}$$

where μ_p^0 is the polymer viscosity at zero shear rate, μ_w is the aqueous phase viscosity, A_{P1}, A_{P2}, and A_{P3} are input parameters obtained from experiments. The factor $C_{SEP}^{S_p}$ represents the dependence of polymer viscosity on salinity and hardness. The effective salinity, C_{SEP}, is given by Eq. 3-3. S_P is an input parameter corresponding to the slope of $\frac{\mu_p^0 - \mu_w}{\mu_w}$ versus C_{SEP} on a log-log plot (Figure 3.3). Figure 3.4 gives a plot of modeled polymer viscosity as a function of polymer concentration.

Meter's equation (Meter and Bird, 1964) is used to model the shear thinning behavior of polymer solution. The apparent viscosity of polymer solution μ_p is given by

$$\mu_p = \mu_w + \frac{\mu_P^0 - \mu_w}{1 + (\frac{\dot{\gamma}}{\dot{\gamma}_{1/2}})^{P_\alpha - 1}} \tag{3-5}$$

where $\dot{\gamma}_{1/2}$ is the shear rate at which the viscosity is the average of μ_P^0 and μ_w. P_α is a input parameter. The in-situ shear rate is modeled by the modified Blake Kozeny capillary bundle equation (Lin, 1981; Sorbie, 1991; Camilleri *et al*., 1987)

$$\dot{\gamma} = \frac{\dot{\gamma}_c |\vec{u}_w|}{\sqrt{\bar{k} k_{rw} \phi S_w}} \tag{3-6}$$

where $\dot{\gamma}_c$ (in $\sec^{-1}$) is an empirical shear rate coefficient from laboratory experiments, which accounts for non-ideal effects such as slip at the pre walls (Wreath *et al*.,1990; Sorbie, 1991). The average permeability $\bar{k}$ (in Darcy) is calculated from

$$\bar{k} = \left[\frac{1}{k_x} \left(\frac{u_w^x}{|\vec{u}_w|} \right)^2 + \frac{1}{k_y} \left(\frac{u_w^y}{|\vec{u}_w|} \right)^2 + \frac{1}{k_z} \left(\frac{u_w^z}{|\vec{u}_w|} \right)^2 \right] \tag{3-7}$$

$|\vec{u}_w|$ (in ft/day) is the magnitude of the Darcy velocity for water phase in each element and computed as

$$|\vec{u}_w| = \sqrt{(u_w^x)^2 + (u_w^y)^2 + (u_w^z)^2} \tag{3-8}$$

An alternative calculation of $|\vec{u}_w|$ is available for the wellblocks given by

$$|\vec{u}_w| = \frac{|q_w|}{2\pi r_{w,eff} L} \tag{3-9}$$

where q_w is the volumetric flow rate for each wellblock, L is the length of the open wellbore, $r_{w,eff}$ is the effective well radius as an input parameter with default value of the well radius. An input flag, ISHEAR, enables the alternative calculation of $|\vec{u}_w|$. Its default value is "false". This alternative calculation of $|\vec{u}_w|$ reduces the grid effect on shear rate and subsequent viscosity calculations.

A plot of calculated viscosity versus shear rate is shown in Figure 3.5.

3.1.3 Permeability Reduction

For many polymers, polymer reduces mobility solely by the increasing viscosity. However, in the case of HPAM, it also causes the effective permeability reduction, which reduces the mobility in addition to viscosity increase. The total mobility reduction contribution of polymer is measured by the resistance factor, R_F, defined as the ratio of the injectivity of water to that of a single-phase polymer solution flowing under the same conditions (Lake, 1989)

$$R_F = \frac{k_w / \mu_w}{k_p / \mu_p} = \frac{k_w}{k_p} \cdot \frac{\mu_p}{\mu_w} \tag{3-10}$$

where k_w is the effective permeability of water, k_p is the effective permeability of polymer solution.

To measure the permeability reduction effect alone, a permeability reduction factor R_k is defined as

$$R_k = \frac{k_w}{k_p} \tag{3-11}$$

The permeability reduction caused by polymer solution is irreversible and is an indicator of the degree of the channel-blocking of polymer solution. This permanent effect is called the residual resistance factor, R_{RF}, defined as

$$R_{RF} = \frac{\text{mobility before polymer solution}}{\text{mobility after polymer solution}} \tag{3-12}$$

here R_{RF} is nearly equal to R_k, but R_F is generally much larger than R_k.

The permeability reduction factor R_k is modeled as

$$R_k = 1 + \frac{(R_{k\max} - 1) b_{rk} C_p}{1 + b_{rk} C_p} \tag{3-13}$$

where

$$R_{k\max} = \min\left(\left[1 - \frac{c_{rk} (A_{P1} C_{SEP}^{S_p})^{1/3}}{\left(\sqrt{k_x k_y} / \phi \right)^{1/2}} \right]^{-4}, \quad rkcut \right) \tag{3-14}$$

where c_{rk} and b_{rk} are input parameters obtained from laboratory data. The input parameter *rkcut* is used as the upper limit of permeability reduction. Here R_k is sensitive to polymer type, polymer concentration, molecular weight, degree of hydrolysis, shear rate, salinity, permeability, and porosity. Typical plots of R_k as function of permeability and polymer concentration are given in Figures 3.6 and 3.7. The viscosity of the aqueous phase is multiplied by R_k to account for the permeability reduction.

3.1.4 Inaccessible Pore Volume

Dawson and Lantz first reported that polymer molecules travel faster than other species in water phase when the polymer retention is low (Dawson and Lantz, 1972).

Many laboratory experiments have confirmed this phenomenon (Willhite and Dominguez, 1977; Chauveteau, 1982). Dawson and Lantz named this phenomenon as inaccessible pore volume (IPV). The effect of inaccessible pore volume accelerates the polymer flow velocity, which offsets the delay caused by polymer retention. There are two explanations for IPV. The one proposed by Dawson and Lantz is that the polymer is excluded from certain pores that have smaller size than the polymer molecules, which means polymer travels a shorter pathway than other smaller size species. Thus even if the Darcy velocity is the same, the breakthrough time is shorter. The second explanation is based on the idea of the wall exclusion effect of the porous media to large polymer molecules (Chauveteau and Zaitoun, 1981; Auvray, 1981). Here polymer molecules aggregate in the center of the pore and travel with high velocities. IPV is more pronounced when polymer molecular weight increases and the ratio of permeability to porosity decreases.

An input constant, the effective pore volume, used to model the inaccessible pore volume effect, is defined as

$$\phi_e = 1 - IPV / \phi \tag{3-15}$$

The porosity in the mass conservation equation for polymer is multiplied by the effective pore volume as

$$\frac{\partial(\phi\phi_e C_p S_w)}{\partial t} + \nabla \cdot C_P u_w - \phi\phi_e S_w D_p \nabla C_p = q_p \tag{3-16}$$

3.2 POLYMER MODULE IMPLEMENTATION

An input flag in IPARS, POLYMER, is used to enable the polymer module. The default value is "false". When the POLYMER model is enabled, species 1, 2, and 3 in TRCHEM must be polymer, anion, and divalent cations, respectively. Polymer properties are modeled in **trpolymer.df** in TRCHEM. The phase-summed variable ϕ_i^* in Eq. 2-15 for polymer is modified with respect to inaccessible pore volume. In every concentration step, polymer adsorption is calculated after solving Eq. 2-15 and the polymer concentration is updated. The polymer viscosity and permeability reduction are calculated only once after all concentration steps. The flow chart of the polymer module is shown in Figure 3.8.

3.3 NUMERICAL EXAMPLES

Five numerical examples are presented here. Cases 1 and 2 are run to verify IPARS with UTCHEM. The parallel capability of IPARS is also tested in Case 1. In Cases 3 and 4, we investigate the influence of shear rate calculations in both homogeneous and heterogeneous reservoirs, respectively. In Case 5 we study the grid effects in polymer flood simulating.

3.3.1 Case 1: 3D Homogeneous Isotropic Reservoir

An isotropic homogeneous reservoir is considered in this case. All boundaries are closed to flow. Fluids and rock are incompressible. Physical dispersion/diffusion is neglected. One quarter of a 5-spot well pattern is simulated. The injector is rate

constrained. A 0.05 *wt%* polymer solution is continuously injected into the reservoir at a rate of 20 *bbls/day* for 1000 days. The producer is pressure constrained with bottomhole pressure of 300 *psi*. The wells penetrate through the entire reservoir thickness. Table 3.1 lists the reservoir description, fluid properties and polymer property input parameters. Brook-Corey type relative permeabilities and capillary pressures are used (Figure 3.9). Figure 3.10 shows the reservoir geometry and well locations.

IPARS polymer simulations are tested on both single processor and multiple processors. For the purpose of verification, the results are compared with UTCHEM. Here single point upstream is used to control numerical dispersion in both IPARS and UTCHEM. The modeled polymer properties are presented in Figures 3.11 through 3.13. The low shear polymer viscosity corresponding to the injected polymer concentration of 0.05 *wt%* is about 8.65 *cp* (Figure 3.11). The non-Newtonian shear thinning behavior is shown in Figure 3.12, where the viscosity is reduced to about 1.93*cp* at shear rate of about 100 sec^{-1}. The polymer adsorption is about 6$\mu g/g$ as shown in Figure 3.13.

The simulation results are shown for a horizontal slice. Profiles of water pressure, water saturation, polymer concentration, and polymer viscosity at 500 days and 1000 days are plotted in Figures 3.14 through 3.21 for single processor IPARS and UTCHEM. Histories of injector bottomhole pressure, oil cut, cumulative oil recovery, and effluent polymer concentration are shown in Figures 3.22 through 3.25 for UTCHEM, and both single processor and multiple processor IPARS. The well data agree very well between IPARS and UTCHEM. There is a very slight discrepancy in the profiles due to different

visualization softwares used to create these images. The single processor result and multiple processor results of IPARS are identical.

3.3.2 Case 2: 3D Heterogeneous Anisotropic Reservoir

This case simulates a polymer flooding pilot test based on Chateaurenard field (Putz, 1988). Takaqi *et al*. (1991) reported a successful simulation using UTCHEM. A 3D heterogeneous anisotropic reservoir with unconfined inverted 5-spot well pattern is modeled for the verification purpose and results are compared with those obtained from UTCHEM. Single point upstream is used to control numerical dispersion in both IPARS and UTCHEM. All boundaries are closed to flow. Fluids and rock are incompressible. Physical dispersion/diffusion is neglected. Capillary pressure is neglected and Brook-Corey type relative permeability is used. The permeability distribution, porosity distribution, and relative permeabilities are illustrated in Figures 3.26 through 3.28.

The polymer solution is continuously injected at a variable injection rate for 742 days followed by a chase water flood. The injection scheme and polymer concentration grading are shown in Figures 3.29 and 3.30. The producers are pressure constrained with bottomhole pressures of 300 *psi*. The wells penetrate through the entire reservoir thickness. Table 3.2 lists the reservoir description, fluid properties and polymer property input parameters for Case 2.

The modeled polymer properties are presented in Figures 3.31 through 3.33. Figure 3.31 shows the low shear polymer viscosity as a function of injected polymer concentration. The non-Newtonian shear thinning behavior is shown in Figure 3.32 for

0.1 *wt%* polymer solution with the plateau value of 28.6 *cp*. Figure 3.33 shows the polymer adsorption as a function of polymer concentration with the plateau value of about 64 $\mu g/g$.

The profiles are shown for 2D areal slices of the top and bottom layers. Profiles of water pressure, water saturation, polymer concentration, and polymer viscosity at 1500 days are plotted in Figures 3.34 through 3.41. Histories of injector bottomhole pressure, cumulative oil recovery, oil cut, and effluent polymer concentration for each producer are shown in Figures 3.42 through 3.45. The comparison is very satisfactory between the results of IPARS and UTCHEM.

3.3.3 Case 3: Grid Effect Study for Homogeneous Isotropic Reservoir

Two uniform grids are generated from the reservoir in Case 2 with 15x15x3 and 105x105x3 gridblocks. Case 2 is modified to a homogeneous isotropic reservoir to avoid the need for permeability and porosity scale-up. The permeability is 1500*md* and the porosity is 0.2. All other input parameters and injection scheme are the same as Case 2. We simulated each case with different shear rate calculations of either Eq. 3-8 or Eq. 3-9. Here, we name the coarse grid with Eq. 3-8 as Run 1, the coarse grid with Eq. 3-9 as Run 2, the fine grid with Eq. 3-8 as Run 3, and the fine grid with Eq. 3-9 as Run 4.

The injector bottomhole pressure history is compared in Figure 3.46. As expected, there is a large difference between pressures of Run1 (peak about 6500 *psi*) and Run 2 (peak about 2800 *psi*) since linear fluxes are much smaller compared to radial flow flux. This will result in lower shear rate and higher polymer viscosity in the

wellblock in Run 1 compared to Run 2. Therefore the bottomhole pressure of Run1 is much higher than that of Run 2. For fine mesh of Runs 3 and 4, the difference in bottomhole pressure is much smaller because of the much smaller velocity difference. The difference between Run 2 and Run 4 is from the grid effect on polymer concentration. With the same injection rate and injection polymer concentration, the polymer concentration in large injection wellblock (coarse mesh) is lower than that in small injection wellblock (fine mesh) at the beginning. The polymer viscosity in the wellblock of Run 2 is lower than that of Run 4. Therefore, the bottomhole pressure of Run 2 is lower than that of Run 4. As the injection polymer concentration is decreased, the grid effect on both shear rate and polymer concentration is also reduced. And finally the grid effect disappears when the polymer concentration of the wellblock approaches to zero.

The history of average reservoir pressure is compared in Figure 3.47. The difference in average reservoir pressure is much smaller than the difference in bottomhole pressure since the impact of shear rate calculation is only for near wellblock region and the average polymer concentration is nearly the same. The cumulative oil recovery and average reservoir oil saturation histories are compared in Figures 3.48 and 3.49. The cumulative oil recovery and average reservoir oil saturation are very similar for these runs. It seems that the choice of the grid has very little impact on the cumulative oil recovery and the average reservoir oil saturation. However, the performance of individual producers is affected by the grid sizes and shear rate calculations as shown in Figure 3.50. The oil recoveries from each producer are very similar in the fine grid

simulations of Runs 3 and 4. The oil recoveries of Run 2 are in better agreement with the fine mesh simulations compared to Run 1. The results imply that the alternative shear rate calculation of Eq. 3-9 reduces the grid effect present with the coarse mesh. The oil cut and the effluent polymer concentration in individual producer are shown in Figures 3.51 and 3.52 respectively. The results of Runs 3 and 4 are very close. The difference between results of Runs 1 and 2 are relatively small compared to the difference between fine mesh and coarse mesh, which implies that the grid resolution and subsequent numerical dispersion is more crucial than the shear rate calculation for oil cut and effluent polymer concentration. The differences in oil cut and effluent polymer concentration between coarse and fine mesh vary from producer to producer.

We conclude that the alternative flux calculation in the wellblocks effectively reduces the grid effect mainly caused by shear rate and subsequent impact on polymer viscosity. The most sensitive parameter is the injection bottomhole pressure where it is computed more accurately with the alternative wellblock flux computation. Overall results, such as cumulative oil recovery and average reservoir oil saturation are not very sensitive to the grid resolution. However the performance of each producer is greatly impacted by the grid sizes. The above conclusions are drawn for homogeneous isotropic reservoir. We will investigate the influence of wellblock shear rate calculations in a heterogeneous anisotropic reservoir in the next subsection.

3.3.4 Case 4: Grid Study in Heterogeneous Anisotropic Reservoir

Case 2 with different wellblock shear rate calculation is compared. Here, Run 1 stands for the simulation with Eq. 3-8 and Run 2 stands for the simulation with Eq. 3-9.

The injector bottomhole pressure is nearly 3 times higher in Run 1 compared to Run 2 (Figure 3.53) similar to the trend observed in Case 3 with homogeneous permeability. The average reservoir pressure shown in Figure 3.54 indicates slightly higher values for Run 1 compared to Run 2. The cumulative oil recovery shown in Figure 3.55 gives similar results for both simulations. The average reservoir oil saturation is not sensitive to the wellblock shear rate calculations (Figure 3.56). However, there are relatively small differences in oil recovery from each producer as shown in Figure 3.57. The oil cut and the effluent polymer concentration histories in each producer are shown in Figures 3.58 and 3.59. The shear rate calculations have very little effect on oil cut and polymer concentration in each producer.

3.3.5 Case 5: Scale-up Problem

In this case, we compare the simulation results of different grids generated from the same geological model. Seven different grids are generated for an anisotropic heterogeneous reservoir described in Table 3.3. We used four areal meshes as shown in Figure 3.60. The initial oil saturation is 0.8 and the reservoir is at hydrostatic equilibrium. The permeability and porosity distributions, residual water and oil saturations are scaled based on a single-phase scale-up scheme and shown in Figures 3.61 through 3.66 for the finest grid (Grid02) and the coarsest grid (Grid04). The reservoir dimensions are slightly

different, while the total pore volume and original oil in place are kept the same. The water/oil capillary pressure is neglected and Brook-Corey type relative permeability is used.

There are 10 injection wells and 7 production wells to form a 7-spot well pattern. The wells are partially penetrated. The well locations are adjusted with the grids to make sure the wells are in the center of each element. Figure 3.67 shows the well locations for Grid02 and Grid04. Injectors are rate constrained and the injectors on the reservoir boundary are treated as half a well where their injection rates are half of that of the center injectors. The producers are pressure constrained with the bottomhole pressures of 300*psi*. The injection starts with water preflush for 300 days (about 4PV) until the overall water cut from all producers reaches 0.98; a slug with 0.15wt% polymer is then injected for 220 days (about 1PV) at a lower injection rate; followed by water postflush for 80 days. The injection scheme is listed in Table 3.4. Table 3.5 lists the reservoir description, fluid properties and polymer property input parameters for Case 5.

These simulations are performed on Bevo's cluster located in the Center for Subsurface Modeling. The cluster has 90 dual-core AMD Athlon processors with core frequency of 2.00 GHz and memory of 2 GB per core. The number of processors, the CPU time, and time steps are shown in Table 3.6. Simulations with few elements are run on a single processor and those with more elements are run on up to 24 processors. The total CPU time ranged from 2,534*sec* to as high as 124,229*sec*. The computational efficiency is not the main purpose of this case, so the time steps and number of processors are not optimized.

The modeled polymer properties are presented in Figures 3.68 through 3.70. The low shear polymer viscosity corresponding to the injected polymer concentration of 0.15 *wt%* is about 12 *cp* (Figure 3.68). The non-Newtonian shear thinning behavior is indicated in Figure 3.69, where the viscosity is reduced to about 4 *cp* at shear rate of about 100 sec^{-1}. We use low polymer adsorption of about 7 $\mu g/g$ (Figure 3.70).

Figure 3.71 shows the average reservoir pressure for same vertical resolution but different areal resolution grids (Grids 01, 02, 03 and 04). The average reservoir pressures of coarse areal meshes (Grids 03 and 04) are higher than those of fine areal meshes (Grids 01 and 02) during the preflush water flood (first 300 days). The difference of average reservoir pressure (about 100psi) is from the different reservoir properties after areal scale-up. The change in average reservoir pressure after the polymer flood starts is complex due to the combined effects of polymer properties and scale-up. The difference in average reservoir pressure significantly reduces after the polymer flood switches to water flood. The average reservoir pressures for same areal resolution but different vertical resolution are shown in Figures 3.72 and 3.73 for areal meshes of 43x47 (Grids 01, 05 and 06) and 22x24 (Grids 03 and 07) respectively. For grids with the same areal mesh, the average reservoir pressure during waterflood is not sensitive to the scale-up in the vertical direction. However the average reservoir pressure during the polymer injection increases more rapidly when more layers are used. Simulations with finer areal mesh yield higher oil recovery than those using coarser areal mesh but with the same vertical resolution as shown in Figure 3.74. The difference in cumulative oil recovery increases at early times of waterflood and is stable until the polymer flood begins, and it

reduces a little due to lower injection rate imposed during polymer flood. The results indicate that even waterflood results show great sensitivity to the choice of the grid as a result of single-phase upscaling procedure for reservoir properties. The cumulative oil recoveries for same areal resolution but different vertical resolution are shown in Figures 3.75 and 3.76 for areal meshes of 43x47 and 22x24 respectively. The cases with fewer vertical layers yield higher oil recovery due to less permeability contrast as a result of property averaging and better vertical equilibrium.

Figures 3.77 through 3.79 illustrate comparisons of average reservoir oil saturation for grids with different areal resolutions or different vertical resolutions.

The oil cut increases significantly after the polymer flood starts regardless of the grid resolution as shown in Figures 3.80 through 3.82. Figure 3.80 indicates that the simulations with coarser areal mesh breakthrough earlier than those with finer areal mesh but same vertical resolution because of larger numerical dispersion associated with larger grid sizes. Figures 3.81 and 3.82 show that the oil cut in the grids with more vertical layers increases more than that of the grids with fewer vertical layers after the polymer flood starts. This increase in oil cut confirms that polymer flood effectively sweeps and produces the oil left by waterflood due to geological heterogeneity.

The effluent polymer concentration in producer no. 1 (the central producer) is compared in Figures 3.83 through 3.85 for grids with different areal resolutions or different vertical resolutions. Figure 3.83 shows the earlier breakthrough of polymer in coarse areal mesh as observed in Figure 3.80. The effluent polymer concentration of the

grid with more vertical layers is slightly higher than that of the grid with fewer vertical layers.

Figures 3.86 and 3.87 show the areal cross sections of oil saturation in the top, middle, and bottom layers at 300 days and 600 days for Grid01 and Grid04. It is evident that there is more oil left behind at the end of the flood for the coarse grid of Grid04 compared to the fine mesh of Grid01.

3.4 SUMMARY

A polymer module is implemented in TRCHEM module of IPARS framework, which enables parallel simulations of non-Newtonian polymer flow through porous media. Polymer properties including power law viscosity, adsorption, inaccessible pore volume, and permeability reduction are modeled. The polymer adsorption is modeled as a function of polymer concentration, salinity, and hardness. The polymer viscosity is treated as a function of polymer concentration, salinity, hardness, and shear rate. The shear thinning behavior of polymer solution is modeled. An alternative wellblock shear rate calculation is available to reduce the grid effect for coarse mesh simulations. Permeability reduction is modeled as a function of polymer concentration, salinity, hardness, permeability and porosity. Inaccessible pore volume is also considered.

Five numerical examples have been successfully simulated with the polymer module. The results of Case 1 and Case 2 have been compared to those obtained from UTCHEM and no significant difference is observed indicating the accuracy of the

module. The parallel capability is tested in Case 1. The results of single processor and multiple processors are compared and they are identical.

The gird effect on the simulation results is investigated in Case 3 and Case 4. We observed that the alternative wellblock flux calculation effectively reduces the grid effect caused by shear rate calculation for coarse mesh. The most sensitive parameter to the grid sizes is injection bottomhole pressure. Some parameters, such as cumulative oil recovery and average reservoir oil saturation are not sensitive to the grid sizes. However, the grid resolution does affect the performance of individual producers, such as oil recovery, oil cut, and effluent polymer concentration. The above conclusions are applicable to both homogeneous isotropic and heterogeneous anisotropic reservoirs studied.

In Case 5, we compared the simulation results of 7 different grids generated from a reservoir by a single phase upscaling scheme. Simulations with fine areal meshes yield higher oil recovery than those using coarse areal meshes but with the same vertical resolution. The results indicate that even waterflood results show great sensitivity to the choice of the grid size as a result of single-phase upscaling procedure for reservoir properties. The cases with fewer vertical layers yield higher oil recovery due to less permeability contrast as a result of property averaging and better vertical equilibrium.

Table 3.1 Input Data for Case 1

Parameters	Values	Parameters	Values
Ω [ft]	400x400x20	a_{41}	0.7
grids	50x50x1	a_{42}	0.0
ϕ	0.2	b_4	100
K [md]	100	b_{rk}	1000
S_{wirr}	0.37	c_{rk}	0.0186
S_{ar}	0.35	β	10
k_{rw}^0	0.11	S_p	0.17
k_{aw}^0	0.95	C_{SE1}	0.01
n_w	1.0	$\dot{\gamma}_{1/2}$	20
n_a	2.16	$\dot{\gamma}_c$	10
C_{pc}	9.0	ϕ_e	0.8
E_{pc}	2.0	P_α	1.8
$P_{o,init}$ [psi]	510.15	A_{p1}	81
$S_{o,init}$	0.6	A_{p2}	2700
ρ_w [lb/ft^3]	62.42	A_{p3}	2500
ρ_o [lb/ft^3]	53.05	$c_{poly,init}$[wt%]	0.0
μ_w [cp]	0.86	$c_{anion,inj}$ [meq/ml]	0.3
μ_o [cp]	4.0	$c_{cation,inj}$[meq/ml]	0.001
$c_{anion,init}$ [meq/ml]	0.4	$c_{poly,inj}$[wt%]	0.05
$c_{cation,init}$[meq/ml]	0.003		

Table 3.2 Input Data for Case 2

Parameters	Values	Parameters	Values
Ω [ft]	1640.505x1640.505x10.824	a_{41}	8.66
grids	15x15x3	a_{42}	0.0
S_{wirr}	0.2	b_4	100
S_{ar}	0.2	b_{rk}	100
k_{rw}^0	0.2	c_{rk}	0.2
k_{aw}^0	1.0	β	20
n_w	1.5	S_p	-0.3
n_a	2.0	C_{SE1}	0.01
$P_{o,\,init}$ [psi]	967.06	$\dot{\gamma}_{1/2}$	280
$S_{o,\,init}$	0.62	$\dot{\gamma}_c$	130
ρ_w [lb/ft^3]	62.4964	ϕ_e	0.85
ρ_o [lb/ft^3]	55.6214	P_α	2.2
μ_w [cp]	0.73	A_{p1}	38.47
μ_o [cp]	40.0	A_{p2}	1600
$c_{anion,\,init}$ [meq/ml]	0.00831	A_{p3}	0
$c_{cation,\,init}$ [meq/ml]	0.00551	$c_{anion,\,inj}$ [meq/ml]	0.00831
$c_{poly,\,init}$ [wt%]	0.0	$c_{cation,\,inj}$ [meq/ml]	0.00551

Table 3.3 Grids Description for Case 5

	Ω [ft]	**grids**	**Total Element**	**Active Ω [ft]**	**Active grids**	**Active elements**	**Pore Volume [bbls]**	**OOIP [bbls]**
Grid01	2100x2400x37	43x47x19	38399	1650x1875x37	37x40x19	28120	462311	3705849
Grid02	2100x2400x37	86x94x19	153596	1650x1875x37	74x80x19	112480	462311	3705849
Grid03	2100x2400x37	22x24x19	10032	1725x1875x37	19x20x19	7220	462311	3705849
Grid04	2100x2400x37	11x12x19	2508	1875x1875x37	10x10x19	1900	462311	3705849
Grid05	2100x2400x37	43x47x10	20210	1650x1875x37	37x40x10	14800	462311	3705849
Grid06	2100x2400x37	43x47x5	10105	1650x1875x37	37x40x5	7400	462311	3705849
Grid07	2100x2400x37	22x24x10	5280	1725x1875x37	19x20x10	3800	462311	3705849

Table 3.4 Injection Scheme for Case 5

Wells	**Preflush Rate [stb/day]** **(** $0 < t \leq 300$ **days)**	**Polymer flooding Rate [stb/day]** **(** $300 < t \leq 520$ **days)**	**Postflush Rate [stb/day]** **(** $520 < t \leq 600$ **days)**
Injector 1-Injector 6	8000	2500	2500
Injector 7-Injector 10	4000	1250	1250

Table 3.5 Input Data for Case 5

Parameters	Values	Parameters	Values
k_{rw}^0	0.3	a_{41}	1.0
k_{aw}^0	0.7	a_{42}	0.0
n_w	2.0	b_4	100
n_a	2.0	b_{rk}	100
$S_{o,\,init}$	0.8	c_{rk}	0.04
ρ_w $[lb/ft^3]$	62.42	β	1
ρ_o $[lb/ft^3]$	54.3472	S_p	-0.4
μ_w $[cp]$	0. 3	C_{SE1}	0.01
μ_o $[cp]$	2.7	$\dot{\gamma}_{1/2}$	35
$c_{anion,\,init}$ [meq/ml]	0.0513	$\dot{\gamma}_c$	4
$c_{cation,\,init}$ [meq/ml]	0.0	ϕ_e	1.0
$c_{poly,\,init}$ [wt%]	0.0	P_α	1.55
$c_{anion,\,inj}$ [meq/ml]	0.0513	A_{p1}	30
$c_{cation,\,inj}$ [meq/ml]	0.0	A_{p2}	280
$c_{poly,\,inj}$ [wt%]	0.15	A_{p3}	350

Table 3.6 Parallel Computation Information for Case 5

	Processors	**CPU time [sec]**	**Initial Δt [day]**	**Δt multiplier**	**Max Δt [day]**	**Min Δt [day]**
Grid01	8	14271	0.002	1.001	0.02	0.0002
Grid02	24	124229	0.001	1.001	0.01	0.0001
Grid03	4	11078	0.005	1.001	0.05	0.0005
Grid04	1	2534	0.01	1.001	0.1	0.001
Grid05	4	11908	0.002	1.001	0.02	0.0002
Grid06	4	7422	0.002	1.001	0.02	0.0002
Grid07	2	6806	0.005	1.001	0.05	0.0005

Table 3.7 Simulation Results Summary Table for Case 5

	Average Oil Saturation			**Average Oil Cut [fraction]**			**Oil Recovery [%OOIP]**		
	after WF	after PF	Final	after WF	after PF	Final	after WF	after PF	Final
Grid01	0.353	0.276	0.268	0.00188	0.00562	0.00115	55.8	65.5	66.5
Grid02	0.350	0.274	0.265	0.00186	0.00554	0.00109	56.3	65.8	66.8
Grid03	0.413	0.324	0.315	0.00213	0.00607	0.00112	48.4	59.5	60.6
Grid04	0.425	0.342	0.332	0.00210	0.00646	0.00150	46.9	57.3	58.5
Grid05	0.335	0.263	0.255	0.00194	0.00532	0.00112	58.2	67.1	68.1
Grid06	0.317	0.252	0.244	0.00198	0.00510	0.00115	60.4	68.5	69.5
Grid07	0.400	0.313	0.304	0.00207	0.00633	0.00118	49.9	60.9	62.0

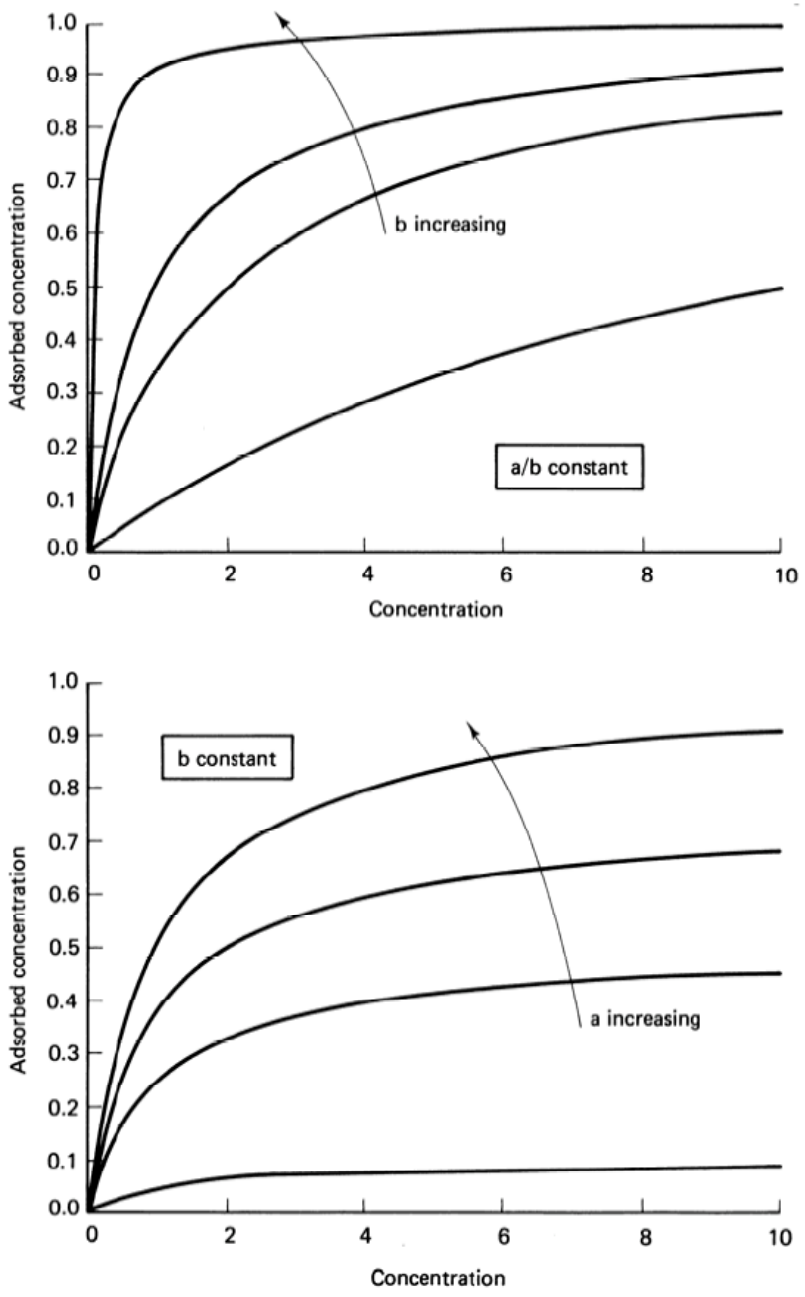

Figure 3.1 Typical Langmuir-Type Isotherm Adsorption Curves (from Lake, 1989)

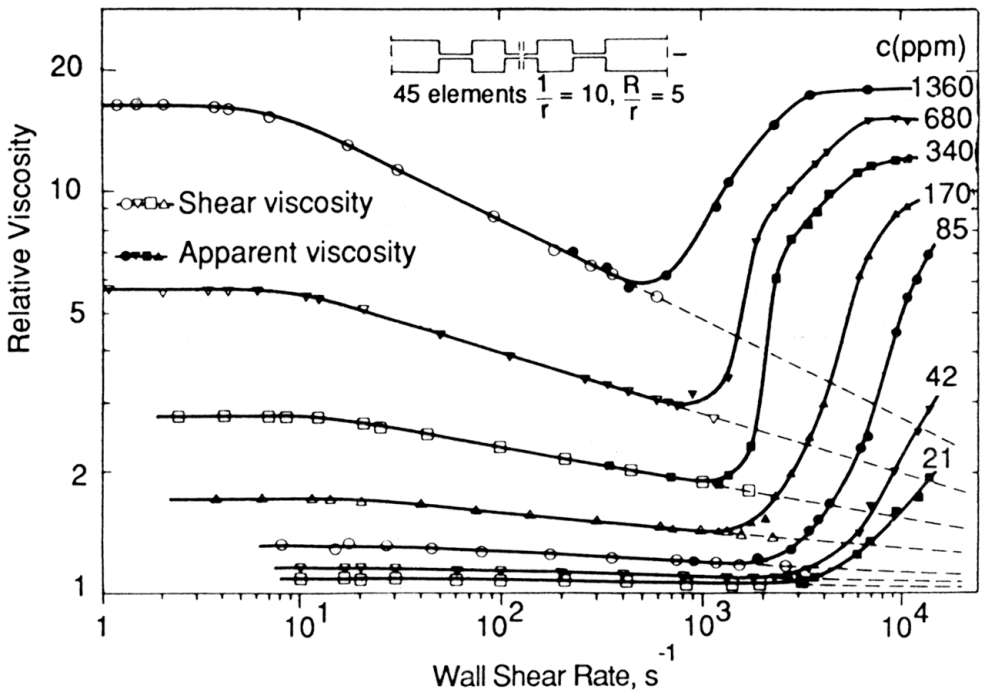

Figure 3.2 Relative Viscosity of HPAM versus Shear Rate (from Chauveteau, 1981)

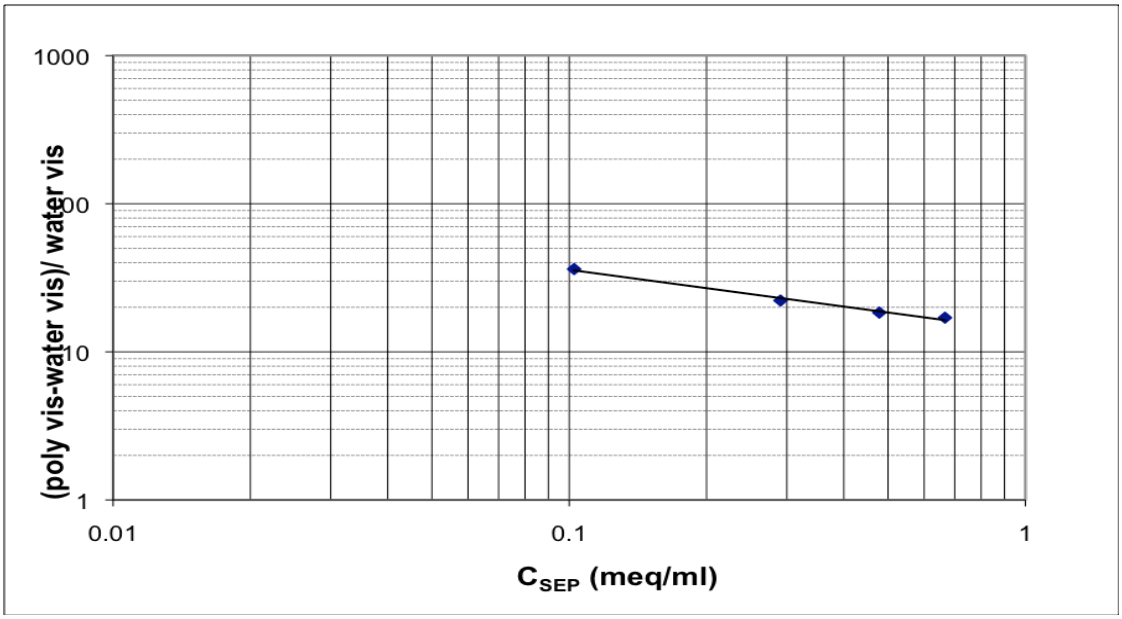

Figure 3.3 Effect of Salinity on Polymer Viscosity

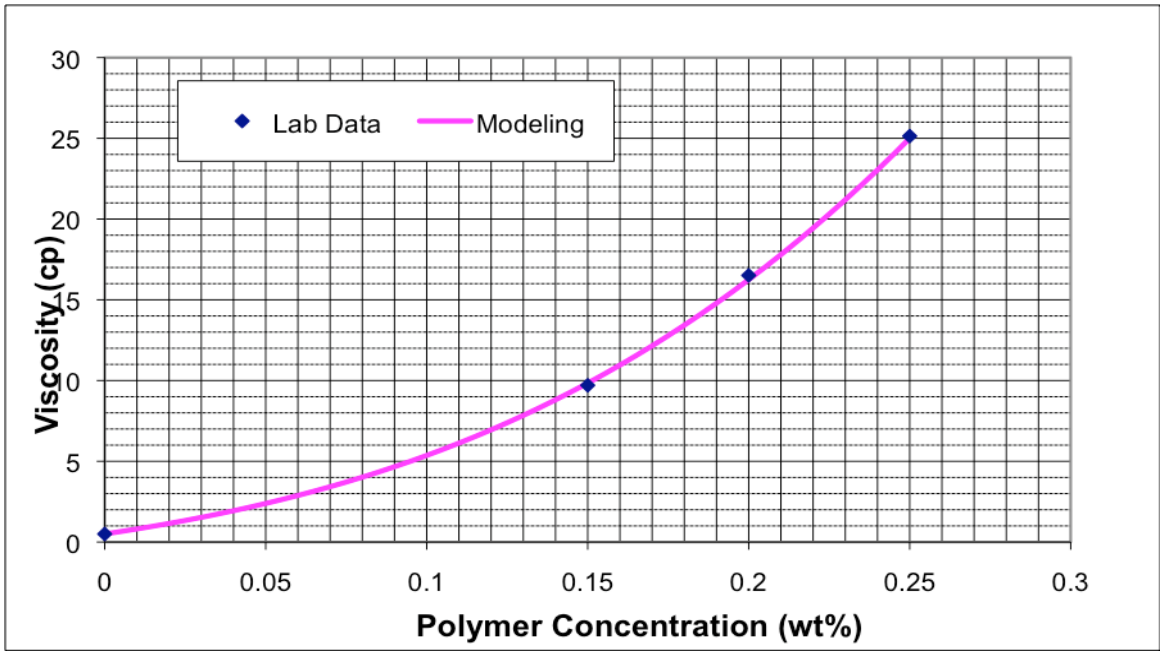

Figure 3.4 Polymer Viscosity versus Polymer Concentration

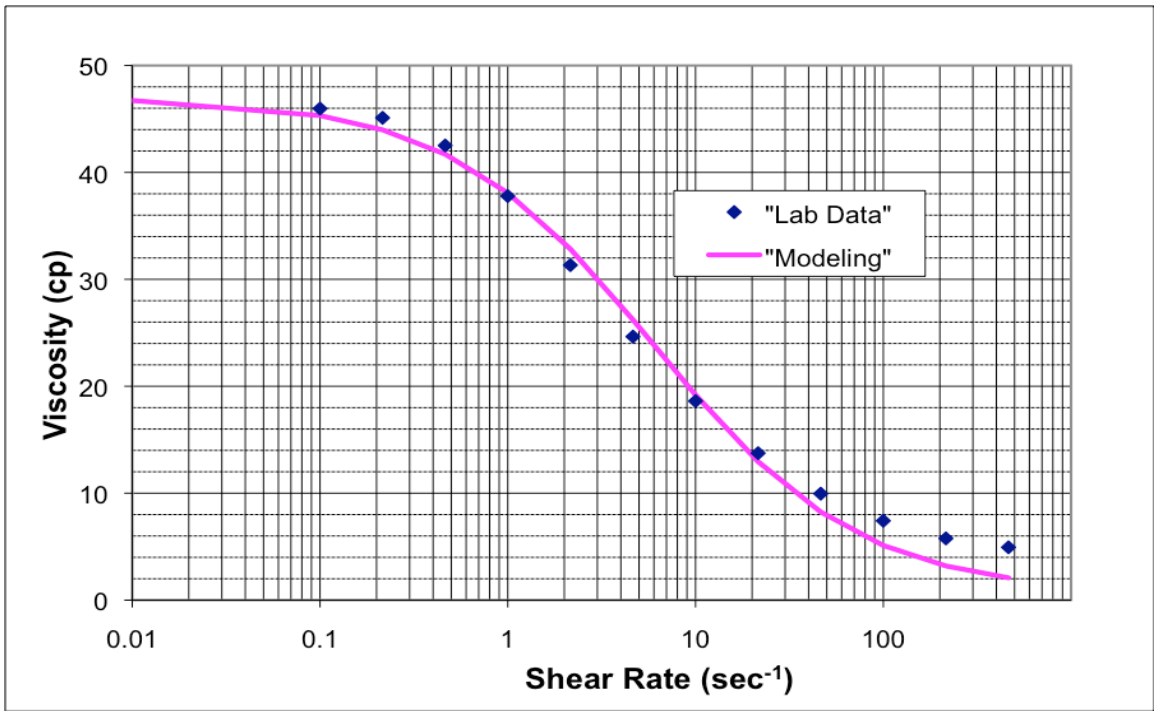

Figure 3.5 Polymer Viscosity versus Shear Rate

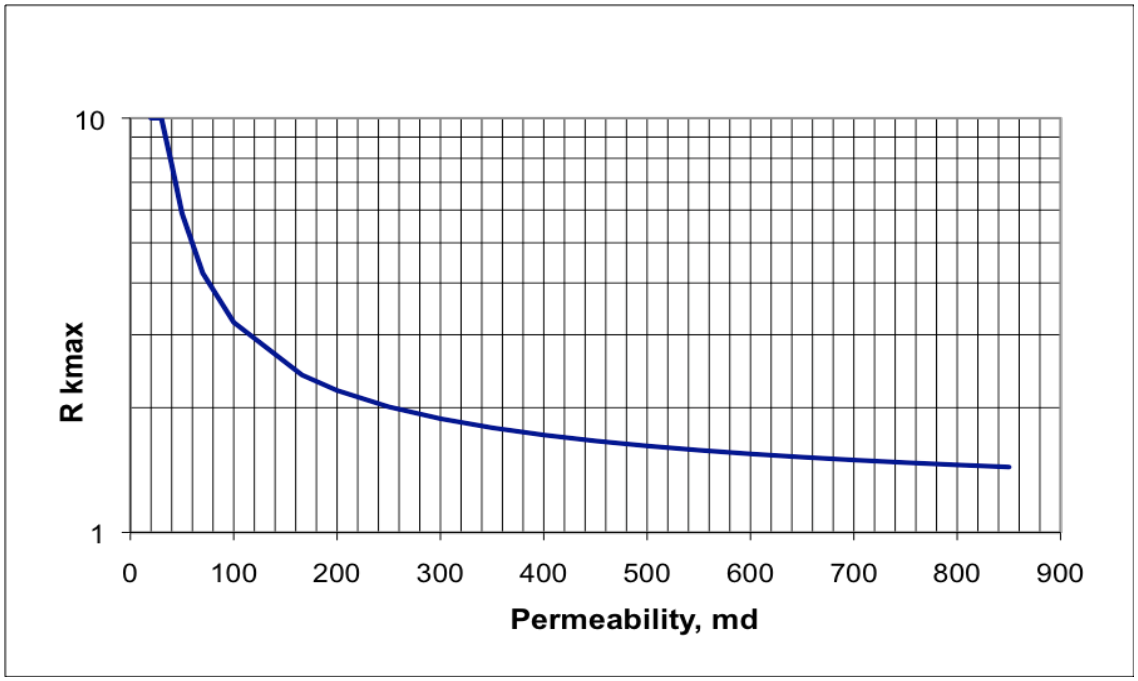

Figure 3.6 Maximum Permeability Reduction Factor ($R_{k\max}$) versus Permeability

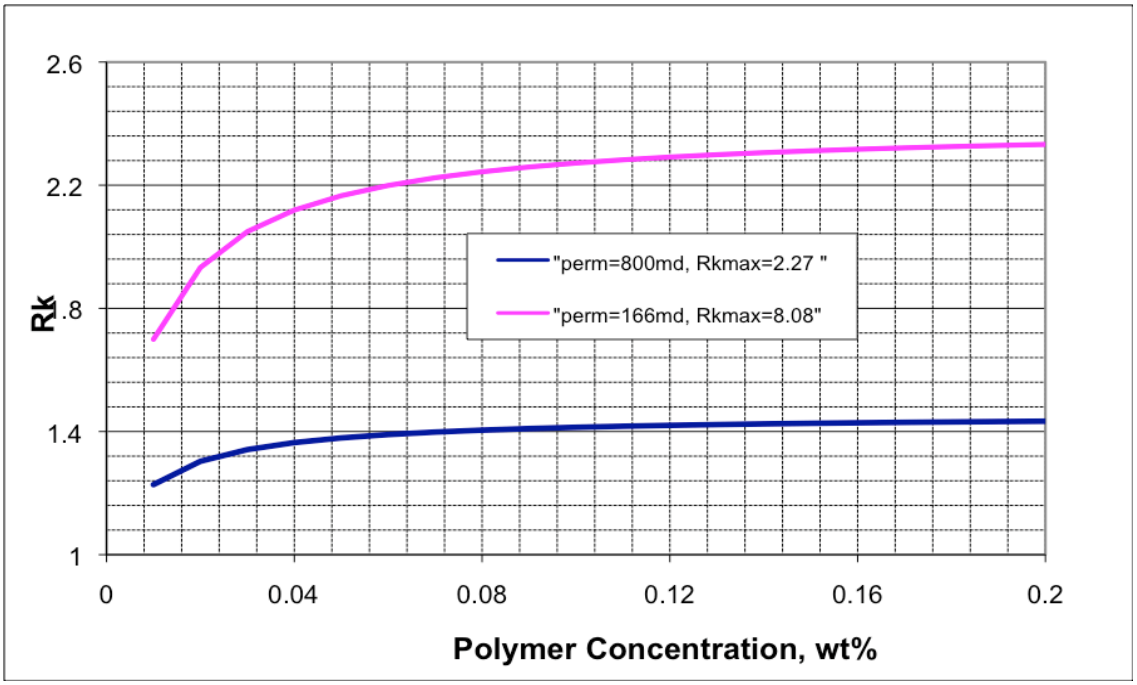

Figure 3.7 Permeability Reduction Factor (R_k) versus Polymer Concentration

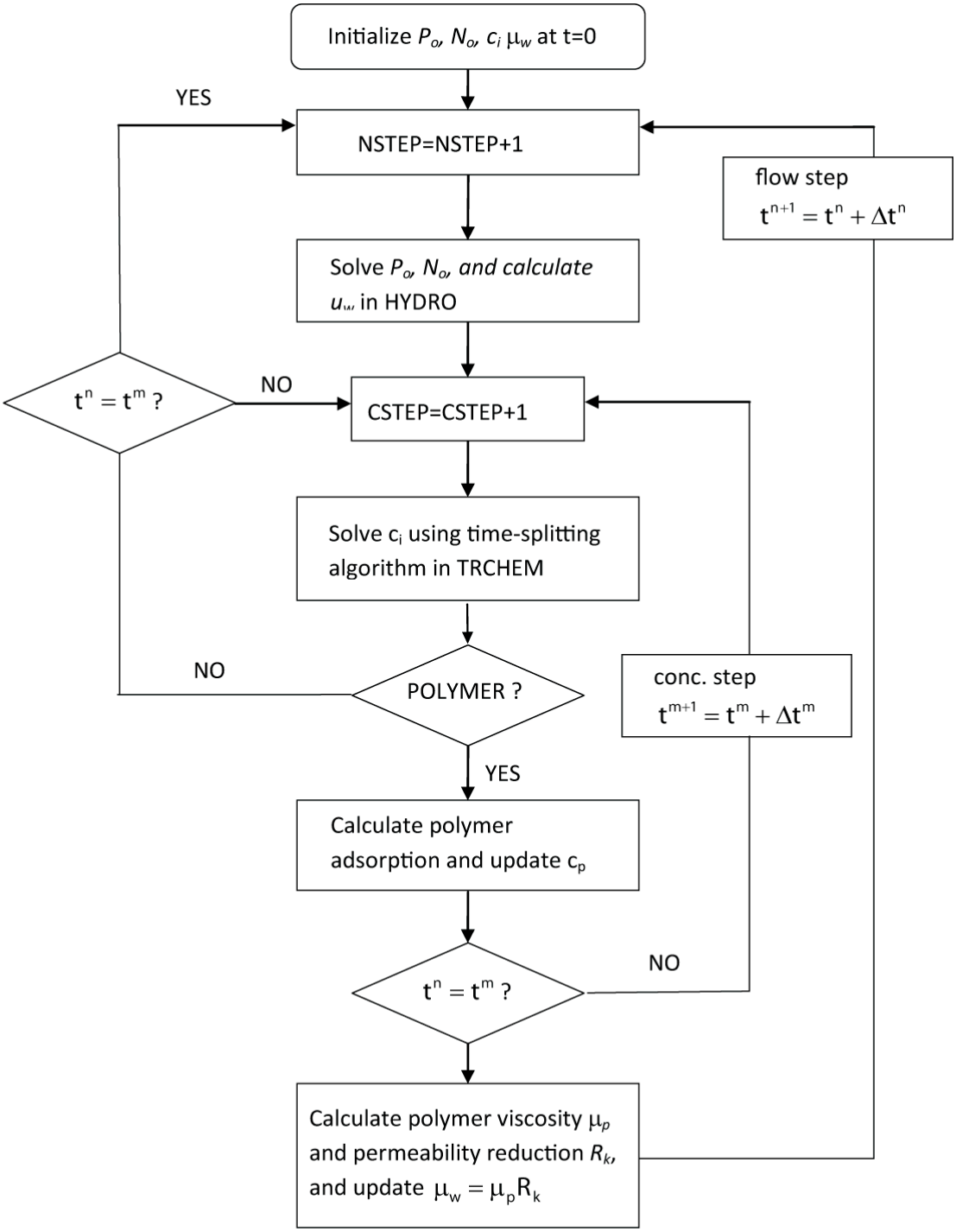

Figure 3.8 Flow Chart for Polymer Flood Module

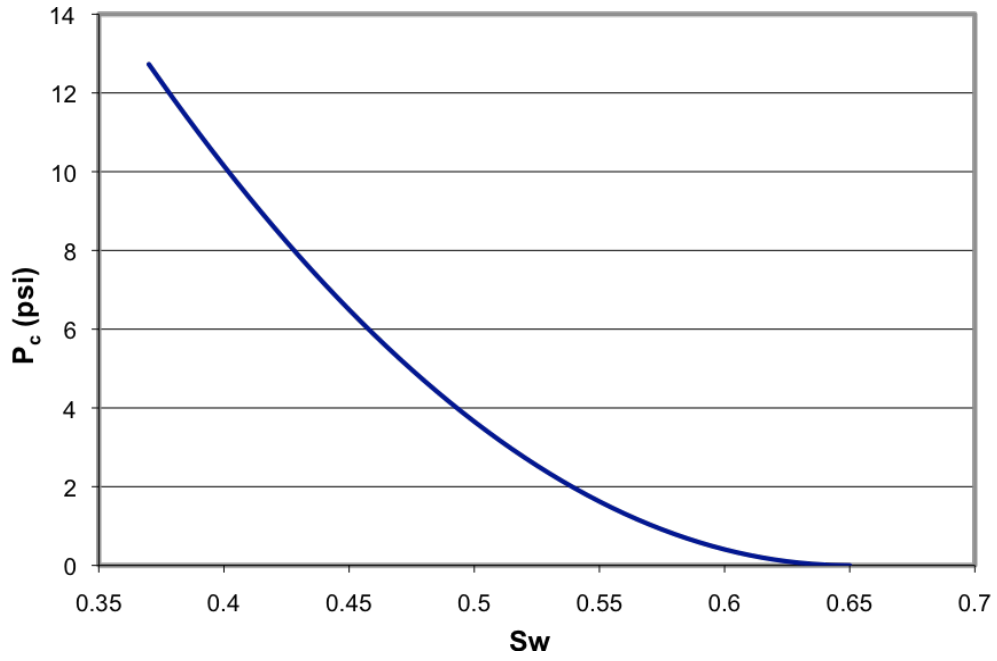

(a) Oil/Water Capillary Pressure versus Water Saturation

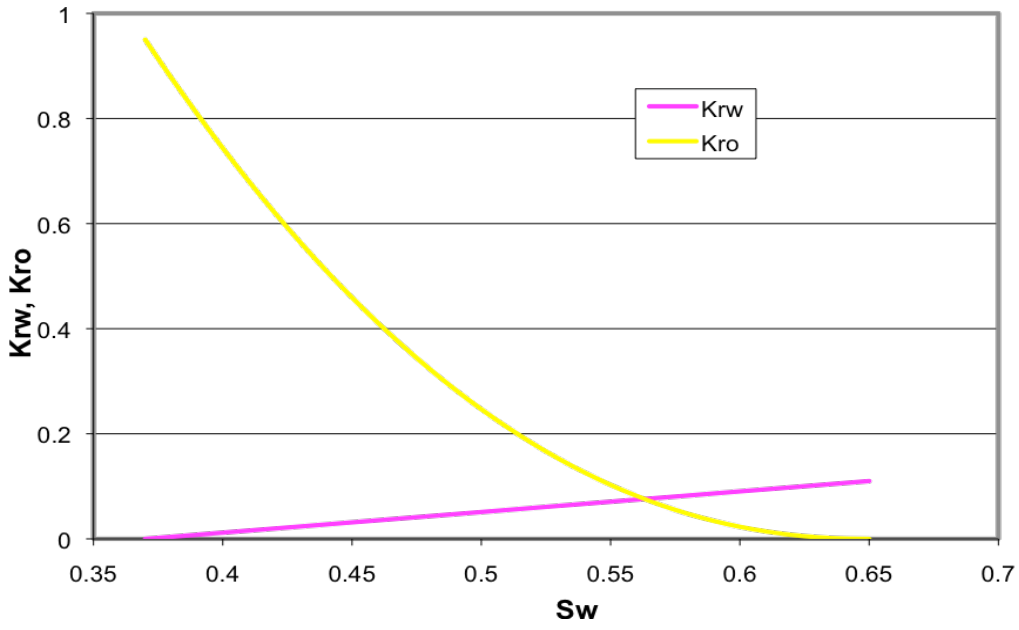

(b) Relative Permeability versus Water Saturation

Figure 3.9 Oil/water Capillary Pressure and Relative Permeability Curves for Case 1

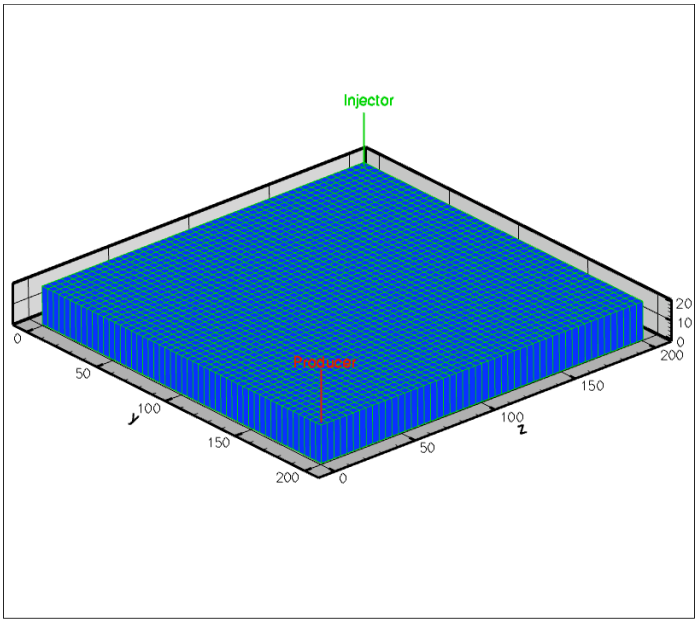

Figure 3.10 Reservoir Geometry and Well Locations for Case 1

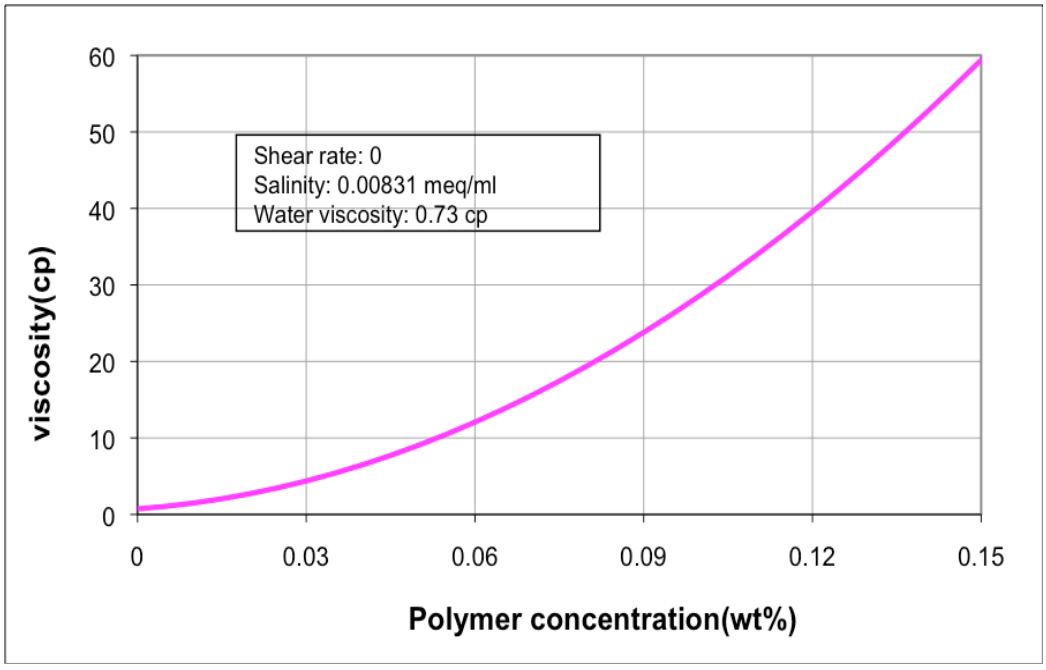

Figure 3.11 Bulk Polymer Viscosity as a Function of Polymer Concentration for Case 1

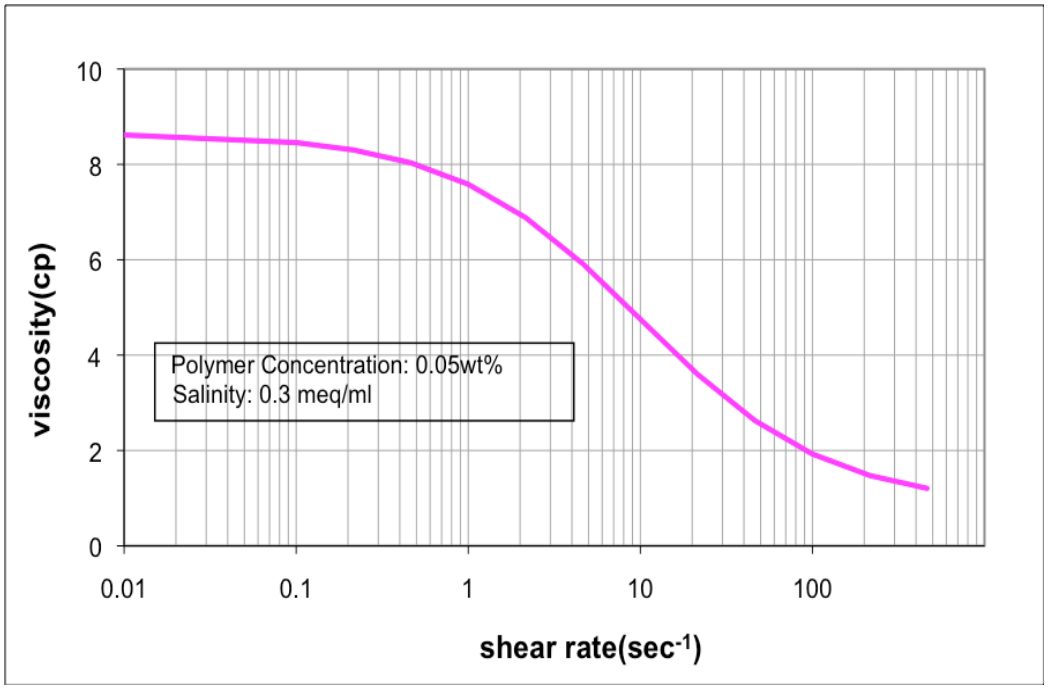

Figure 3.12 Bulk Polymer Viscosity as a Function of Shear Rate for Case 1

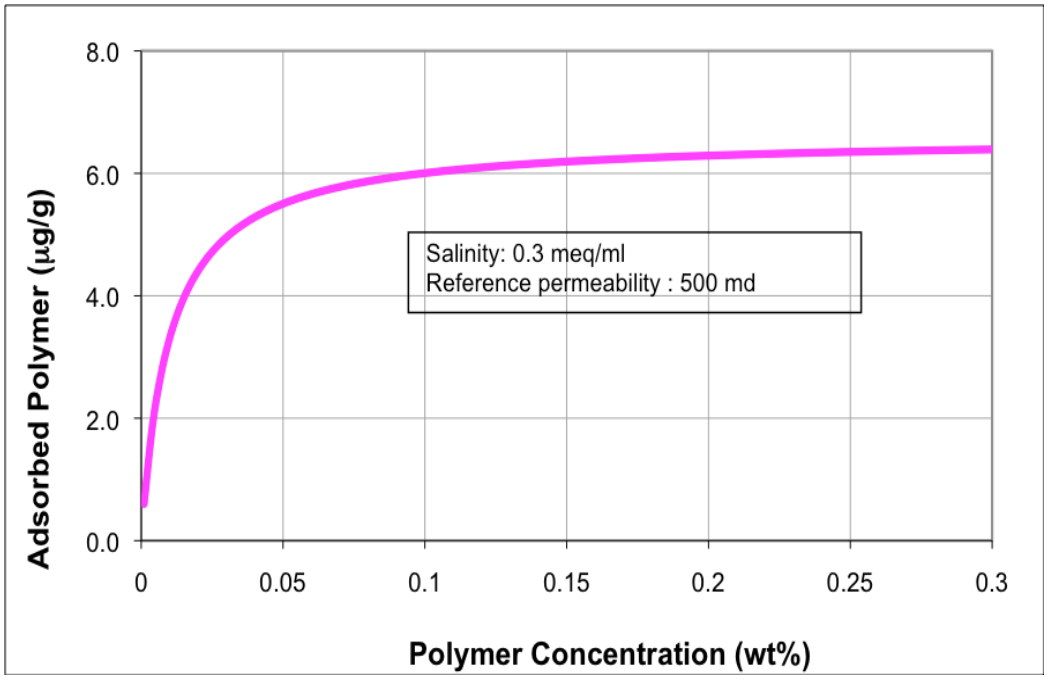

Figure 3.13 Polymer Adsorption as a Function of Polymer Concentration for Case 1

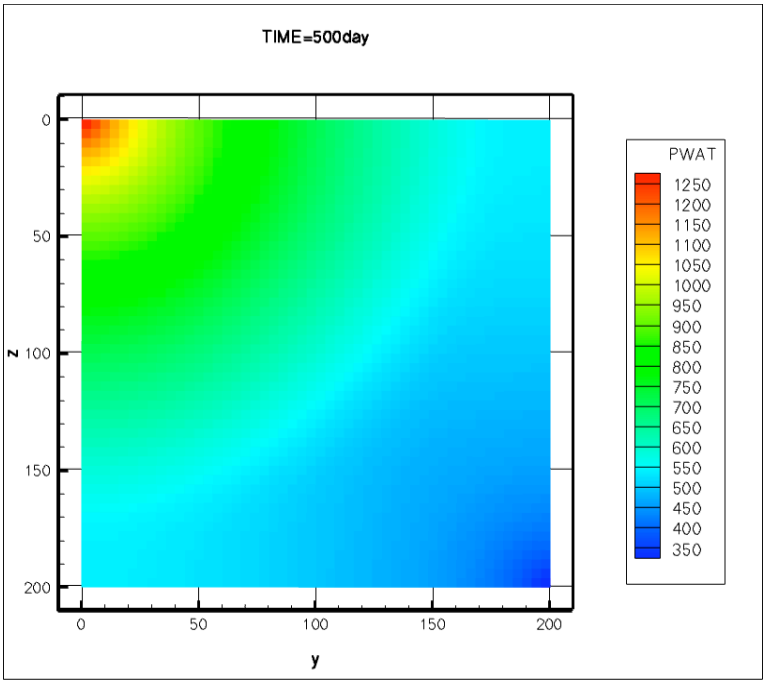

(a) IPARS

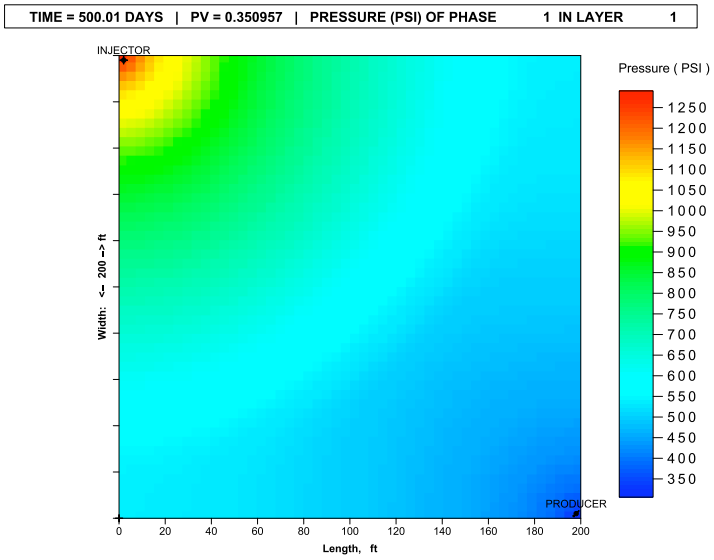

(b) UTCHEM

Figure 3.14 Water Pressure Profiles for Case 1 at 500 Days

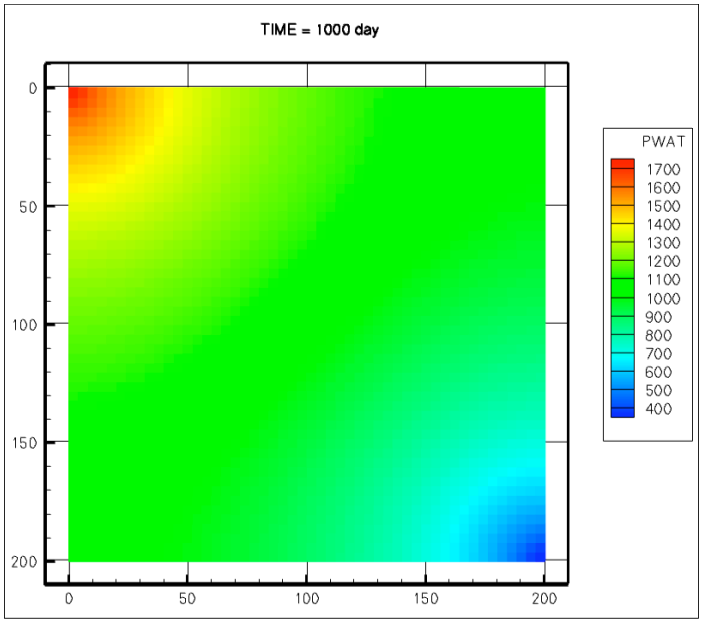

(a) IPARS

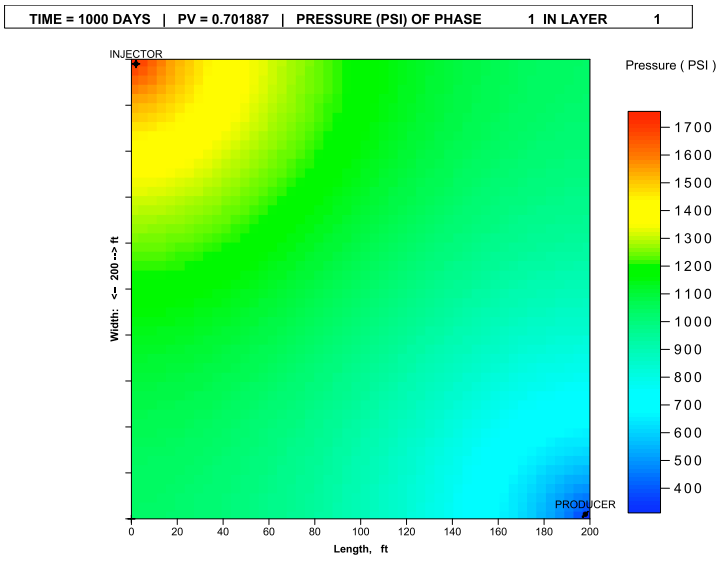

(b) UTCHEM

Figure 3.15 Water Pressure Profiles for Case 1 at 1000 Days

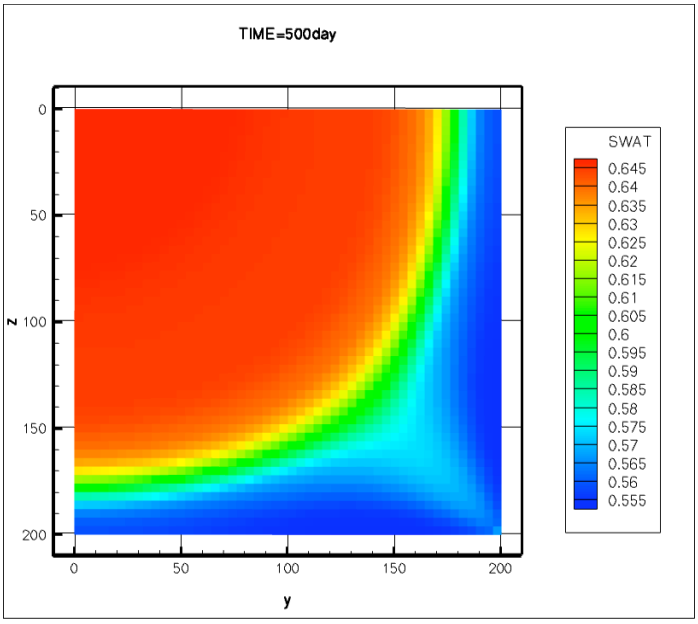

(a) IPARS

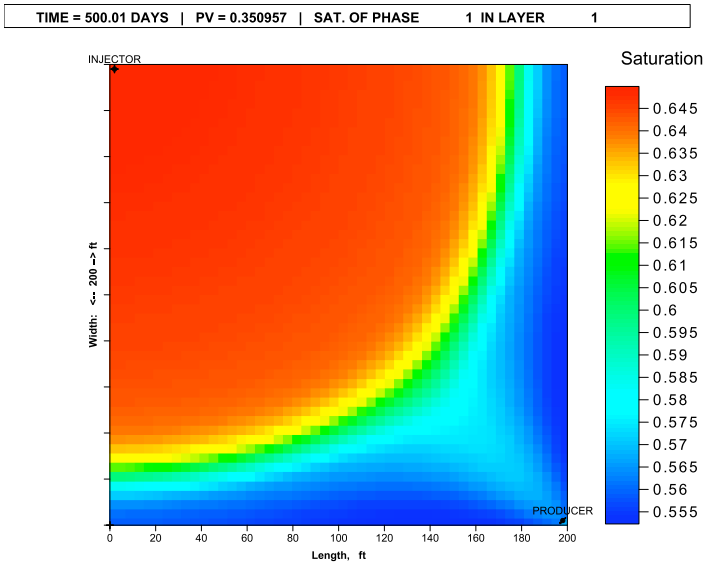

(b) UTCHEM

Figure 3.16 Water Saturation Profiles for Case 1 at 500 Days

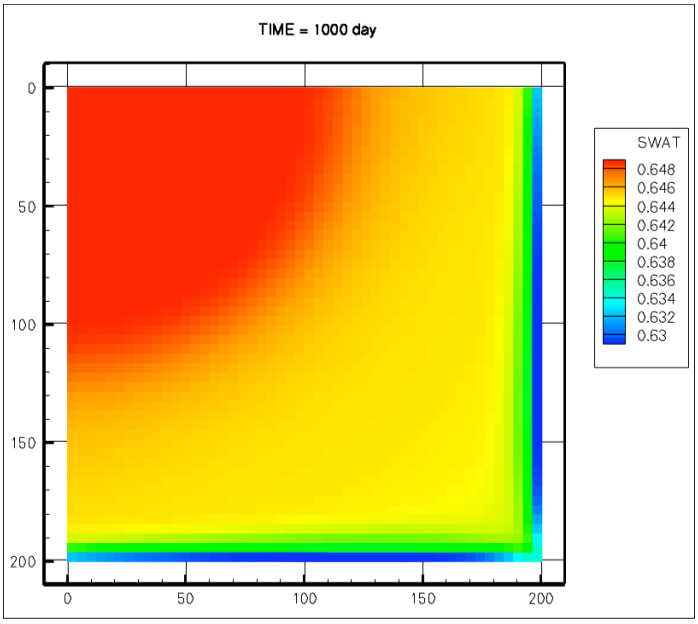

(a) IPARS

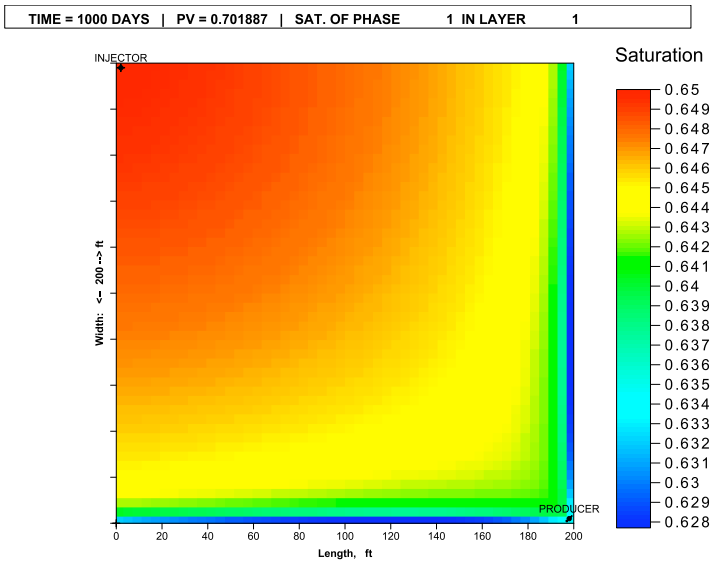

(b) UTCHEM

Figure 3.17 Water Saturation Profiles for Case 1 at 1000 Days

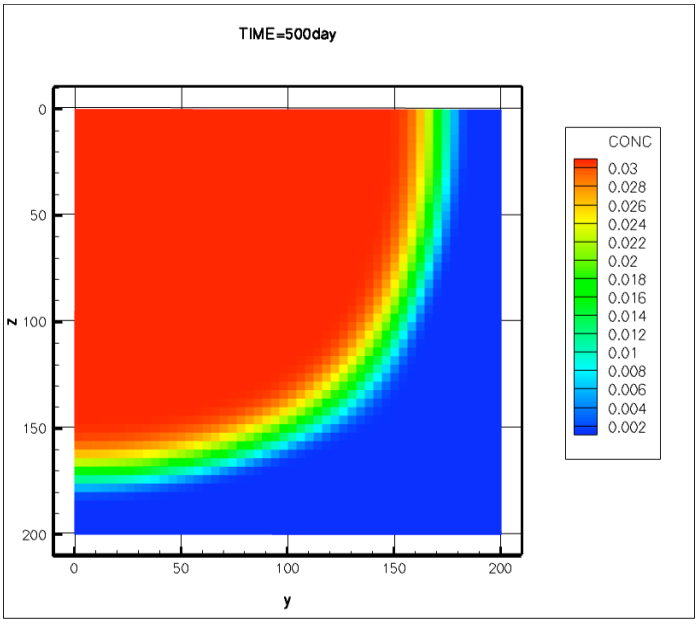

(a) IPARS

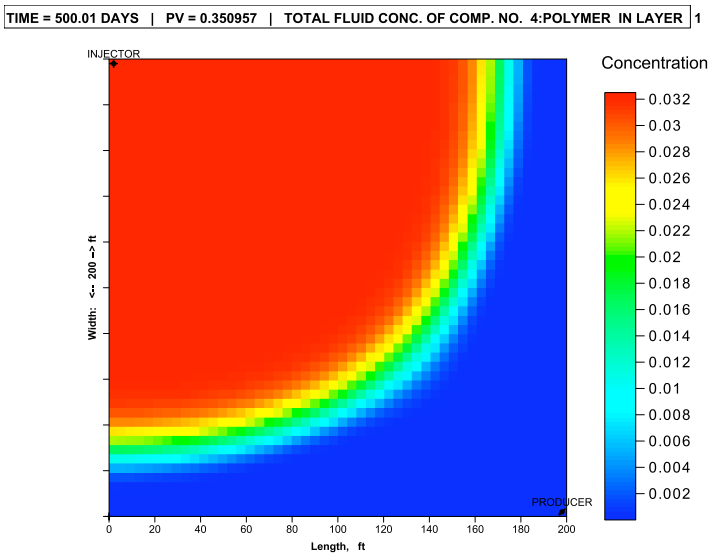

(b) UTCHEM

Figure 3.18 Polymer Concentration Profiles for Case 1 at 500 Days

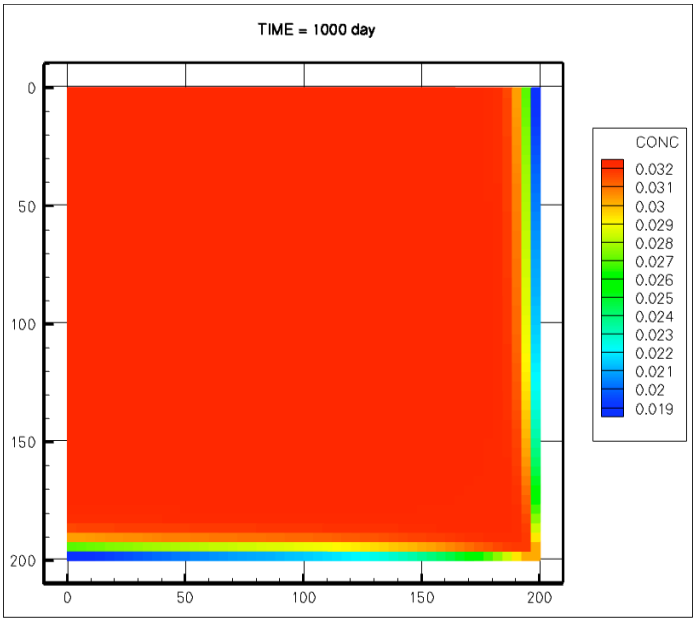

(a) IPARS

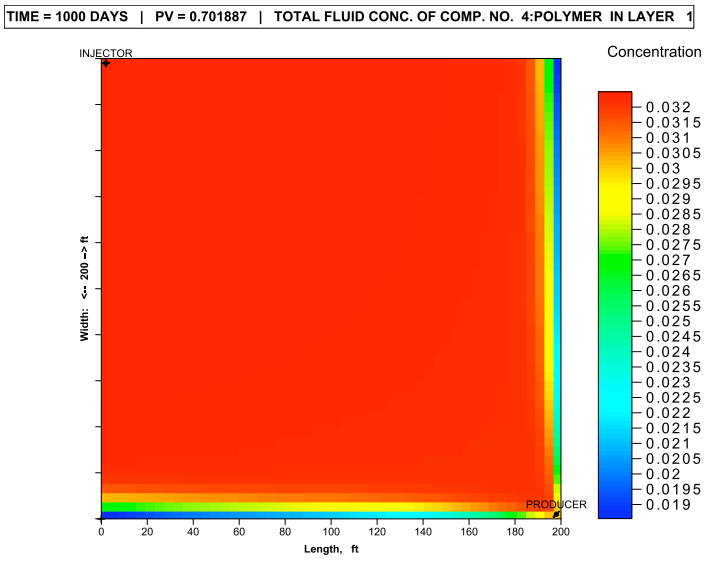

(b) UTCHEM

Figure 3.19 Polymer Concentration Profiles for Case 1 at 1000 Days

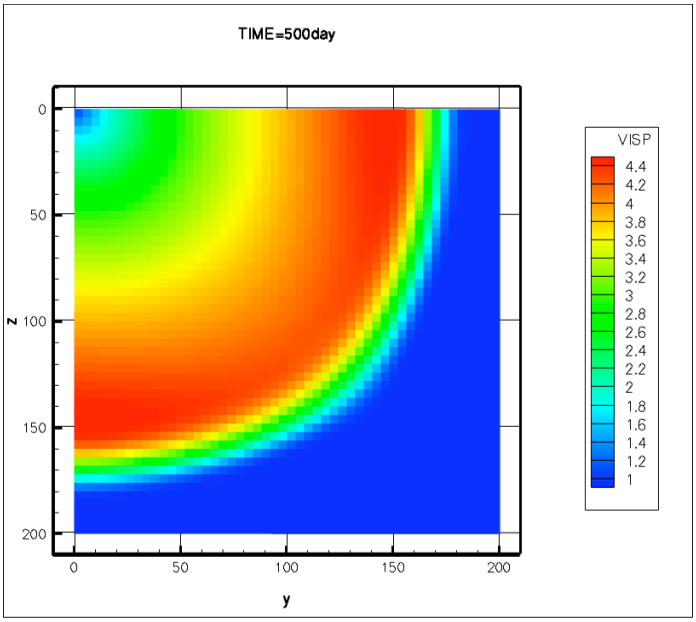

(a) IPARS

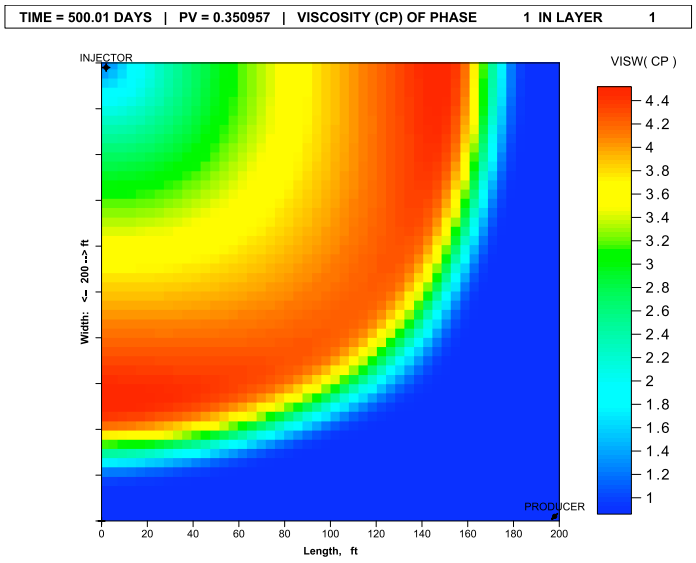

(b) UTCHEM

Figure 3.20 Polymer Viscosity Profiles for Case 1 at 500 Days

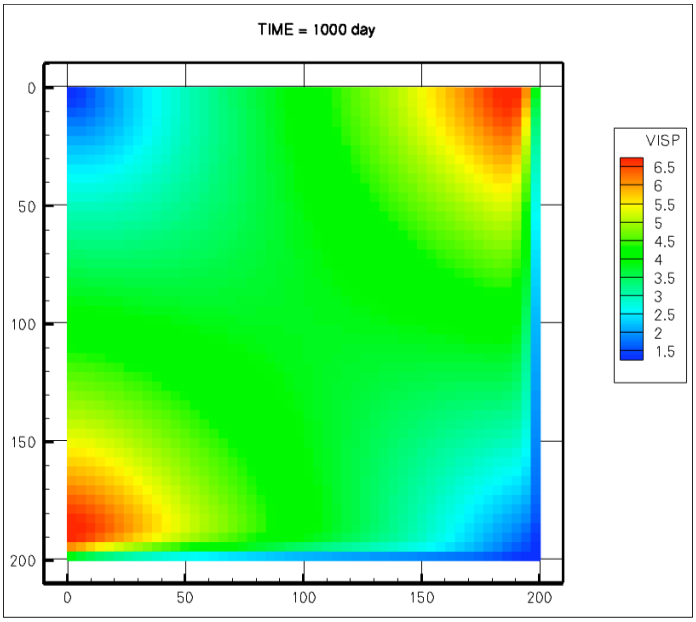

(a) IPARS

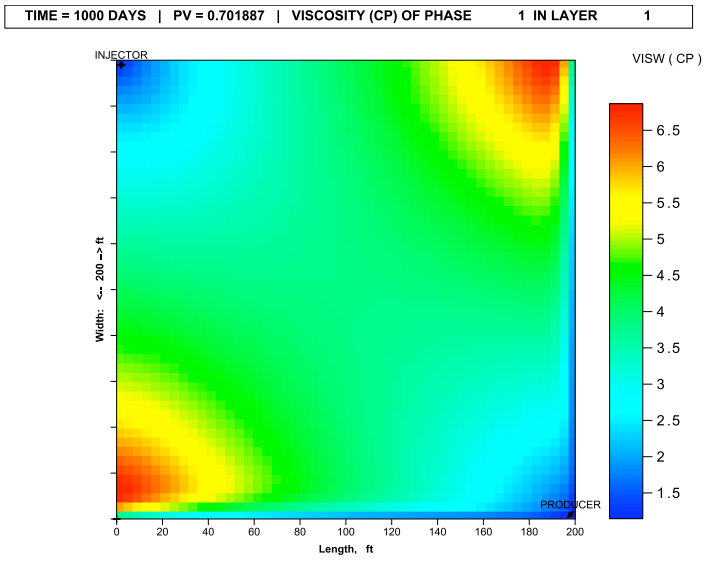

(b) UTCHEM

Figure 3.21 Polymer Viscosity Profiles for Case 1 at 1000 Days

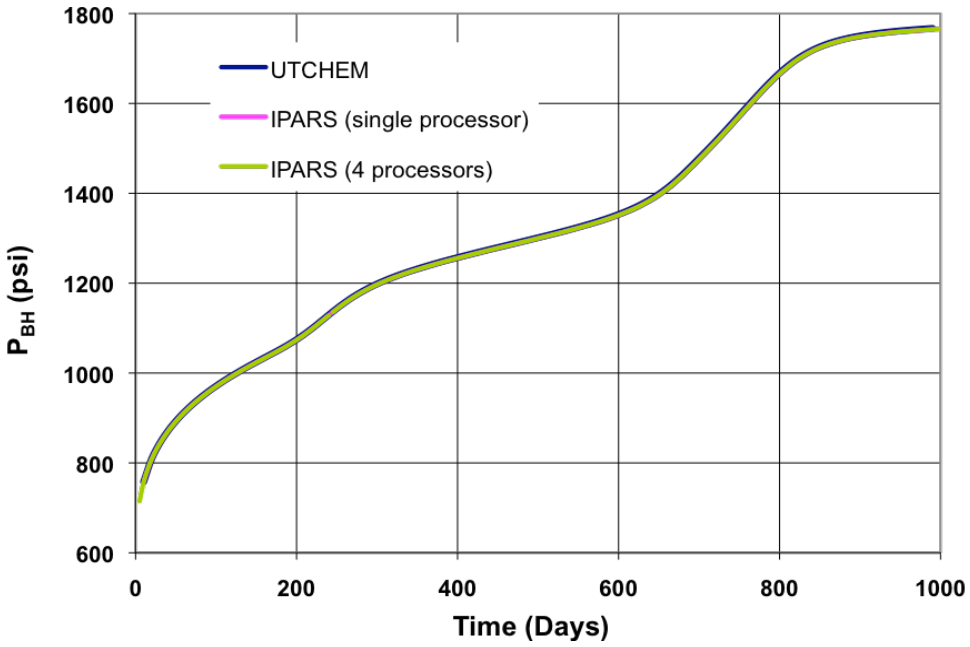

Figure 3.22 Injector Bottomhole Pressure History for Case 1

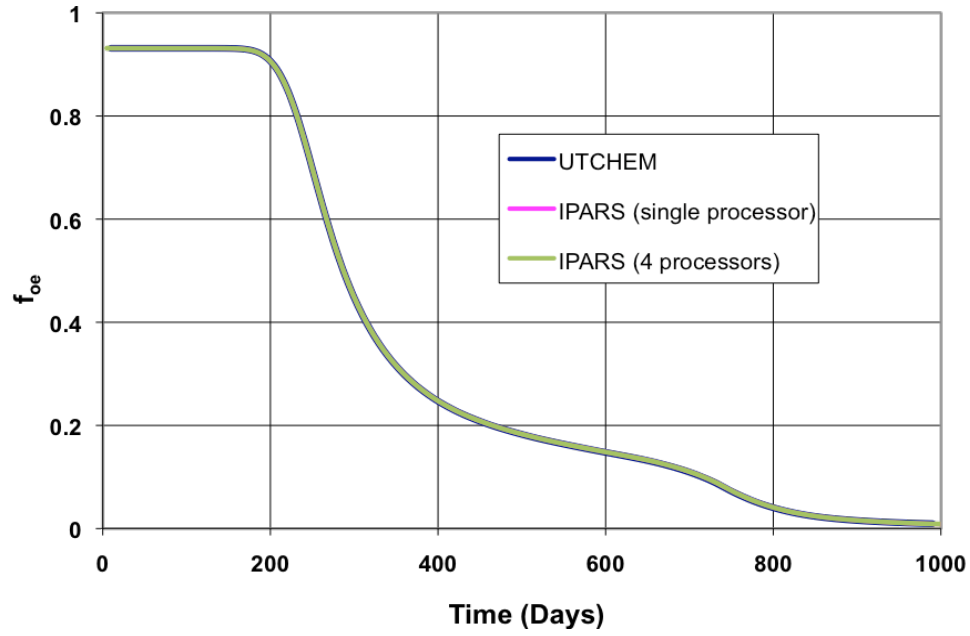

Figure 3.23 Oil Cut History for Case 1

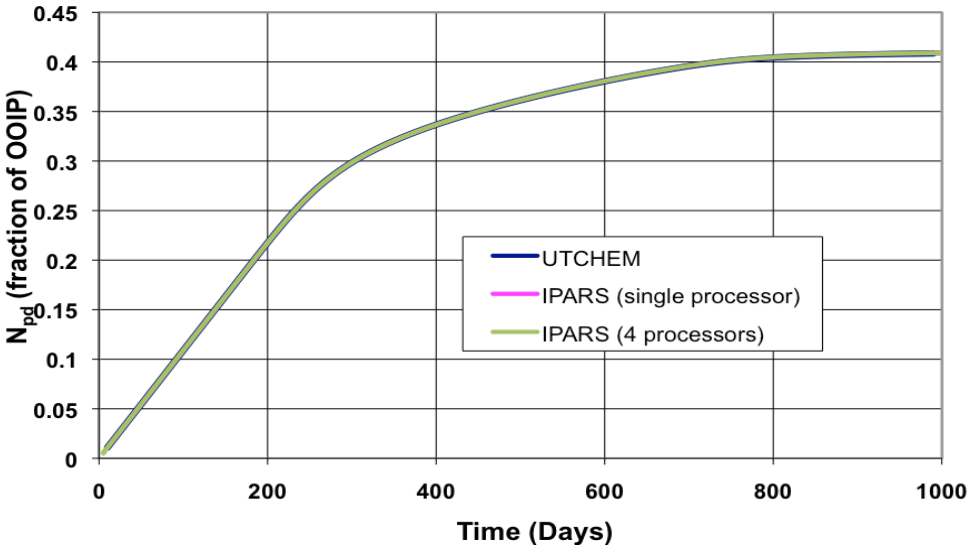

Figure 3.24 Cumulative Oil Recovery for Case 1

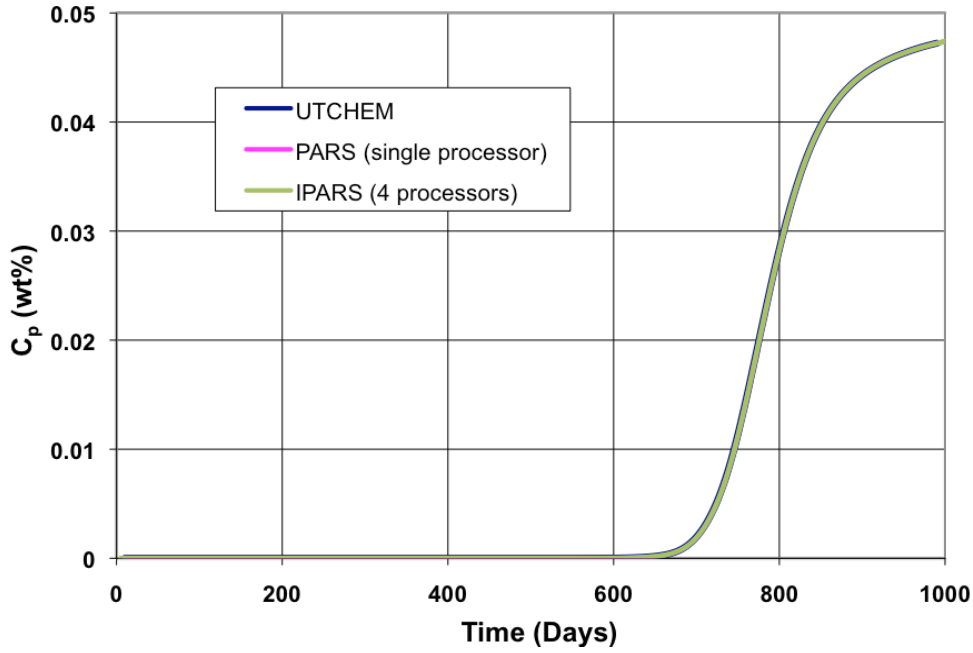

Figure 3.25 Effluent Polymer Concentration History for Case 1

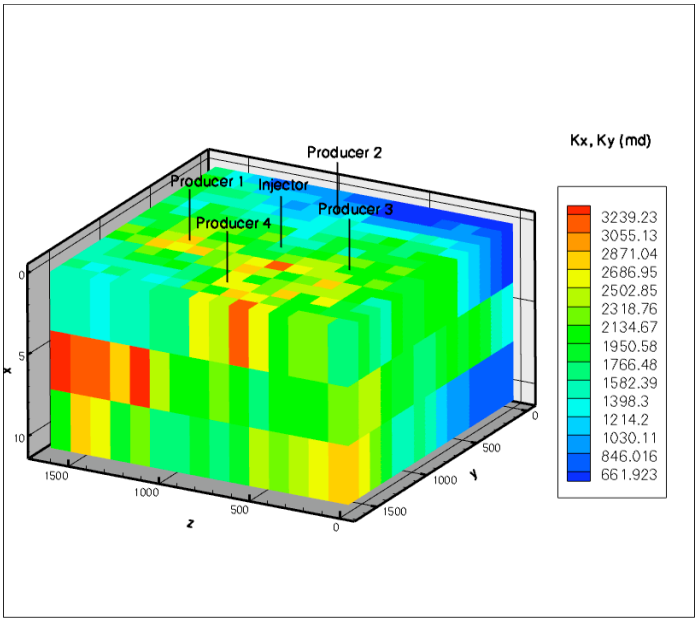

Figure 3.26 Permeability Distribution and Well Locations for Case 2

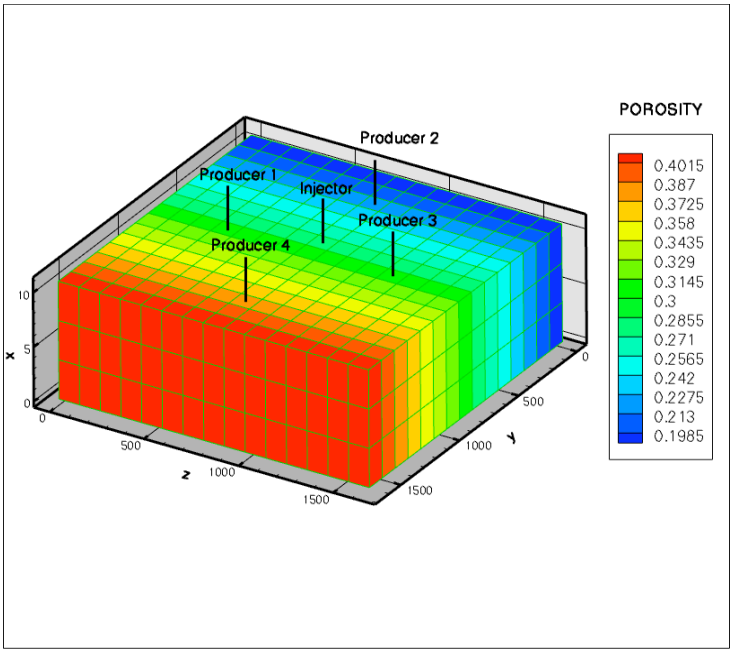

Figure 3.27 Porosity Distribution for Case 2

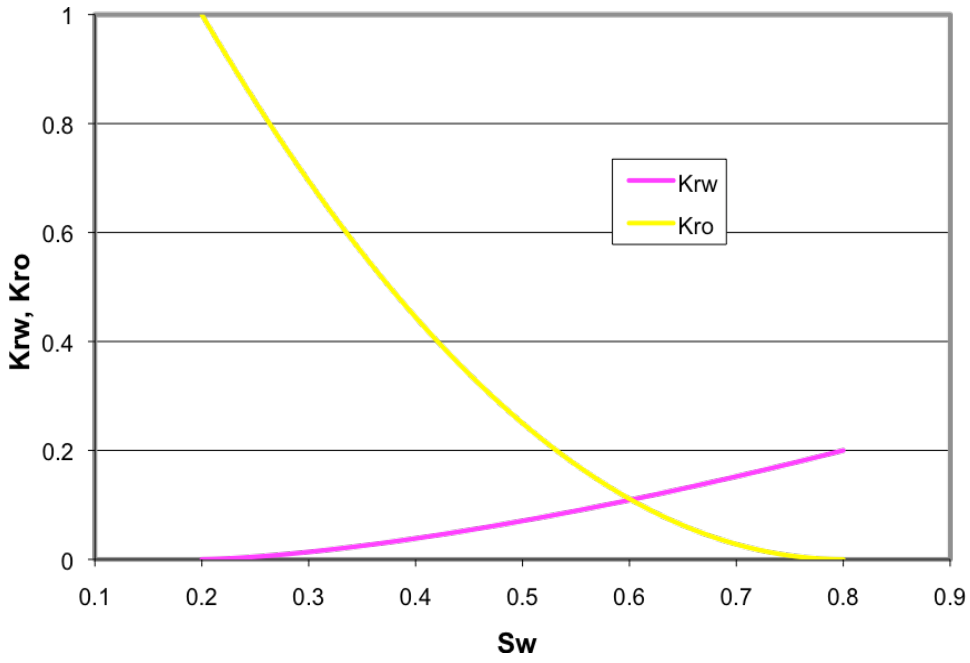

Figure 3.28 Relative Permeability Curves for Case 2

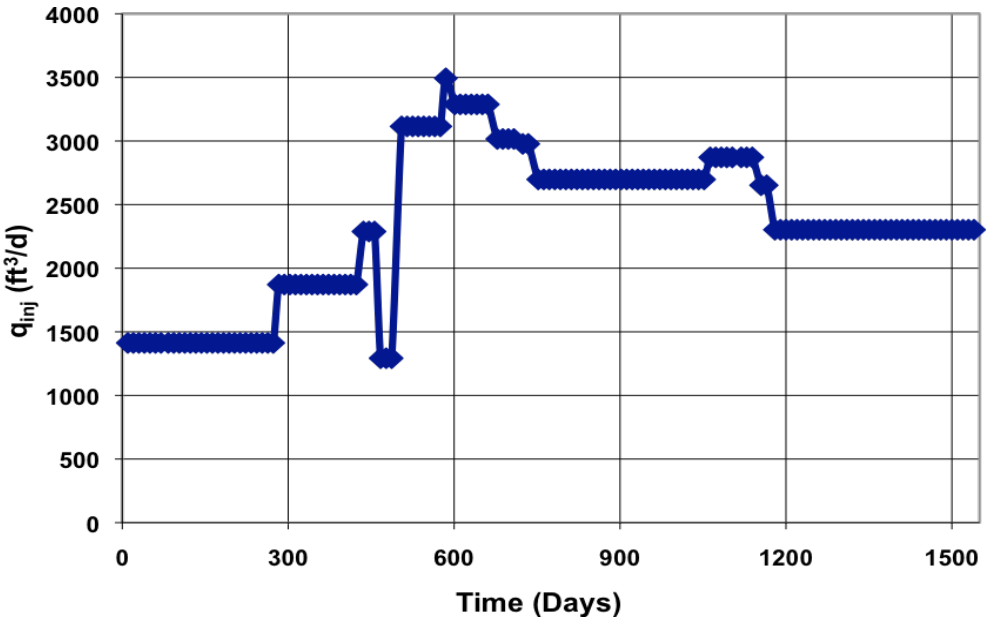

Figure 3.29 Injection Rate Scheme for Case 2

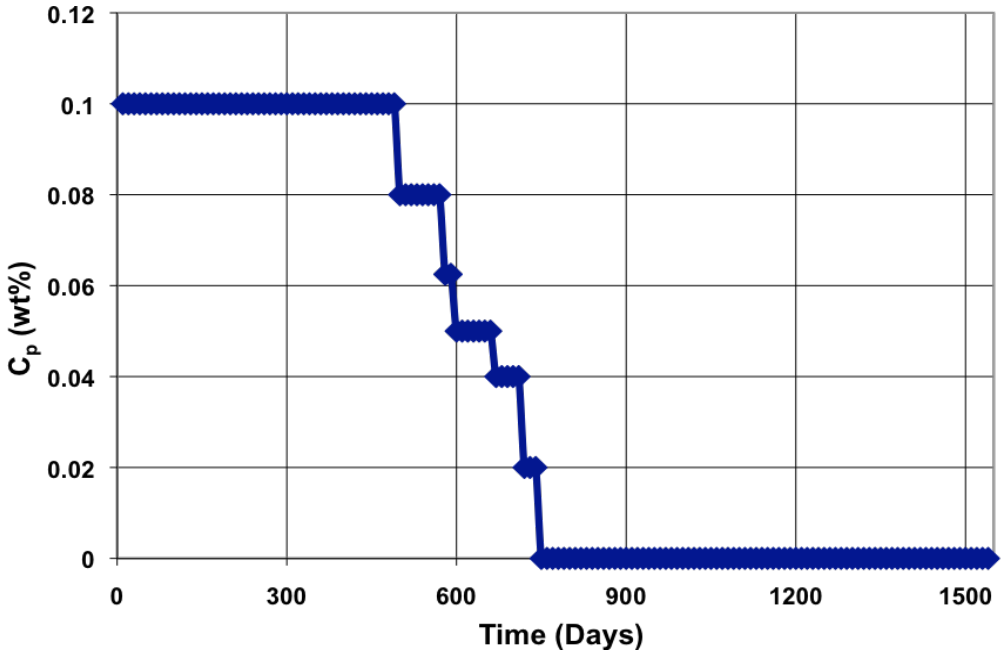

Figure 3.30 Polymer Concentration Grading Injection Scheme for Case 2

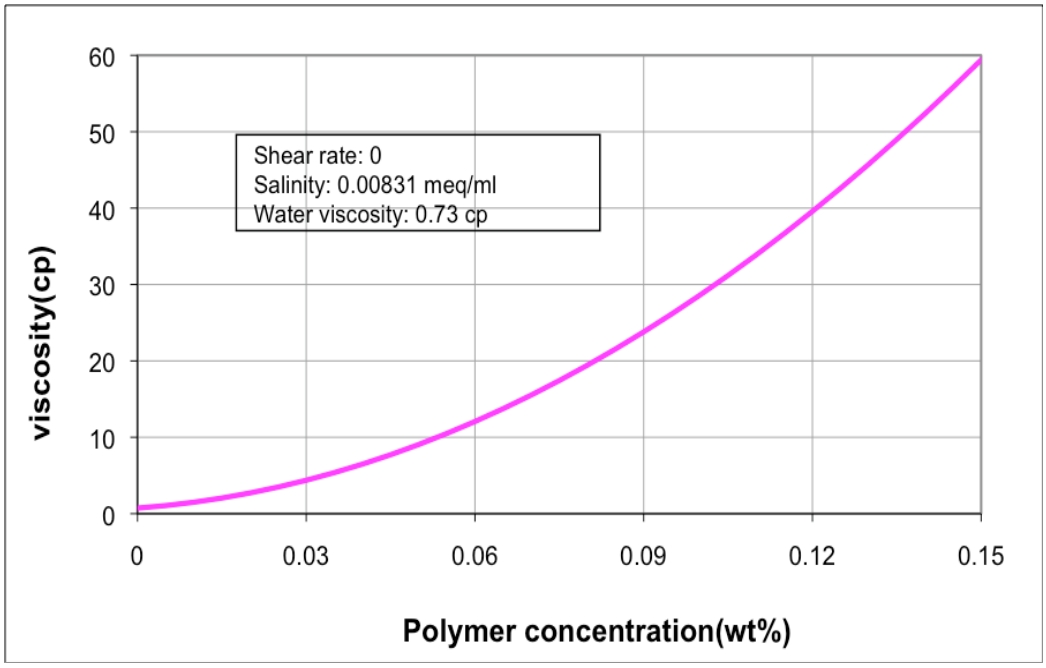

Figure 3.31 Bulk Polymer Viscosity as a Function of Polymer Concentration for Case 2

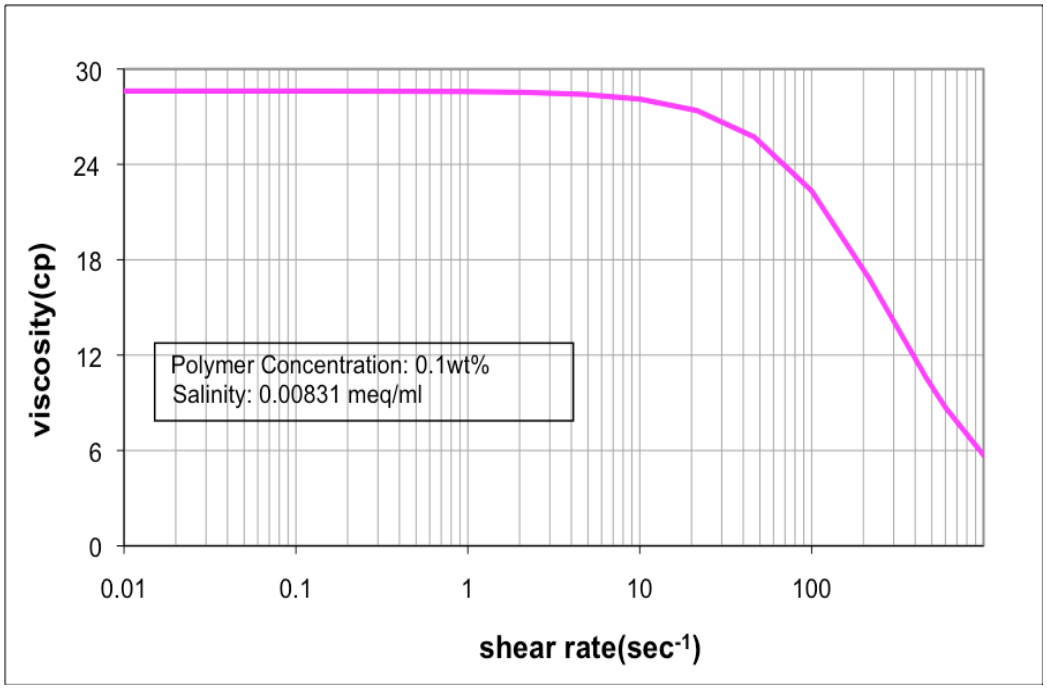

Figure 3.32 Bulk Polymer Viscosity as a Function of Shear Rate for Case 2

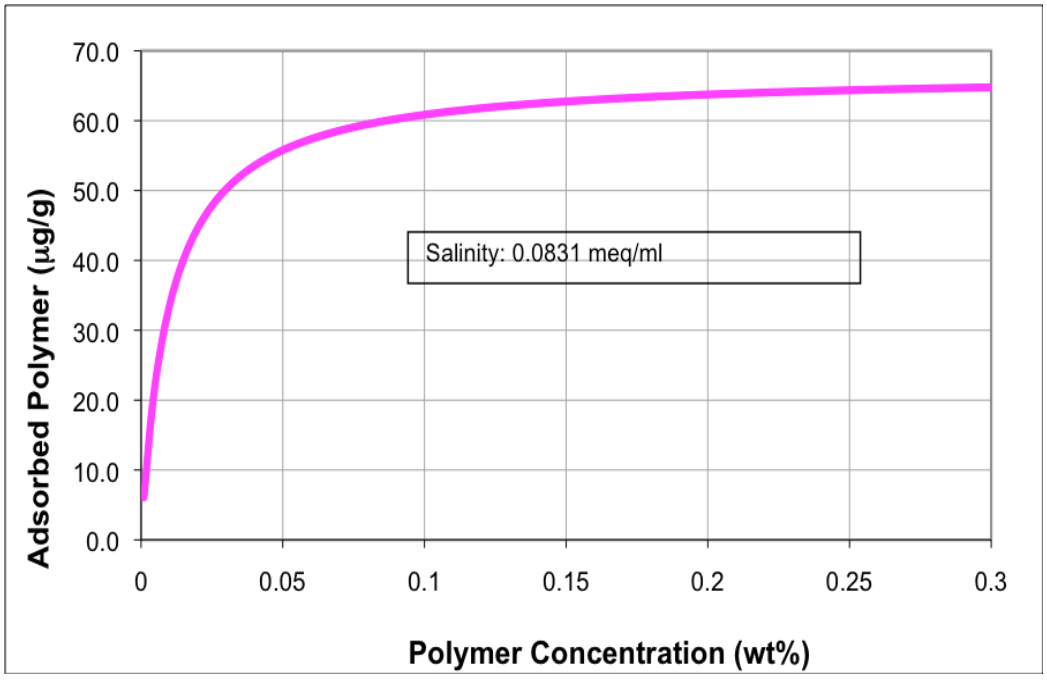

Figure 3.33 Polymer Adsorption as a Function of Polymer Concentration for Case 2

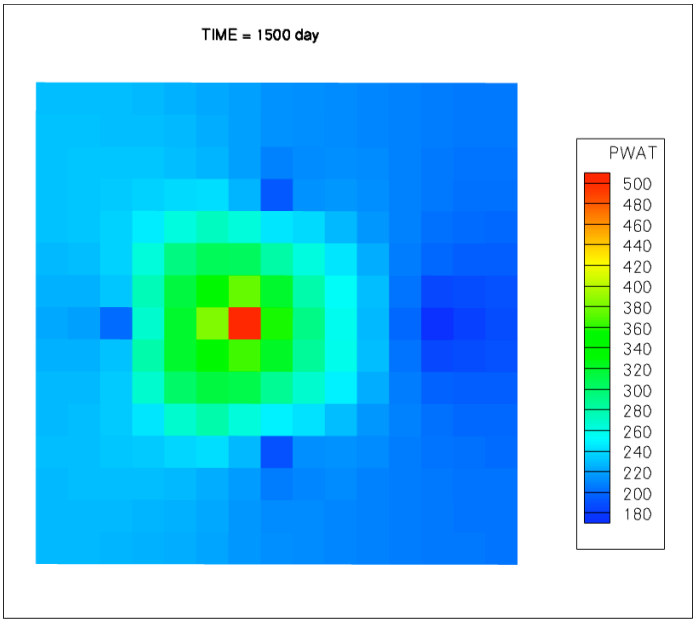

(a) IPARS

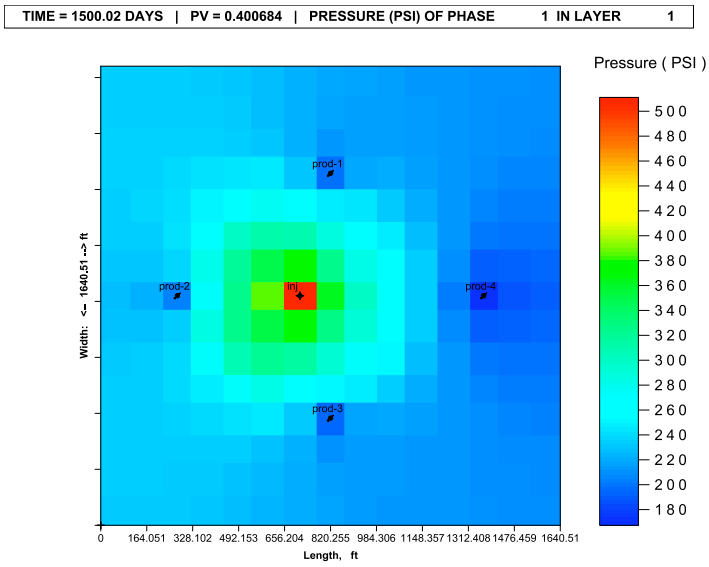

(b) UTCHEM

Figure 3.34 Water Pressure Profiles in Top Layer at 1500 Days for Case 2

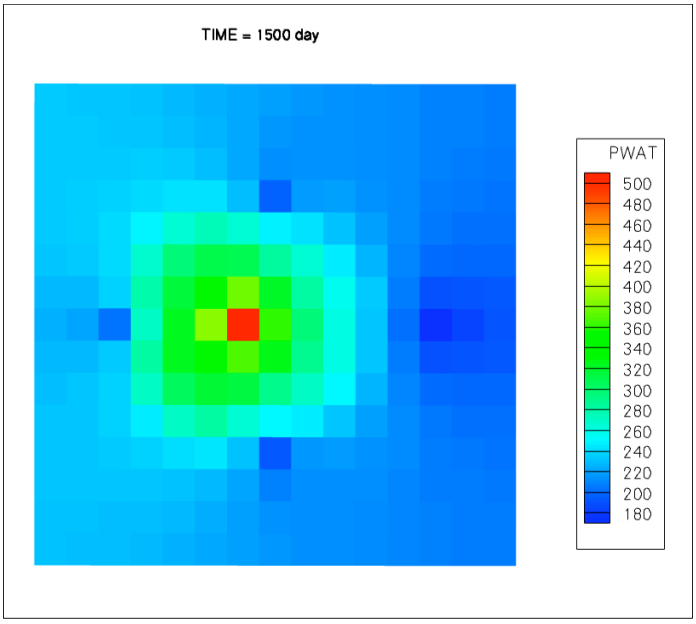

(a) IPARS

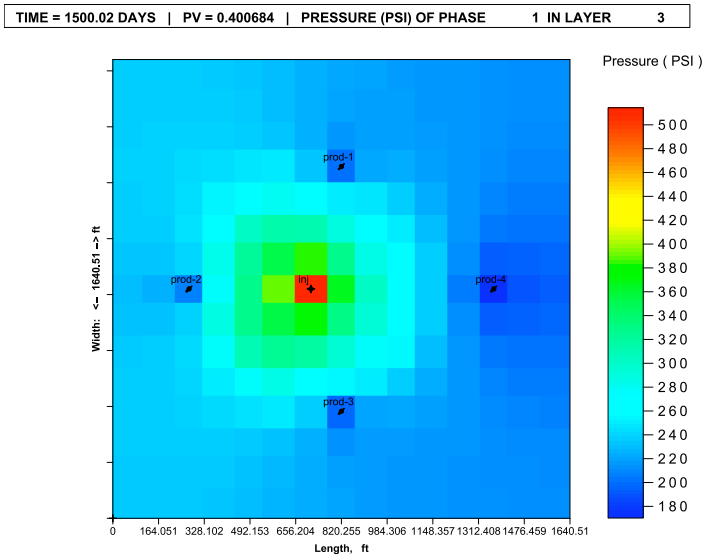

(b) UTCHEM

Figure 3.35 Water Pressure Profiles in Bottom Layer at 1500 Days for Case 2

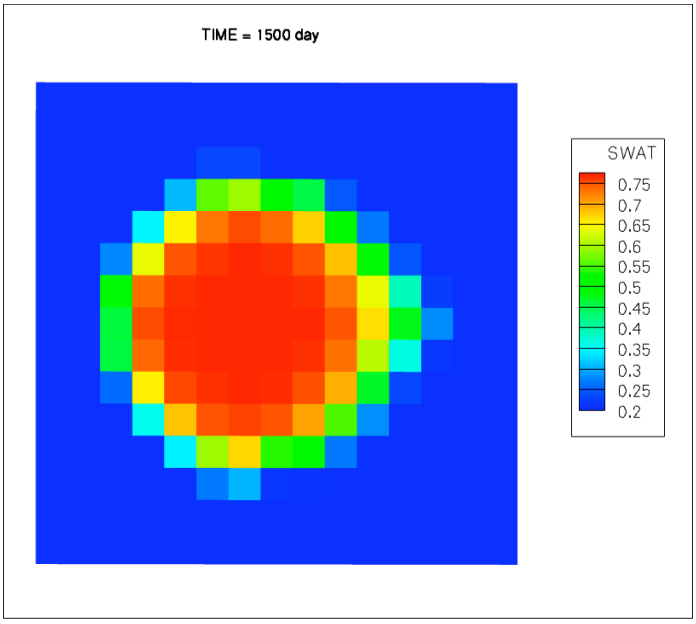

(a) IPARS

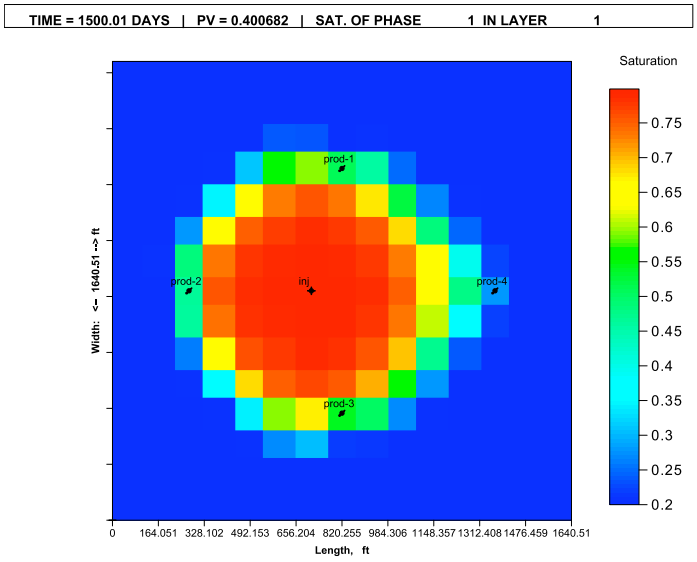

(b) UTCHEM

Figure 3.36 Water Saturation Profiles in Top Layer at 1500 Days for Case 2

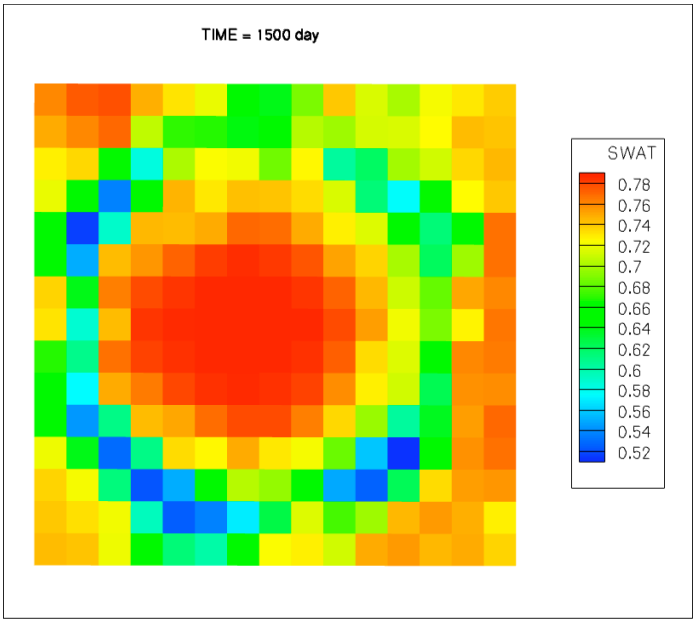

(a) IPARS

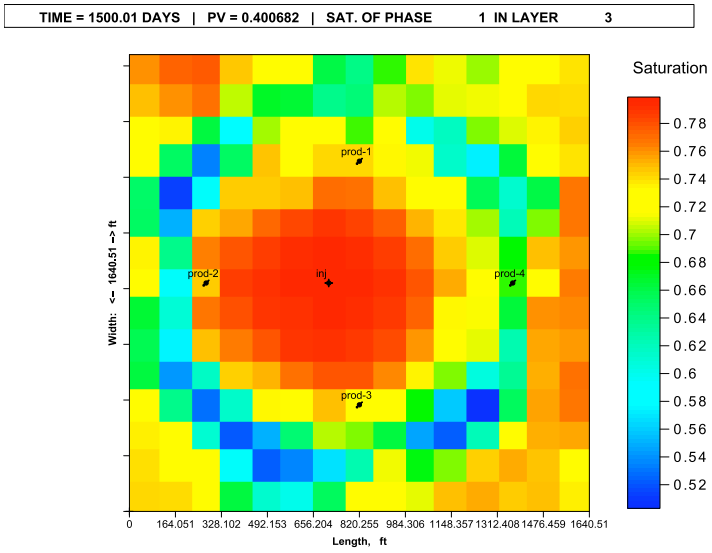

(b) UTCHEM

Figure 3.37 Water Saturation Profiles in Bottom Layer at 1500 Days for Case 2

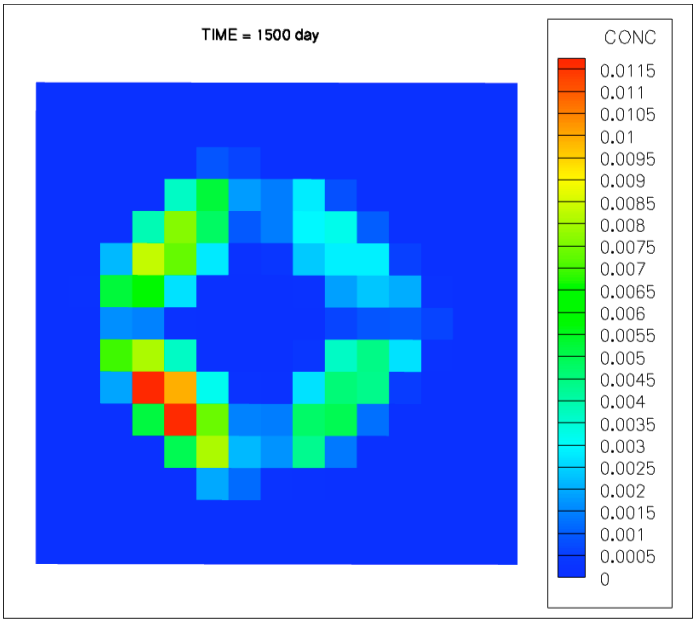

(a) IPARS

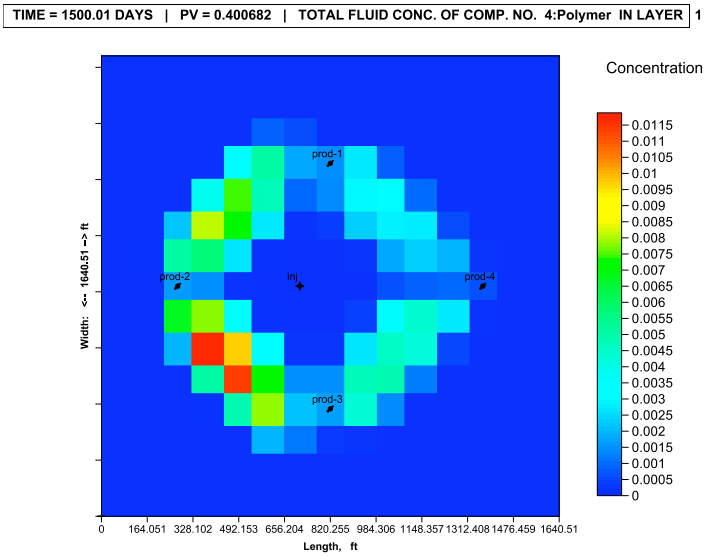

(b) UTCHEM

Figure 3.38 Polymer Concentration Profiles in Top Layer at 1500 Days for Case 2

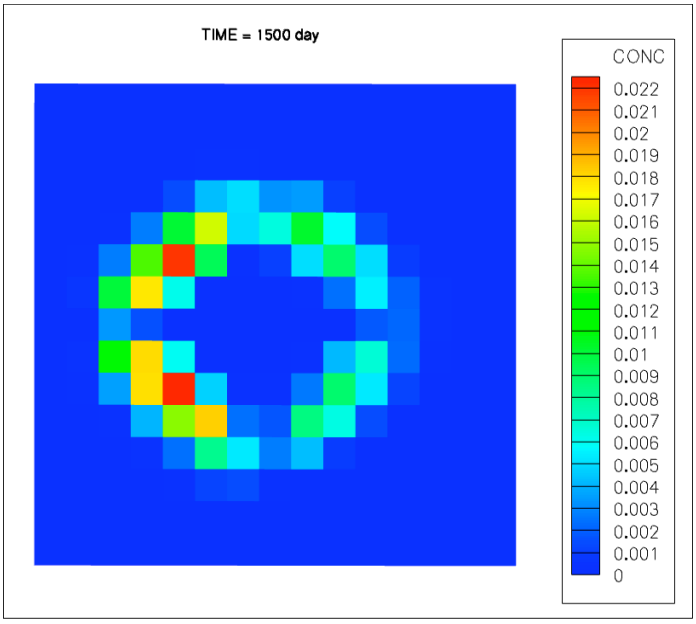

(a) IPARS

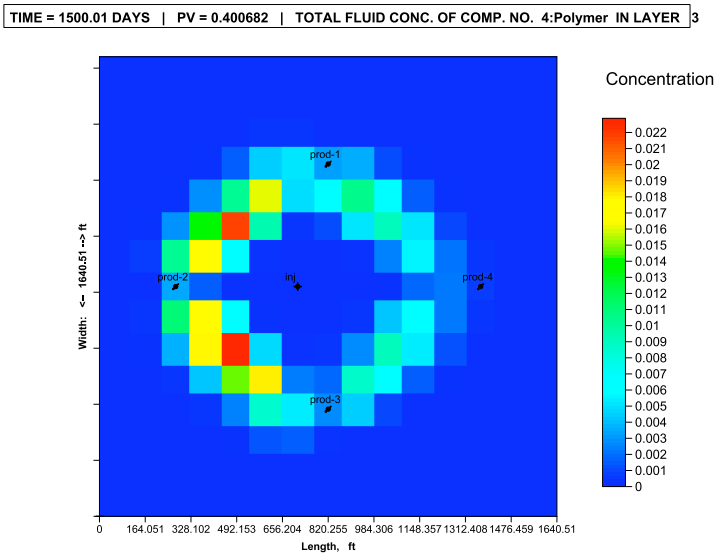

(b) UTCHEM

Figure 3.39 Polymer Conc. Profiles in Bottom Layer at 1500 Days for Case2

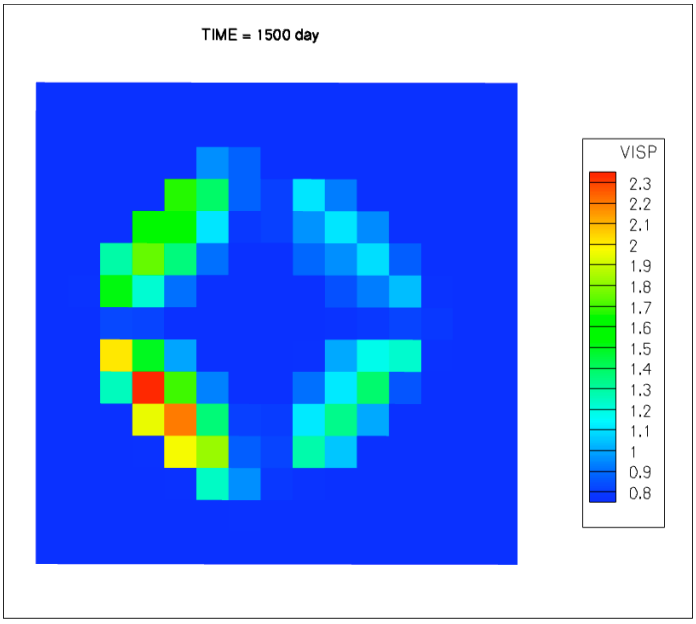

(a) IPARS

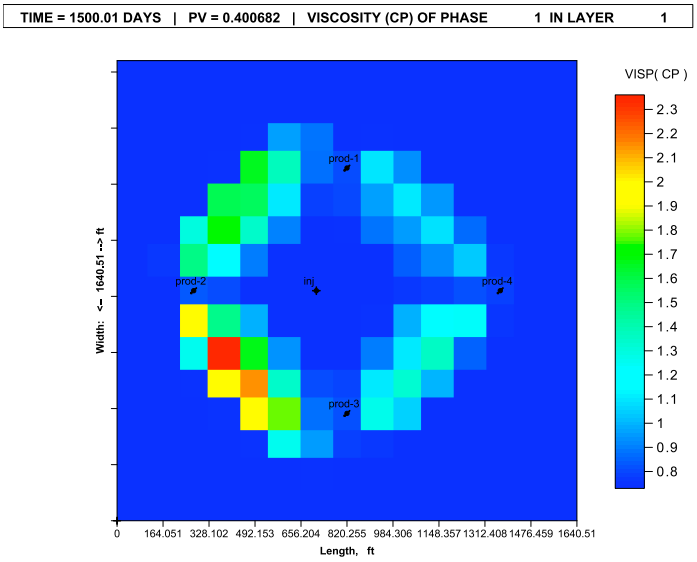

(b) UTCHEM

Figure 3.40 Polymer Viscosity Profiles in Top Layer at 1500 Days for Case 2

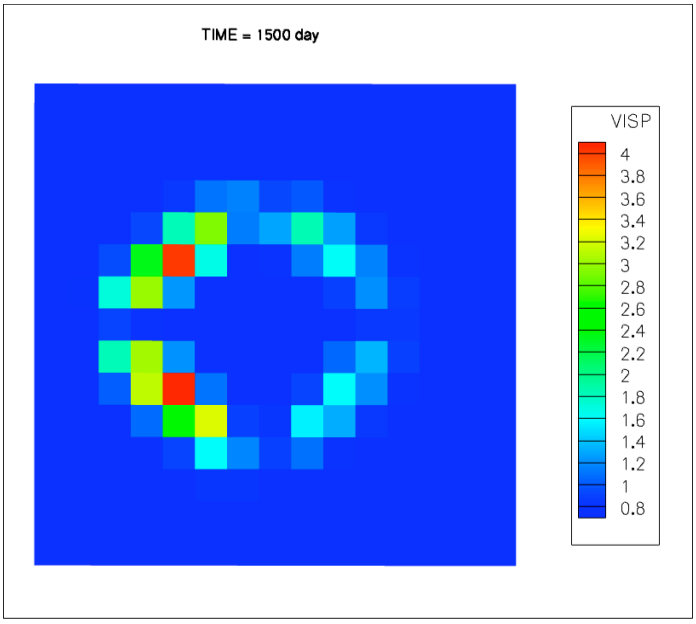

(a) IPARS

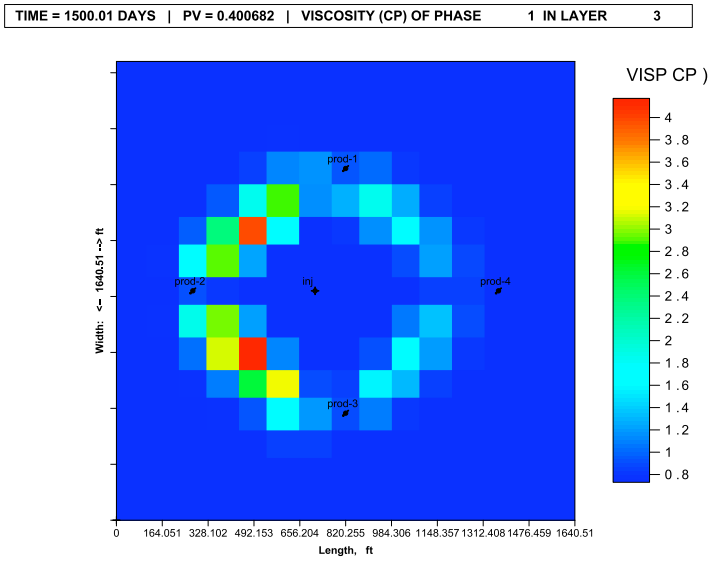

(b) UTCHEM

Figure 3.41 Polymer Viscosity Profiles in Bottom Layer at 1500 Days for Case 2

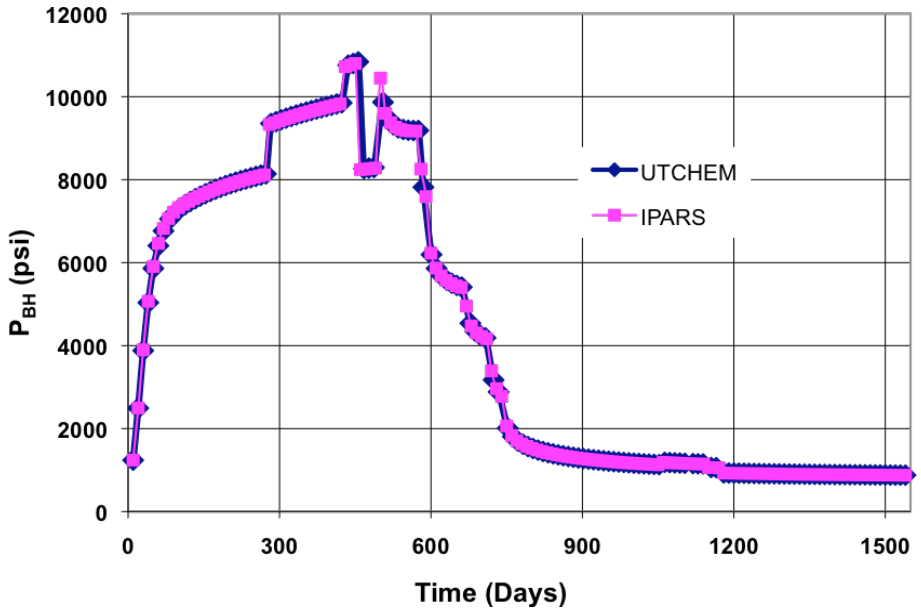

Figure 3.42 Injector Bottomhole Pressure History for Case 2

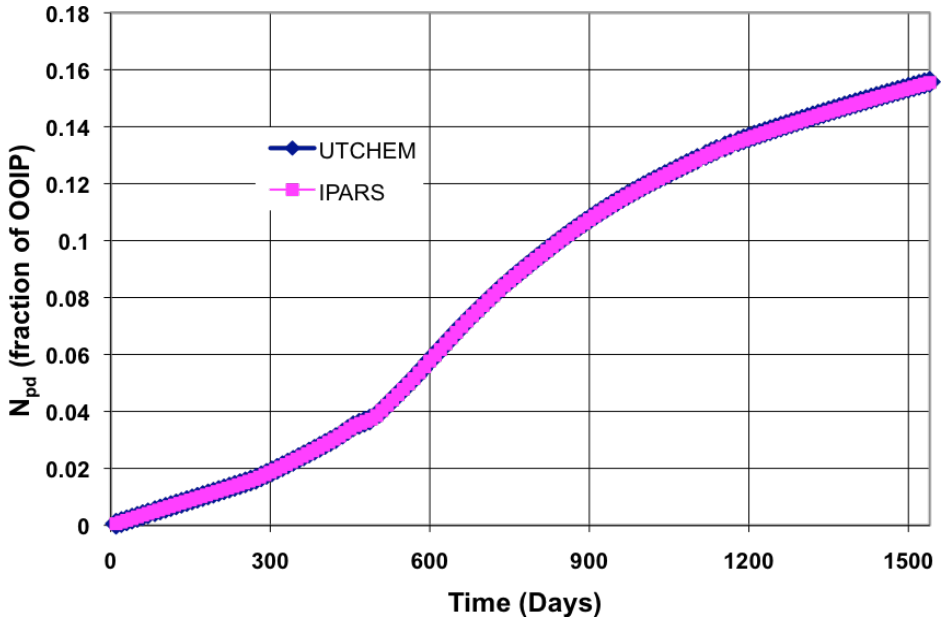

Figure 3.43 Cumulative Oil Recovery of Case 2

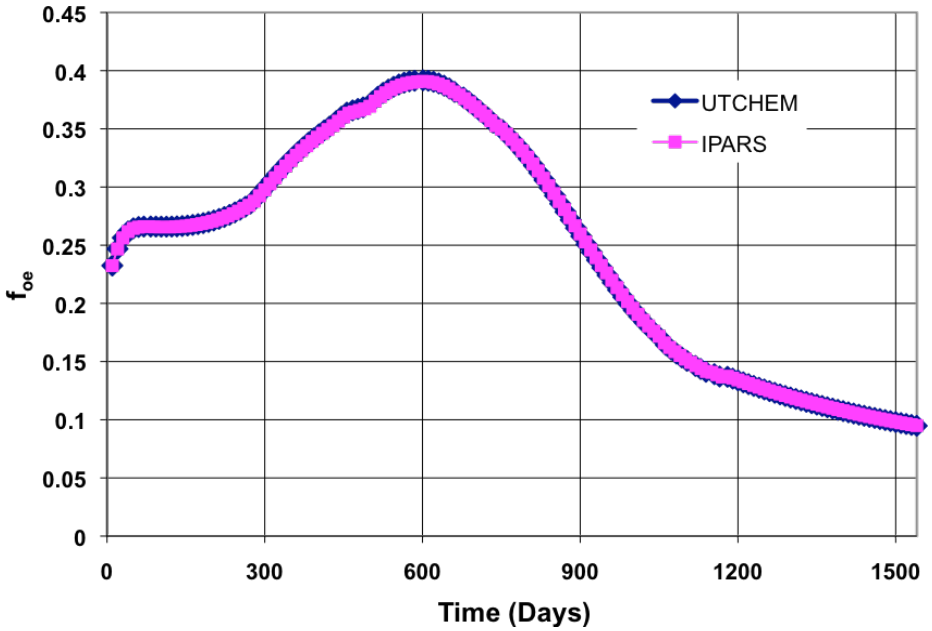

(a) Producer 1

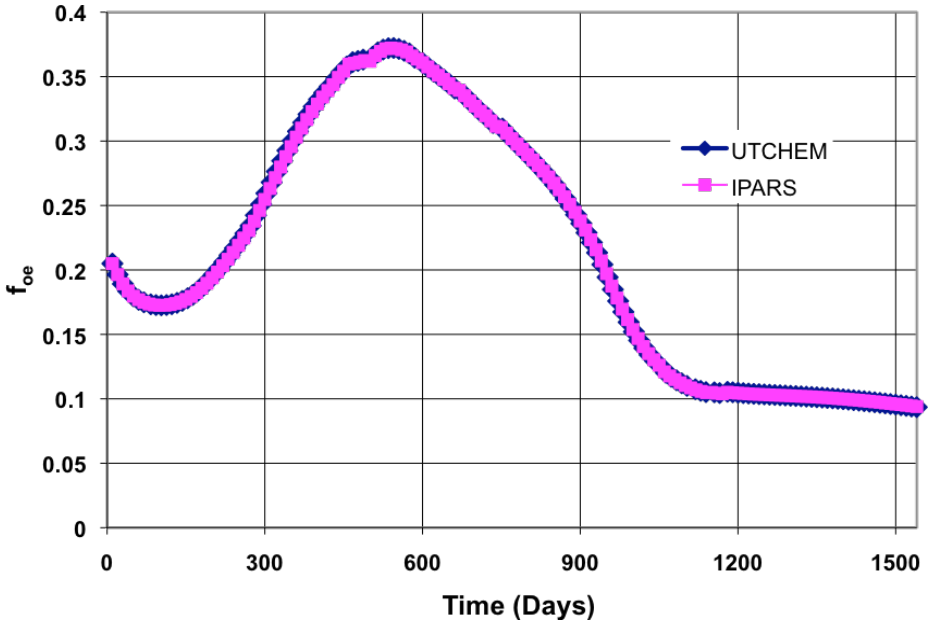

(b) Producer 2

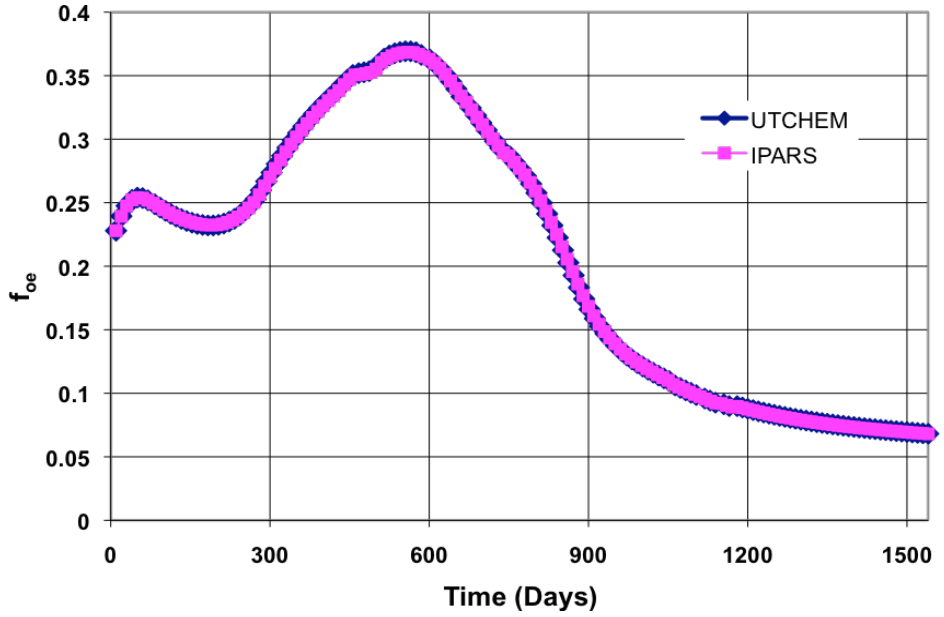

(c) Producer 3

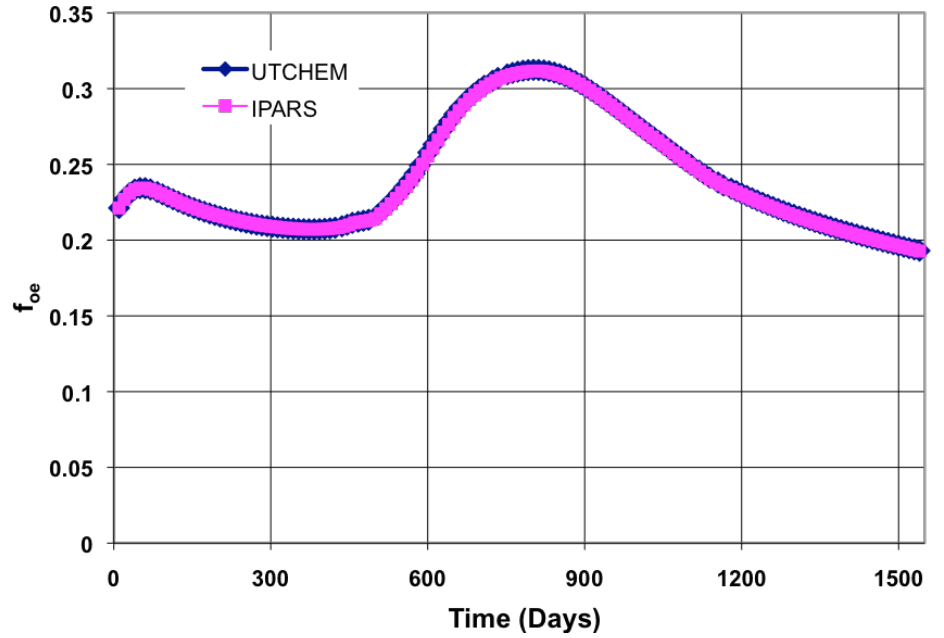

(d) Producer 4

Figure 3.44 Oil Cut Histories for Case 2

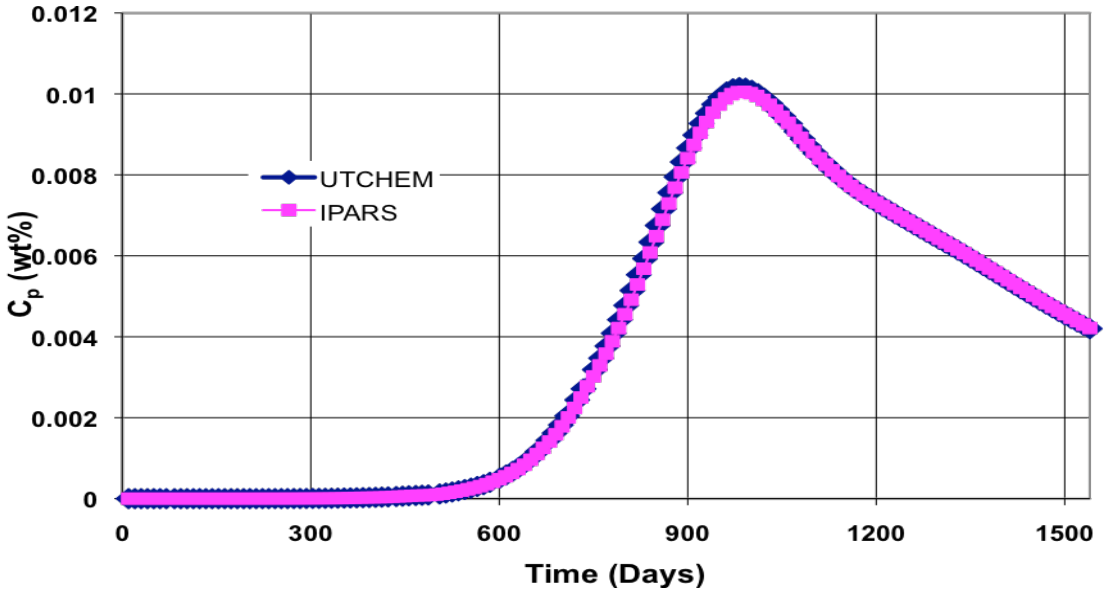

(a) Produer 1

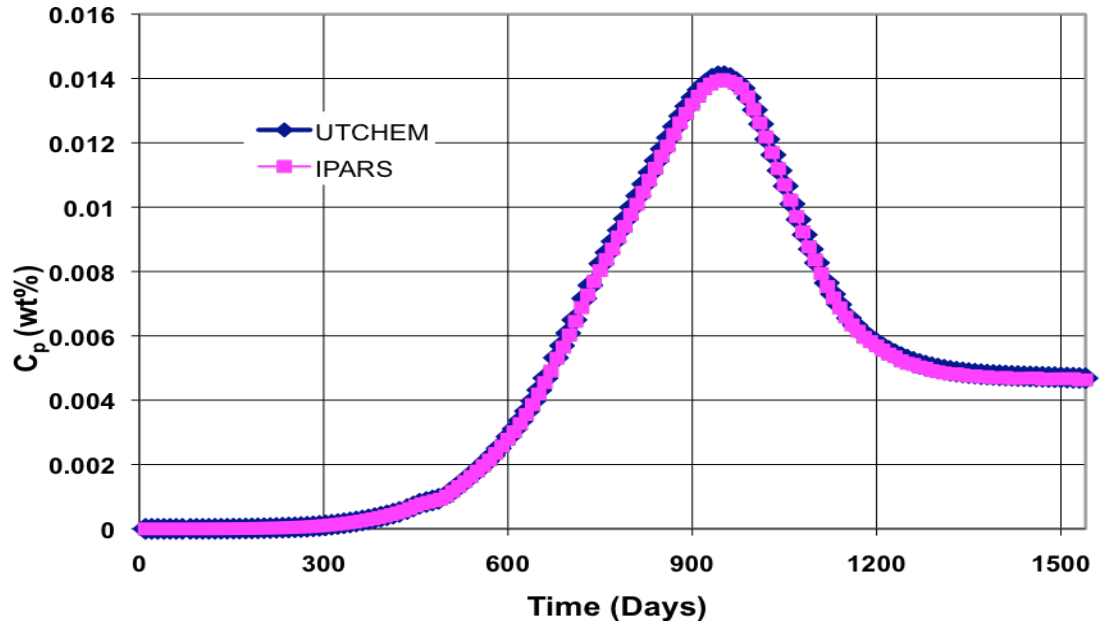

(b) Producer 2

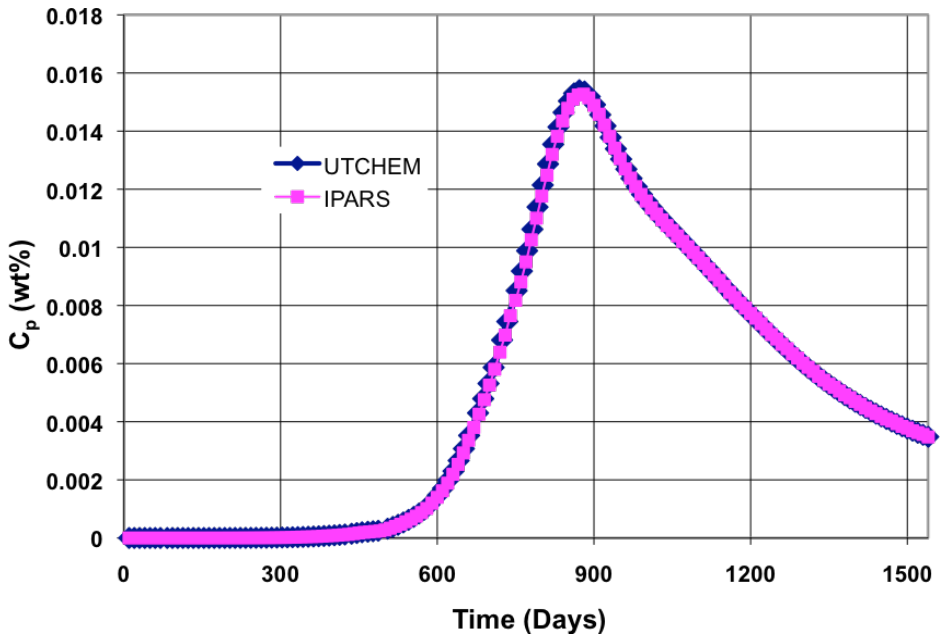

(c) Producer 3

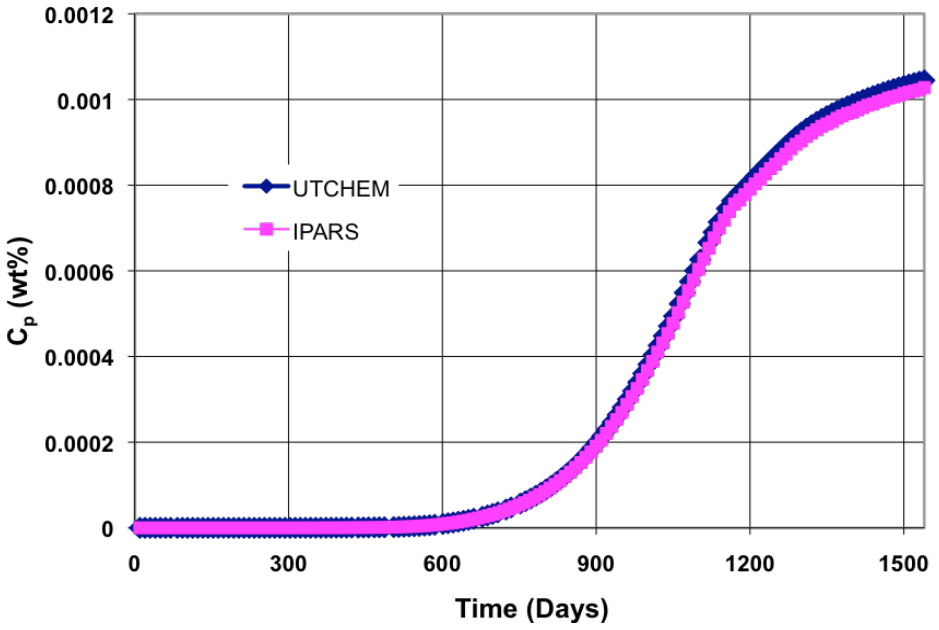

(d) Producer 4

Figure 3.45 Effluent Polymer Concentration Histories for Case 2

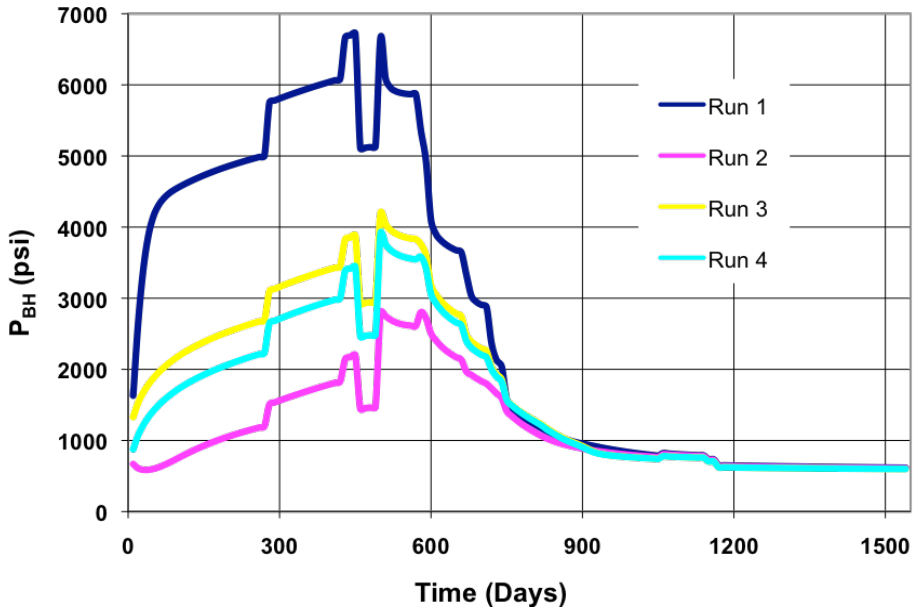

Figure 3.46 Injector Bottomhole Pressure History for Case 3

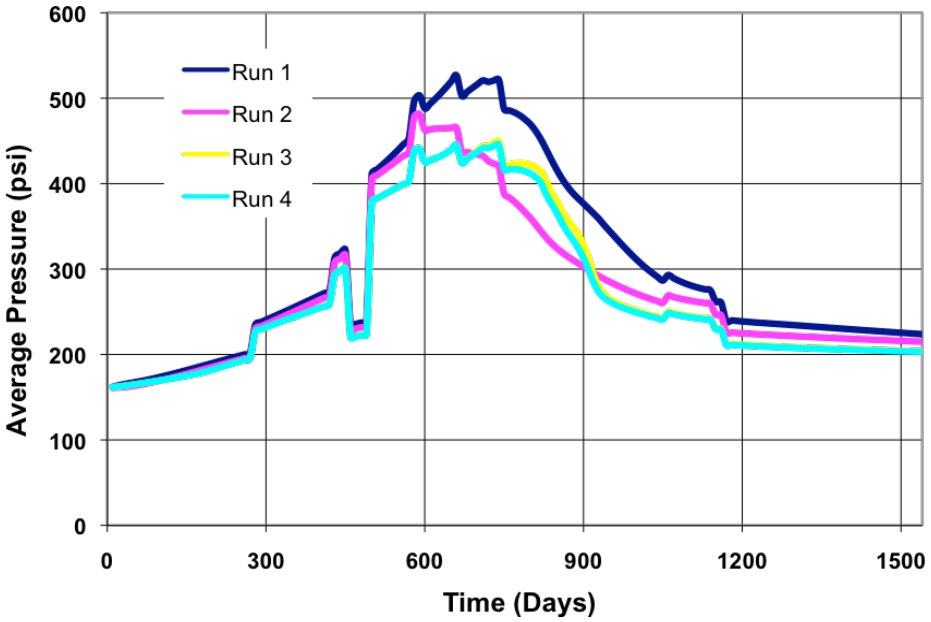

Figure 3.47 Average Reservoir Pressure History for Case 3

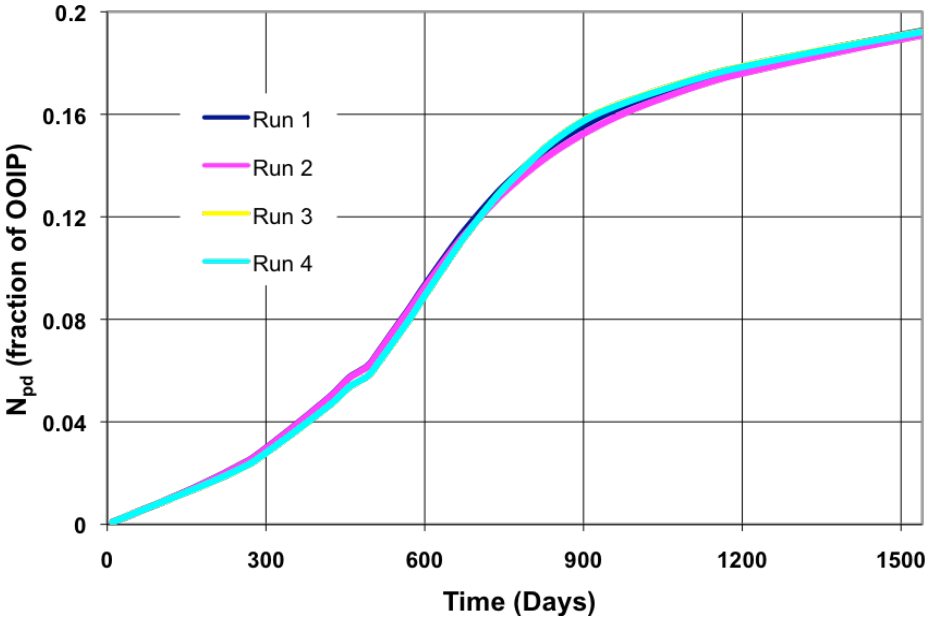

Figure 3.48 Cumulative Oil Recoveryfor Case 3

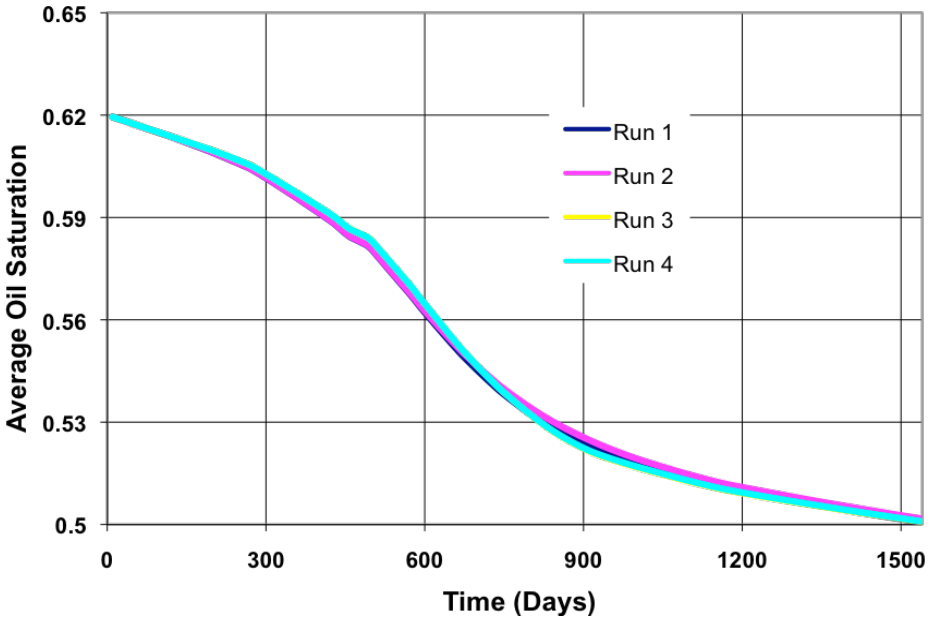

Figure 3.49 Average Reservoir Oil Saturation History for Case 3

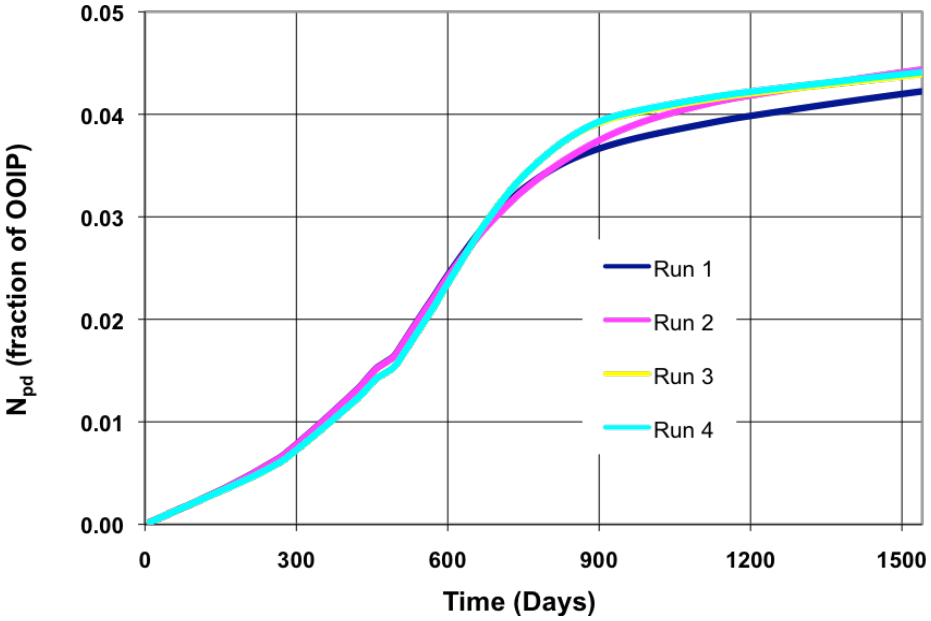

(a) Producer 1

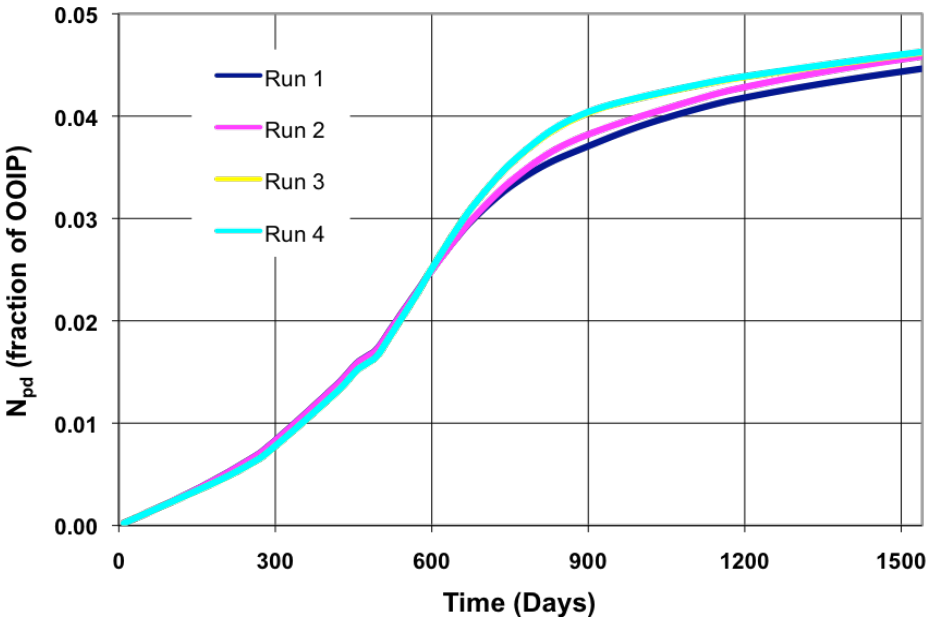

(b) Producer 2

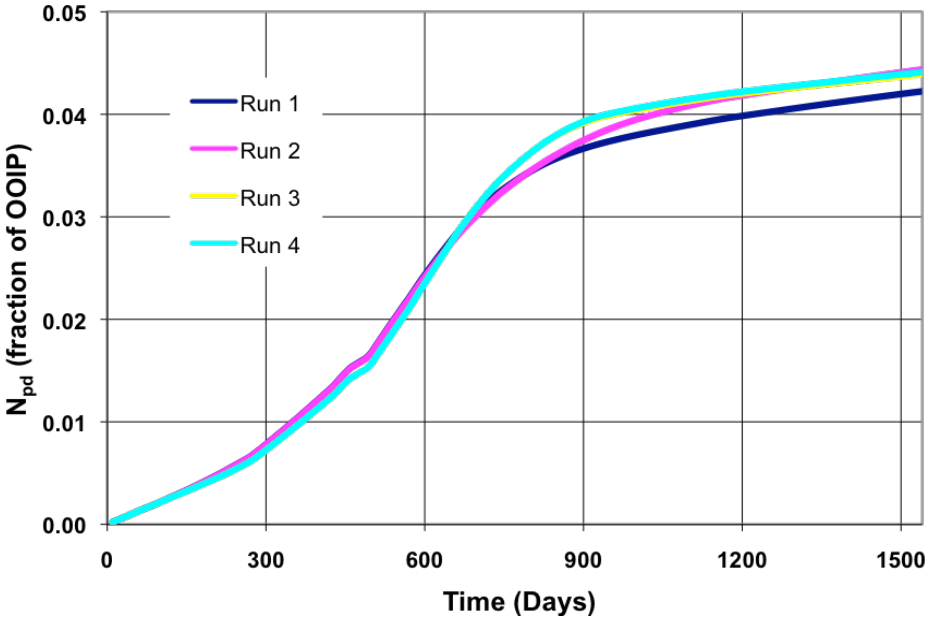

(c) Producer 3

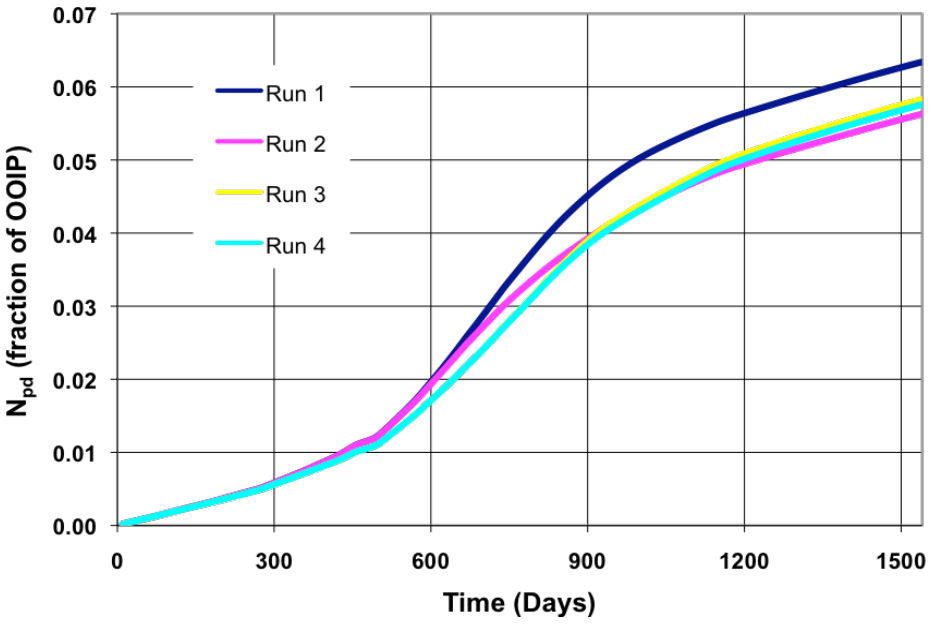

(d) Producer 4

Figure 3.50 Individual Producers Oil Recovery in Case 3

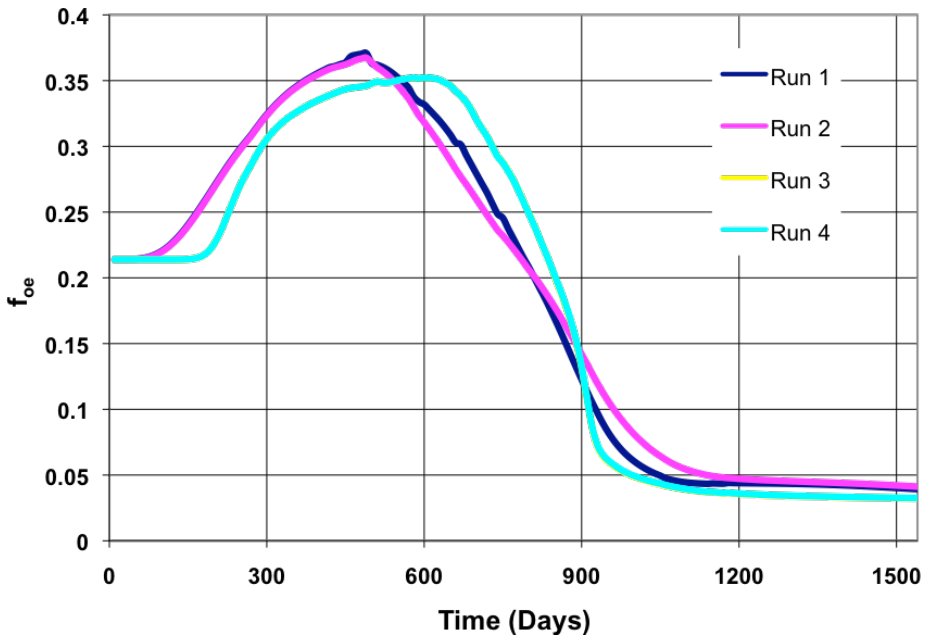

(a) Producer 1

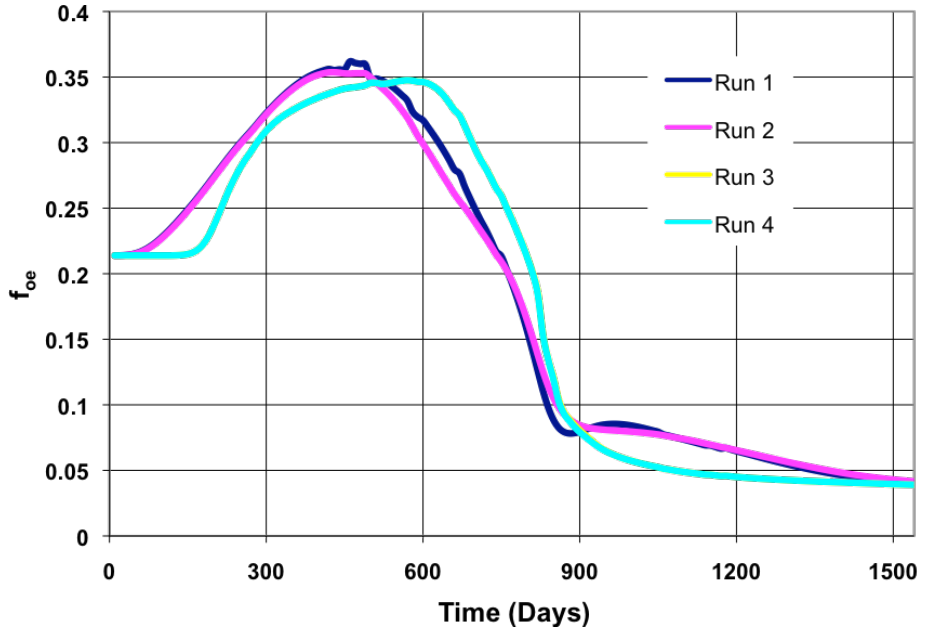

(b) Producer 2

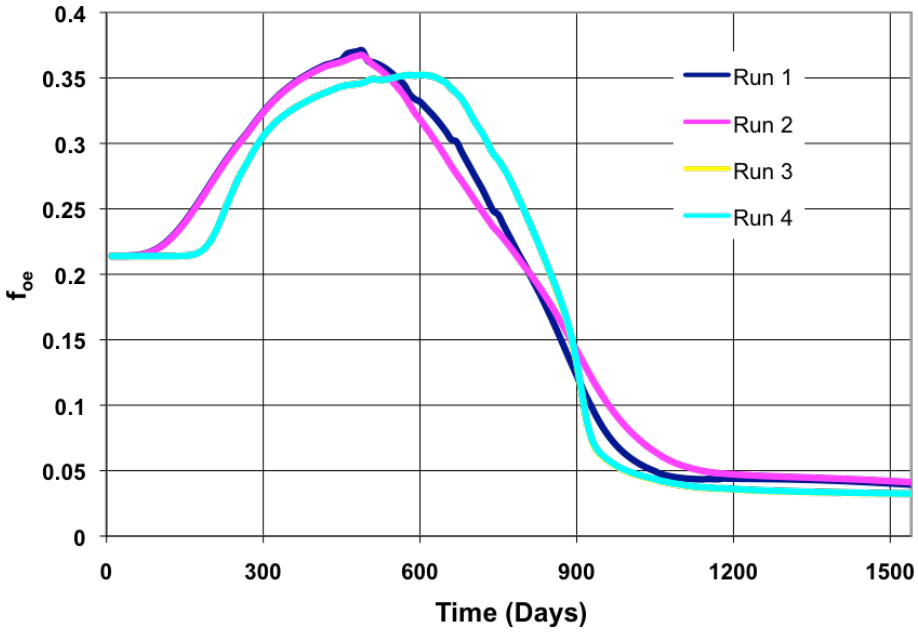

(c) Producer 3

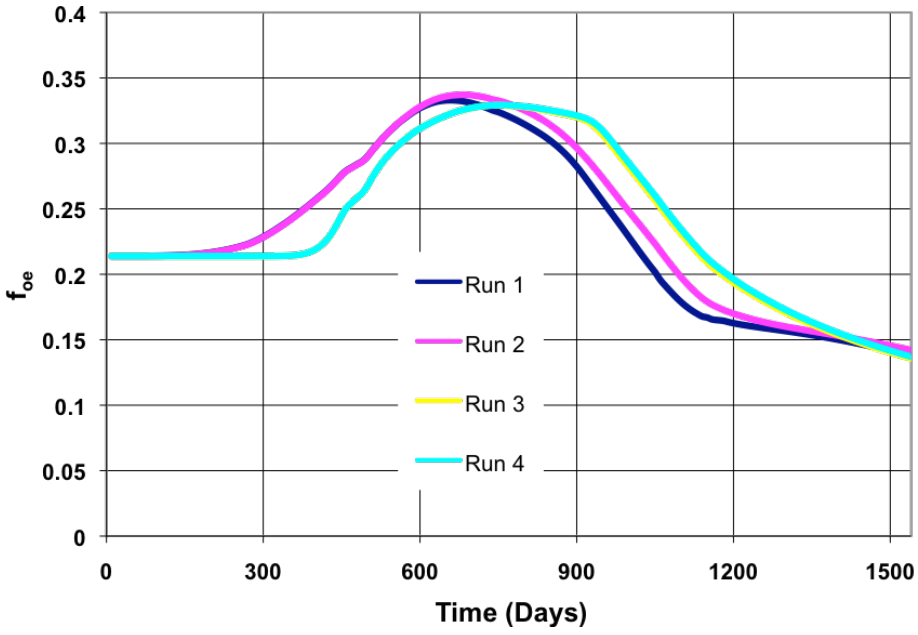

(d) Producer 4

Figure 3.51 Oil Cut of Individual Producers in Case 3

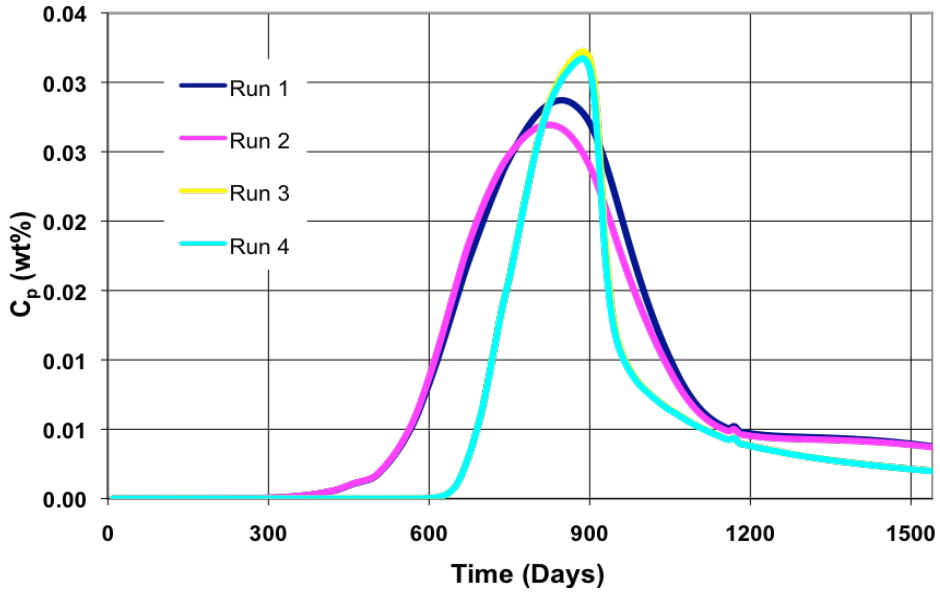

(a) Producer 1

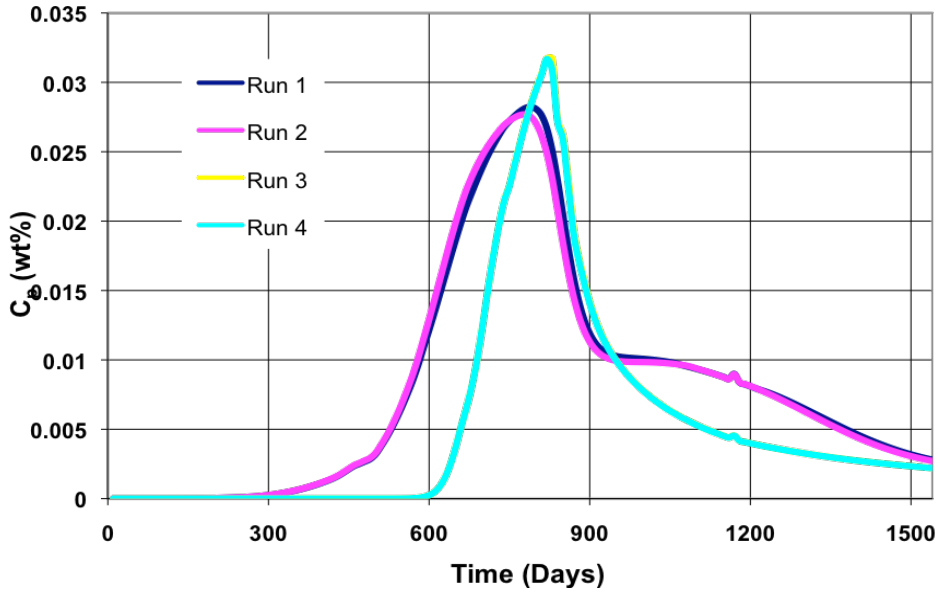

(b) Producer 2

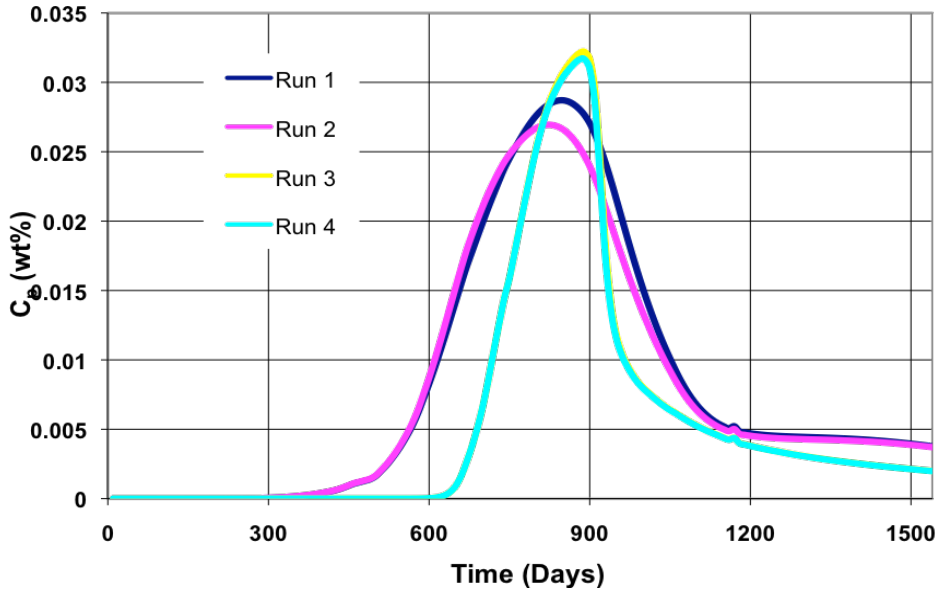

(c) Producer 3

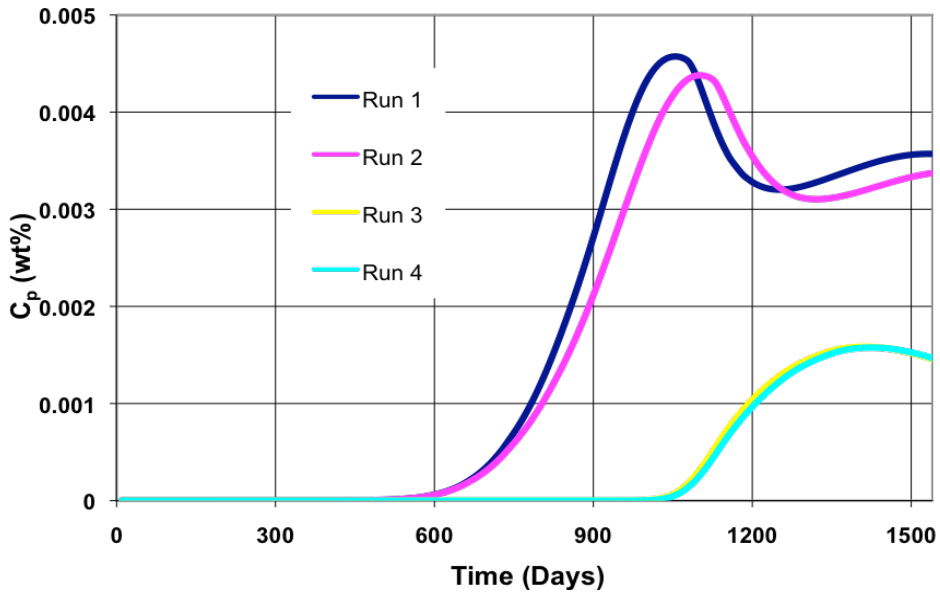

(d) Producer 4

Figure 3.52 Effluent Polymer Concentration in Individual Producers for Case 3

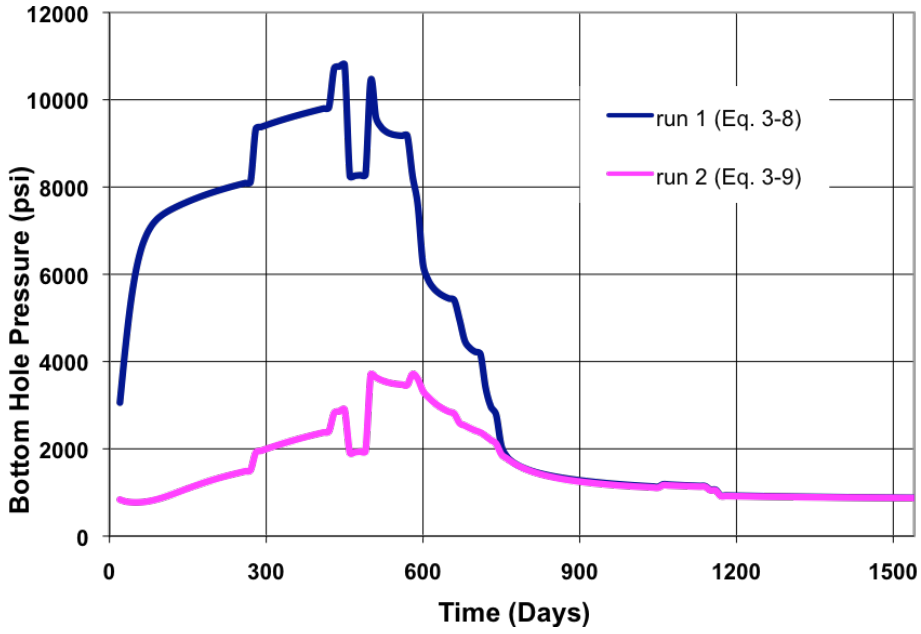

Figure 3.53 Injector Bottomhole Pressure History for Case 4

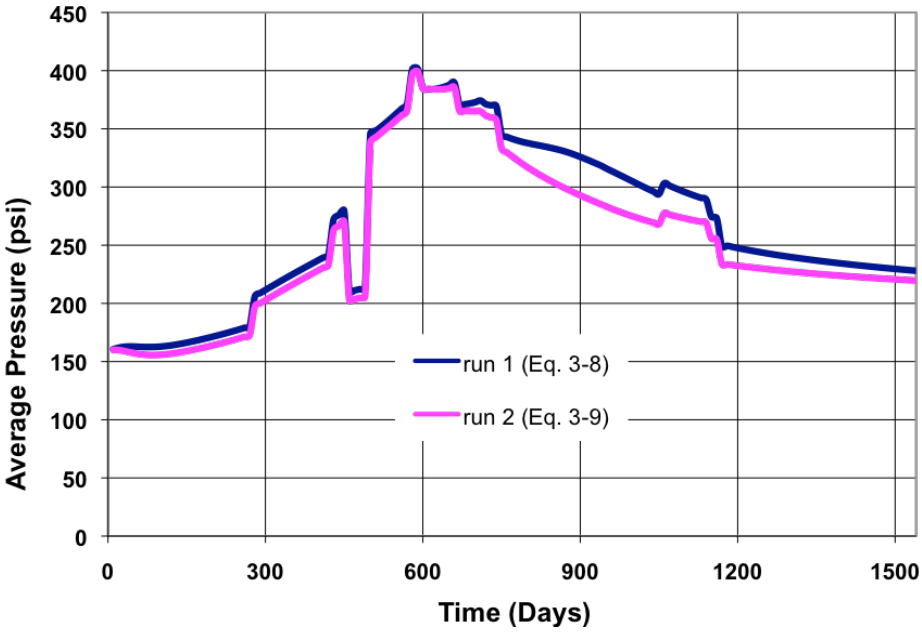

Figure 3.54 Average Reservoir Pressure History for Case 4

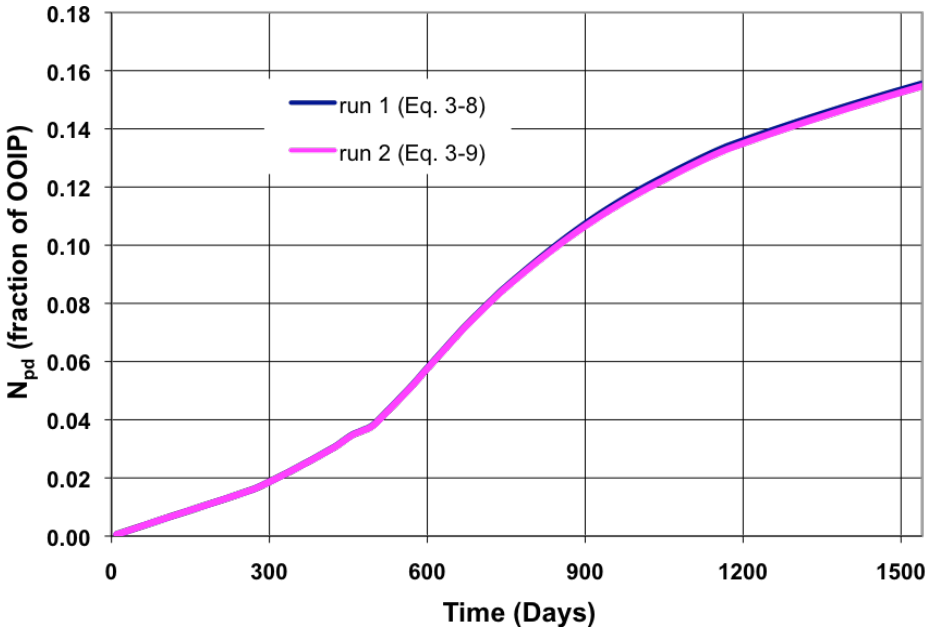

Figure 3.55 Culmulative Oil Recovery for Case 4

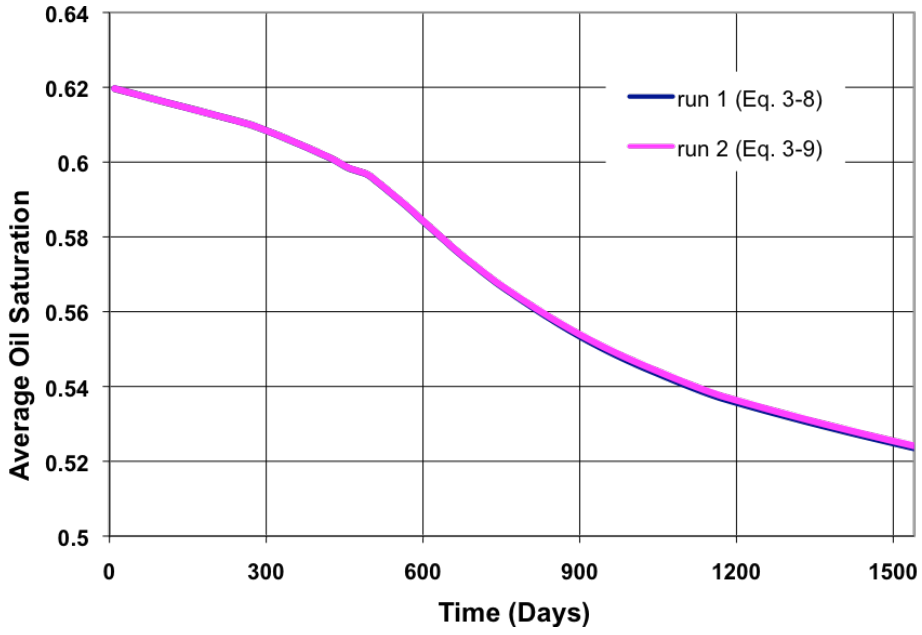

figure 3.56 Averge Reservoir Oil Saturation History for Case 4

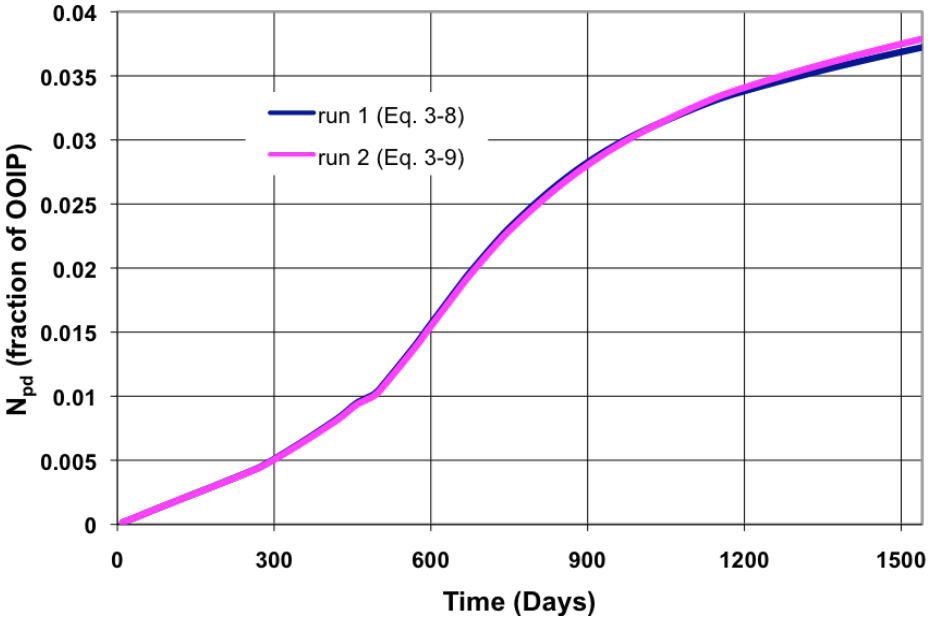

(a) Producer 1

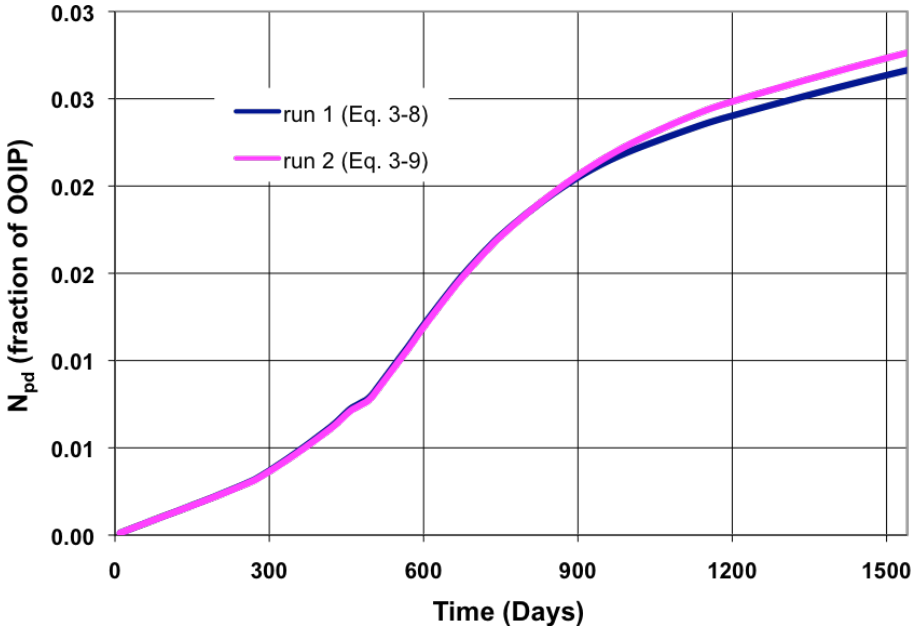

(b) Producer 2

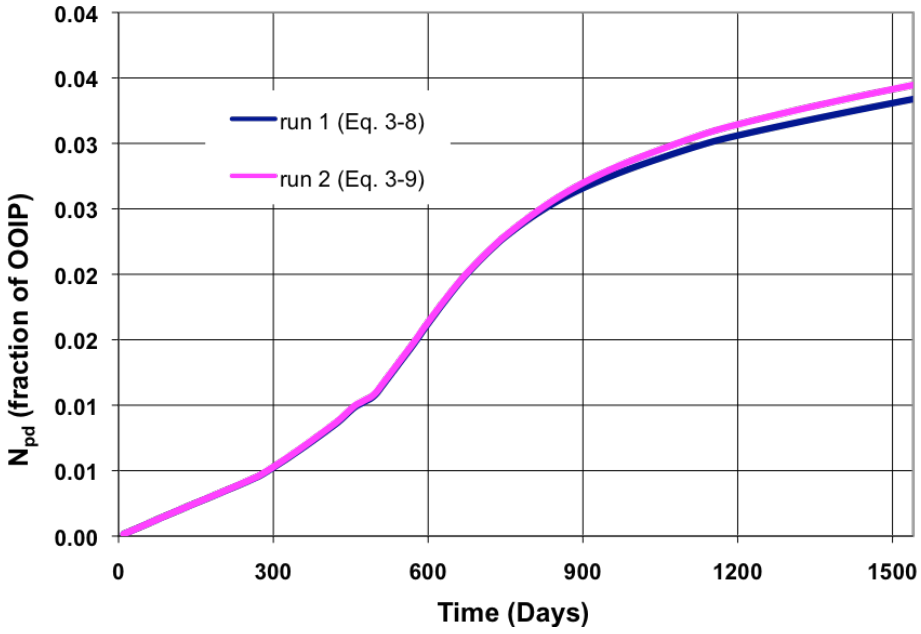

(c) Producer 3

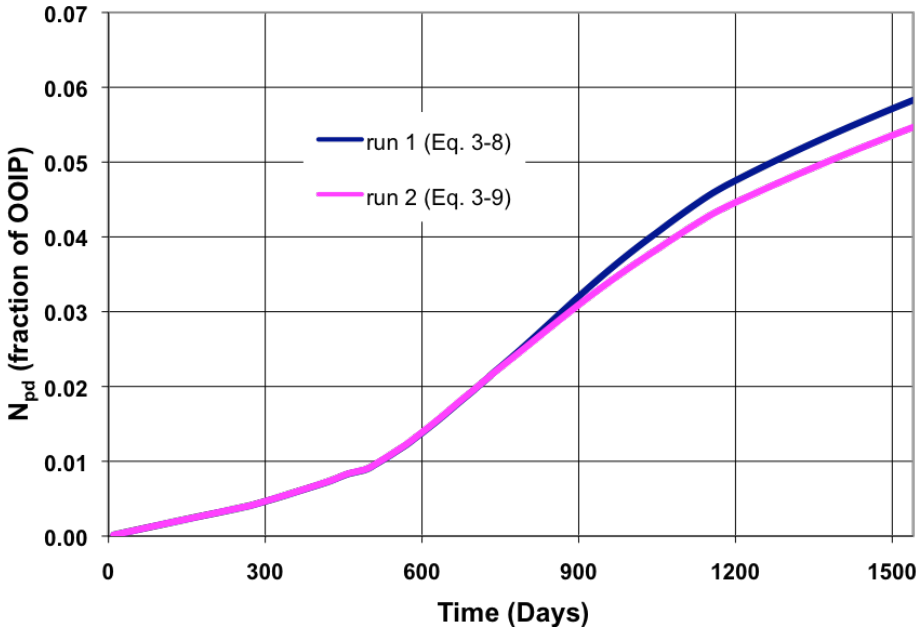

(d) Producer 4

Figure 3.57 Individual Producers Oil Recovery for Case 4

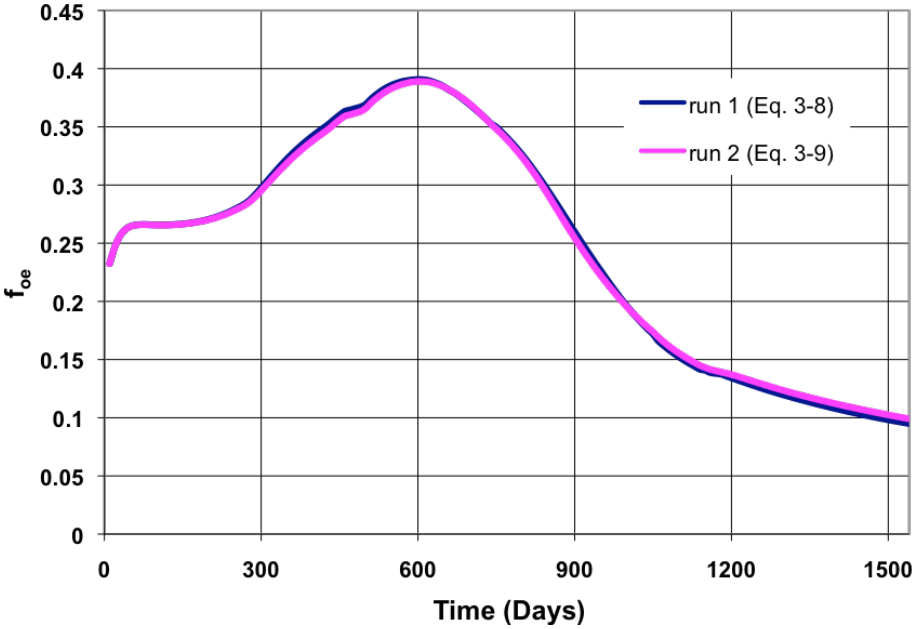

(a) Producer 1

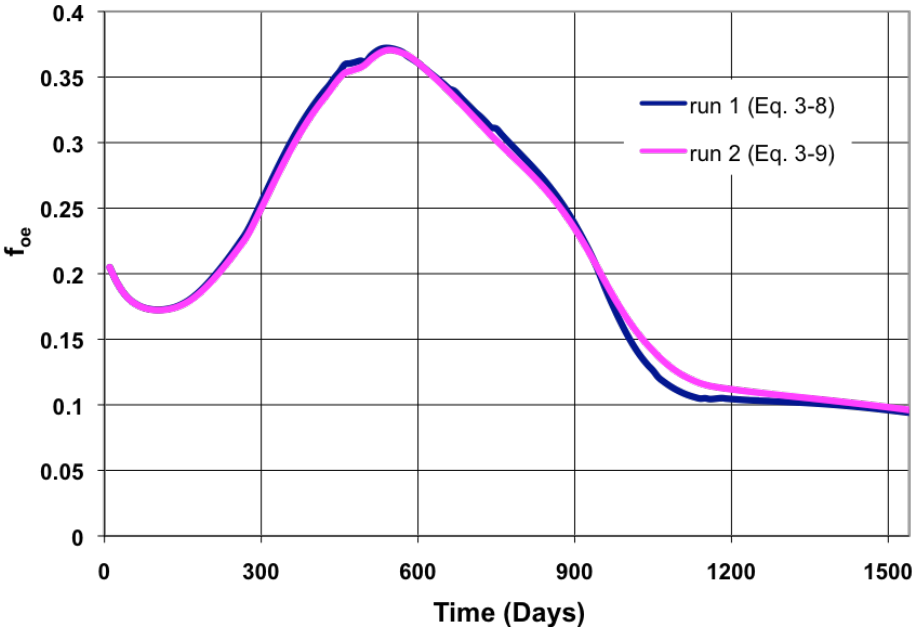

(b) Producer 2

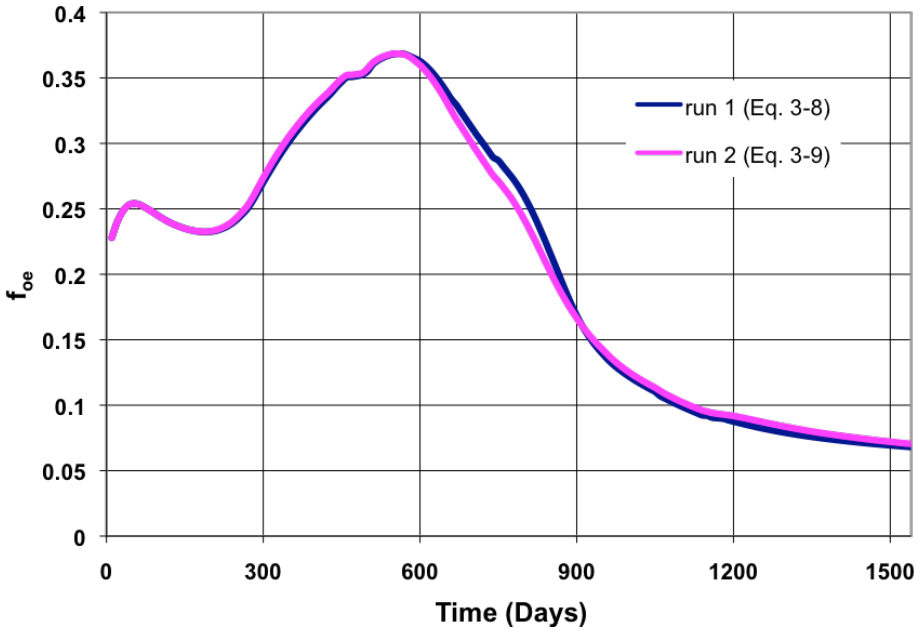

(c) Producer 3

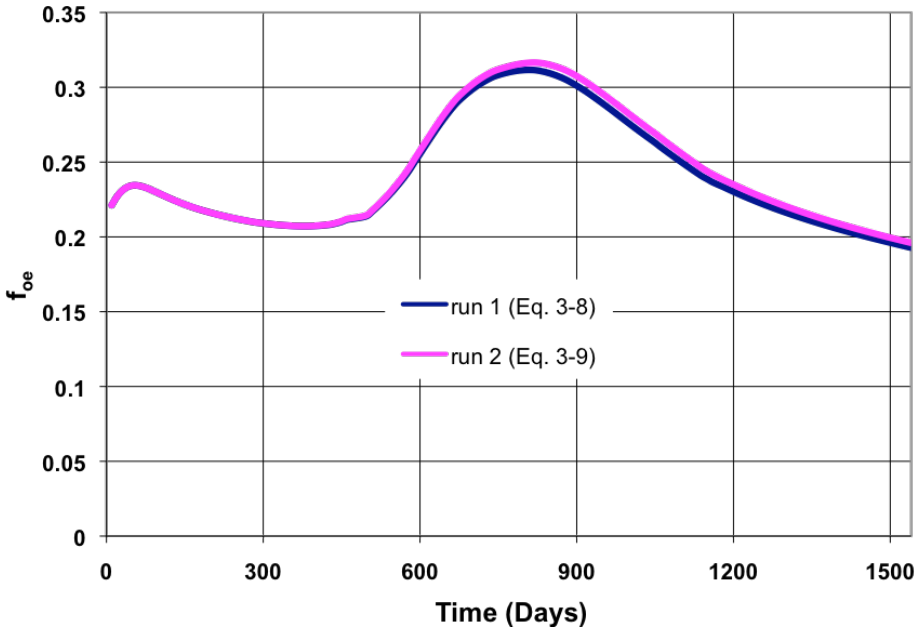

(d) Producer 4

Figure 3.58 Oil Cut of Individual Producers for Case 4

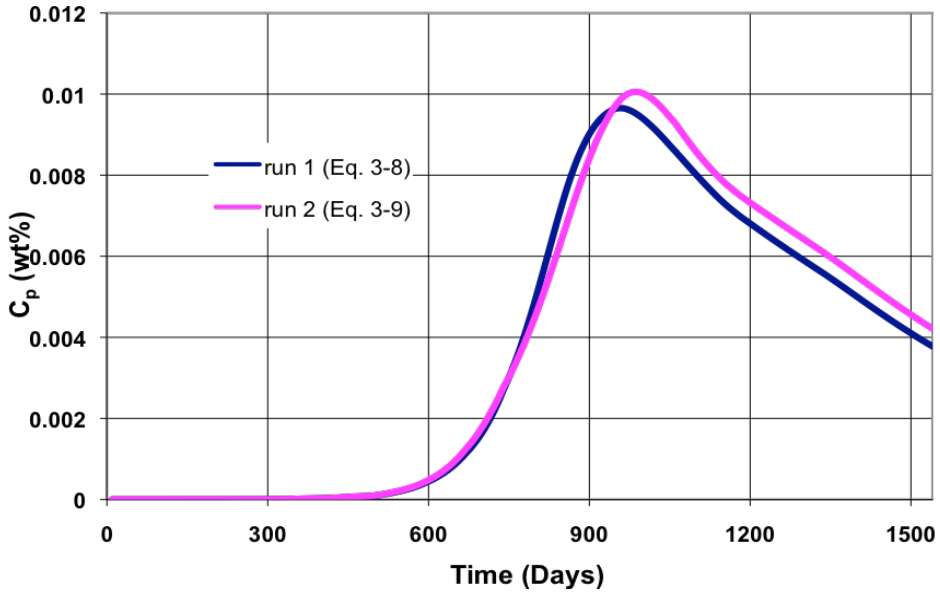

(a) Producer 1

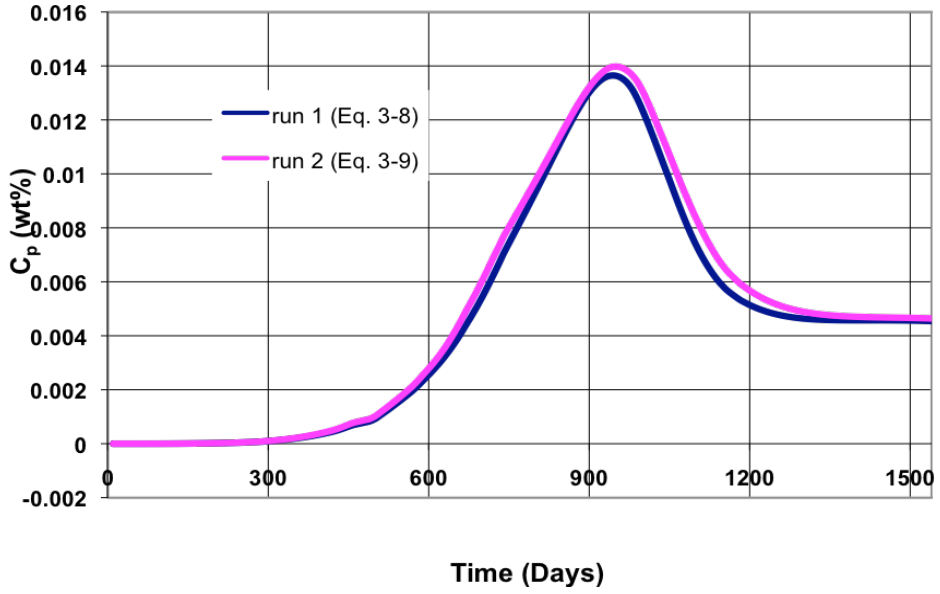

(b) Producer 2

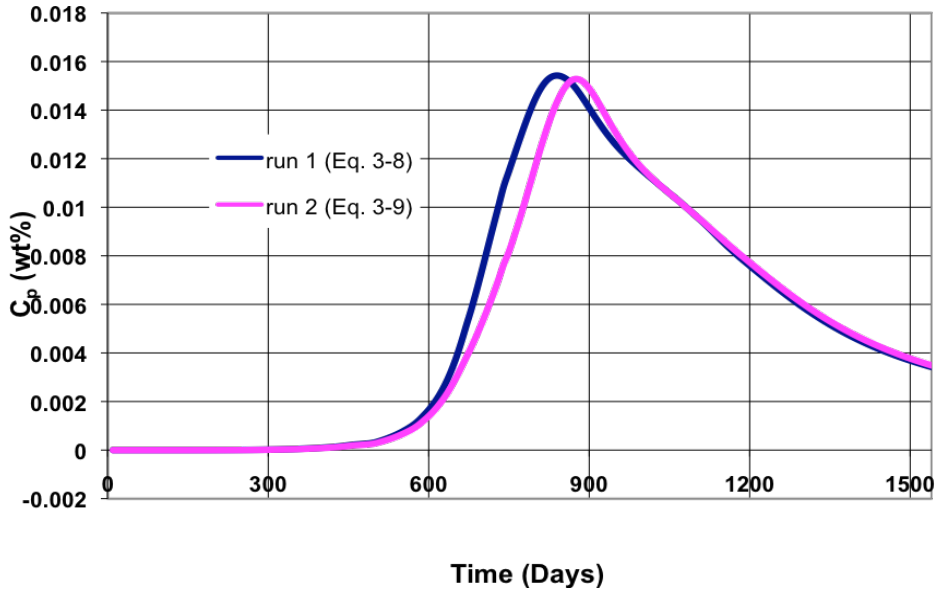

(c) Producer 3

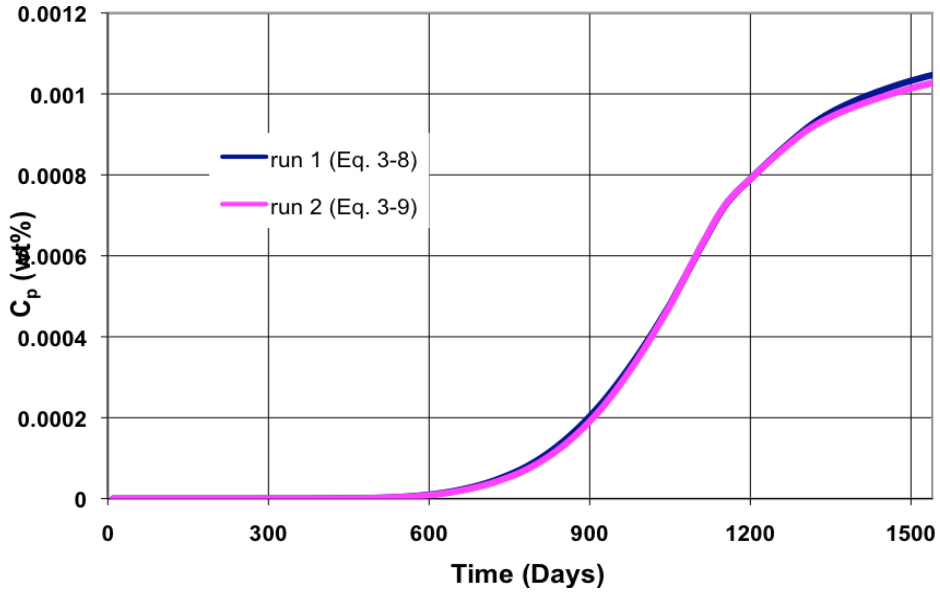

(d) Producer 4

Figure 3.59 Effulent Polymer Concentration in Individual Producers for Case 4

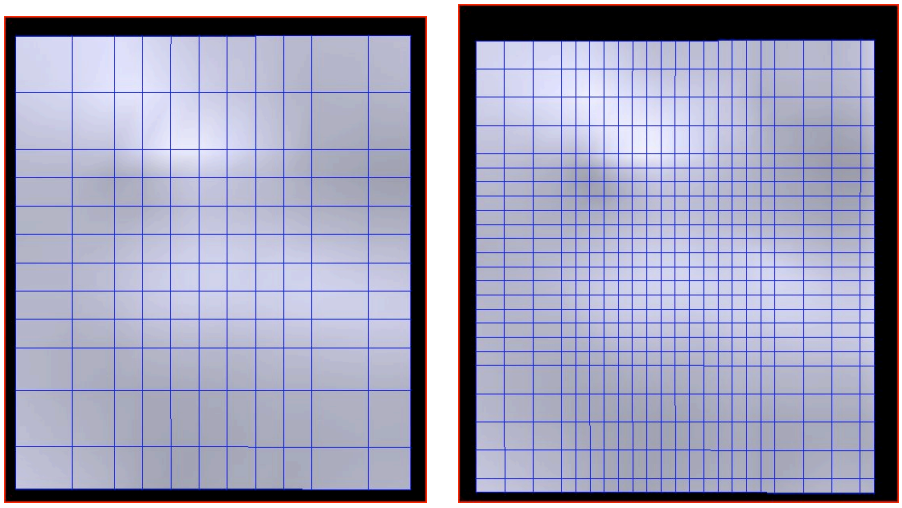

(a) Type 1 (11x22)

(b) Type 2 (22x24)

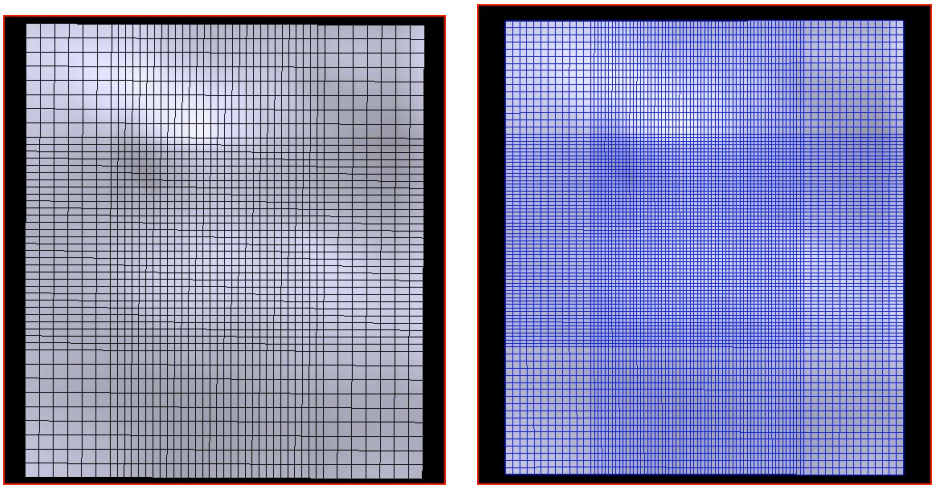

(c) Type 3 (43x47)

(d) Type 4 (86x94)

Figure 3.60 Different Areal Meshes for Case 5

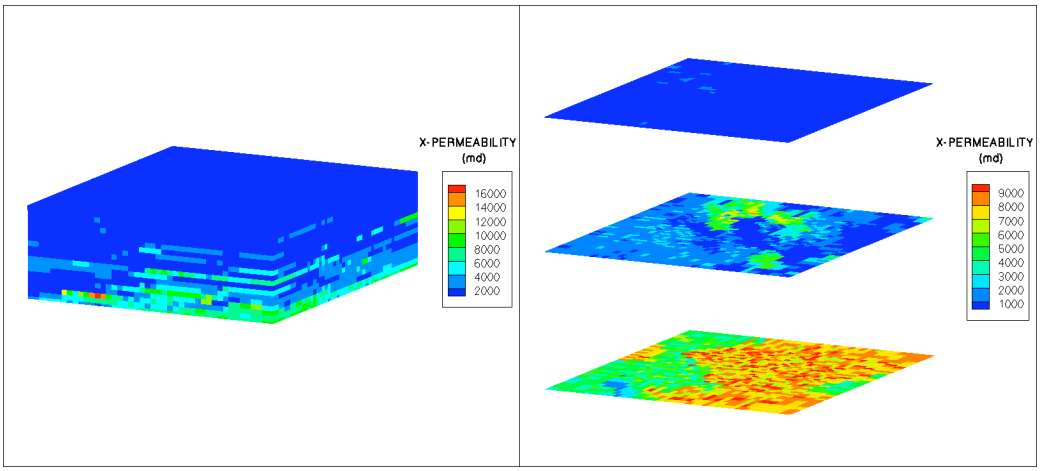

(a) X-Permeability of Grid02

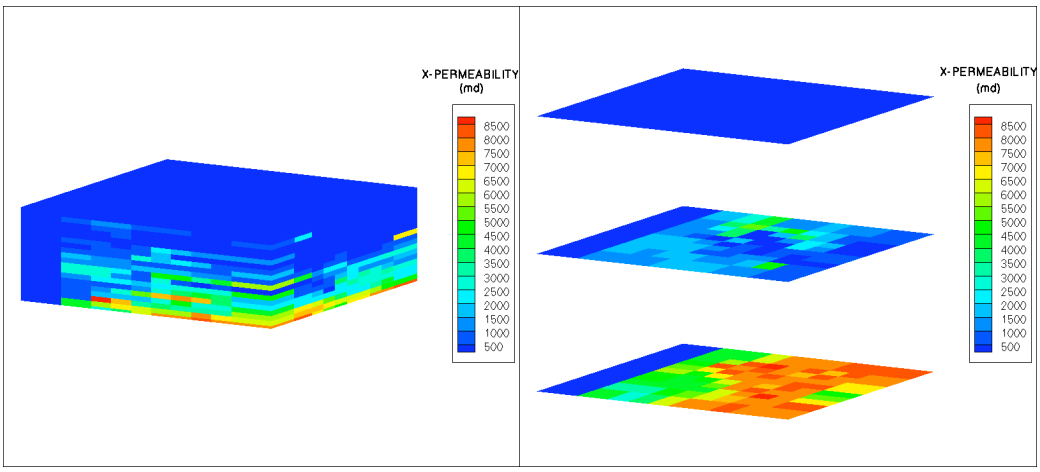

(b) X-Permeability of Grid04

Figure 3.61 X-Permeability Distributions for Case 5 with Grid02 and Grid04

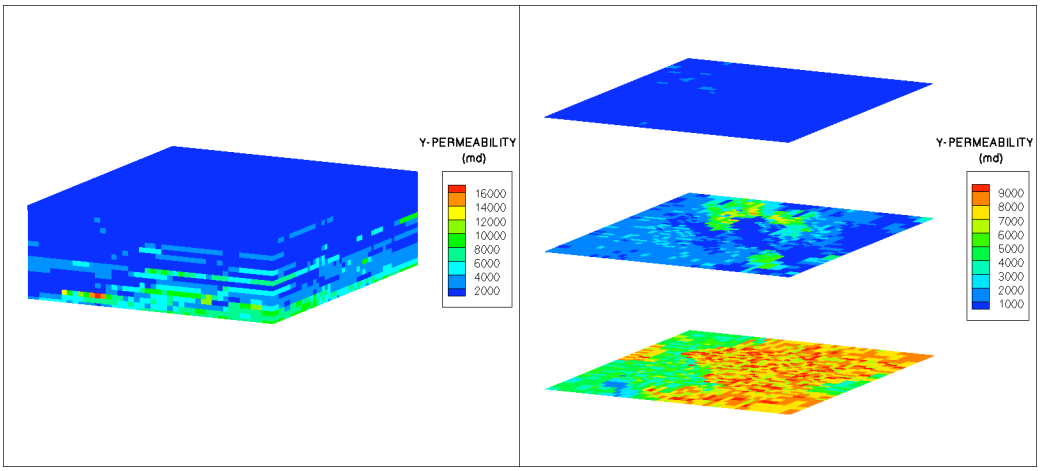

(a) Y-Permeability of Grid02

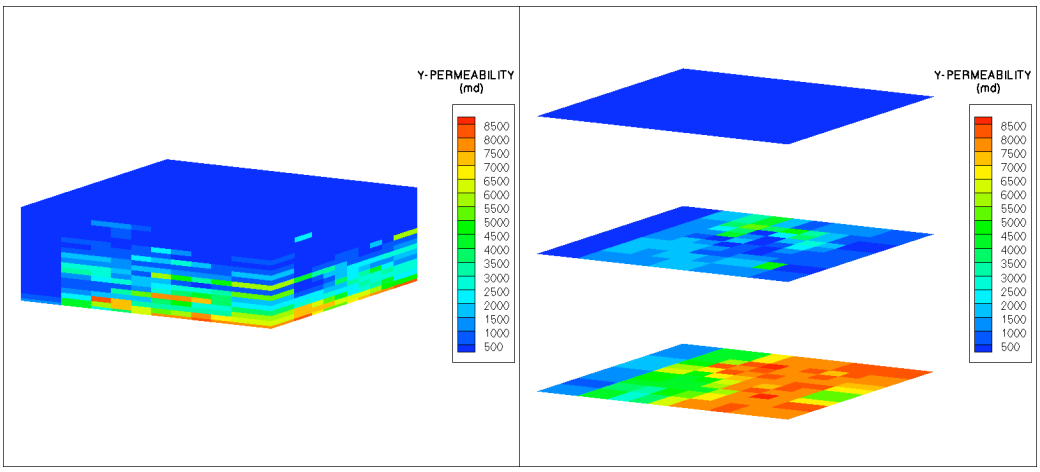

(b) Y-Permeability of Grid04

Figure 3.62 Y-Permeability Distributions for Case 5 with Grid02 and Grid04

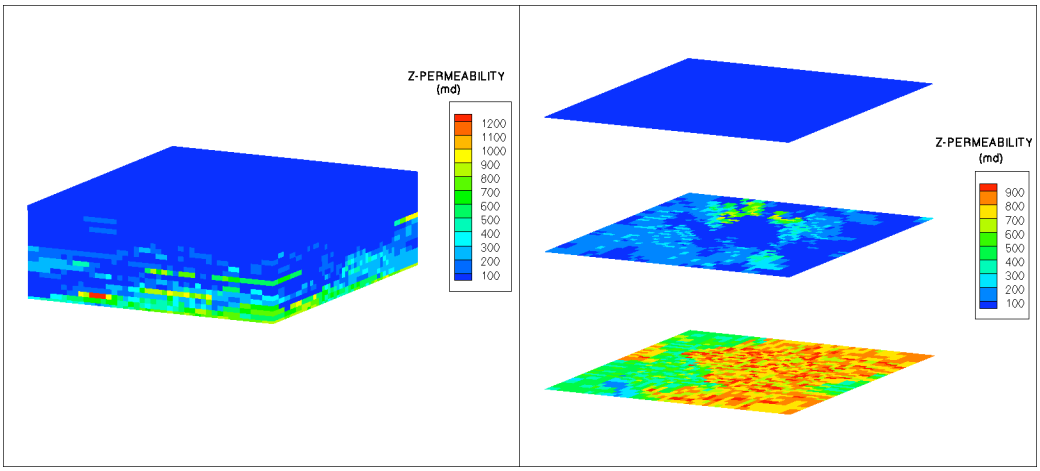

(a) Z-Permeability of Grid02

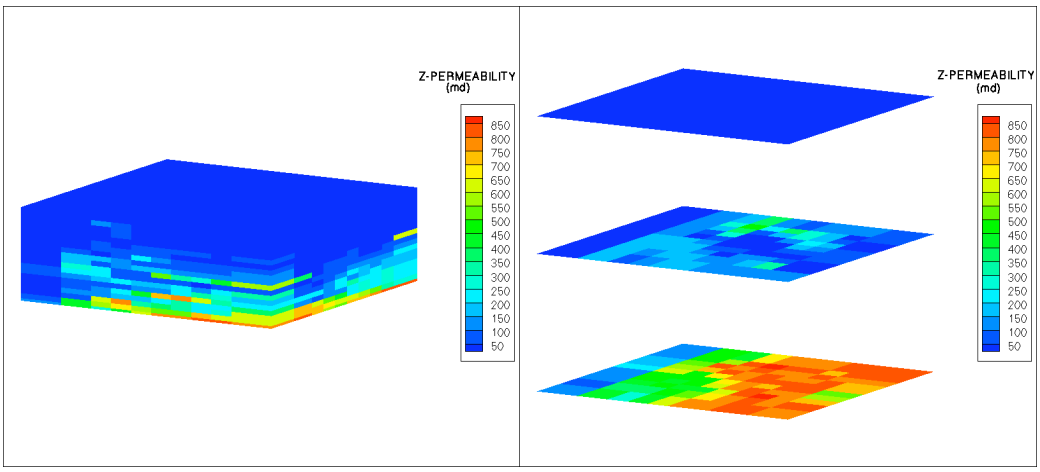

(b) Z-Permeability of Grid04

Figure 3.63 Z-Permeability Distributions for Case 5 with Grid02 and Grid04

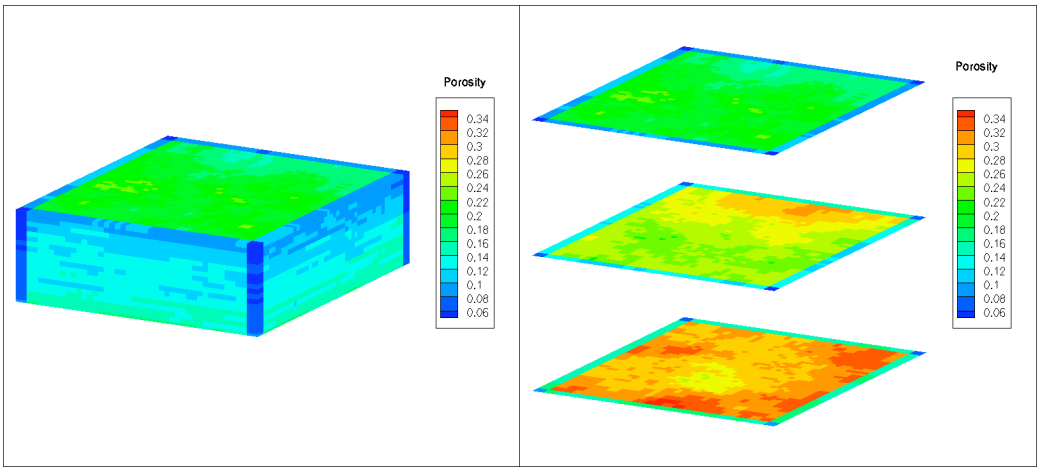

(a) Porosity Distribution of Grid02

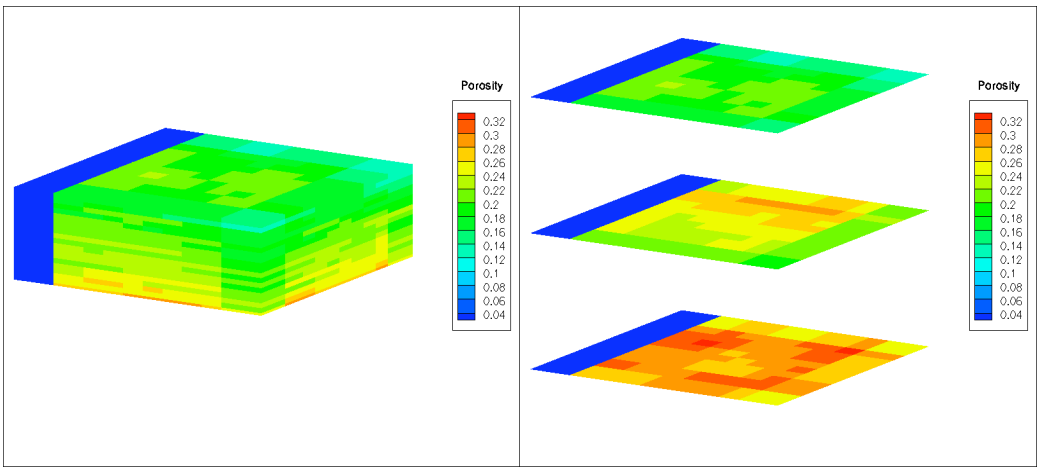

(b) Porosity Distribution of Grid 04

Figure 3.64 Porosity Distributions for Case 5 with Grid02 and Grid04

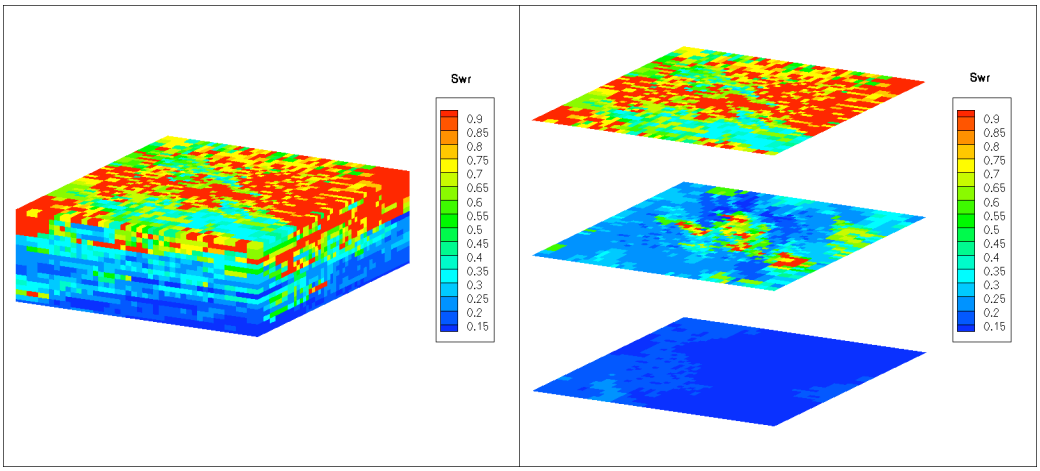

(a) Residule Water Saturation of Grid02

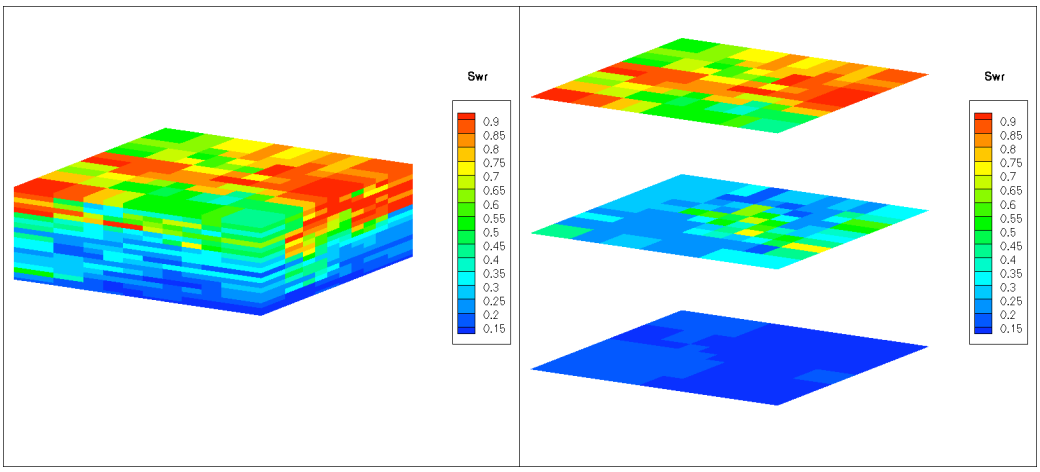

(b) Residual Water Saturation of Grid04

Figure 3.65 Residual Water Saturations for Case 5 with Grid02 and Grid04

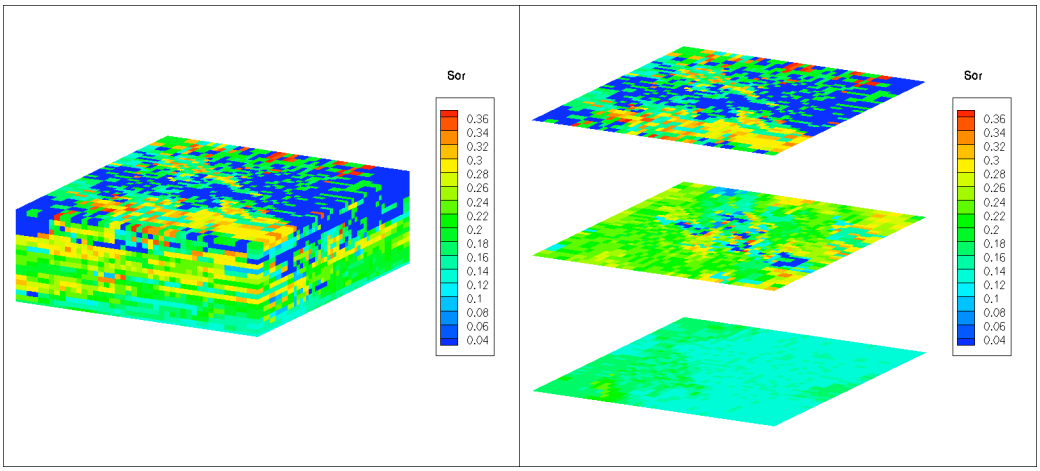

(a) Residaul Oil Saturation of Grid02

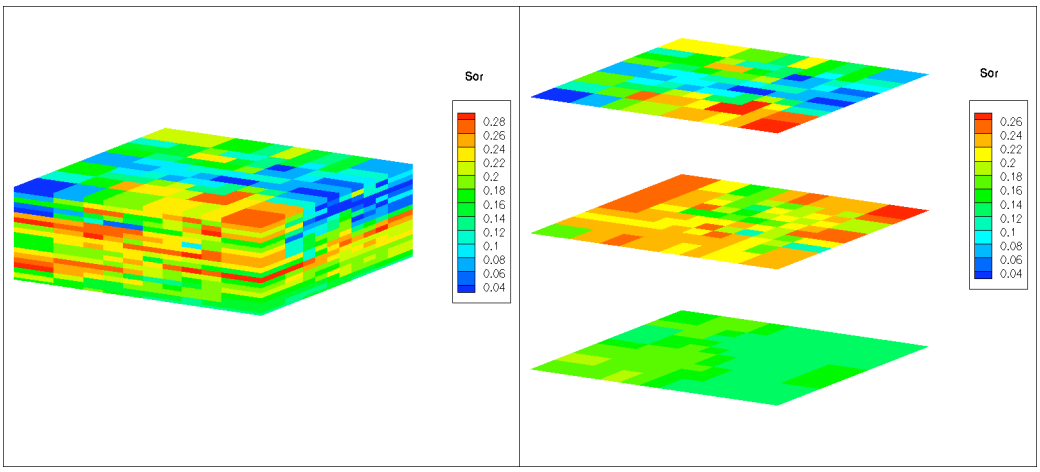

(b) Residual Oil Saturation of Grid04

Figure 3.66 Residual Oil Saturations for Case 5 with Grid02 and Grid04

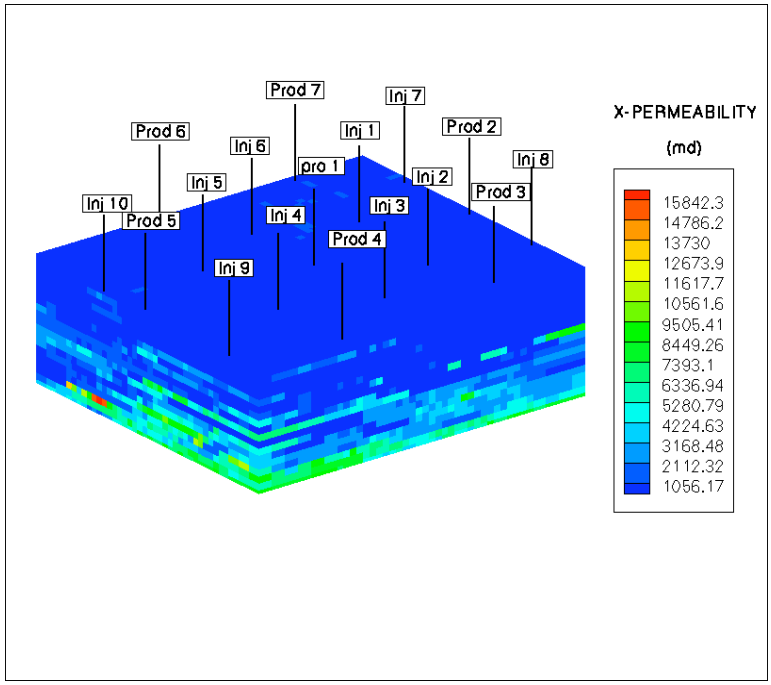

(a) Grid02 (Finest Mesh)

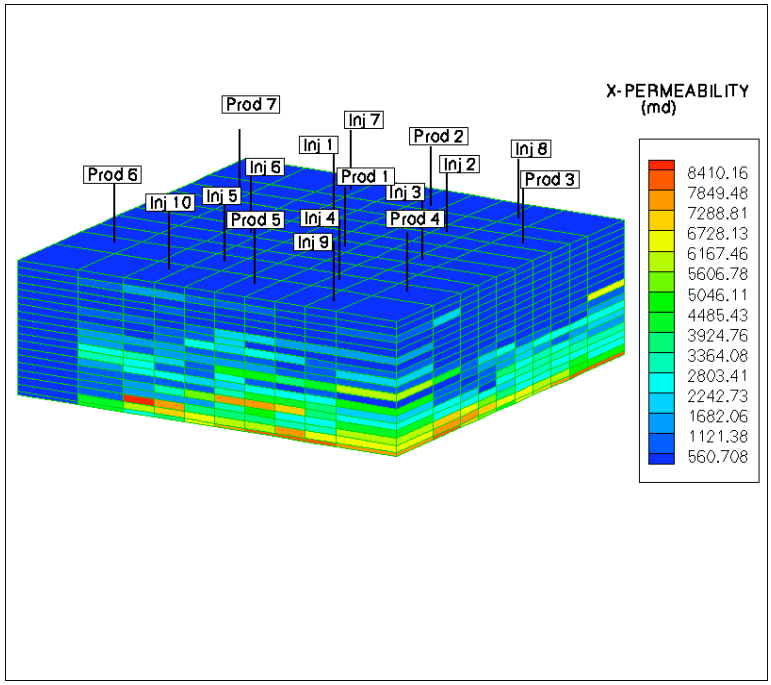

(b) Grid04 (Coarsest Mesh)

Figure 3.67 Well Locations for Case 5 with Grid02 and Grid04

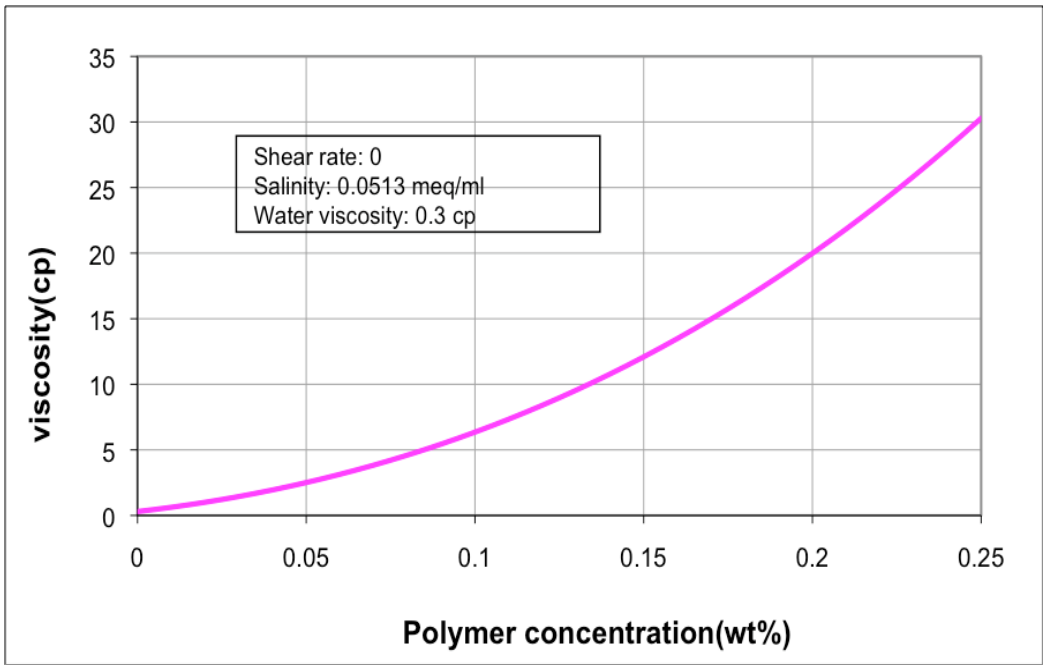

Figure 3.68 Bulk Polymer Viscosity as a Function of Polymer Concentration for Case 5

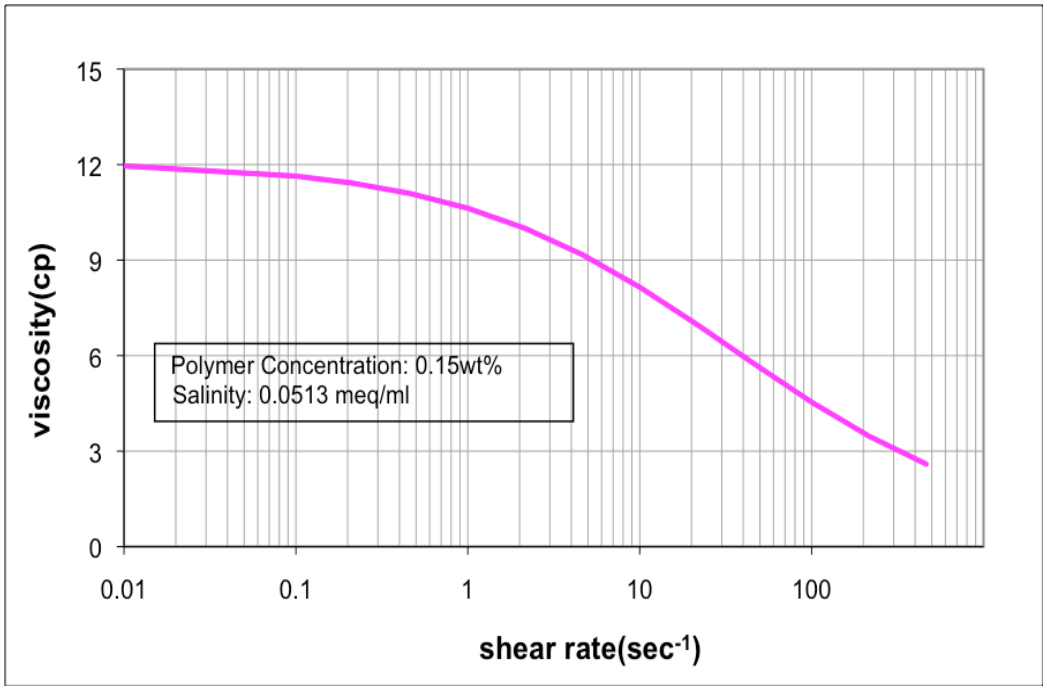

Figure 3.69 Bulk Polymer Viscosity as a Function of Shear Rate for Case 5

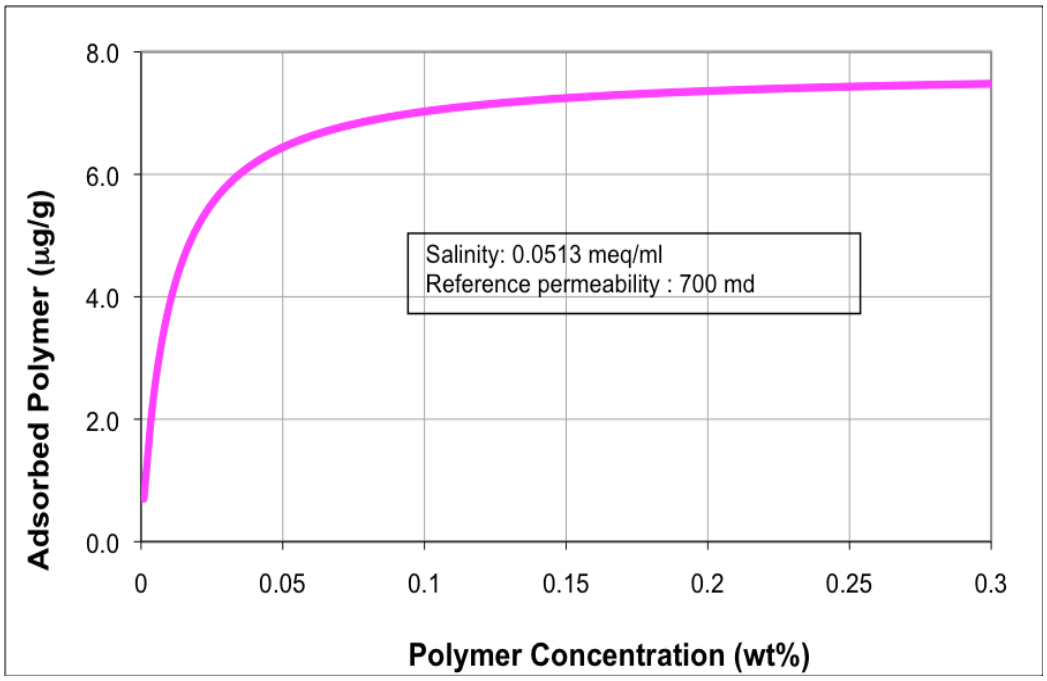

Figure 3.70 Polymer Adsorption as a Function of Polymer Concentration for Case 5

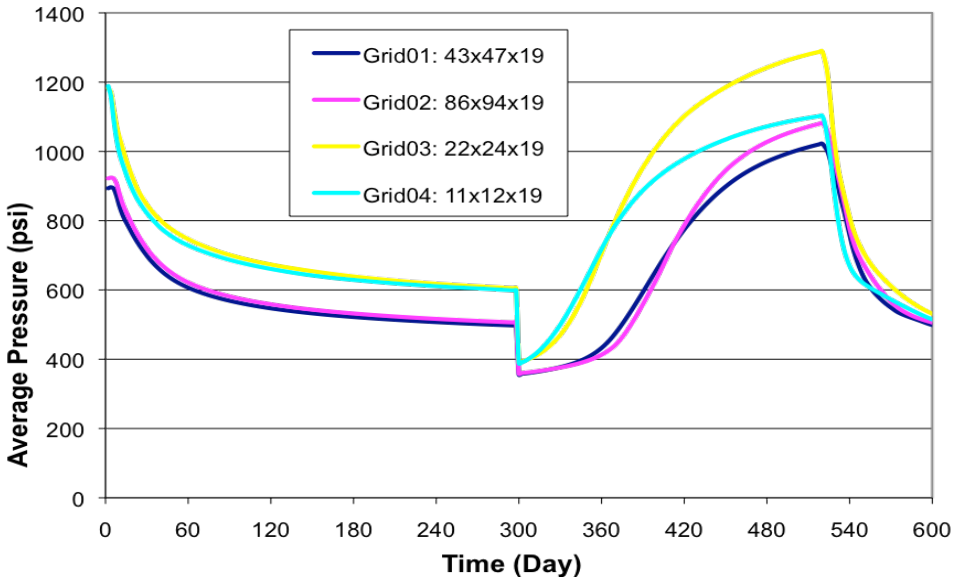

Figure 3.71 Average Reservoir Pressure History for Case 5

with Same Vertical Resolution but Different Areal Resolution

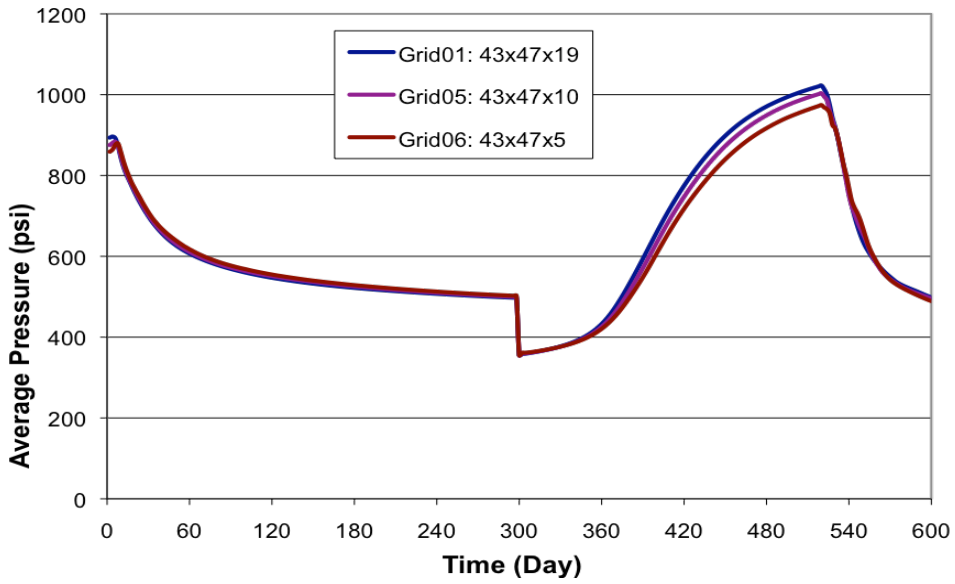

Figure 3.72 Average Reservoir Pressure History for Case 5 with Different Vertical Resolution for Areal Mesh of 43x47

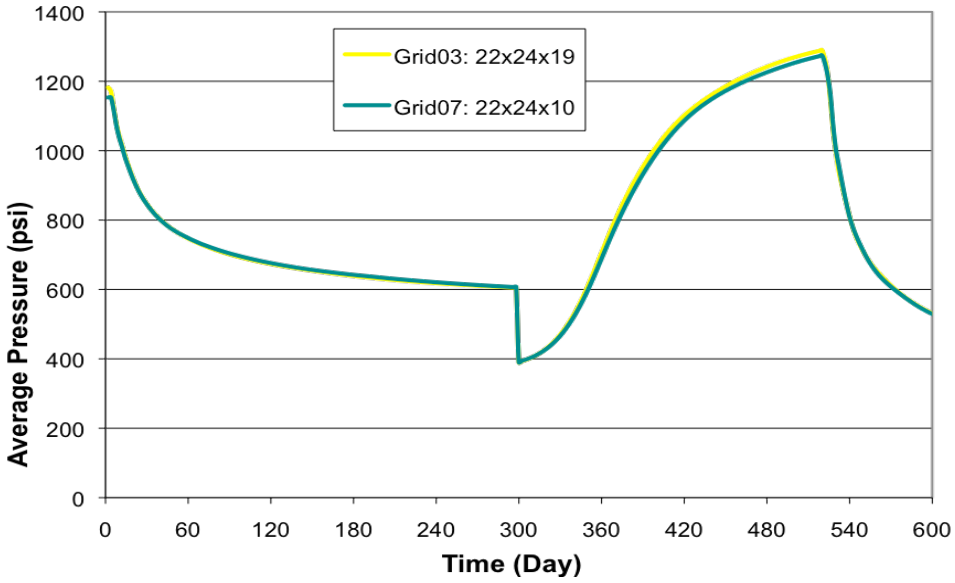

Figure 3.73 Average Reservoir Pressure History for Case 5 with Different Vertical Resolution for Areal Mesh of 22x24

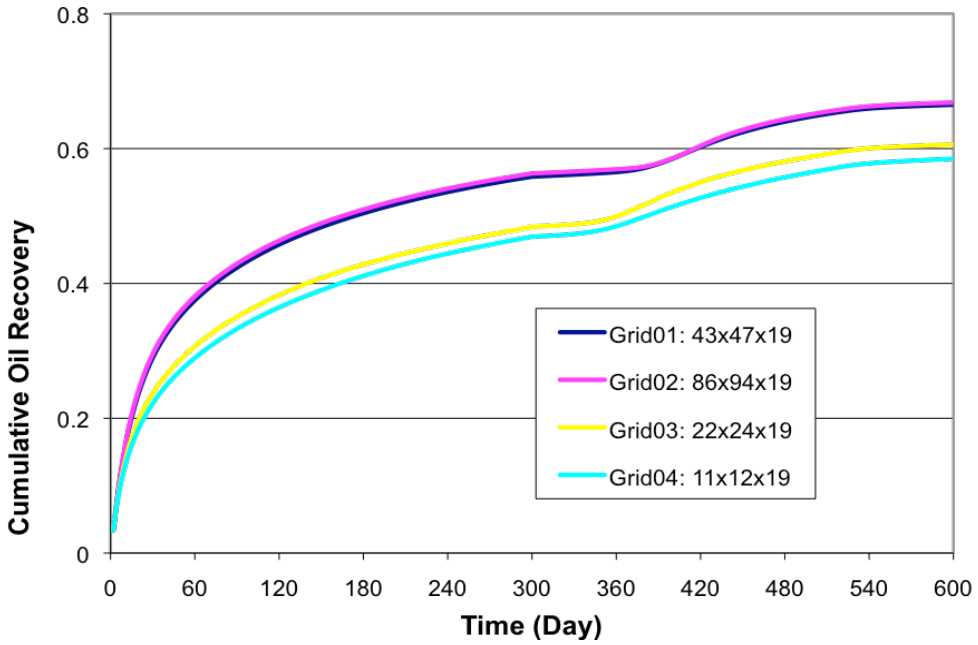

Figure 3.74 Cumulative Oil Recovery for Case 5 with Same Vertical Resolution but Different Areal Resolution

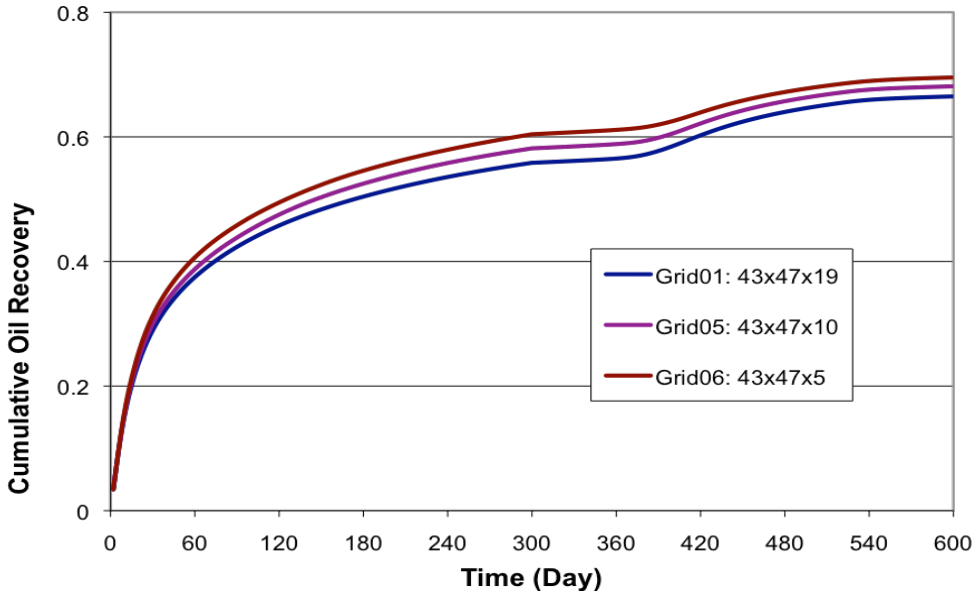

Figure 3.75 Cumulative Oil Recovery for Case 5 with Different Vertical Resolution for Areal Mesh of 43x47

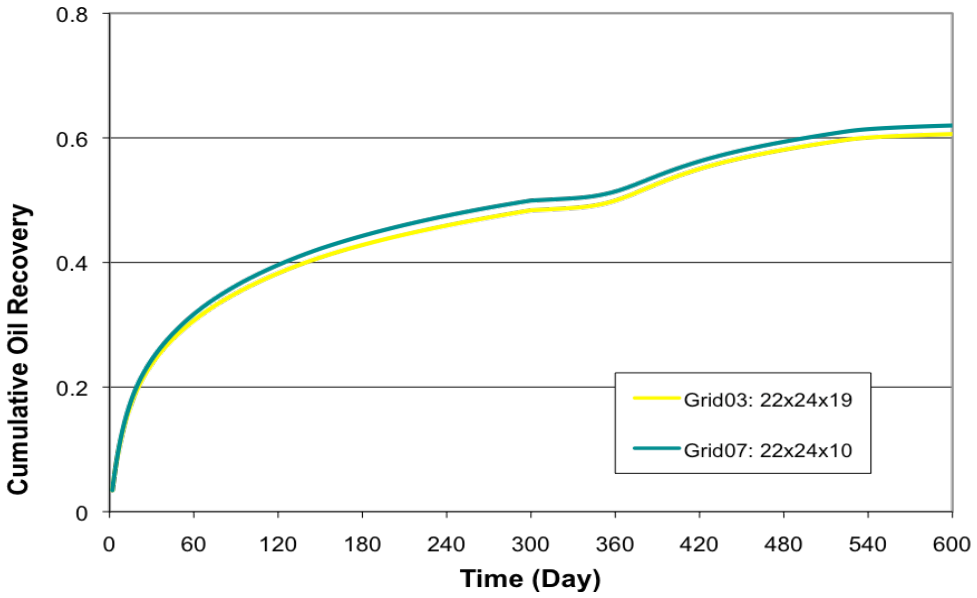

Figure 3.76 Cumulative Oil Recovery for Case 5

with Different Vertical Resolutionfor Areal Mesh of 22x24

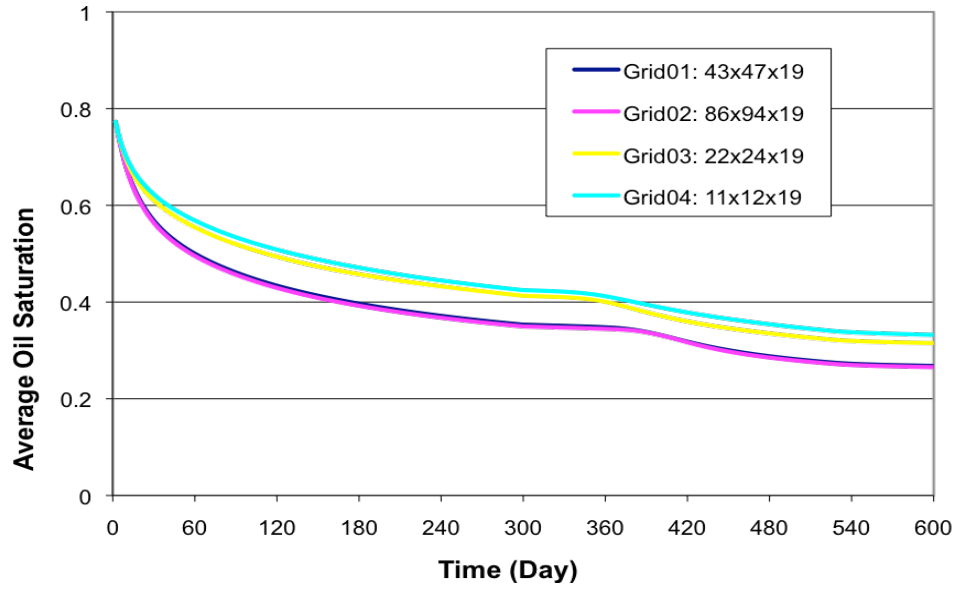

Figure 3.77 Average Reservoir Oil Saturation History for Case 5

with Same Vertical Resolution but Different Areal Resolution

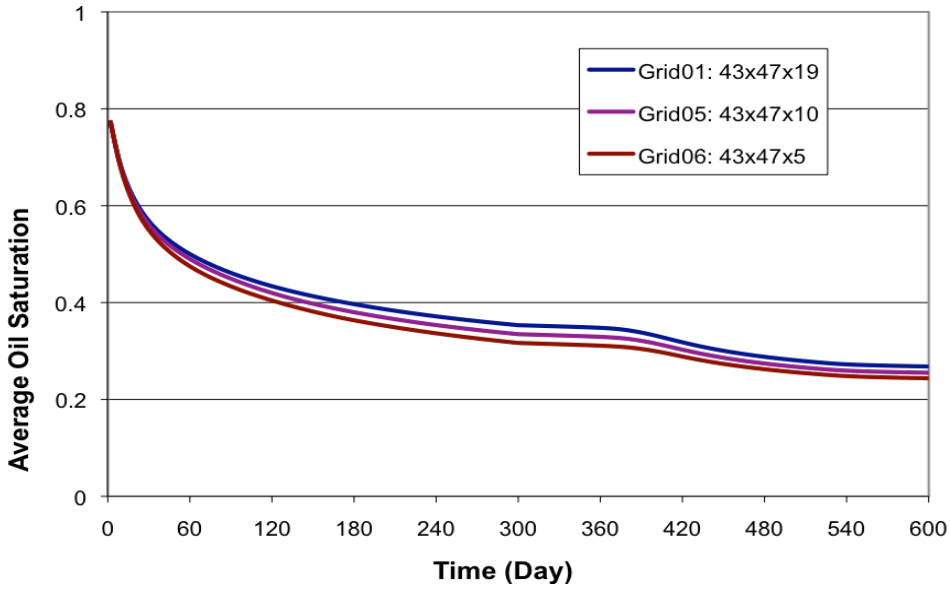

Figure 3.78 Average Reservoir Oil Saturation History for Case 5 with Different Vertical Resolution for Areal Mesh of 43x47

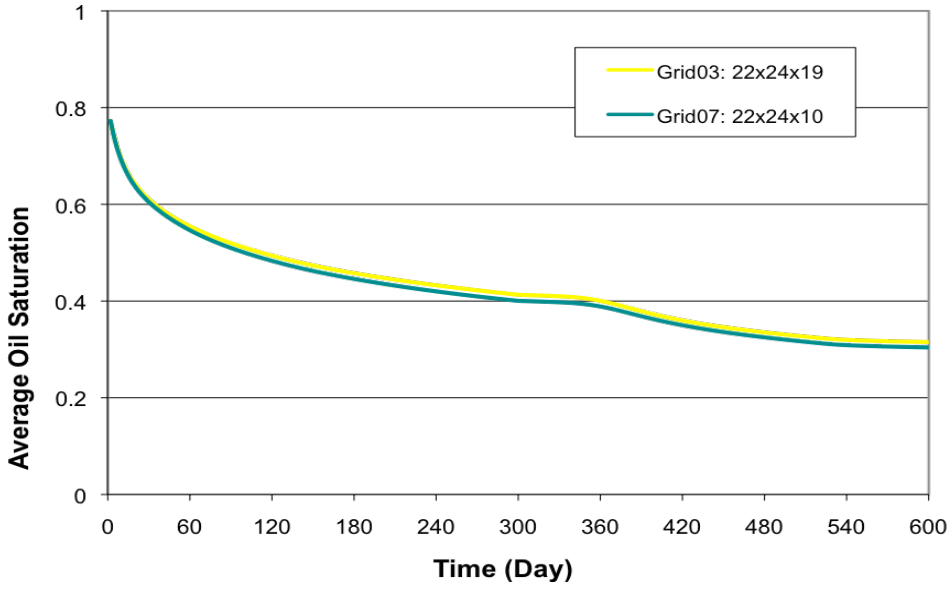

Figure 3.79 Average Reservoir Oil Saturation History for Case 5 with Different Vertical Resolution for Areal Mesh of 22x24

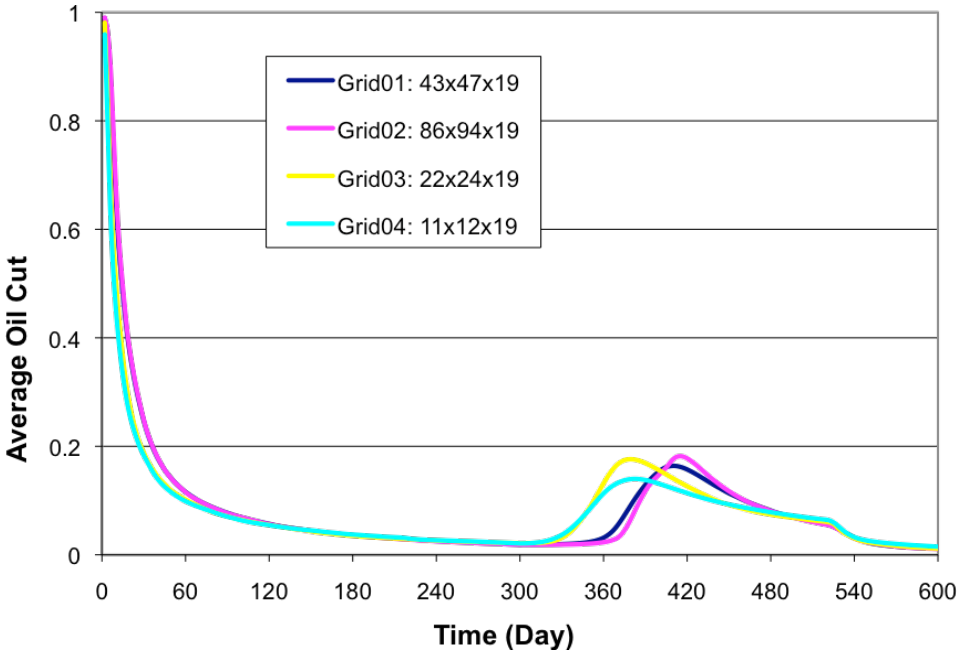

Figure 3.80 Overall Oil Cut History for Case 5

with Same Vertical Resolution but Different Areal Resolution

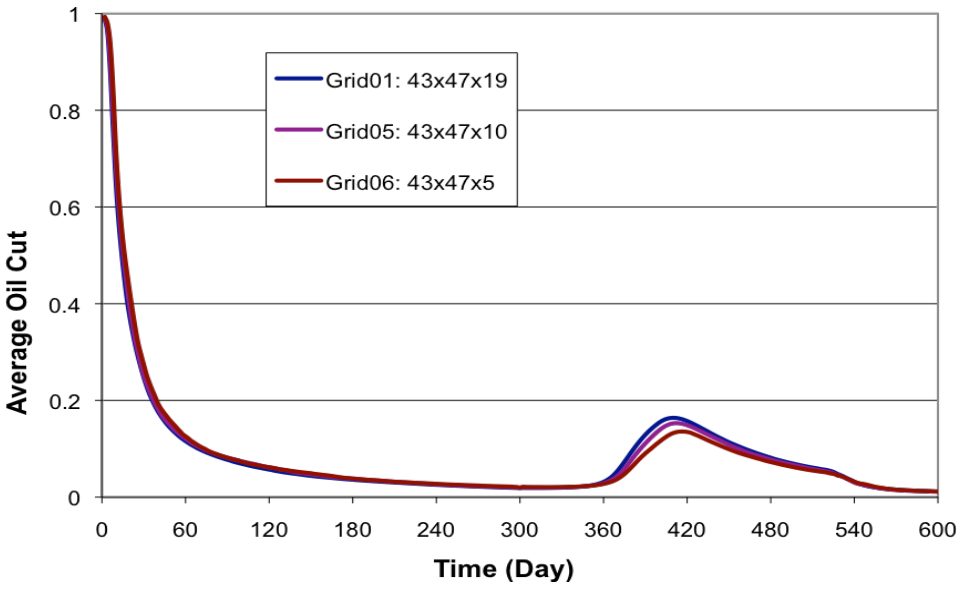

Figure 3.81 Overall Oil Cut History for Case 5

with Different Vertical Resolution for Areal Mesh of 43x47

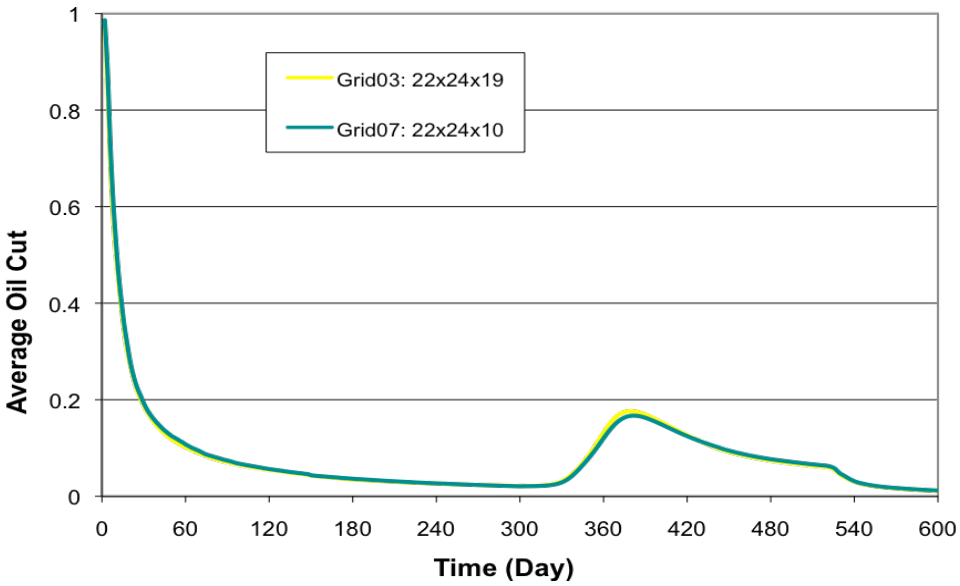

Figure 3.82 Overall Oil Cut History for Case 5

with Different Vertical Resolution for Areal Mesh of 22x24

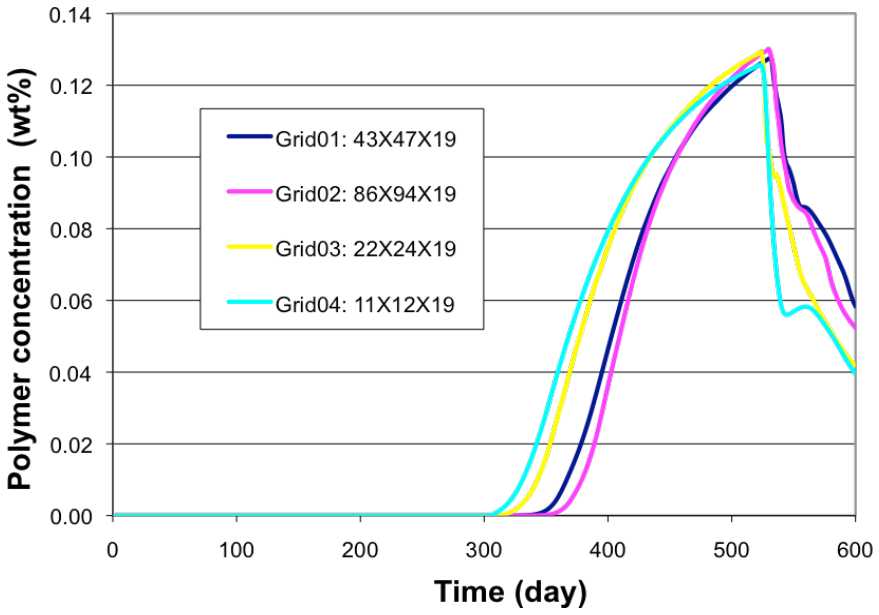

Figure 3.83 Effluent Polymer Concentration in Producer 1 for Case 5

With Same Vertical Resolution but Different Areal Resolution

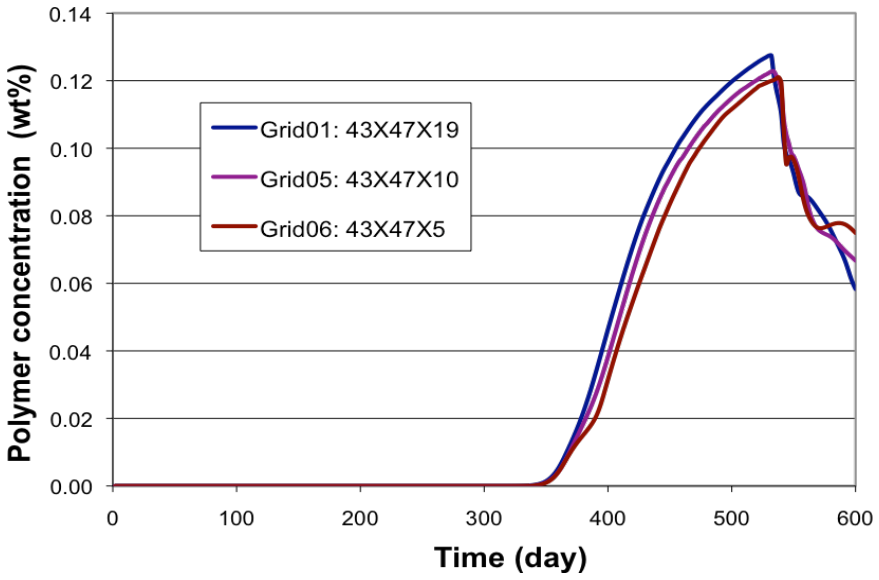

Figure 3.84 Effluent Polymer Concentration in Producer 1 for Case 5

With Different Vertical Resolution for Areal Mesh of 43x47

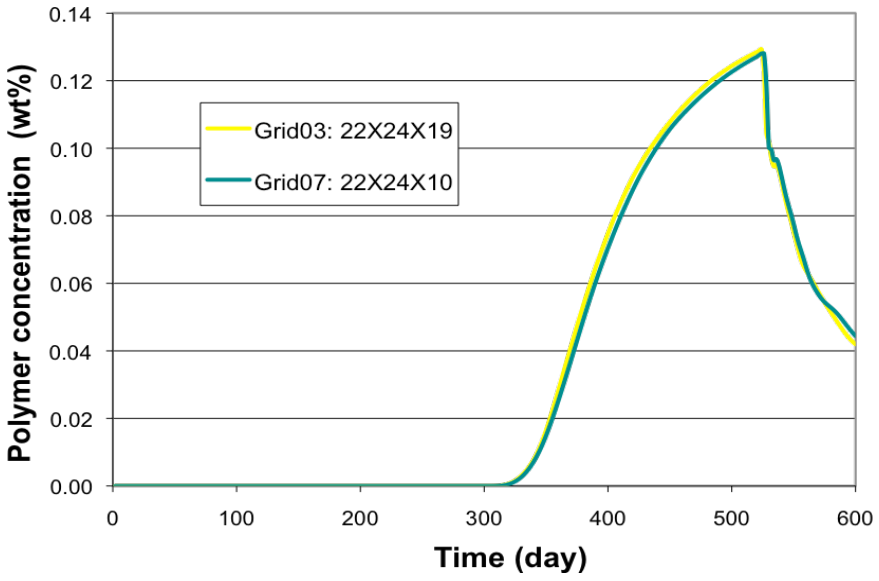

Figure 3.85 Effluent Polymer Concentration of Producer 1 for Case 5

With Different Vertical Resolution for Areal Mesh of 22x24

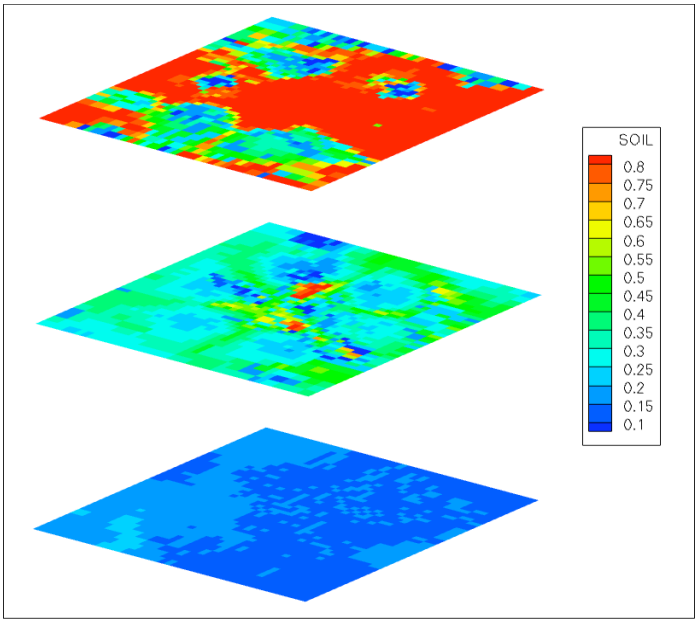

(a) t=300 Days

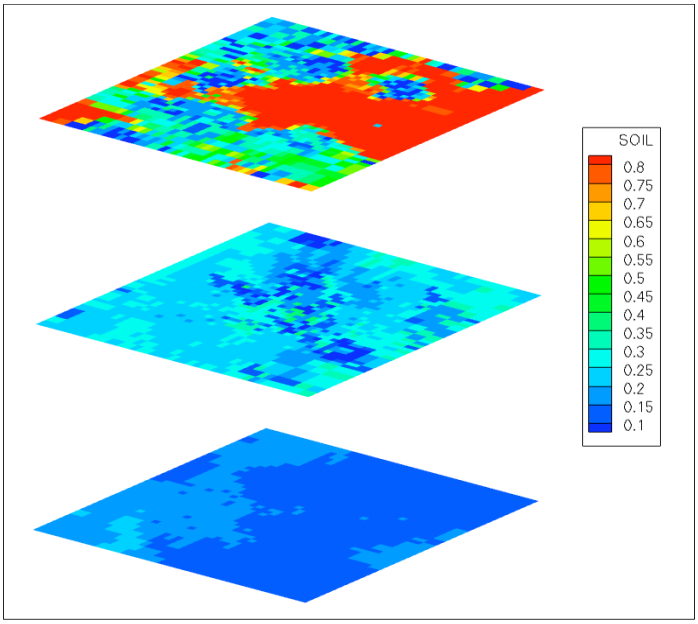

(b) t=600 Days

Figure 3.86 Oil Saturation Profiles of Case 5/Grid01 at 300 and 600 Days

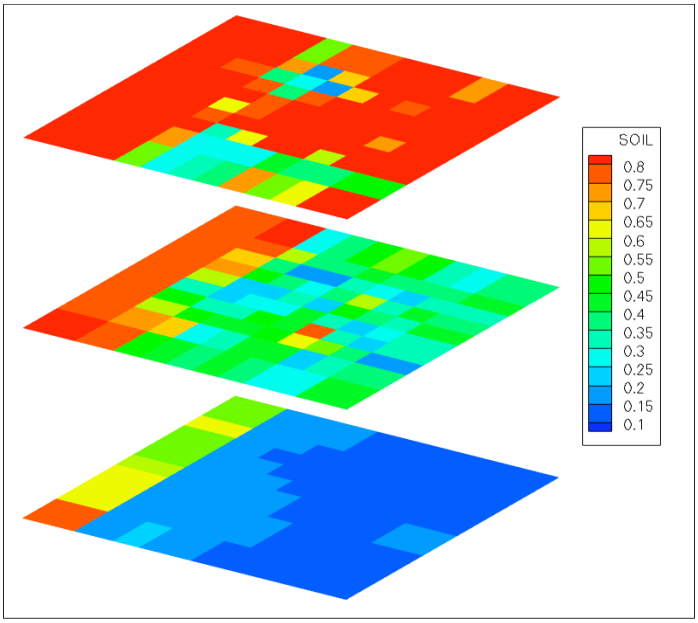

(a) t=300 Days

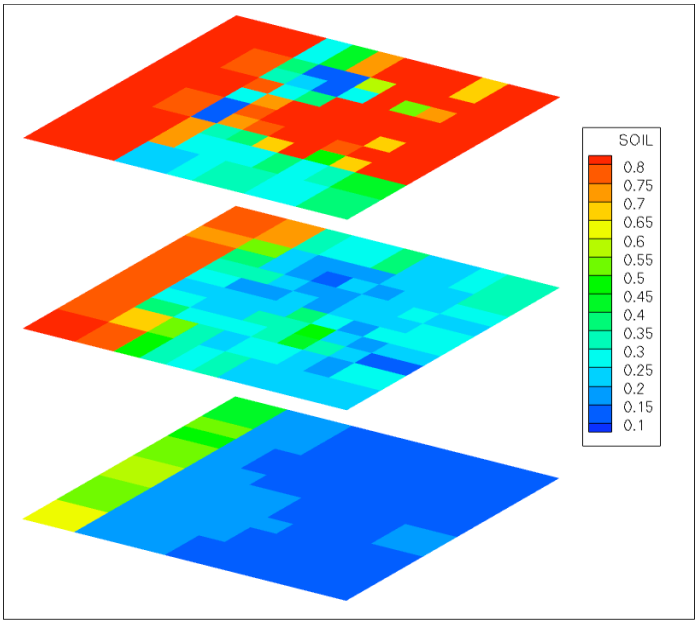

(b) t=600 Days

Figure 3.87 Oil Saturation Profiles of Case 5/Grid04 at 300 and 600 Days

PART II

MODELING INFILTRATION IN VADOSE ZONE

CHAPTER 4

INTRODUCTION

Modeling flow and transport through the unsaturated (vadose) zone impacts several DOD civil works and military applications. These include monitoring and remediating groundwater contamination at DOD sites, modeling exchange mechanism between surface water and groundwater, and improving the ability to detect surface and buried landmines, improvised explosive device, and other targets. The vadose zone is the portion of the subsurface between the land surface and the water table, where both air and water (and possibly non-aqueous phase liquids) are present. Water in the vadose zone has a pressure head less than atmospheric, and is retained by a combination of adhesion and capillary action. The amount of water filling the pore space is termed moisture content. In the unsaturated zone, moisture content is a fraction of porosity (which is the fraction of pore space to total volume of soil), while in the saturated zone, water fills the pore space and moisture content equals porosity.

The flow of water in an unsaturated zone is a complex phenomenon involving transfers of water, air and vapor through dynamic pathways under the influence of hydraulic, temperature, density and osmotic gradients in a porous medium. Since a ground water system is generally open to the air, it is a common practice that the flow of

the air phase is neglected and the pressure in the air phase is assumed to be atmospheric. This is because in most of the cases, the mobility of air is much larger than that of water due to the viscosity difference between the two fluids. Based on this assumption, the well-known Richards equation (RE) can be deduced by combining Darcy's law with the equation of continuity (Richard, 1931). Richards equation is widely used in simulating the water flow in the underground water system. There are numerous numerical simulators based on Richards equation and many of them can simulate groundwater flow fairly accurate (Milly, 1988; Tocci *et al*., 1997; Miller *et al.*, 1998).

On the other hand, considering the air phase as a separate phase in the simulation of groundwater movement, a complete two-phase air-water formulation can be developed. The two-phase approach of simulating the groundwater movement was originally inspired by the two-phase flow model of oil reservoir simulation. The two-phase model is physically more realistic than RE model, since the relative permeabilities are considered in two-phase model, which reflect the competition between two phases varied with the type of soil.

Morel-Seytoux and Billica (1985) presented a two-phase numerical model for the prediction of infiltration and water content profiles evolution in a soil column. Their model can easily be reduced to the one-phase flow equation by setting a parameter to zero. They compared the two-phase algorithm with the one-phase algorithm and found that the two-phase algorithm is more stable than the one-phase algorithm when the water contents are high in a portion of the column and the two-phase algorithm is less expensive. Touma and Vauclin (1986) conducted several experiments on a sandy soil column to analyze the

influences of the soil airflow on the process of water infiltration. They compared a numerical solution of air-water simultaneous flow model with the experimental data and with the traditional one-phase flow model. Their results showed that the air movement might significantly affect the water flow. Vauclin (1989) described the physics of water flow in vados zone as a two-phase flow problem. His work showed that the Richards equation yields relatively poor results because of large mass balance errors and erroneous estimates of infiltration.

Moridis and Reddell (1991) developed a two-phase, three-dimensional, block-centered finite difference model for the secondary water recovery by air. They identified two types of nonlinearities that associated with the air-water two-phase flow model: 1) weak nonlinearities associated with pressure dependent properties; 2) strong nonlinearities associated with capillary pressure and relative permeabilities. They resolved the instabilities caused by these nonlinearities. Celia and Bining (1992) simulated the water infiltration experiments perfomed by Touma and Vauclin (1986) using a two-phase flow model. Their key observation is that the presence of air in a soil column retards the motion of infiltrating water when the air has no path to escape. Schrefler and Zhan (1993) presented a fully coupled model for both water and air flow in deforming porous media. They showed that their model is able to solve problems where significant air effects occur.

1D-comparison of the Richards equation and the two-phase flow model was reported by Gimse and Tegnander (1994). Forsyth *et al*. (1995) developed a variable substitution method for saturated-unsaturated flow. They compared their method to the

RE model and the two-phase model and observed that the two-phase model is in good agreement with RE model, except that trapping of the air phase occurs. They also observed that the two-phase model is easier to solve numerically, even for very dry and heterogeneous problems. Tegnander (2001) compared the Richards equation and the fractional flow model in a 2D flow via varying relative permeability. She concluded that the difference between the Richards' equation and the fractional flow model greatly depends on the mobility ratio and the maximum capillary pressure; when the mobility ratio is greater than 100, these two models are equivalent.

In this work, we use 3D two-phase simulators and compare the results with a 3D simulator based on the Richards equation for flow and transport through vadose zone. Multiphase flow simulators such as IPARS and UTCHEM, both developed at the University of Texas at Austin, are used in this project. Comparisons are made to the RE model that is implemented in PyADH (a Python module for Adaptive Hydraulics), which is under development at the U.S. Army Engineer Research and Development. The purpose of these studies is to ascertain, under common scenarios such as infiltration or injection of water into initially dry soils, the similarities and differences of the two models, the ability of each model to simulate such infiltration processes under realistic scenarios, and to investigate the numerical efficiencies and difficulties which arise in these models.

CHAPTER 5

MODELING INFILTRATION IN VADOSE ZONE USING RICHARDS EQUATION AND AIR-WATER TWO PHASE FLOW MODEL

5.1 SIMULATORS OVERVIEW

5.1.1 IPARS

As mentioned before, IPARS supports eight physical models. Air-water model is one of them. The air-water model in IPARS (Jenkins, 2002) uses an expanded mixed finite element discretization. The current implementation assumes structured grids. The model is fully implicit. In this project GMRES with AMG preconditioner is used to solve the linear system of equations arising at the Newton iterations at each time step.

5.1.2 UTCHEM

UTCHEM is a three-dimensional multiphase, multicomponent, variable temperature, finite-difference numerical simulator. UTCHEM is capable of modeling transient and steady state 3D advective and dispersive flow and mass transport in saturated and unsaturated porous media. The flow equations are comprised of a mass-balance equation for each species and an aqueous-phase pressure equation that is obtained by an overall mass balance on volume-occupying components. The other phase pressures are computed by adding the capillary pressure between phases.

Up to four phases are considered: aqueous, oleic, surfactant-rich microemulsion, and gas phases depending on the relative amounts and effective electrolyte concentrations (salinity) of the phase environment. The flow equations allow for compressibility of soil and fluids, dispersion and molecular diffusion, and phase behavior and are complemented by constitutive relations. The solution method is implicit in pressure and explicit in concentration (IMPES type). The JCG algorithm is used in solving pressure equation. Initial conditions are prescribed for the saturation, concentration, temperature, and pressure fields, respectively, together with rock properties. Component flow rates and/or pressures (Neumann/Dirichlet conditions) are defined in the injecting and producing wells. Inflow and outflow boundaries can also be defined by prescribing surface flux or surface pressures. UTCHEM has been used to simulate field scale problems and laboratory experiments. For more information about UTCHEM and relevant references, see (Delshad and Pope, 2000) and (Delshad *et al*., 2002).

5.1.3 PyADH

PyADH is a toolkit for constructing numerical solutions of nonlinear partial differential equations arising in continuum mechanics, in particular subsurface and surface multiphase flows and multi-component reactive transport phenomena. The computational core of the code is a set of algorithms that assembles and solves a fully discrete nonlinear algebraic system of equations from a description of the coefficients and boundary conditions of a generic system of (at most) second order nonlinear partial

differential equation. PyADH allows a range of discrete finite element types on unstructured meshes in 1, 2, or 3 dimensions including conforming and non-conforming Galerkin finite elements and various bases for local polynomial spaces of orders 1-5. Likewise a range of variable order time discretizations is used including backward difference formulas of Runge-Kutta methods. These discretizations are equipped with stabilization mechanisms including the variational multiscale method (Hughes, 1995), shock-capturing diffusion, and problem-specific Riemann solvers (for discontinuous Galerkin).

The Richards Equation model used in this project employs a conservative head-based formulation (Kees and Miller, 2002) and a locally conservative variational multiscale method that converges at second order for smooth problems on unstructured meshes (Kees *et al.*, 2008).

5.2 MODEL FORMULATION

5.2.1 Flow Equations

Here we describe the key equations in each simulator related to the infiltration in the vadose zone. Both multiphase flow simulators solve for mass conservation law, and pressure equation taking into account soil compressibility, air and water fluid compressibility, capillary pressure, and relative permeabilities. Physical properties such as relative permeability and capillary pressure depend on the aquifer properties, *i.e.* permeability and porosity. For heterogeneous aquifer properties, a J-Leverett function

can be used to compute the capillary pressure as a function of the given aquifer permeability and porosity in each grid block.

5.2.1.1 Air-water Model in IPARS

The air-water model in IPARS was originally developed by Lee and Noh (1999) and revised by Jenkins (2000). In this model, the air is compressible and modeled by the real gas law.

The air-water model is similar to the oil-water model. The only difference is the non-wetting phase is the air phase. In air-water model, the primary unknowns are the water pressure (P_w) and the water saturation (S_w). The mass balance equations are given by

$$\frac{\partial(\phi\rho_\alpha S_\alpha)}{\partial t} + \nabla \cdot \rho_\alpha \vec{u}_\alpha = q_\alpha, \qquad \alpha = a, w \tag{5-1}$$

Darcy's law, saturation constraint, and the capillary pressure definition are the same as Eq. (2-2, 2-4, 2-5), but substituting the oil phase with the air phase. The water phase is slightly compressible. Equation (2-6) gives the density of the water phase. The air phase is compressible. The density of the air phase is given by

$$\rho_a = \frac{P_a M}{Z(P_a)RT} \tag{5-2}$$

where M is the molecular weight of air, R is the gas constant, T is the temperature, and $Z(P_a)$ is the compressibility factor which is a function of the air pressure.

Reformulating the above equations, we obtain governing equations with respect to two primary unknowns as

$$\frac{\partial[\phi\rho_a(1-S_w)]}{\partial t} - \nabla\cdot\{\rho_a\vec{\vec{K}}\frac{k_{ra}}{\mu_a}[\nabla(P_w+P_c)-\rho_a g\nabla D]\} = q_a \tag{5-3}$$

$$\frac{\partial(\phi\rho_w S_w)}{\partial t} - \nabla\cdot[\rho_w\vec{\vec{K}}\frac{k_{rw}}{\mu_w}(\nabla P_w - \rho_w g\nabla D)] = q_w \tag{5-4}$$

The governing equations are solved over a spatial domain Ω and for time t > 0. Initial and boundary conditions must be specified to close the system. The discretizations in space and in time are the expanded mixed finite element method and backward Euler method, respectively. The discretization details are outlined in (Jenkins, 2002). The governing equations solved fully implicitly using Newton iteration method to solve the nonlinear system of equations arising at each time step.

5.2.1.2 UTCHEM

In UTCHEM (Delshad, 2000 and references therein), water pressure and component concentrations are the primary unknowns. The mass conservation law for component κ is expressed as

$$\frac{\partial(\phi\rho_\kappa\tilde{C}_\kappa)}{\partial t} + \nabla\cdot[\sum_{l=1}^{n_p}\rho_\kappa(C_{\kappa l}\vec{u}_l - D_{\kappa l})] = R_\kappa, \qquad \text{for } \kappa = 1,\ 2,\ ...,\ n_c \tag{5-5}$$

where $\tilde{C}_\kappa$ is the sum over all phases and includes the adsorbed concentration of each species:

$$\tilde{C}_\kappa = (1-\sum_{\kappa=1}^{n_{cv}}\hat{C}_\kappa)\sum_{l=1}^{n_p}S_l C_{\kappa l} + \hat{C}_\kappa \tag{5-6}$$

Ideal mixing with small and constant compressibilities are assumed in UTCHEM including the air phase, so the densities are given by

$$\rho_k = 1 + c_\kappa^0(P_R - P_{R0}) \tag{5-7}$$

The source term R_κ is given by

$$R_\kappa = \phi \sum_{l=1}^{n_p} S_l r_{\kappa l} + (1-\phi) r_{\kappa s} + Q_\kappa \tag{5-8}$$

The Darcy's velocity for each phase is given by

$$\vec{u}_l = -\vec{\vec{K}} \frac{k_{rl}}{\mu_l} (\nabla P_l - \gamma_l \nabla h) \qquad l = 1,\ 2,\ ...,\ n_p \tag{5-9}$$

where γ_l is the phase specific weight and is a function of pressure and composition,

$$\gamma_l = C_{1l}\gamma_{1l} + C_{2l}\gamma_{2l} + C_{3l}\gamma_{3l} + 0.02533 C_{5l} - 0.001299 C_{6l} + C_{8l}\gamma_{8l} \qquad \text{for } l = 1,\ ...,\ n_p \tag{5-10}$$

and

$$\gamma_{\kappa l} = \gamma_{\kappa R}[1 + c_\kappa^0 (P_l - P_{R0})] \tag{5-11}$$

The capillary pressure is defined as

$$P_{c1l} = P_l - P_1 \qquad l = 2,\ 4 \tag{5-12}$$

The concentration constraint is

$$\sum_{\kappa=1}^{n_{cv}} C_{\kappa l} = 1 \tag{5-13}$$

The definitions for variables in the above equations are as follows:

- $\tilde{C}_\kappa$ = overall volume of component κ per unit pore volume;
- ρ_κ = density of pure component κ at a reference phase pressure P_R relative to its density at reference pressure P_{R0};
- n_p = number of phases;
- $C_{\kappa l}$ = volume of component κ in phase l per phase volume;
- $D_{\kappa l}$ = dispersive flux, which is not considered in this chapter;

- n_{cv} = total number of volume-occupying components;
- $\hat{C}_\kappa$ = adsorbed concentration of component κ;
- c_κ^0 = compressibility constant of component κ;
- $r_{\kappa l}$ = reaction rates for component κ in phase l;
- $r_{\kappa s}$ = reaction rates for component κ per bulk volume;
- Q_κ = injection/production rate for component κ per bulk volume;
- $\gamma_{\kappa R}$ = component κ specific weight at a reference pressure P_{R0};
- h = vertical depth.

Summing up the mass conservation equations Eq. (5-5) over all volume-occupying components such as water and air in this chapter, inserting Darcy's Law Eq. (5-9) and using the concentration constraints Eq. (5-13) and capillary pressure definition Eq. (5-12), we obtain the pressure equation in terms of the reference pressure (water phase):

$$\phi c_t \frac{\partial P_1}{\partial t} + \nabla \cdot (\vec{\vec{K}} \lambda_{rTc} \nabla P_1) = -\nabla \cdot (\sum_{l=1}^{n_p} \vec{\vec{K}} \lambda_{rTc} \nabla h) + \nabla \cdot (\sum_{l=1}^{n_p} \vec{\vec{K}} \lambda_{rTc} \nabla P_{cl1}) + \sum_{\kappa=1}^{n_{cv}} Q_\kappa \tag{5-14}$$

where the relative mobility is defined as

$$\lambda_{rlc} = \frac{k_{rl}}{\mu_l} \sum_{l=1}^{n_{cv}} \rho_l C_{\kappa l} \tag{5-15}$$

and the total relative mobility with the correction for fluid compressibility is

$$\lambda_{rTc} = \sum_{l=1}^{n_p} \lambda_{rlc} \tag{5-16}$$

c_t is the total compressibility, which is the volume-weighted sum of the rock c_r and component compressibilities c_κ^0:

$$c_t = c_r + \sum_{\kappa=1}^{n_{cv}} c_\kappa^0 \tilde{C}_\kappa \tag{5-17}$$

The rock is assumed slightly compressible. The porosity ϕ is given as a function of pressure:

$$\phi = \phi_R[1 + c_r(P_R - P_{R0})] \tag{5-18}$$

The phase saturation in the vadose zone in the absence of nonaqueous liquid phase can be computed from

$$S_1 = C_1, \qquad S_2 = C_2 \tag{5-19}$$

where the subscript 1 stands for the water phase and the subscript 2 stands for the air phase.

5.2.1.3 PyADH

The Richards equation formulation in PyADH (Kees and Miller, 2002) is based on following assumptions:

- The air phase pressure is assumed to be constant;
- The solid phase is immobile;
- No interphase mass exchange;
- No internal sources and sinks.

The mass balance equation for the water phase is given by

$$\frac{\partial(\theta_w \rho_w)}{\partial t} + \nabla \cdot (\rho_w \vec{u}_w) = 0 \quad \text{in } \Omega \times [0, T] \tag{5-20}$$

where θ_w is the moisture content, which is related to the water saturation by

$$\theta_w = \phi S_w \tag{5-21}$$

ρ_w has the same form as IPARS.

More parameters are defined to develop Richards equation formulation. The hydraulic conductivity, K_s, is defined as

$$K_s = \frac{\rho_{w0} g k_i}{\mu_w}$$

where ρ_{w0} is the water density at reference pressure P_0, k_i is the intrinsic permeability of the porous media. Furthermore, the pressure head for each phase is defined as

$$\psi_\alpha = \frac{P_\alpha}{\rho_{w0} g} \qquad \alpha = a, w \tag{5-22}$$

The capillary head is used in PyADH rather than capillary pressure, which is given in terms of the pressure head as

$$\psi_c = \psi_a - \psi_w \tag{5-23}$$

The Darcy Law in terms of the pressure head is given by

$$\vec{u}_w = -K_s k_{rw} (\nabla \psi_w - \frac{\rho_w}{\rho_{w0}} \nabla h) \tag{5-24}$$

Inserting Eq. (5-23) into Eq. (5-20), we obtain Richards Equation

$$\frac{\partial(\theta_w \rho_w)}{\partial t} - \nabla \cdot [\rho_w K_s k_{rw} (\nabla \psi_w - \frac{\rho_w}{\rho_{w0}} \nabla h)] = 0 \quad \text{in } \Omega \times [0, T] \tag{5-25}$$

where ψ_w is considered the primary unknown. The first term on the left hand side is approximated by an adaptively chosen fixed leading coefficient backward difference formulas (Kees and Miller, 1999) while ψ_w is approximated using the standard piecewise

linear Galerkin finite element space. The algebraic subgrid-scale (ASGS) approximation is used in the context of the variational multiscale method along with a standard isotropic shock-capturing diffusion (Kees *et al*., 2008). The resulting nonlinear systems at each time step are solved using Newton's method and linear systems are solved with the sparse direct solver SuperLU (Demmel, 1999). Once ψ_w solved, the water saturation is calculated from the inverse of the capillary head curve.

5.2.2 Capillary Pressure and Relative Permeability Model

The capillary pressure and relative permeabilities are calculated using a modified Brooks-Corey model (Brooks and Corey, 1964) as described below. For heterogeneous aquifers different relative permeability and capillary pressure curves are used. The capillary pressure is computed in each gridblock based on the values of permeability and porosity using the J-Leverett scaling function.

The water injection in the vadose zone is treated as an imbibition process. In UTCHEM, the imbibition capillary pressure curve of the *i*-th layer with absolute permeability k_i and porosity ϕ_i is given by

$$P_{c,i} = C_{pc}(1 - S_e)^{E_{pc}} \sqrt{\frac{\phi_i}{k_i}} \tag{5-26}$$

where S_e is the effective wetting phase saturation defined by

$$S_e = \frac{S_w - S_{wirr}}{1 - S_{wirr} - S_{or}} \tag{5-27}$$

The constant C_{pc} and E_{pc} are positive input parameters in UTCHEM obtained at a reference permeability and porosity. C_{pc} is define as follows:

$$C_{pc} = P_b \sqrt{\frac{k_{ref}}{\phi_{ref}}} \tag{5-28}$$

where P_b is the maximum capillary pressure.

The imbibition relative permeability model used in air-water model is the same as the one described in section 2.3.

In UTCHEM and PyADH, the relative permeability and capillary pressure models and their coefficients are specified in the input and implemented analytically. In air-water model of IPARS, the input tabular data give the capillary pressure and relative permeability curves. The input tables for IPARS are generated from above models using the same input parameters as UTCHEM.

5.2.3 Well Model and Boundary Conditions

Both wells and boundary conditions are available in IPARS. The well model and boundary conditions in air-water model are very similar to those of HYDRO model, which are described in section 2.4 and 2.5. The user can specify the following combinations of boundary conditions:

1. Water pressure, water saturation
2. Water pressure, air saturation
3. Air pressure, water saturation
4. Water pressure, air pressure

5. Water pressure, water saturation at a reference depth
6. Air and water flux

The injection/production in UTCHEM is modeled via a well. A same well model as that of IPARS in Section 2.4, Peaceman type, is implemented in UTCHEM. The detail about the well model in UTCHEM is described in (Delshad, 2000).

Two types of boundary conditions are available in PyADH: Dirichlet and Neumann boundary condition. For the RE formulation, one boundary condition is imposed per boundary location, either Dirichlet type or Neumann type.

5.3 BENCHMARK PROBLEMS AND COMPUTATIONAL RESULTS

Six different data sets were assembled as benchmark infiltration problems in the unsaturated zone. The data sets are all 3-D with only two phases of water and air flowing. Each case has different aquifer properties, initial conditions, physical properties, and water injection strategies. Injection wells were used as means of introducing water into the vadose zone in the first 4 cases. In last two cases, we use boundary conditions to model the sides of the domain open with a constant atmospheric head.

5.3.1 Case 1: 3D Homogeneous Isotropic with Capillary Pressure

An isotropic homogeneous reservoir is considered for this case. Initially the reservoir is hydrostatic and the water saturation is at its residual value of 0.2. All boundaries are closed to flow. There are 2 water injection wells in the center of the reservoir. The left and right hand sides of the reservoir are open to air by introducing

several boundary wells with a constant pressure of 14.7*psi*. Water is injected through 2 water injection wells for one day, and then shut in (no injection) for 2 days as the redistribution and rest period. The injection wells only penetrate through the first top layer. The boundary wells penetrate through the entire aquifer thickness. Constant volumetric water injection rate ($3 ft^3/day$) is specified for each injection well. Constant bottomhole pressure (14.7*psi*) is specified for each boundary well. Figure 5.1 shows plot of the grids and well locations. Table 5.1 lists the aquifer description, fluid properties, and additional input for Case 1. The well data is given in Table 5.2. Figure 5.2 presents the capillary pressure and relative permeability curves.

The results are shown for an x-z cross section in the middle block in the Y direction. Water saturation profiles at the end of one-day injection and at the end of the rest period are given in Figure 5.3 and 5.4, respectively. Water sinks to the bottom due to the higher density compared to the air phase and spreads laterally during the redistribution period. The results are very similar for UTCHEM and IPARS. The profiles of water and air pressures at the end of one-day injection and at the end of 3 days are shown in Figure 5.5 through 5.8. There is a very slight discrepancy in the phase pressures between the two models.

5.3.2 Case 2: 3D Heterogeneous Anisotropic without Capillary Pressure

The second case involving a larger simulation domain with layered heterogeneity has also been constructed. The x and y direction permeability ranges from 9*D* to 1*D* as given in Table 5.3. The vertical to horizontal permeability ratio is 0.3. The water

saturation is initialized to be at the residual value of 0.20 and hydrostatic water pressure. There are 4 injection wells in the middle of the domain to introduce water in the unsaturated zone. The left and right hand sides of the model are open to air by introducing several boundary wells with a constant pressure of 14.7*psi*. Figure 5.9 gives the simulation model grid, well locations, and permeability arrangement. Water is injected at a constant volumetric rate of $5 ft^3/day$ in each well for a period of 2 days. The injection wells were then closed for a redistribution period of 3 days. The capillary pressure is neglected in this case. The water/air relative permeability is shown in Figure 5.2b. The data for the grid and reservoir and fluid properties that are different from Case 1 are given in Table 5.3. The injection and boundary well data are listed in Table 5.4.

2D x-z cross-sections of water saturation distribution at the end of 2 days injection and at the end of the rest period of 5 days are shown in Figures 5.10 and 5.11, respectively. The water saturation profile shows a slower downward movement due to the heterogeneity and shows more lateral movement in the higher permeability layers. The results of IPARS and UTCHEM are very comparable. Water and air pressure profiles are also shown for 2 and 5 days in Figures 5.12 through 5.15. The profiles are very similar with small discrepancy in the air pressure between the two simulators.

5.3.3 Case 3: 3D Heterogeneous Anisotropic with Capillary Pressure

This benchmark problem is similar to Case 2 with the exception that a different capillary pressure is assigned to each layer. Table 5.5 gives the parameters for capillary pressure function (Eq. 5-26). Figure 5.16 gives the capillary pressure curves for different

layers. Water saturation distributions at 2 and 5 days are shown in Figures 5.17 and 5.18. Due to the capillary pressure and heterogeneity, water never reached the bottom of the model. The water is spread laterally in the layer with lower permeability. The results of water and air pressures are very similar for IPARS and UTCHEM as shown in Figures 5.19 through 5.22.

5.3.4 Case 4: 3D Heterogeneous Anisotropic with Variations in Capillary Pressure and Relative Permeability

This benchmark problem is similar to Case 3 but with different initial water saturation and relative permeability curves for each permeability layer. The water injection rate was increased to $10 ft^3/day$. Table 5.6 gives the initial water saturation and parameters for the relative permeability function (Eq. 2-25, 2-26). Capillary pressure curves for each layer are given in Figure 5.16. Figure 5.23 gives the relative permeability curves for different layers. Water saturation distributions at 2 and 5 days are shown in Figures 5.24 and 5.25. The results of water and air pressure are shown in Figures 5.26 through 5.29. There are slight differences in the water saturation profiles between UTCHEM and IPARS. Water migrates downward faster in IPARS compared to that in UTCHEM. This might be due to using table look up option for capillary pressure and relative permeability with interpolation in IPARS versus the function in UTCHEM.

To compare the efficiency, we compare the computational time of each simulator. UTCHEM runs only on PC. IPARS runs on PC and in parallel. The configuration of computers used in this project is listed in table 5.7. The CPU time for the test cases are

given in Table 5.8. It should be observed that UTCHEM timings are greater than IPARS since UTCHEM is IMPES and IPARS is fully implicit with a more efficient solver. Also, IPARS parallel results are not to scale due to the small problem size.

The previous four test cases had initial conditions of non-equilibrium state, not a fully saturated water at the bottom boundary, and an imbibition capillary pressure function that all caused difficulties for running PyADH code based on Richards equation. In order to compare the results of the two-phase flow simulator IPARS with PyAHD, two new air/water test cases are set up. The fifth event is in a glass tank packed with different sands. The Kueper sandbox problem is modified for water infiltration into an initially air-dry tank. More detailed information is given in the next subsections. The sixth problem is the infiltration of water via a ponded surface in a homogeneous column. The fluid properties of water and air are the same in these two test problems. However, Brooks-Corey ***psk*** relation is used in Kueper sandbox whereas van Genuchten-Mualem ***psk*** is used in the last data set (Kees and Miller, 2002).

5.3.5 Case 5: Kueper Sandbox

5.3.5.1 Physical System

The physical domain was an acrylic glass tank of dimension 70cm x 50cm x 0.6cm. Four different homogeneous quartz sands with uniform grain size distributions were used to pack the tank and obtain a cute heterogeneity pattern (see Figure 6.11 in (Helmig, 1997)). The DNAPL was PCE. The simulation was isothermal (T = 20°C). Brooks-Corey ***psk*** relations were used. Table 5.9 gives the soil properties where p_d is the

entry pressure, λ is the Brooks-Corey parameter associated with the grain-size uniformity, $S_{\omega r}$ is the wetting phase residual saturation, and ϕ is the porosity. The left and right boundaries were maintained at hydrostatic equilibrium. The bottom boundary was no flow. The top boundary was no flow except for a slot of length of 10 cm in the middle, where infiltration from an initial saturation of S_n = 0.4 (non-wetting phase saturation) was assumed. Initially the tank is fully saturated with water. Figure 5.30 shows the experimental setup.

5.3.5.2 Modified Problem for Air/Water in 3D

Instead of DNAPL, air is assumed to be the non-wetting phase. We consider infiltration of water into an initially air-dry tank. We assume the density and viscosity of water to be ρ_w = 997.0 [kg/m^3], ρ_n = 1.205 [kg/m^3], μ_w = 1.002x10^{-3}[kg/m·s], μ_n = 1.81 x10^{-5} [kg/m·s]. The initial conditions are as follows

$$\psi_w = -z\rho_w g$$

$$\psi_a = 0.0$$

$$S_w = \psi_c^{-1}(\psi_a - \psi_w)$$

At a slit on the top of the tank we apply a fixed pressure head in both phases:

$$\psi_w = 0.0 \text{ for } (x, y, 0.7): \ 0.7/3 \le x \le 1.4/3, \ 0 \le y \le 0.07$$

$$\psi_a = 0.0$$

Elsewhere apply no-flow for the wetting phase but allow air to exit the domain. A domain of 0.7m x 0.07m x 0.5m is used with 70 x 1 x 50 elements in IPARS. Two additional elements with larger dimensions are added to the side of the model for an open boundary to air flow only. The top surface is modeled as closed boundary with the

exception of the middle third of the top (elements 24 to 46) with saturated water ($S_w = 1$) and no ponding. Different capillary pressure and relative permeability curve are calculated from following equations. Table 5.9 shows the capillary pressure and relative permeability curve for each type of sand.

$$P_c = p_d \left(\frac{S_w - S_{wr}}{1 - S_{wr}} \right)^{-1/\lambda} \tag{5-29}$$

$$k_{rw} = \left(\frac{S_w - S_{wr}}{1 - S_{wr}} \right)^{\frac{2+3\lambda}{\lambda}} \tag{5-30}$$

$$k_{ra} = \left(1 - \frac{S_w - S_{wr}}{1 - S_{wr}} \right)^2 \left[1 - \left(\frac{S_w - S_{wr}}{1 - S_{wr}} \right)^{\frac{2+\lambda}{\lambda}} \right] \tag{5-31}$$

The drainage capillary pressure and relative permeabilities used in this example are inadequate since the sandbox is already saturated and drained with water and a more general hysteretic relationship for ***psk*** is needed to model the drying and wetting paths. The initial water content in the tank calculated based on the hydrostatic water head and the water content at 26 seconds from IPARS are shown in Figure 5.31. The results are very similar to those obtained by PyAHD as shown in Figure 5.32.

5.3.6 Case 6: Simple Sandbox

This test problem appears in (Miller *et al*., 1998). The wetting fluid infiltrates a homogeneous column of length Z initially drained to equilibrium. The infiltration occurs through a ponded surface boundary condition. Miller *et al*. considered three soil types: san, loam, and clay loam. The ***psk*** -relations are determined using the Mualem-van

Genuchten formulas. The parameters for the soil types are given in Table 5.11. It is notable that this problem is exact the same as Problem B in (Tocci *et al*., 1997). One of the objectives in (Miller *et al*., 1998) was to "document a class of variably saturated flow problems that lack robustness when solved using standard solution approaches". For our purposes, these infiltration problems would satisfy the test problem using dry initial conditions and wetting on the surface, unless the dry initial conditions require something other than drainage to equilibrium.

We consider a smaller 3D domain with dimensional 3m x 3m x 3m and use the sand parameters in Table 5.11. We apply constant pressure heads over the square region defined by

$$1 \le x \le 2;$$

$$1 \le y \le 2;$$

$$z = 3.$$

We run the problem over $0 \le t \le 0.3/4$. The 3D domain is modeled with 30 x 30 x 30 elements. Sand has a constant permeability of 5.04 D and porosity of 0.301. Air and water fluid properties are the same as those used in the previous problem. The residue water saturation of 0.3089 is used. Initial water saturation is computed using the inverse of van Genuchten capillary pressure function and assuming hydrostatic equilibrium state for water. Figure 5.33 gives the initial water pressure and saturation shown on half of the domain. Water infiltration occurs over 1 m^2 in the middle of the domain with a constant head of 10 cm water ponding. All the side boundaries are open to air with a constant pressure of 14.7*psi*. The infiltration period is carried out for 0.075 day.

Input tables used in IPARS for capillary pressure and relative permeabilities versus water saturation are generated using the van Genuchten function for capillary pressure and Mualemclosed form for air and water relative permeabilities as follows:

$$S_e = [1 + (\alpha P_c)^n]^{-m} \tag{5-32}$$

$$k_{rw} = \sqrt{S_e}\left[1 - \left(1 - S_e^{1/m}\right)^m\right]^2 \tag{5-33}$$

$$k_{rw} = (1 - S_e)^2\left(1 - S_e^{1/m}\right)^{2m} \tag{5-34}$$

where

$$S_e = \frac{S_w - S_{wr}}{1 - S_{wr}}, \qquad m = 1/n$$

The profiles of water saturation and the pressure head at 0.075 days from the PyAHD run are shown in Figure 5.34. The maps of water saturation and pressure at 0.075 days from IPARS are shown in Fig. 5.35 in half of the domain. The results are very similar to those obtained by PyAHD.

5.4 Summary

Several air/water infiltration problems were setup allowing for different boundary conditions, initial conditions, and heterogeneities for infiltration. Two multiphase codes, IPARS and UTCHEM were successfully compared. In addition, comparisons with the Richards Equation Model in PyAHD were also made.

A major difficulty in making comparisons of two-phase models and RE arises in nomenclature. In multiphase models, pressure and saturations are generally chosen as primary variable whereas in RE, head and water content are chosen. To add to the

confusion, both water content and saturation while different are both frequently referred to as water fraction. A second difficulty involves applying lookup tables for capillary pressure and relative permeabilities generally used in multiphase flow models whereas specific functional forms such as Brooks-Corey and/or van Genuchten are used by hydrologists. Employing lookup tables can greatly reduce computational time in several large problems.

Two-phase model holds for general porous media and is not limited by several assumptions that must be made for the RE formulations. In particular, RE is applicable only for shallow regions (vadose) that are only several meters in depth and a fully saturated bottom boundary condition must be assumed. In addition, for RE, capillary pressure and relative permeability must have a specific functional form; general standard imbibition equations cannot be dealt with and drainage formulations are assumed even in the case of infiltration. Another disadvantage in using RE instead of a fully two phase model is that the transport of gas cannot be handled when flow is coupled to a transport model.

Table 5.1 Input Data for Case 1

Parameters	Values	Parameters	Values
Ω [*ft*]	68.06x24.66x8.05	$P_{w,i}$ [*psi*]	14.7
grids	50x11x5	$S_{w,i}$	0.2
ϕ	0.4	c_w [psi^{-1}]	6.8e-5
K [*D*]	18	c_a [psi^{-1}]	0.002 (UTCHEM only)
S_{wirr}	0.2	ρ_w [*psi/ft*]	0.433
S_{ar}	0.0	ρ_a [*psi/ft*]	0.002
k_{rw}^0	0.6	μ_w [*cp*]	1.0
k_{aw}^0	1.0	μ_a [*cp*]	0.015
n_w	1.5	M_a [*lb/lbmol*]	28.97 (IPARS only)
n_a	2.5	Z_a	1 (IPARS only)
C_{pc}	2.0	T [°*F*]	60 (IPARS only)
E_{pc}	1.5	R [$\frac{ft^3 psi}{^\circ R \cdot lbmol}$]	10.732
Δx [*ft*]	3.36, 3.06, 2.78, 2.53, 2.30, 2.09, 1.90, 1.73, 1.57, 1.43, 1.30, 1.18, 1.07, 0.97, 0.89, 0.81, 0.73, 0.67, 0.61, 0.55, 0.50, 0.50, 0.50, 0.50, 0.50, 0.50, 0.50, 0.50, 0.50, 0.50, 0.55, 0.61, 0.67, 0.73, 0.81, 0.89, 0.97, 1.07, 1.18, 1.30, 1.43, 1.57, 1.73, 1.90, 2.09, 2.30, 2.53, 2.78, 3.06, 3.36		
Δy [*ft*]	3.6, 2.78, 2.3, 1.9, 1.5, 0.5, 1.5, 1.9, 2.3, 2.78, 3.6		
Δz [*ft*]	1.0, 1.5, 1.75, 1.8, 2.0 (from top to bottom layer)		

Table 5.2 Well Data for Case 1

No.	Type	Well Position	Radius [ft]	Constraint
1	Injection	I=25, J=6 or x=33.78 *ft*, y=12.33 *ft*	0.05	$q_w = 3\,ft^3/day$
2	Injection	I=26, J=6 or x=34.28 *ft*, y=12.33 *ft*	0.05	$q_w = 3\,ft^3/day$
3	Boundary	I=1, J=2 or x=1.68 *ft*, y=4.99 *ft*	0.1	$P_{wf} = 14.7\ psi$
4	Boundary	I=1, J=5 or x=1.68 *ft*, y=11.33 *ft*	0.1	$P_{wf} = 14.7\ psi$
5	Boundary	I=1, J=8 or x=1.68 *ft*, y=15.03 *ft*	0.1	$P_{wf} = 14.7\ psi$
6	Boundary	I=1, J=10 or x=1.68 *ft*, y=19.67 *ft*	0.1	$P_{wf} = 14.7\ psi$
7	Boundary	I=50, J=2 or x=66.38 *ft*, y=4.99 *ft*	0.1	$P_{wf} = 14.7\ psi$
8	Boundary	I=50, J=5 or x=66.38 *ft*, y=11.33 *ft*	0.1	$P_{wf} = 14.7\ psi$
9	Boundary	I=50, J=8 or x=66.38 *ft*, y=15.03 *ft*	0.1	$P_{wf} = 14.7\ psi$
10	Boundary	I=50, J=10 or x=66.38 *ft*, y=19.67 *ft*	0.1	$P_{wf} = 14.7\ psi$

Table 5.3 Input Data for Case 2

Parameters	Values
Ω [*ft*]	136.06x24.66x9.05
k_x [*D*]	9, 6, 1, 4, 1 (from top layer to bottom layer)
k_y [*D*]	9, 6, 1, 4, 1 (from top layer to bottom layer)
k_z [*D*]	2.7, 1.8, 0.3, 1.2, 0.3 (from top layer to bottom layer)
C_{pc}	0
Δx [*ft*]	30.36, 10.06, 2.78, 2.53, 2.30, 2.09, 1.90, 1.73, 1.57, 1.43, 1.30, 1.18, 1.07, 0.97, 0.89, 0.81, 0.73, 0.67, 0.61, 0.55, 0.50, 0.50, 0.50, 0.50, 0.50, 0.50, 0.50, 0.50, 0.50, 0.50, 0.55, 0.61, 0.67, 0.73, 0.81, 0.89, 0.97, 1.07, 1.18, 1.30, 1.43, 1.57, 1.73, 1.90, 2.09, 2.30, 2.53, 2.78, 10.06, 30.36
Δy [*ft*]	3.6, 2.78, 2.3, 1.9, 1.5, 0.5, 1.5, 1.9, 2.3, 2.78, 3.6
Δz [*ft*]	1.0, 1.5, 1.75, 1.8, 3.0 (from top layer to bottom layer)

Table 5.4 Well Data for Case 2

No.	Type	Well Position	Radius [ft]	Constraint
1	Injection	I=24, J=6 or x=67.28ft, y=12.33ft	0.05	$q_w = 3\,ft^3/day$
2	Injection	I=25, J=6 or x=67.28ft, y=12.33ft	0.05	$q_w = 3\,ft^3/day$
3	Injection	I=26, J=6 or x=68.28ft, y=12.33ft	0.05	$q_w = 3\,ft^3/day$
4	Injection	I=27, J=6 or x=68.28ft, y=12.33ft	0.05	$q_w = 3\,ft^3/day$
3	Boundary	I=1, J=2 or x=15.18ft, y=4.99ft	0.1	$P_{wf} = 14.7\,psi$
4	Boundary	I=1, J=5 or x=15.18ft, y=11.33ft	0.1	$P_{wf} = 14.7\,psi$
5	Boundary	I=1, J=8 or x=15.18ft, y=15.03ft	0.1	$P_{wf} = 14.7\,psi$
6	Boundary	I=1, J=10 or x=15.18ft, y=19.67ft	0.1	$P_{wf} = 14.7\,psi$
7	Boundary	I=50, J=2 or x=120.88ft, y=4.99ft	0.1	$P_{wf} = 14.7\,psi$
8	Boundary	I=50, J=5 or x=120.88ft, y=11.33ft	0.1	$P_{wf} = 14.7\,psi$
9	Boundary	I=50, J=8 or x=120.88ft, y=15.03ft	0.1	$P_{wf} = 14.7\,psi$
10	Boundary	I=50, J=10 or x=120.88ft, y=19.67ft	0.1	$P_{wf} = 14.7\,psi$

Table 5.5 Capillary Pressure Input Data for Case 3

Parameters	Values
C_{pc}	2, 2.45, 6, 3, 6 (from top to bottom layer)
E_{pc}	1.5

Table 5.6 Input Data for Case 3

Parameters	Values(from top to bottom layer)
$S_{\omega irr}$	0.22, 0.25, 0.30, 0.28, 0.30
S_{ar}	0.02, 0.05, 0.10, 0.08, 0.10
$k_{r\omega}^{\ 0}$	0.5, 0.45, 0.35, 0.40, 0.35
$k_{a\omega}^{\ 0}$	0.9, 0.85, 0.75, 0.8, 0.75

n_ω	1.5, 1.5, 2.0, 1.8, 2.0
n_a	2.5, 2.5, 3.0, 2.8, 3.0
$S_{\omega i}$	0.22, 0.25, 0.30, 0.28, 0.30

Table 5.7: Computer Systems Configuration

Component	PC	TACC Lonestar Cluster
OS	GNU/LINUX	GNU/LINUX
CPU Model	Dual-Core AMD Opteron (tm) Processor 1210	Dual-Core Xeon 5100 Processors
Core Frequency (GHz)	1.0	2.66
Memory	4 GB	2 GB per core

Table 5.8 CPU Time Consumed

CPU time	IPARS (PC)	IPARS (Lonestar, 8 cores)	UTCHEM (PC)
Case 1	116.032 sec	42.442 sec	144.14 sec
Case 2	128.624 sec	49.502 sec	341.73 sec
Case 3	194.288 sec	65.368 sec	404.03 sec
Case 4	189.756 sec	61.55 sec	699.85 sec

Table 5.9 Kueper Experiment Sand Properties (Brooks-Corey ***psk*** relations)

	P_d [Pa]	λ [-]	S_{wr} [-]	K [m^2]	ϕ
Sand 1	369.73	3.86	0.078	5.041×10^{-10}	0.40
Sand 2	434.45	3.51	0.069	2.051×10^{-10}	0.39
Sand 3	1323.95	2.49	0.098	5.621×10^{-11}	0.39
Sand 4	3246.15	3.30	0.189	8.191×10^{-12}	0.41

Table 5.10 Sample DNAPL properties taken from Domenico and Schwartz (1998)

	γ_g	C_s [mg/L]	K_{ow}	P_v [mm Hg]	ν [cp]
PCE (tetrachloroethylene)	1.631	150	390	14	0.90
TCE (trichloroethylene)	1.466	1100	240	60	0.57

γ_g – specific gravity

C_s – DNAPL solubility in water

K_{ow} – octanol/water partion coefficient

P_v – vapor pressure, at 20° 1 atm = 760 mmHg

v – absolute viscosity, at 25°

Table 5.11 Parameters for Miller *et al.* (1998)

Parameter	Values
θ_r	0.093
θ_s	0.301
α_v [m^{-1}]	5.470
n_v	4.264
K_s [m/day]	5.040
S_s [m^{-1}]	1.0x10-**6**
z [m]	[0, 10.0]
t [days]	[0, 0.18]
$\psi(z,t=0)=\psi_0$ [m]	-z
$\psi(z=0,t>0)=\psi_1$ [m]	0.00
$\psi(z=Z,t>0)=\psi_2$ [m]	0.10
Δz [m]	0.0125
n_n	801

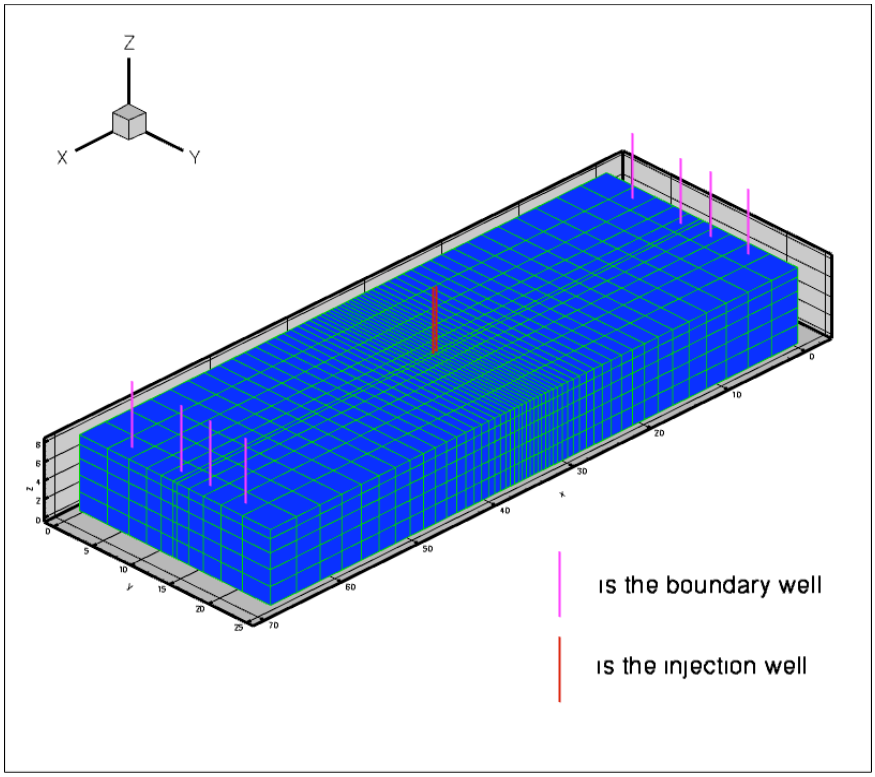

Figure 5.1 Reservoir Geometry and Well Locations for Case 1

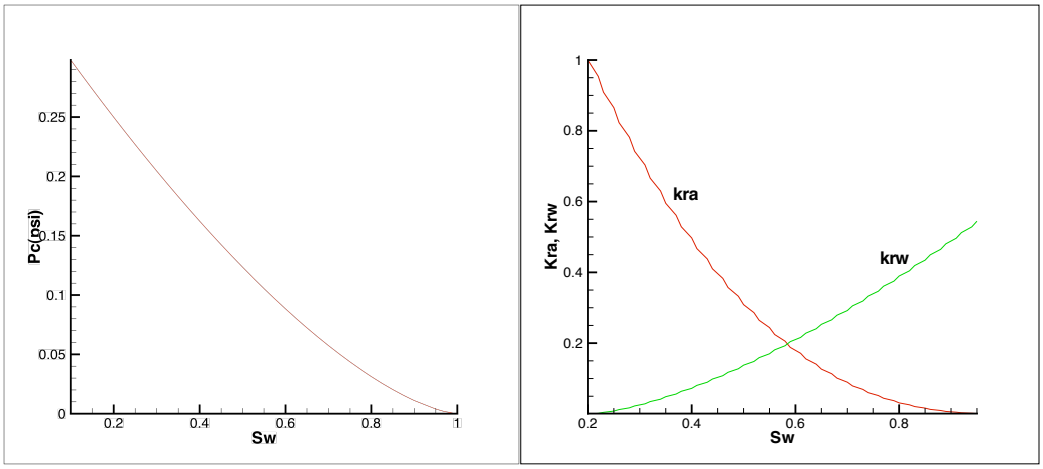

(a) Capillary Pressure Curve (b) Relative Permeability curves

Figure 5.2 Capillary Pressure and Relative Permeability Curves for Case 1

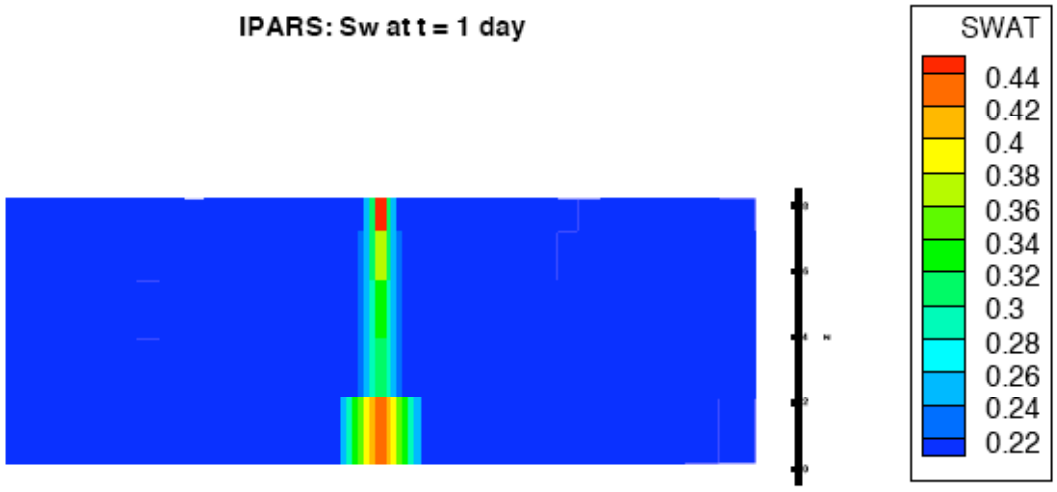

(a) IPARS

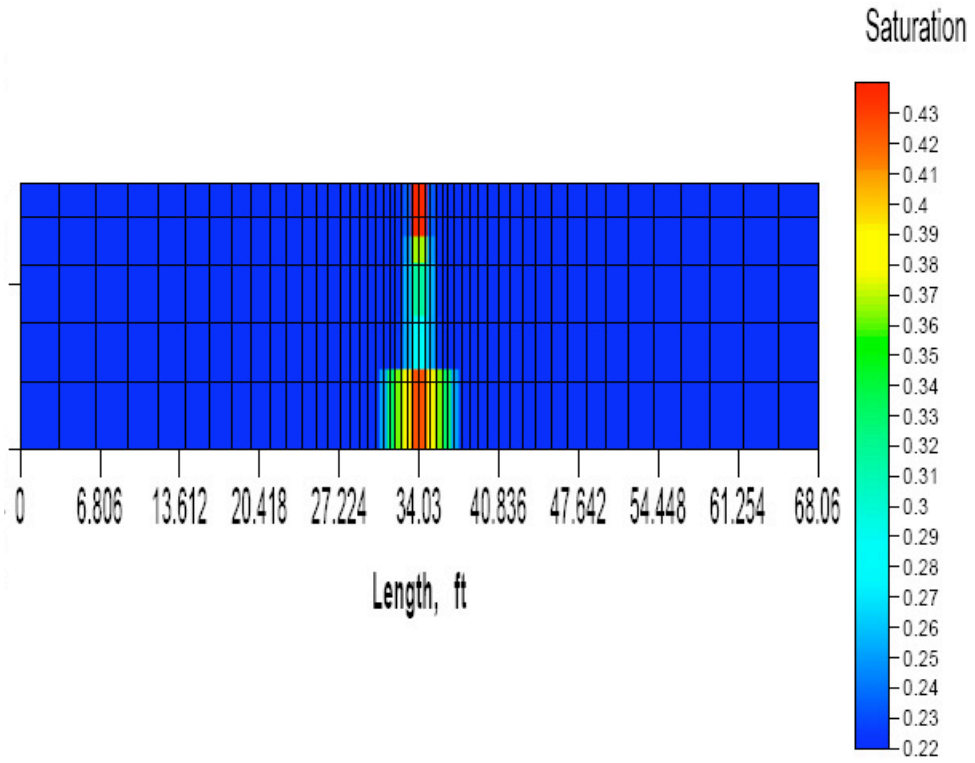

(b) UTCHEM

Figure 5.3 Water Saturation Profiles for Case 1 at 1 Day

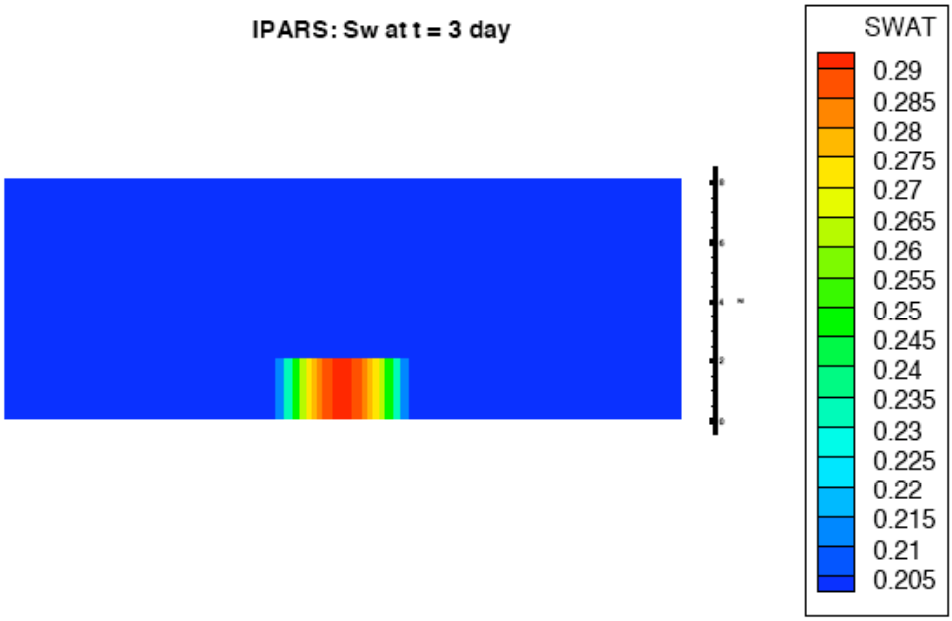

(a) IPARS

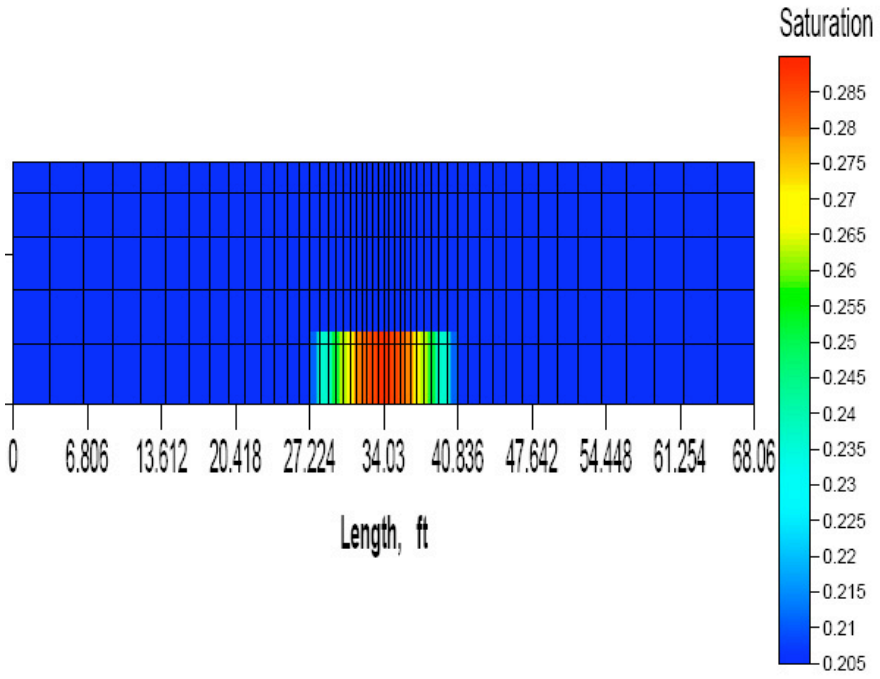

(b) UTCHEM

Figure 5.4 Water Saturation Profiles for Case 1 at 3 Days

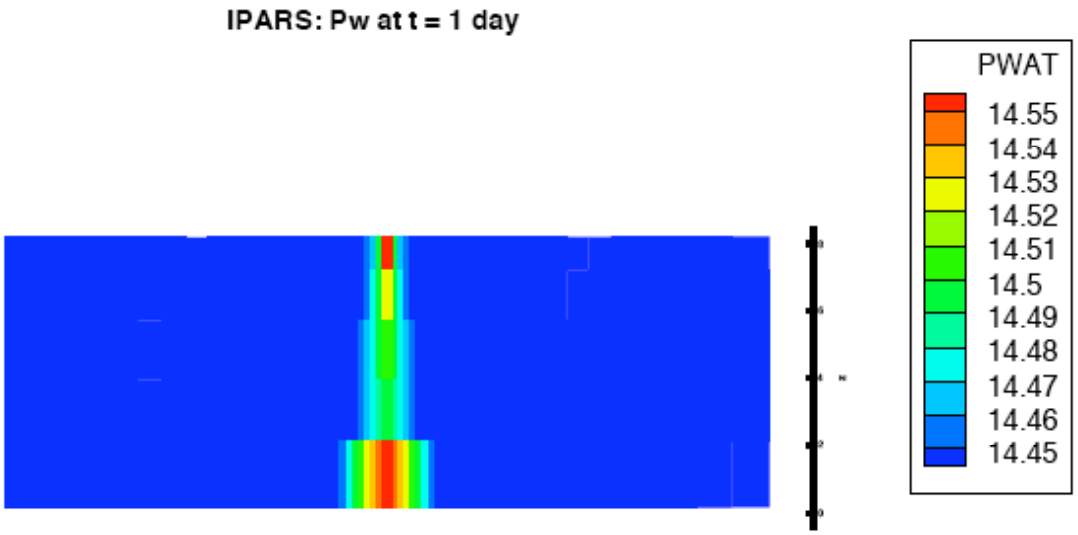

(a) IPARS

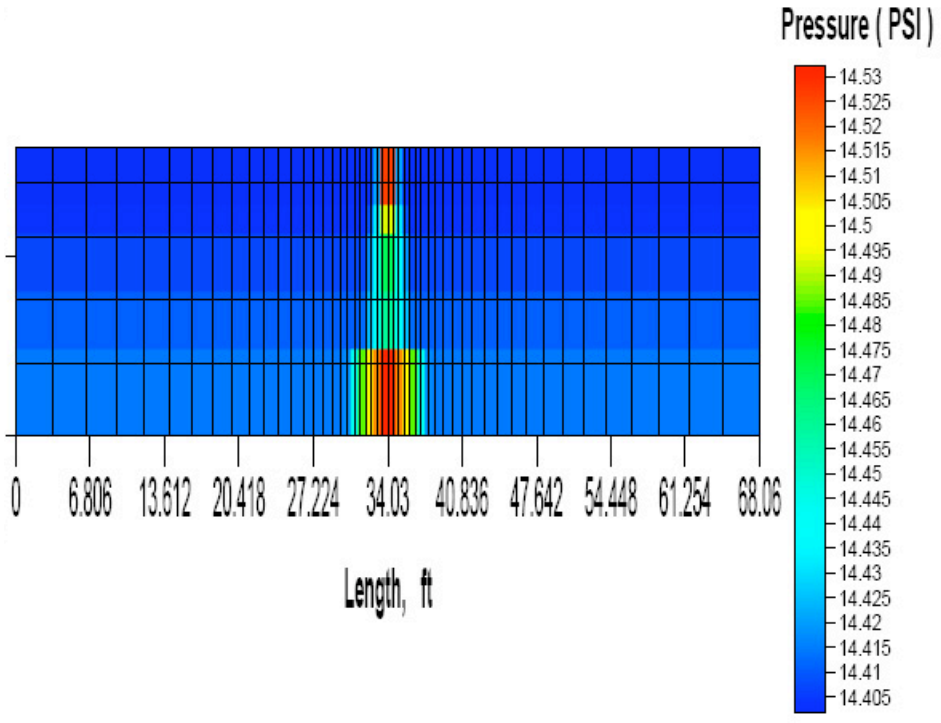

(b) UTCHEM

Figure 5.5 Water Pressure Profiles for Case 1 at 1 Day

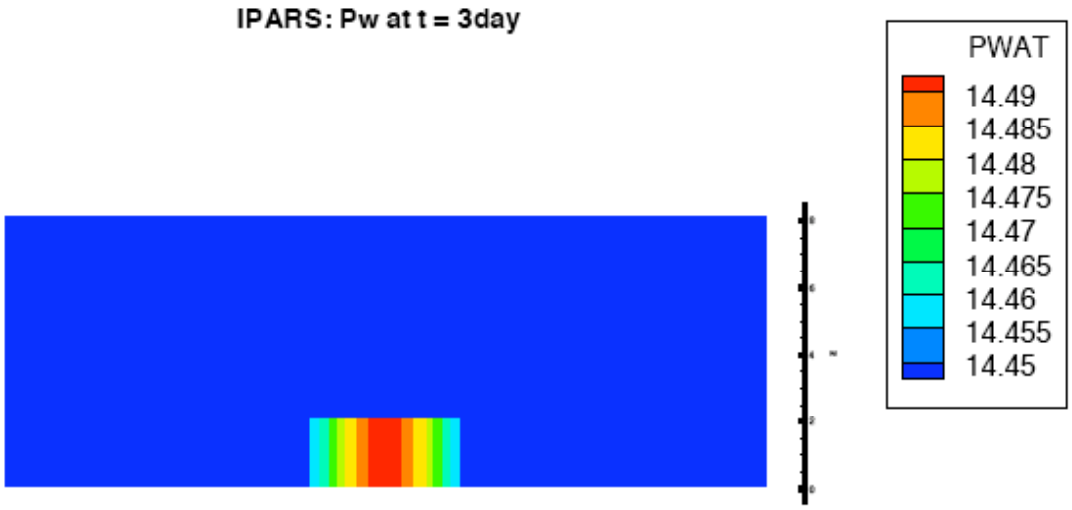

(a) IPARS

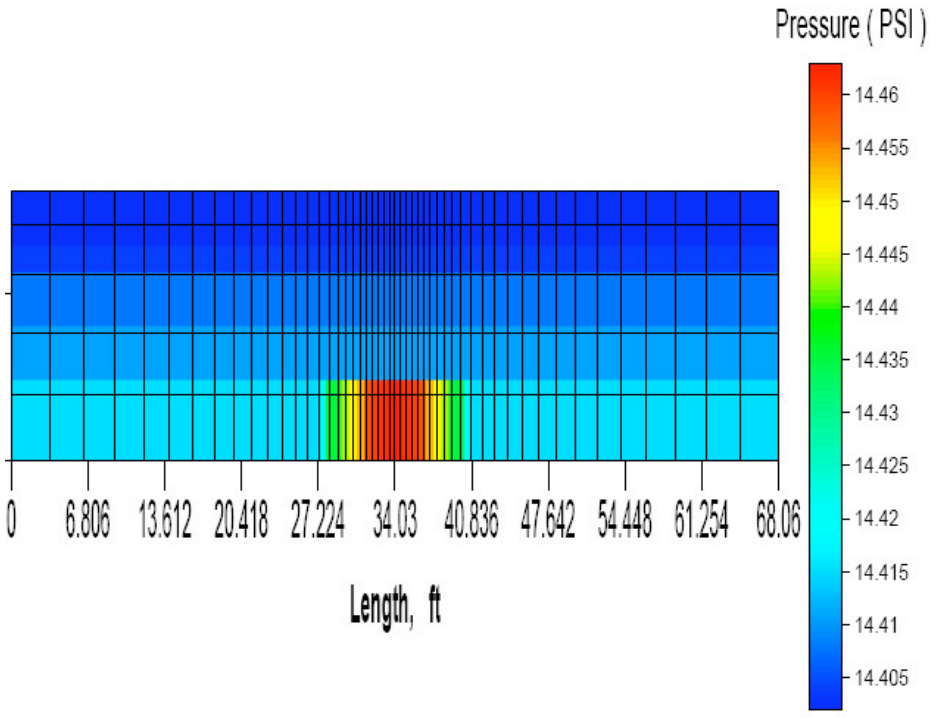

(b) UTCHEM

Figure 5.6 Water Pressure Profiles for Case 1 at 3 Days

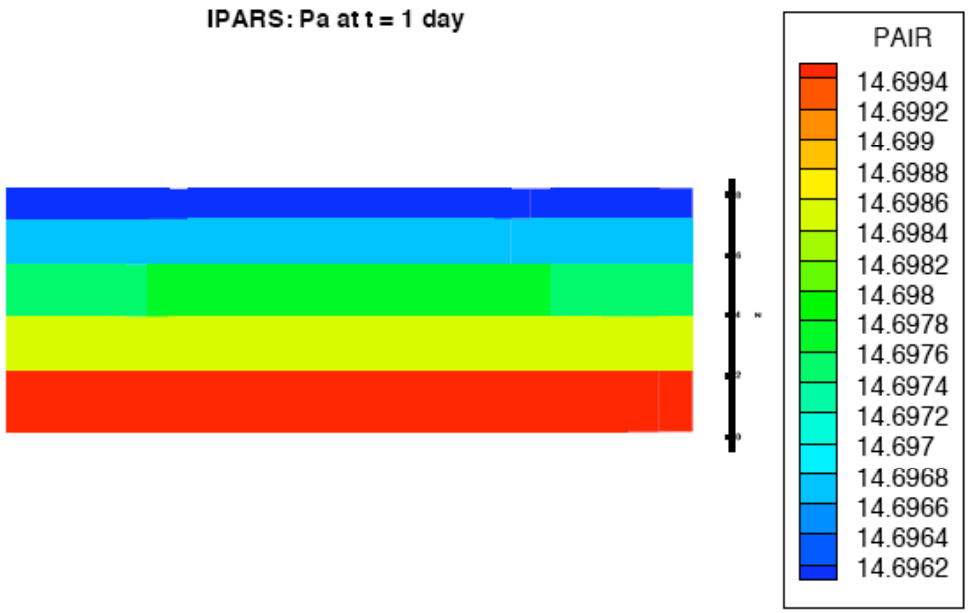

(a) IPARS

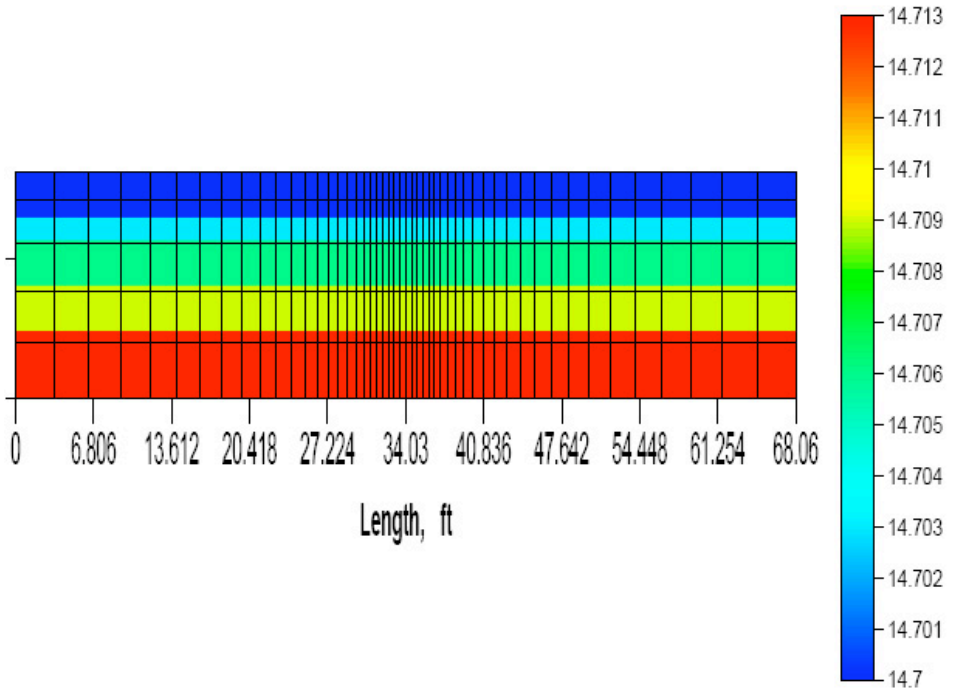

(b) UTCHEM

Figure 5.7 Air Pressure Profiles for Case 1 at 1 Day

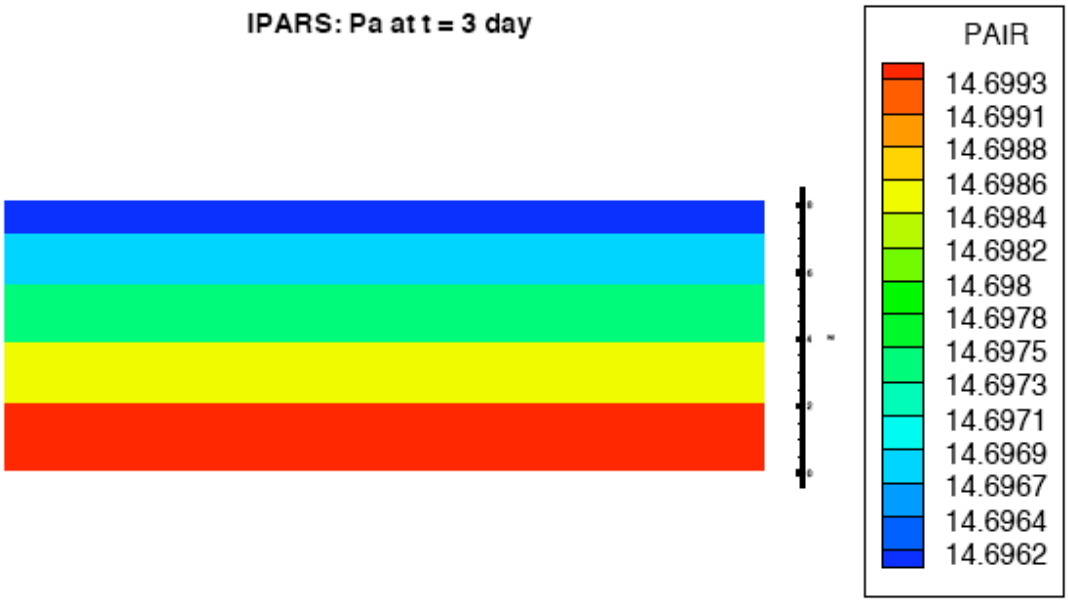

(a) IPARS

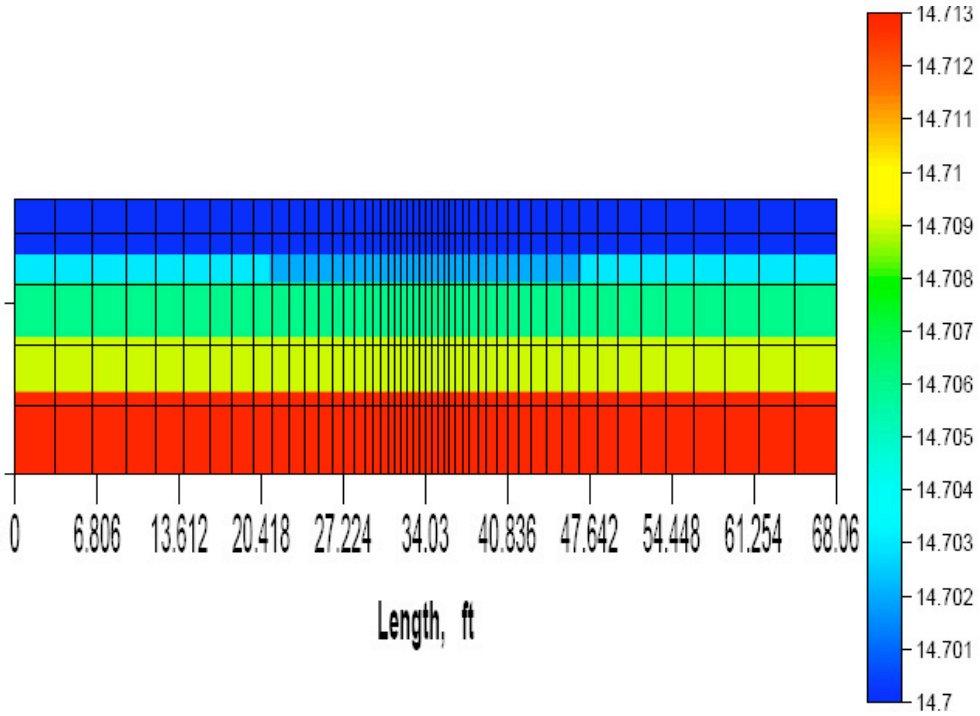

(b) UTCHEM

Figure 5.8 Air Pressure Profiles for Case 1 at 3 Days

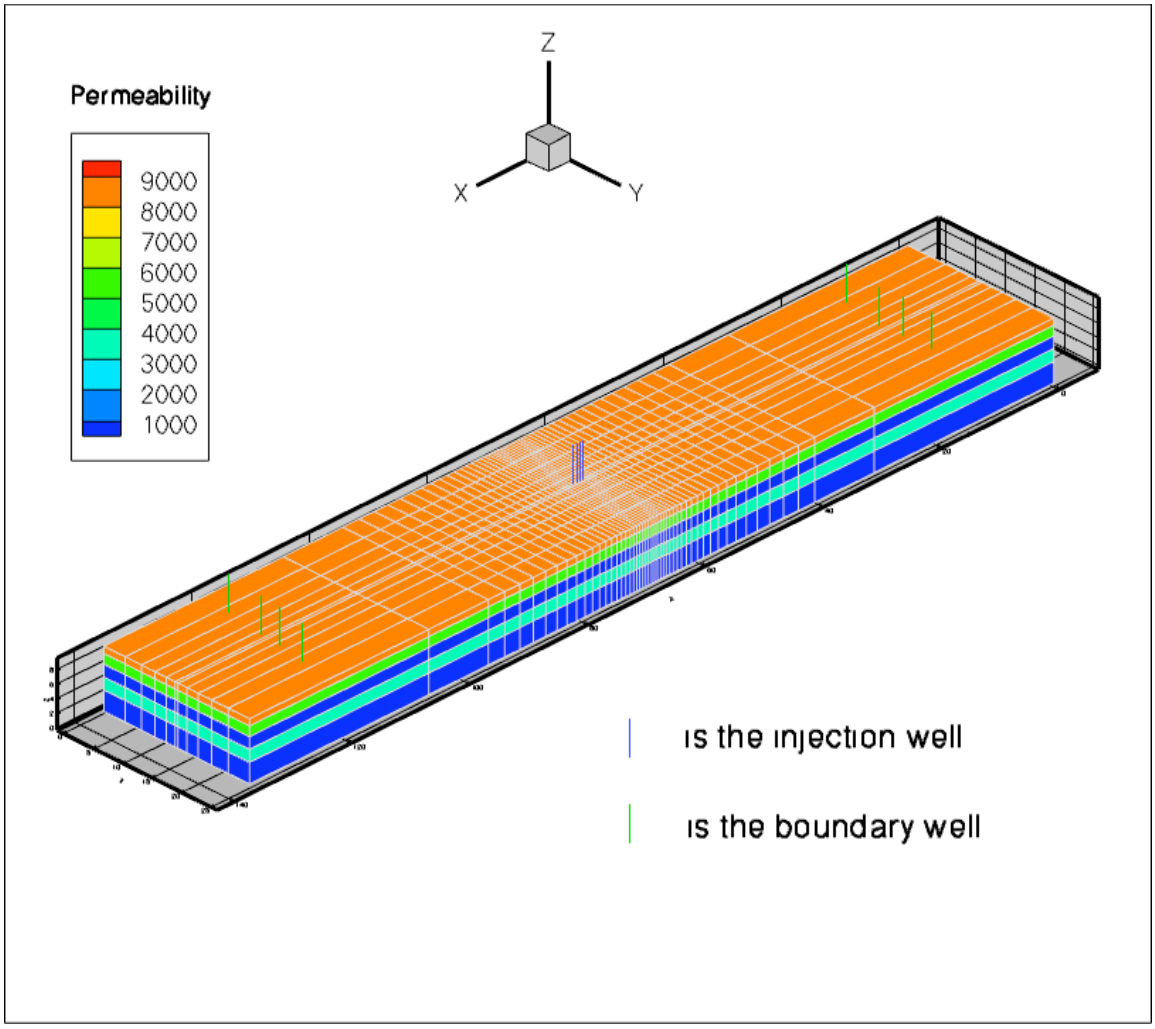

Figure 5.9 Permeability Distribution and Well Locations for Case 2

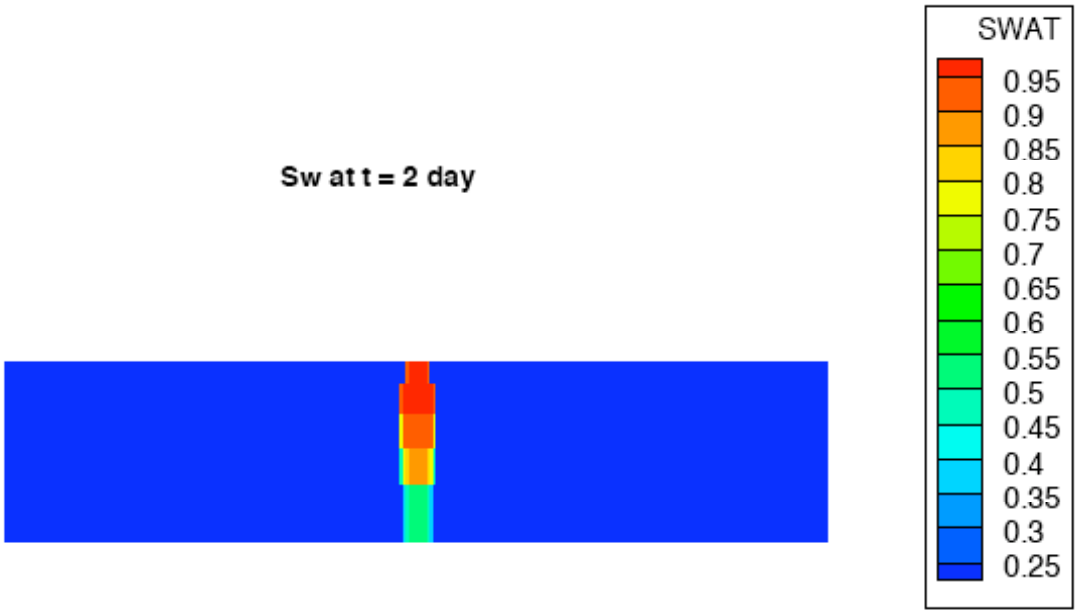

(a) IPARS

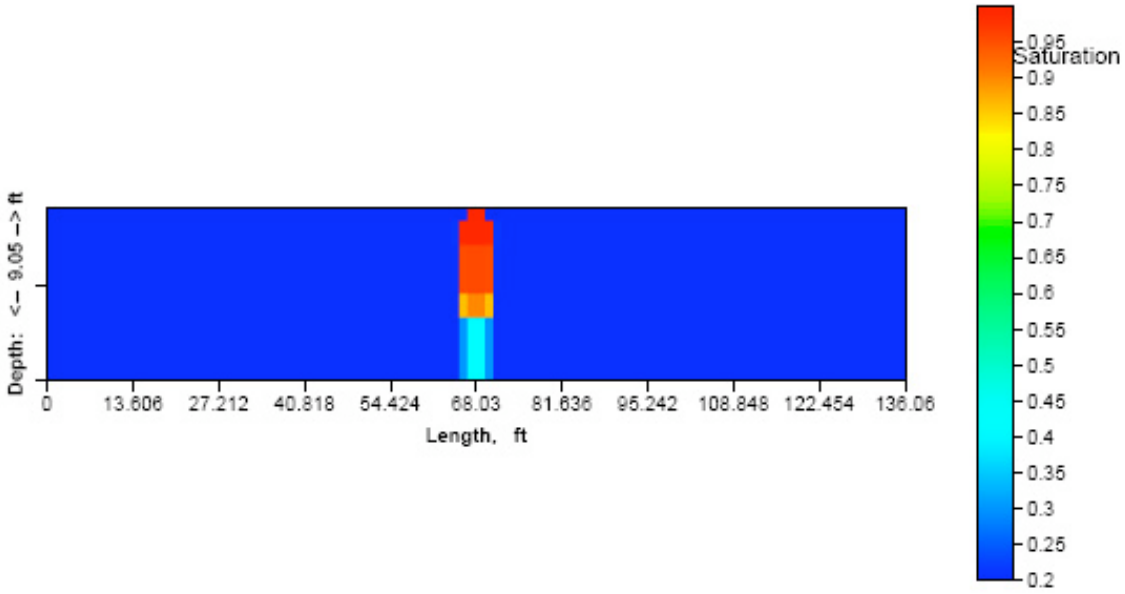

(b) UTCHEM

Figure 5.10 Water Saturation Profiles for Case 2 at 2 Days

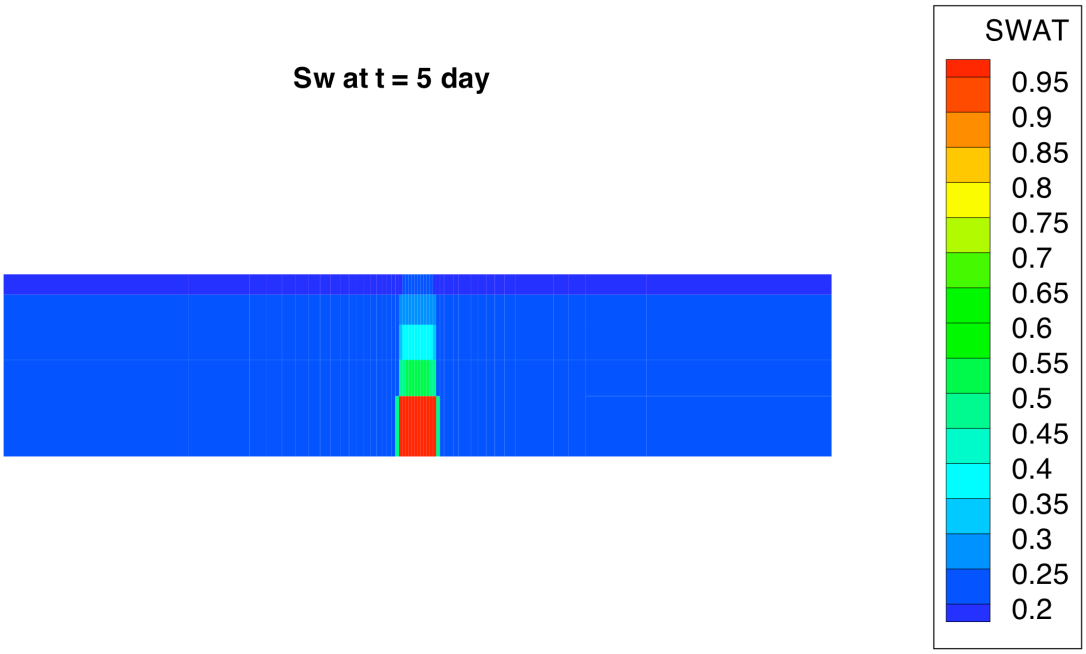

(a) IPARS

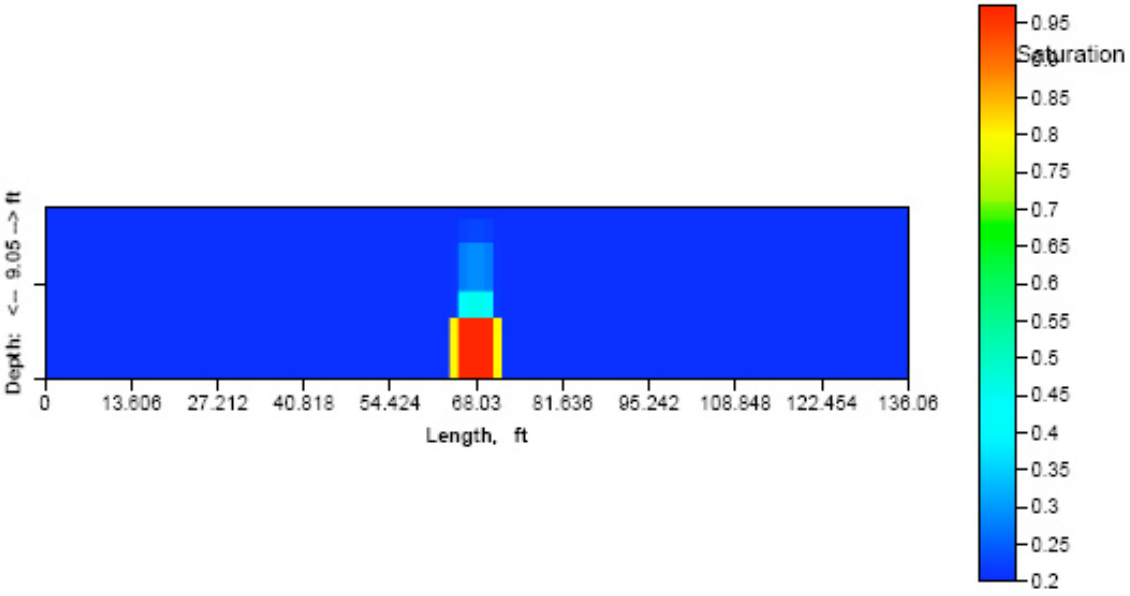

(b) UTCHEM

Figure 5.11 Water Saturation Profiles for Case 2 at 5 Days

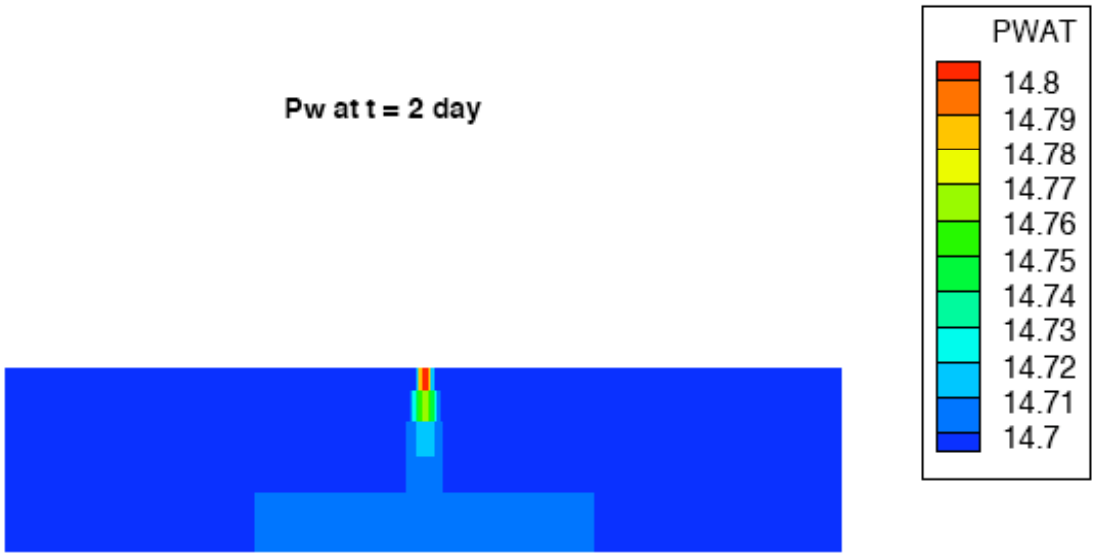

(a) IPARS

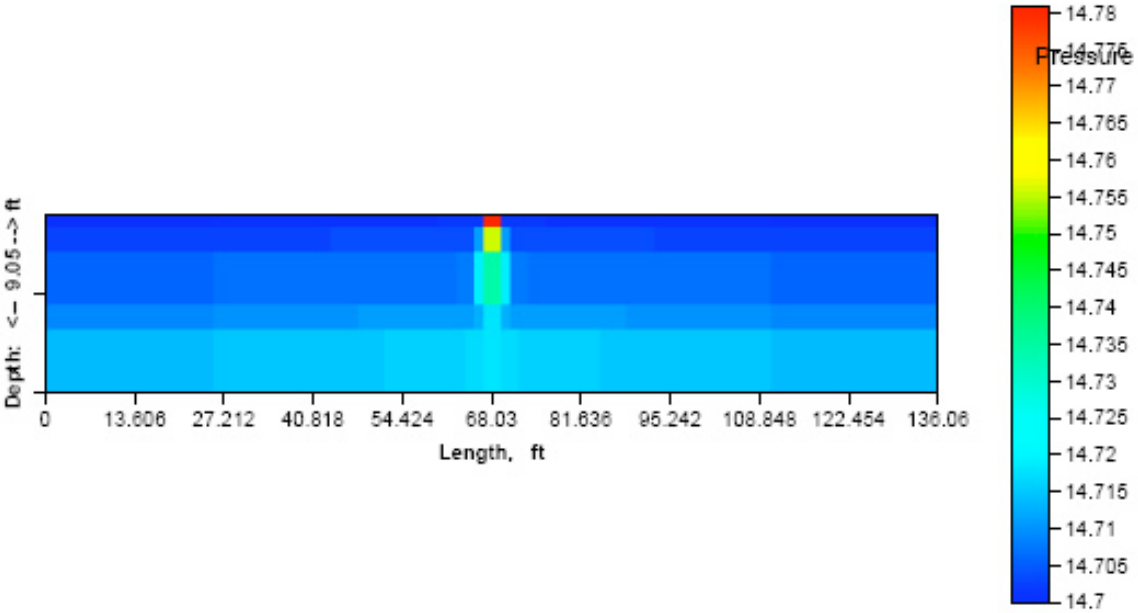

(b) UTCHEM

Figure 5.12 Water Pressure Profiles for Case 2 at 2 Days

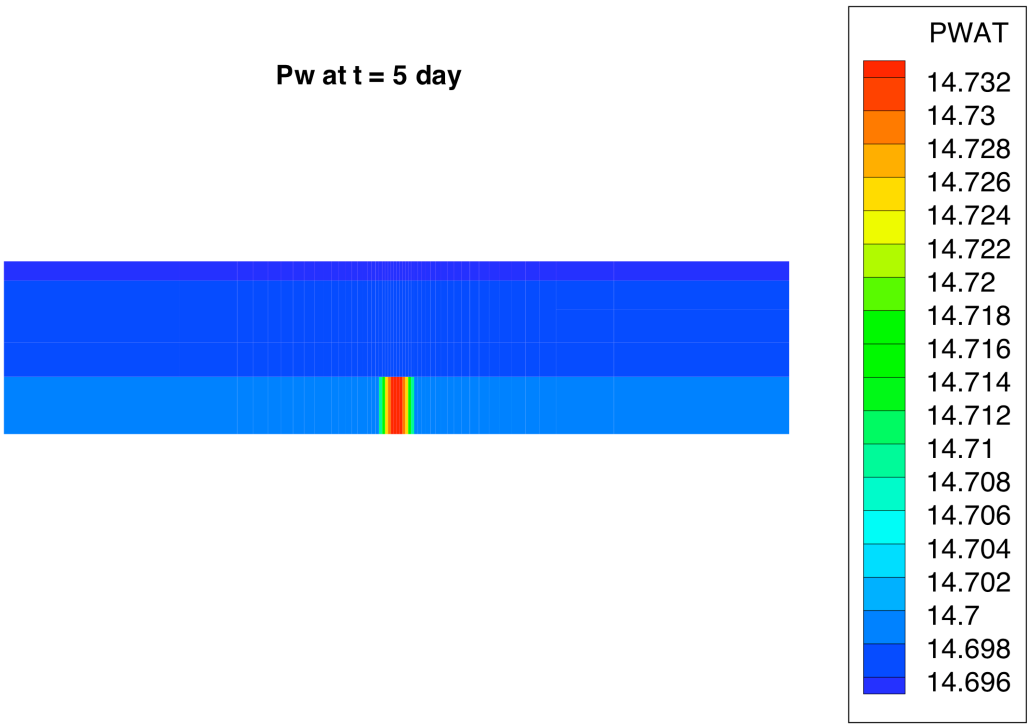

(a) IPARS

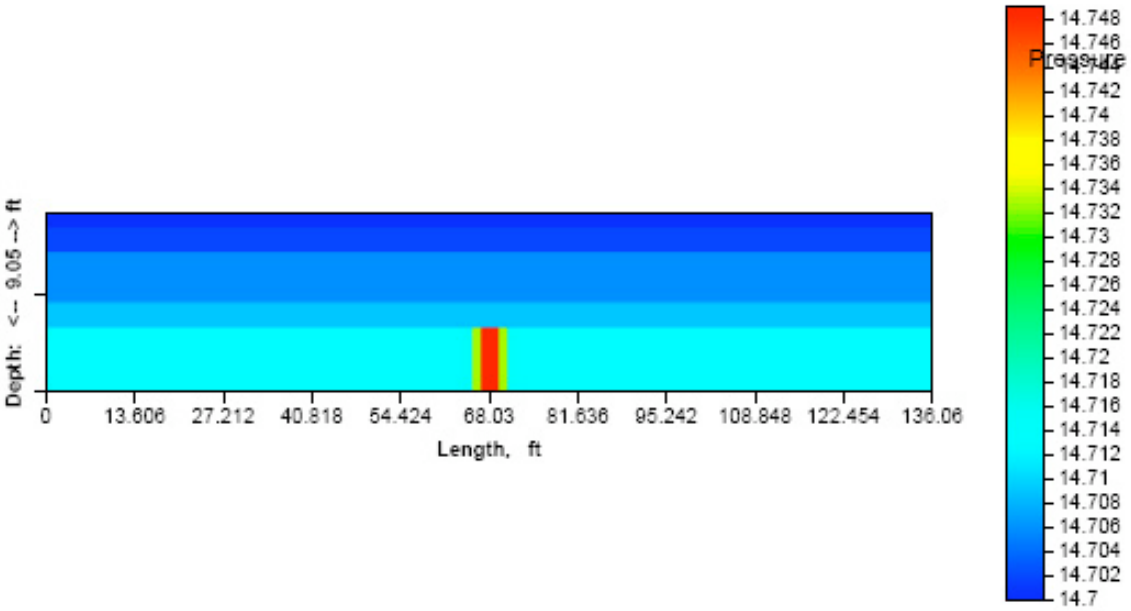

(b) UTCHEM

Figure 5.13 Water Pressure Profiles for Case 2 at 5 Days

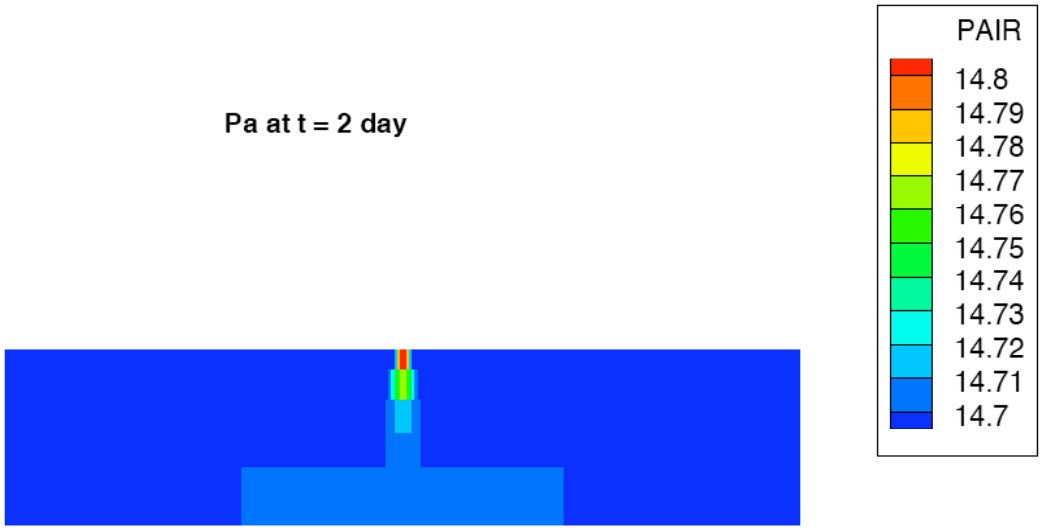

(a) IPARS

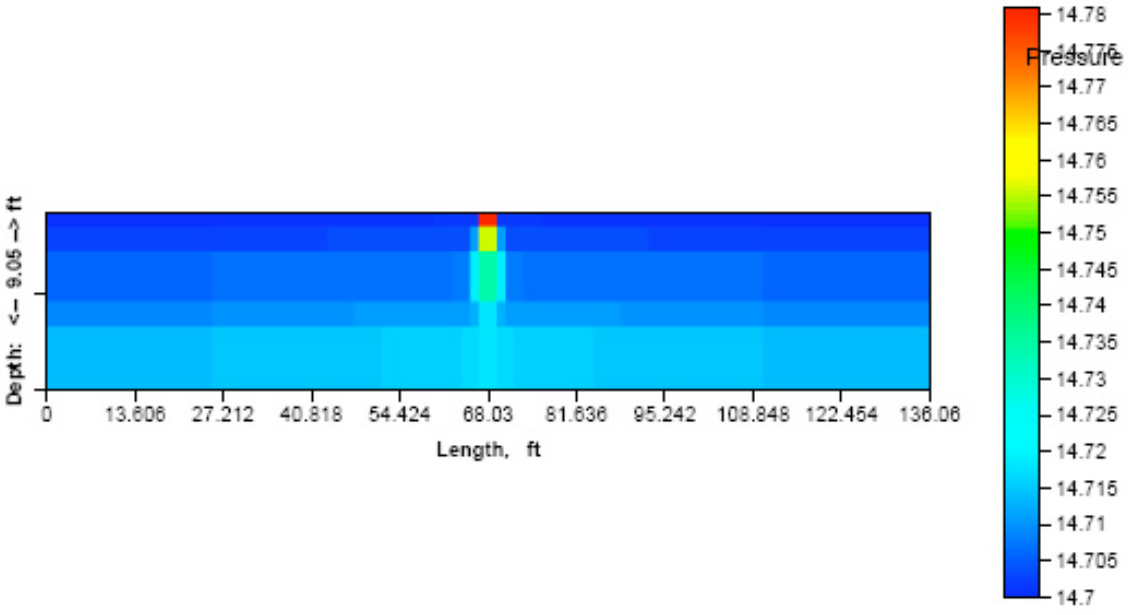

(b) UTCHEM

Figure 5.14 Air Pressure Profiles for Case 2 at 2 Days

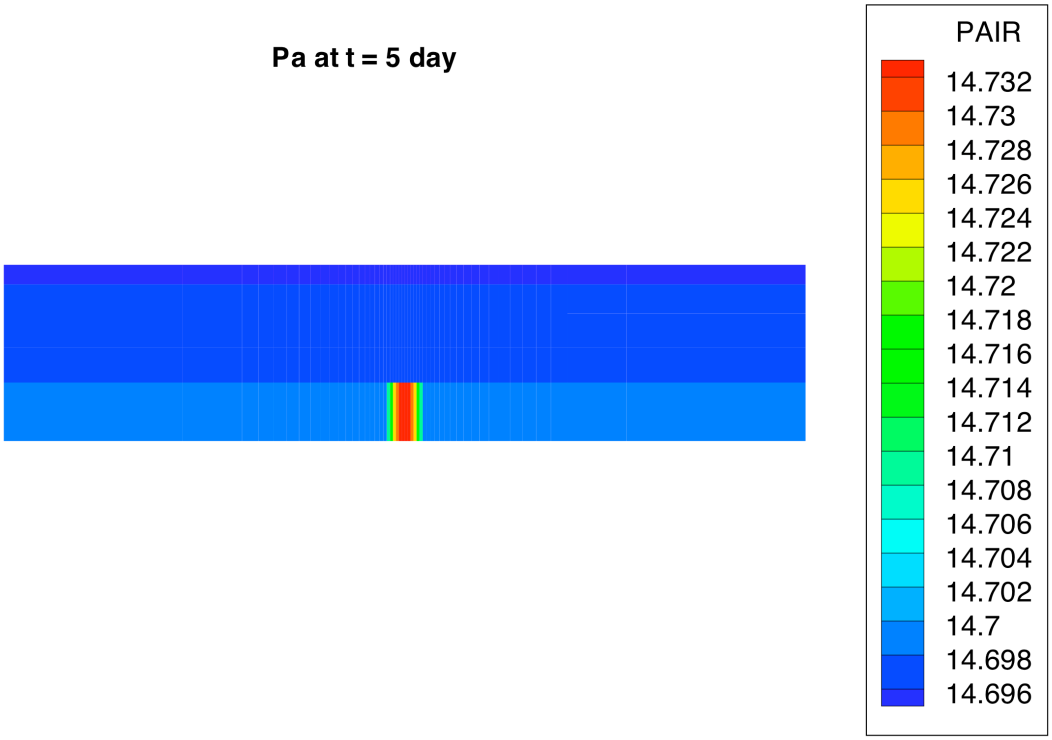

(a) IPARS

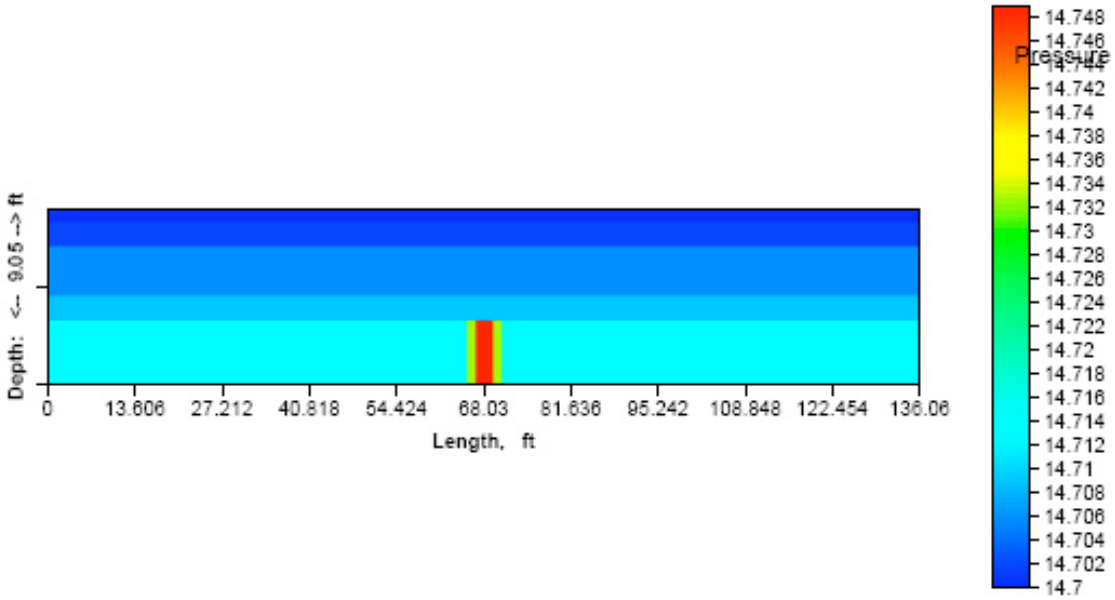

(b) UTCHEM

Figure 5.15 Air Pressure Profiles for Case 2 at 5 Days

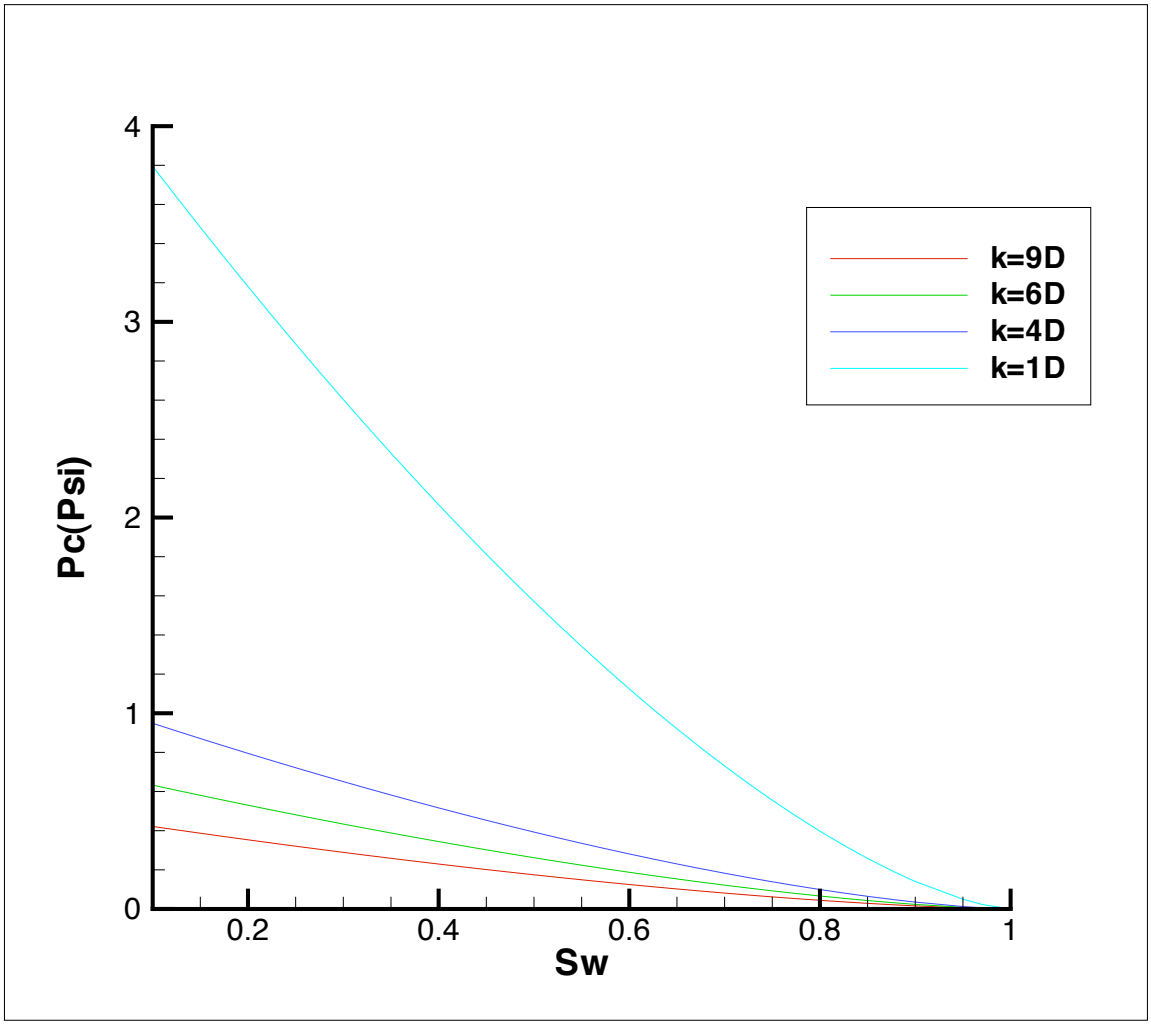

Figure 5.16 Capillary Pressure Curves for Cases 3 and 4

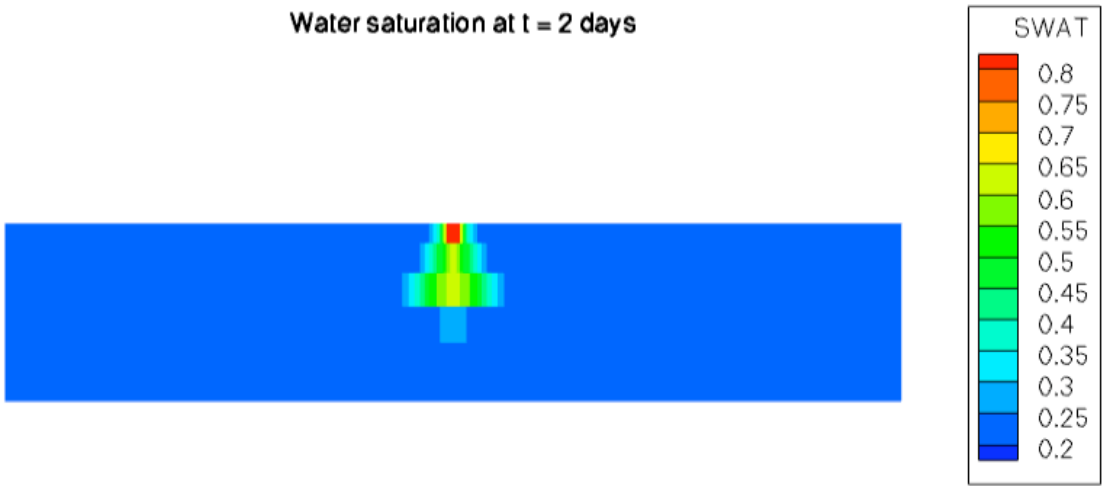

(a) IPARS

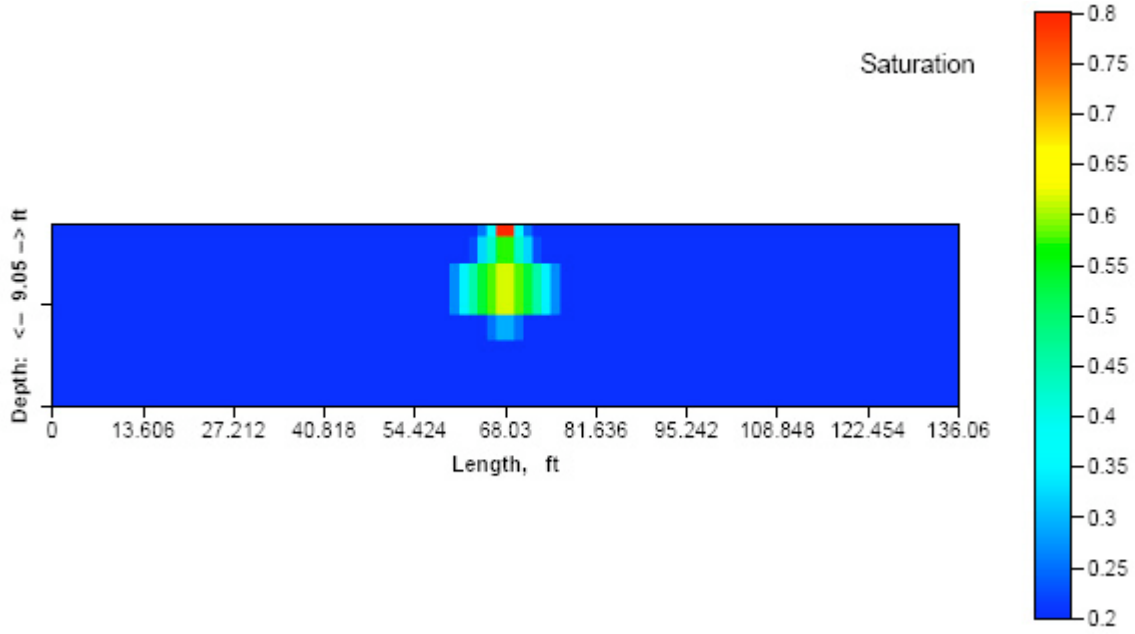

(b) IPARS

Figure 5.17 Water Saturation Profiles for Case 3 at 2 Days

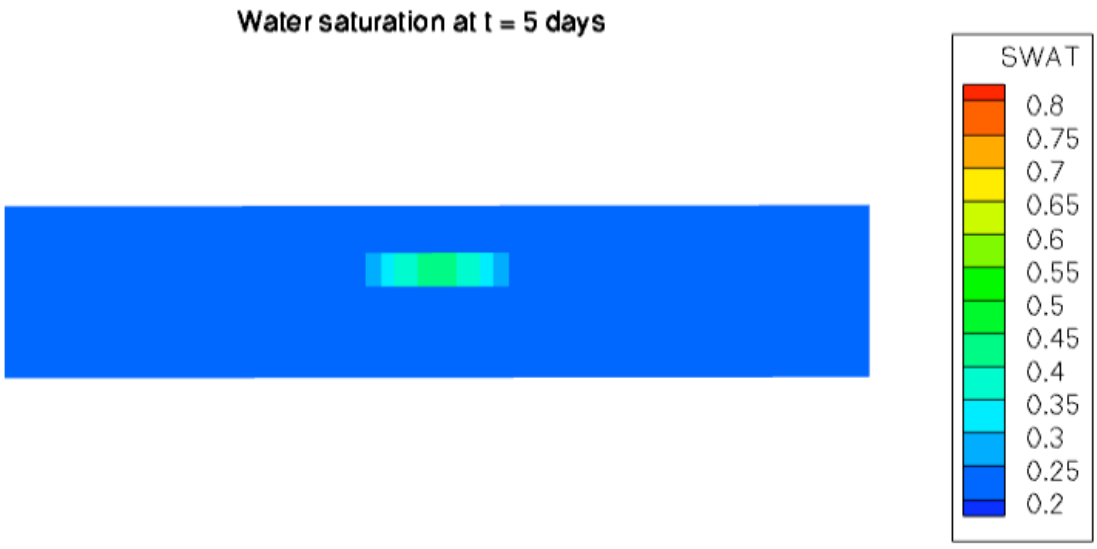

(a) IPARS

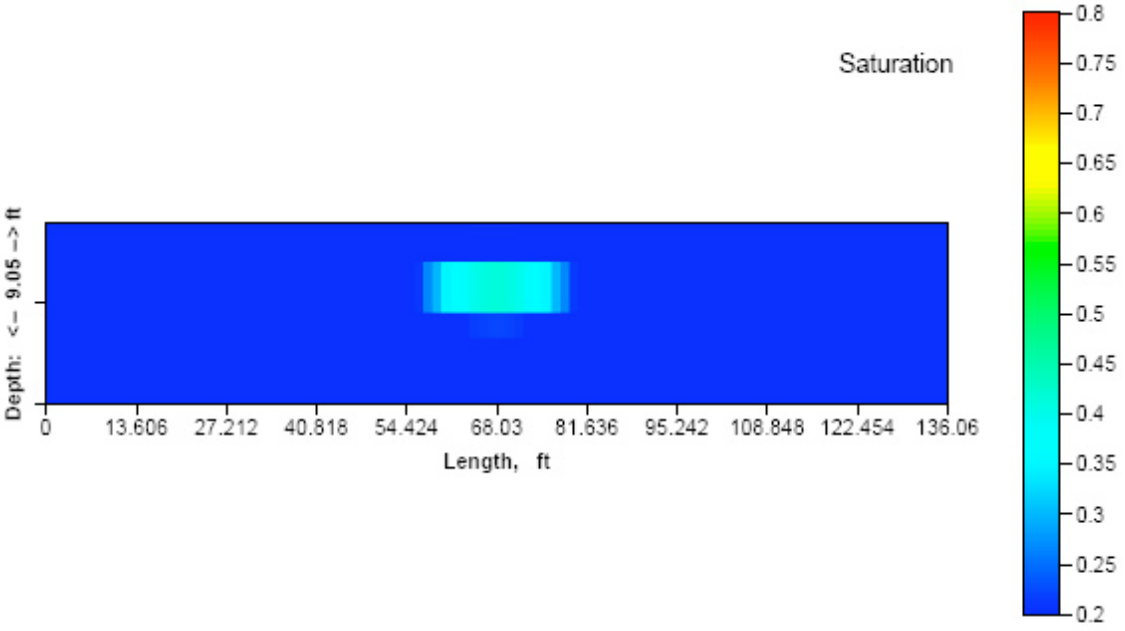

(b) UTCHEM

Figure 5.18 Water Saturation Profiles for Case 3 at 5 Days

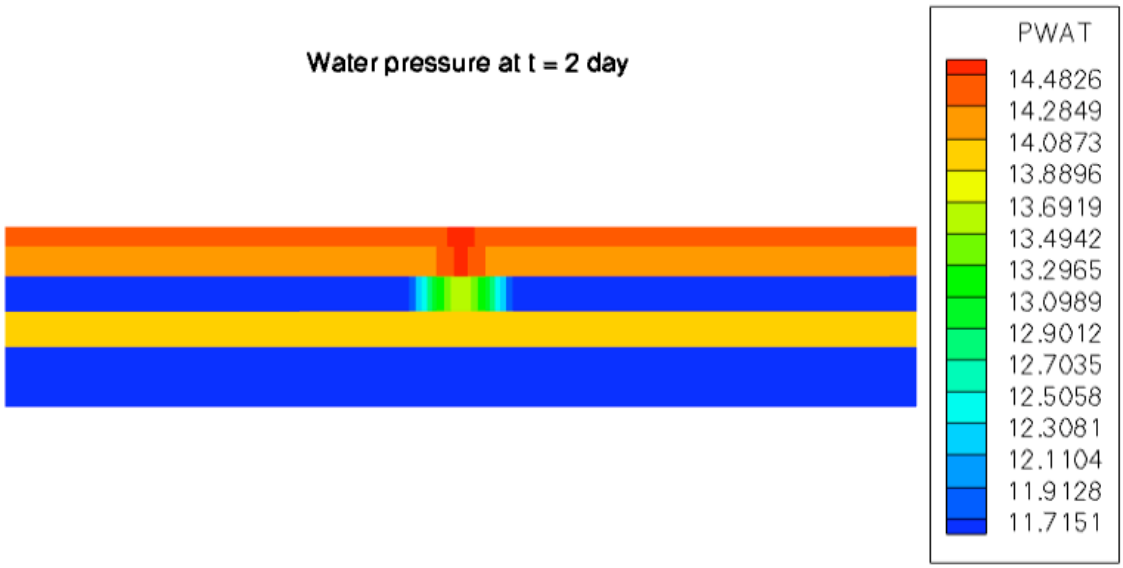

(a) IPARS

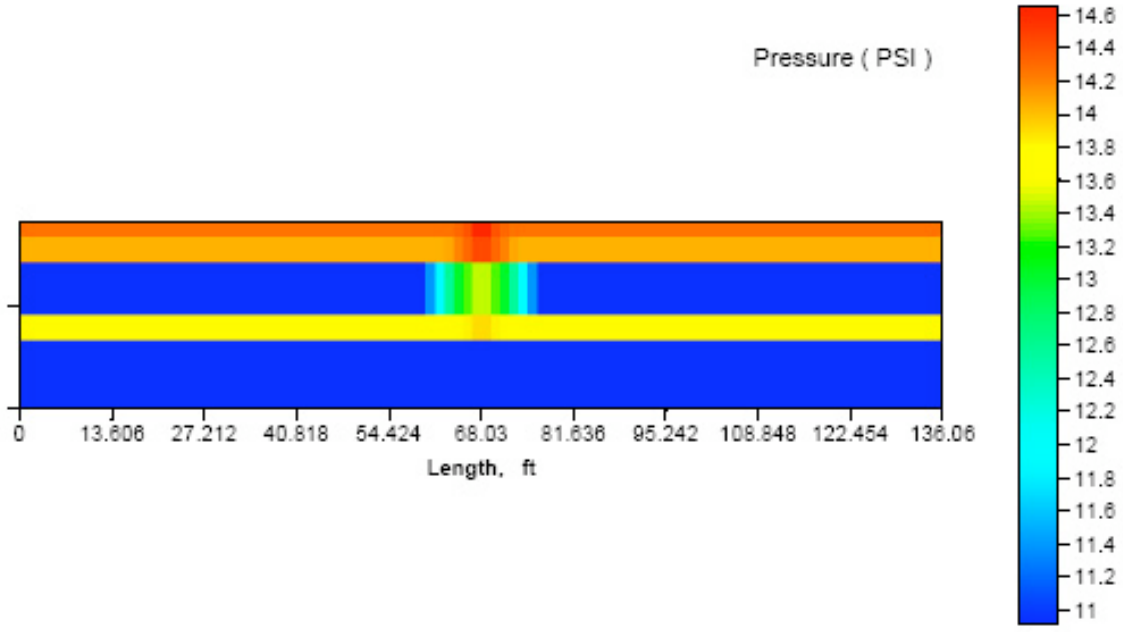

(b) UTCHEM

Figure 5.19 Water Pressure Profiles for Case 3 at 2 Days

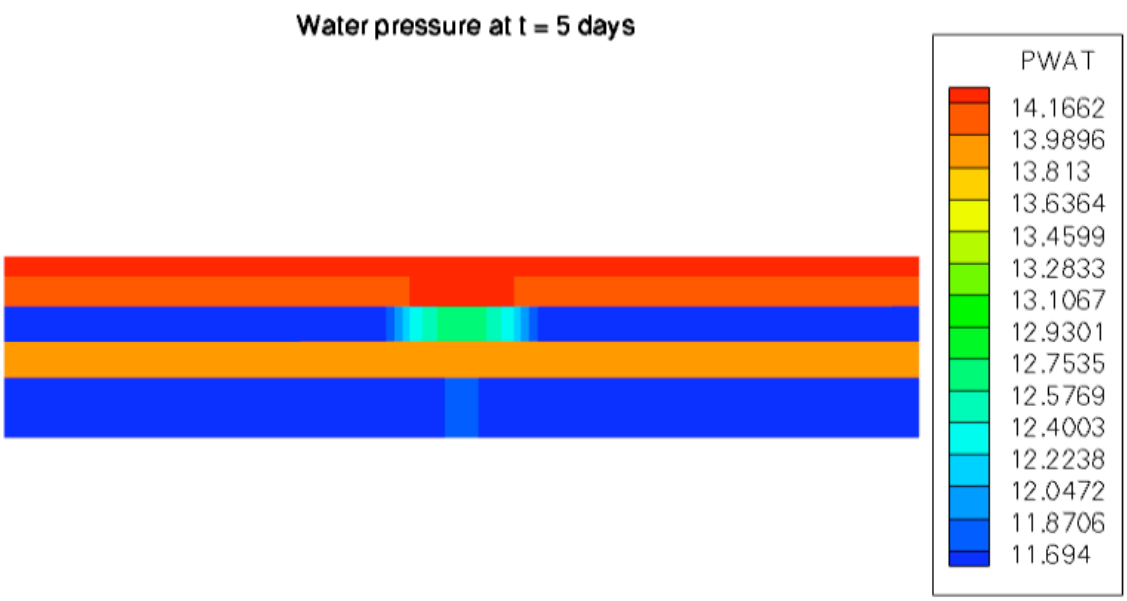

(a) IPARS

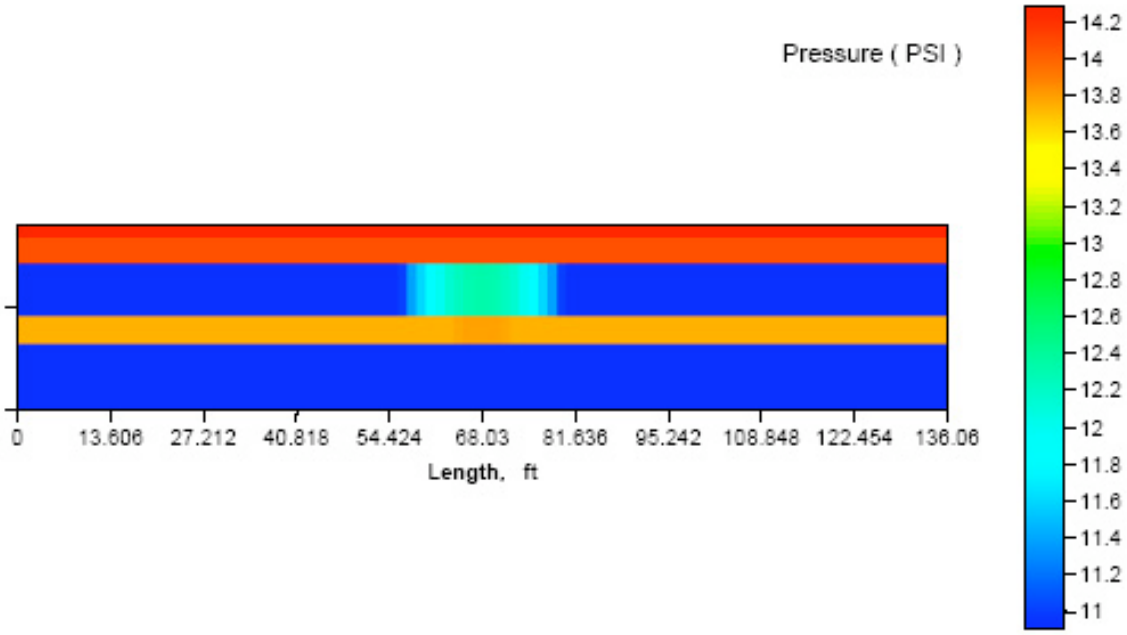

(b) UTCHEM

Figure 5.20 Water Pressure Profiles for Case 3 at 5 Days

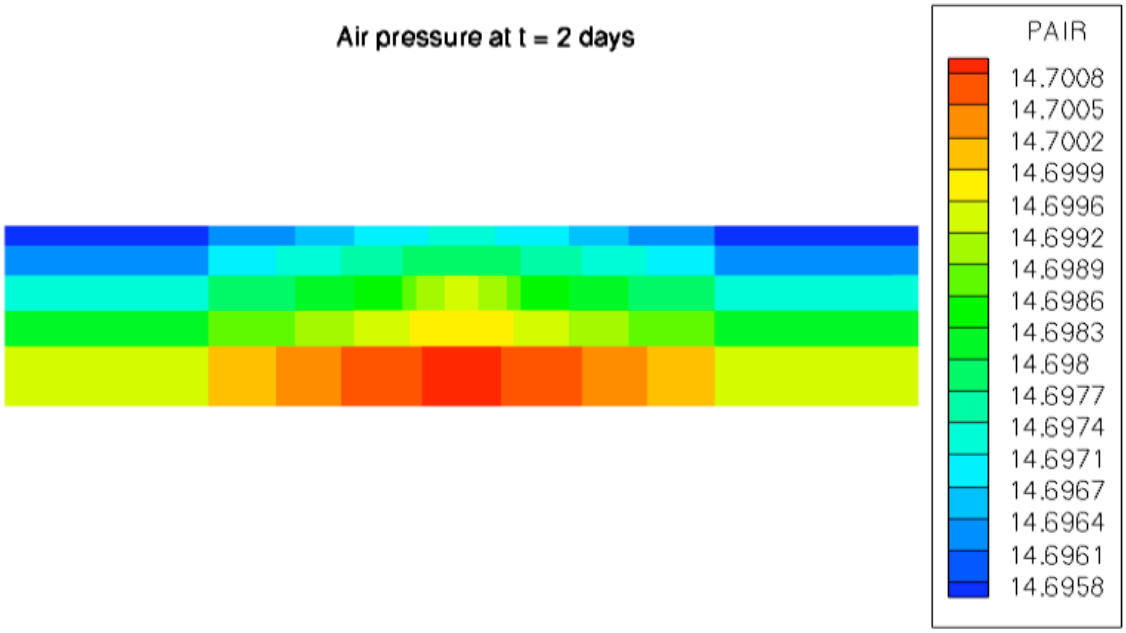

(a) IPARS

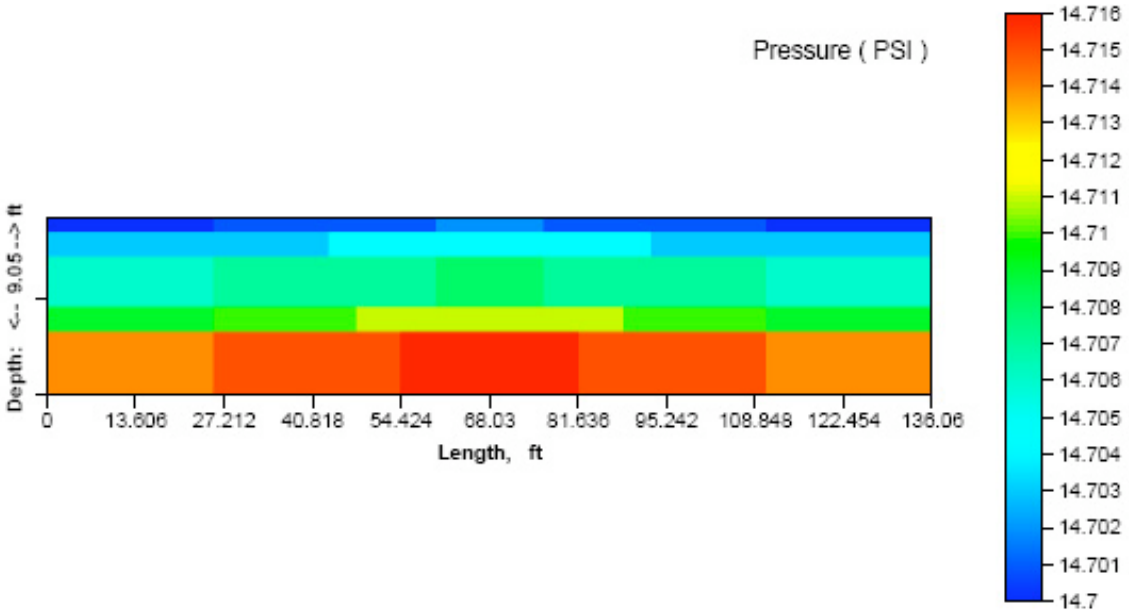

(b) UTCHEM

Figure 5.21 Air Pressure Profiles for Case 3 at 2 Days

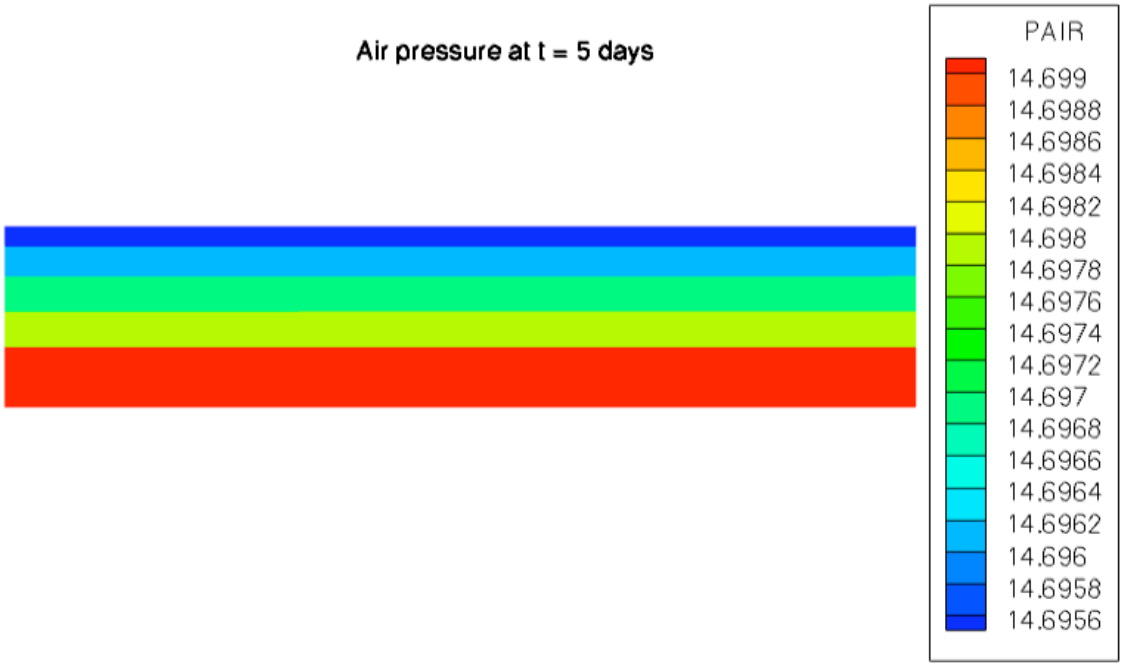

(a) IPARS

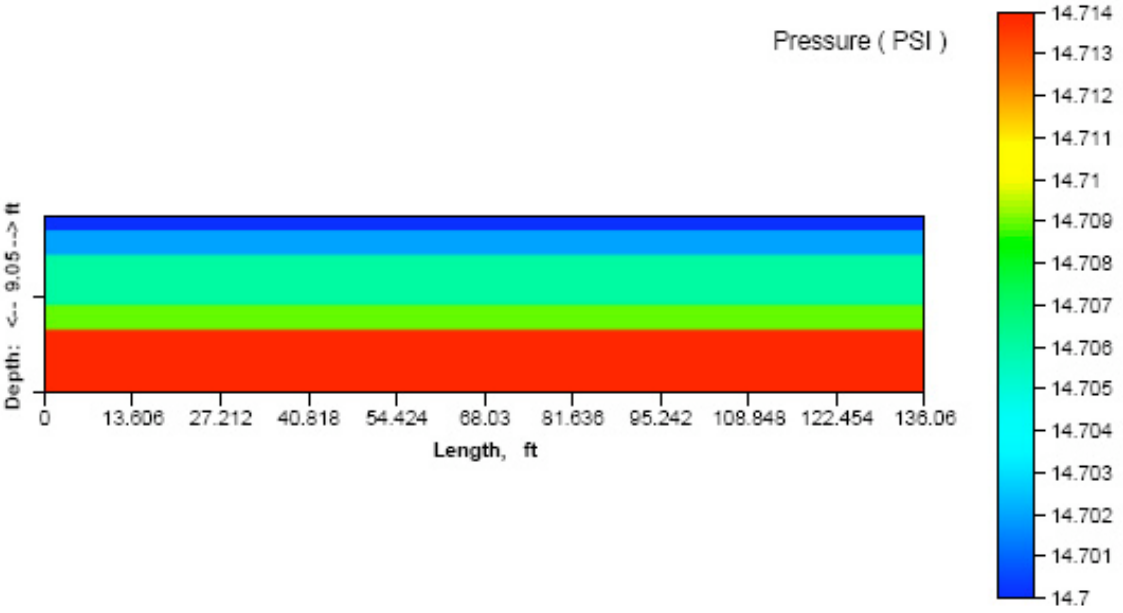

(b) UTCHEM

Figure 5.22 Air Pressure Profiles for Case 3 at 5 Days

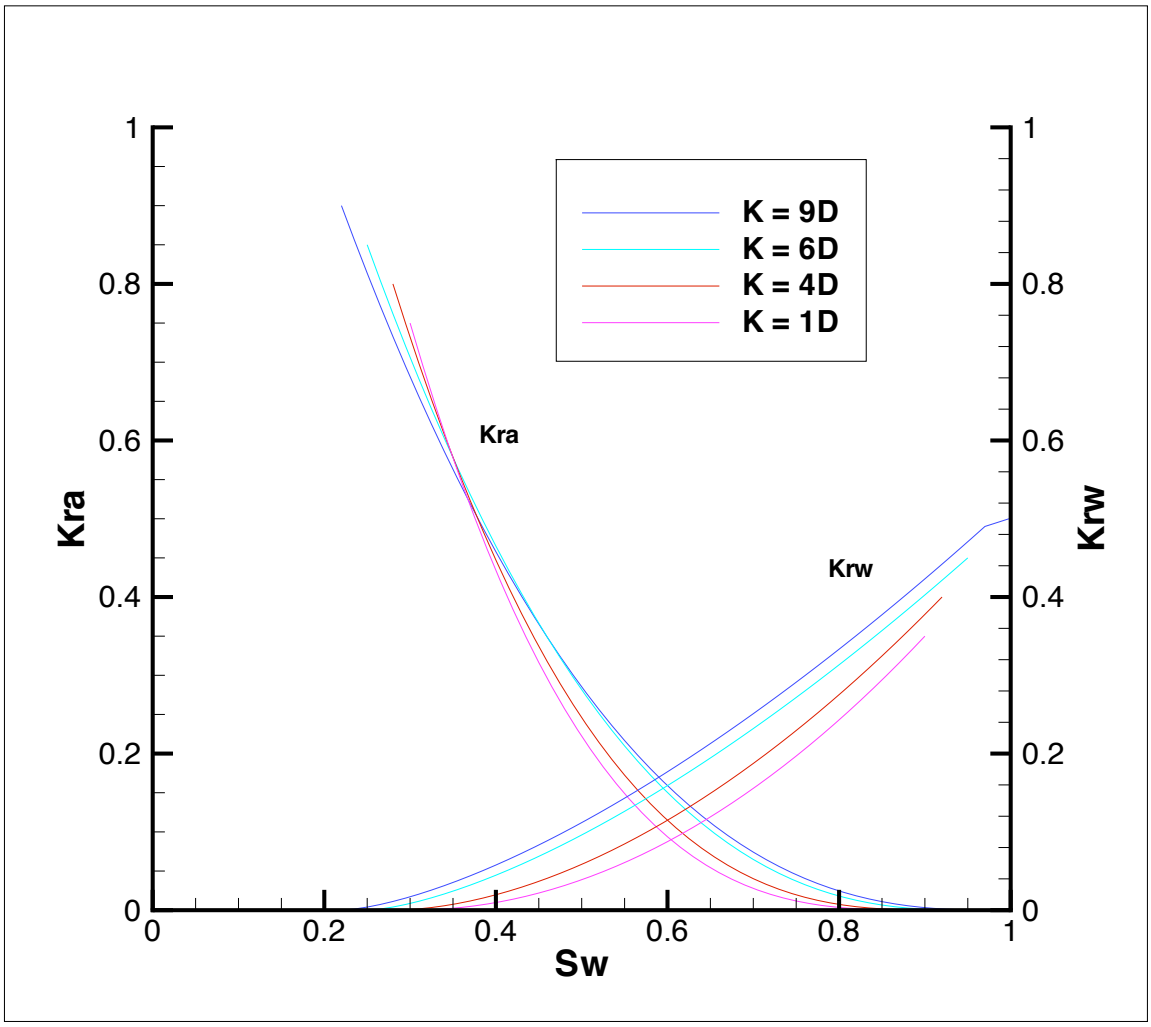

Figure 5.23 Relative Permeability Curves for Case 4

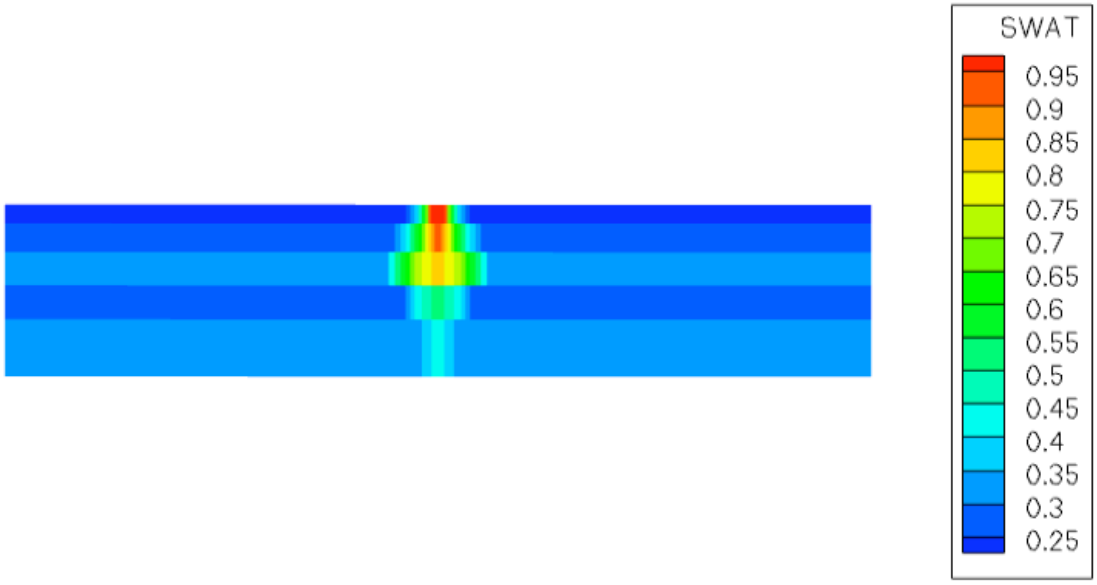

(a) IPARS

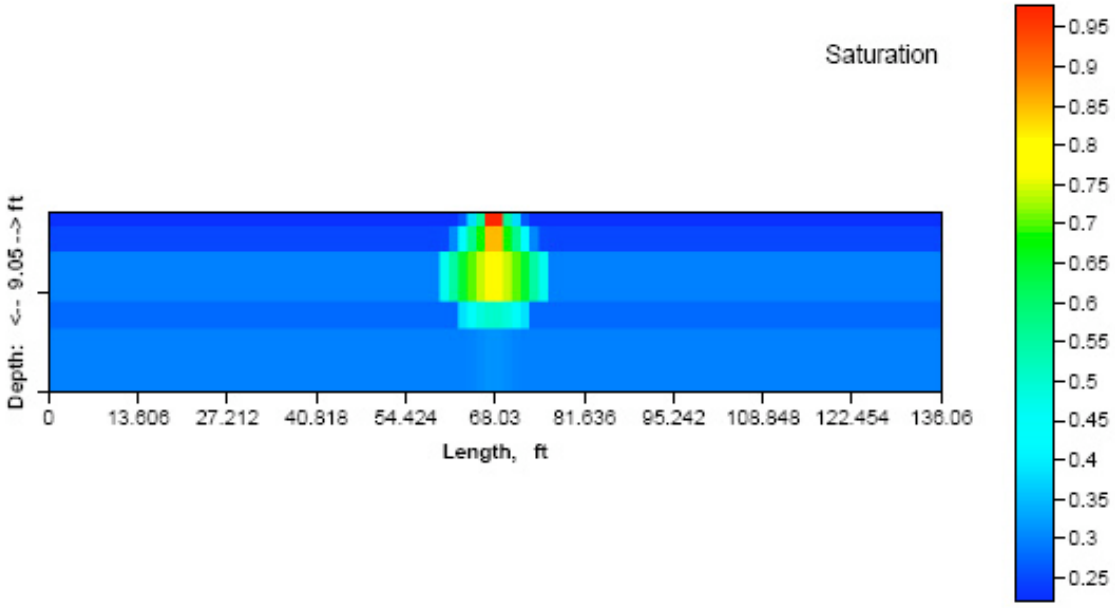

(b) UTCHEM

Figure 5.24 Water Saturation Profiles for Case 4 at 2 Days

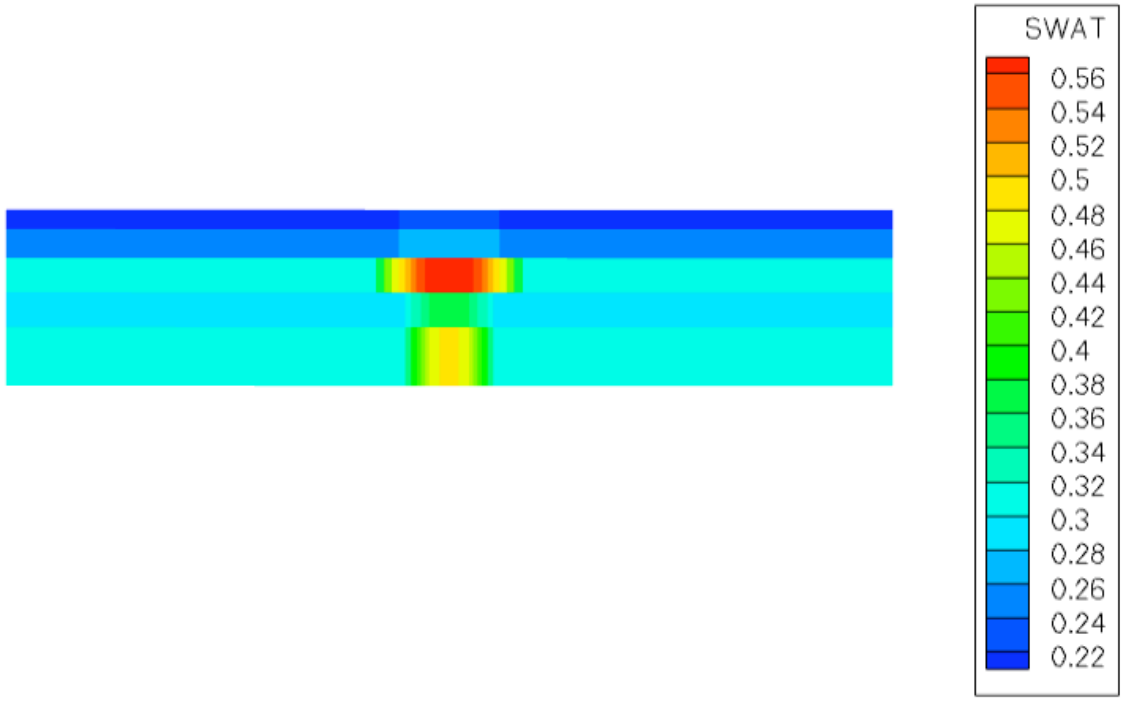

(a) IPARS

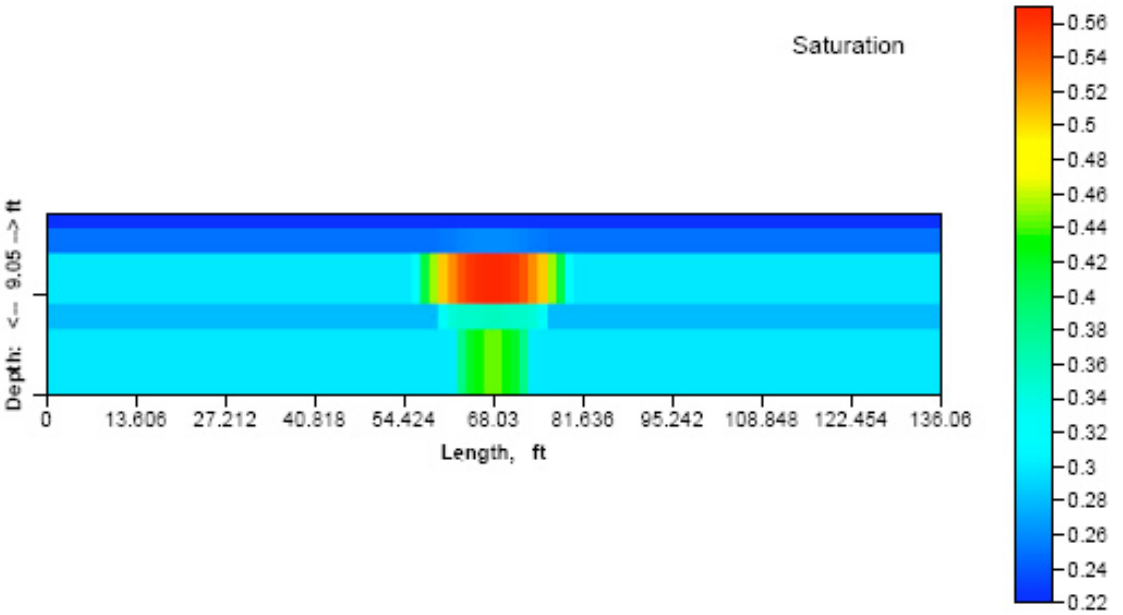

(b) UTCHEM

Figure 5.25 Water Saturation Profiles for Case 4 at 5 Days

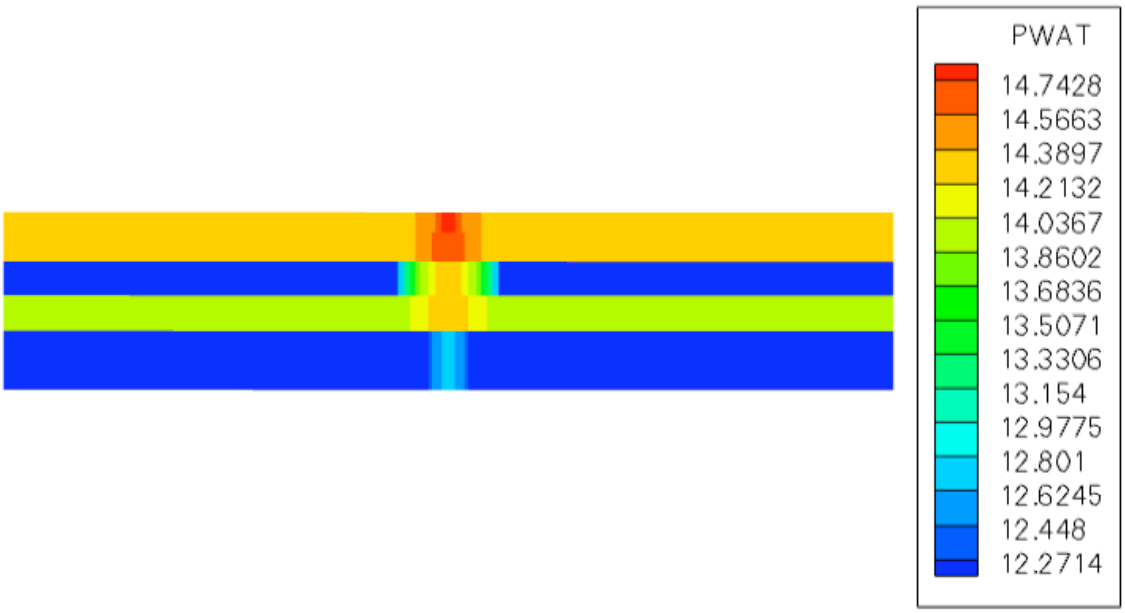

(a) IPARS

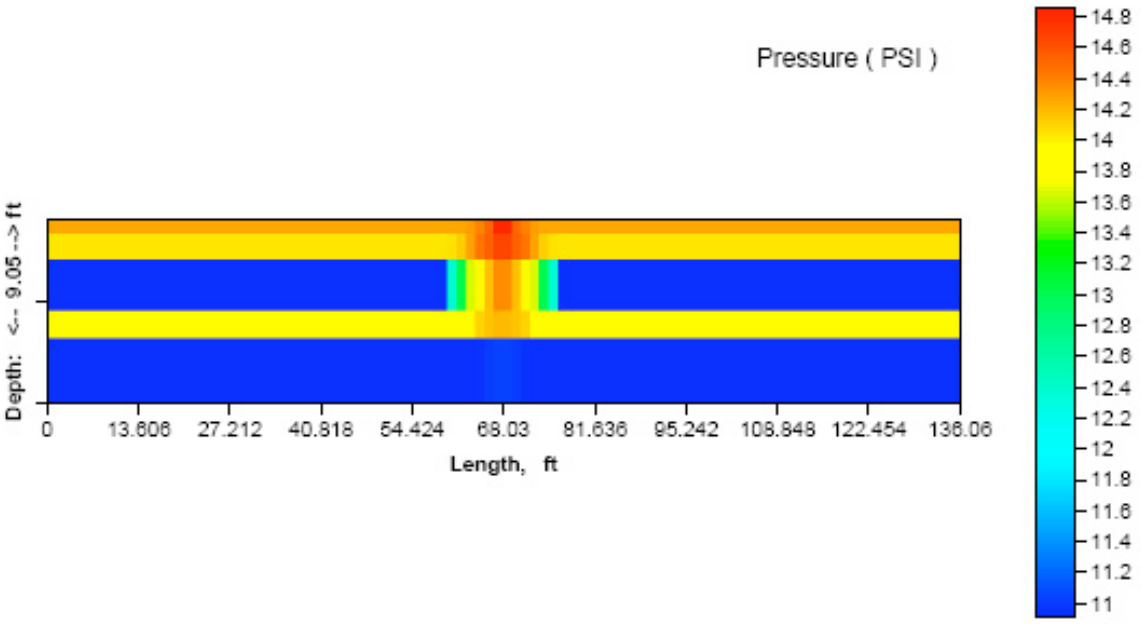

(b) UTCHEM

Figure 5.26 Water Pressure Profiles for Case 4 at 2 Days

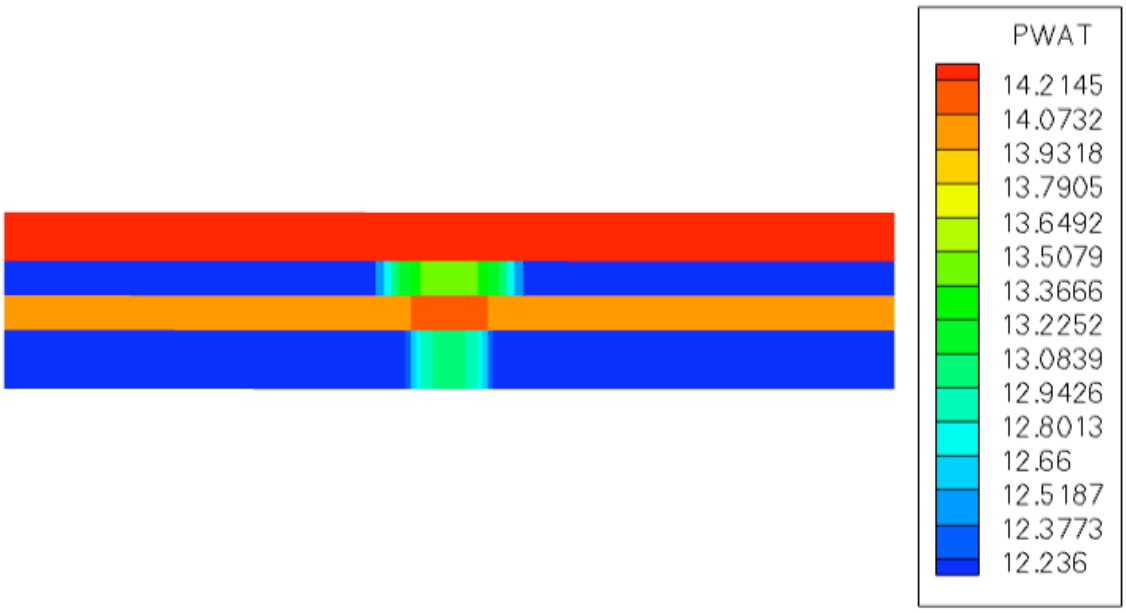

(a) IPARS

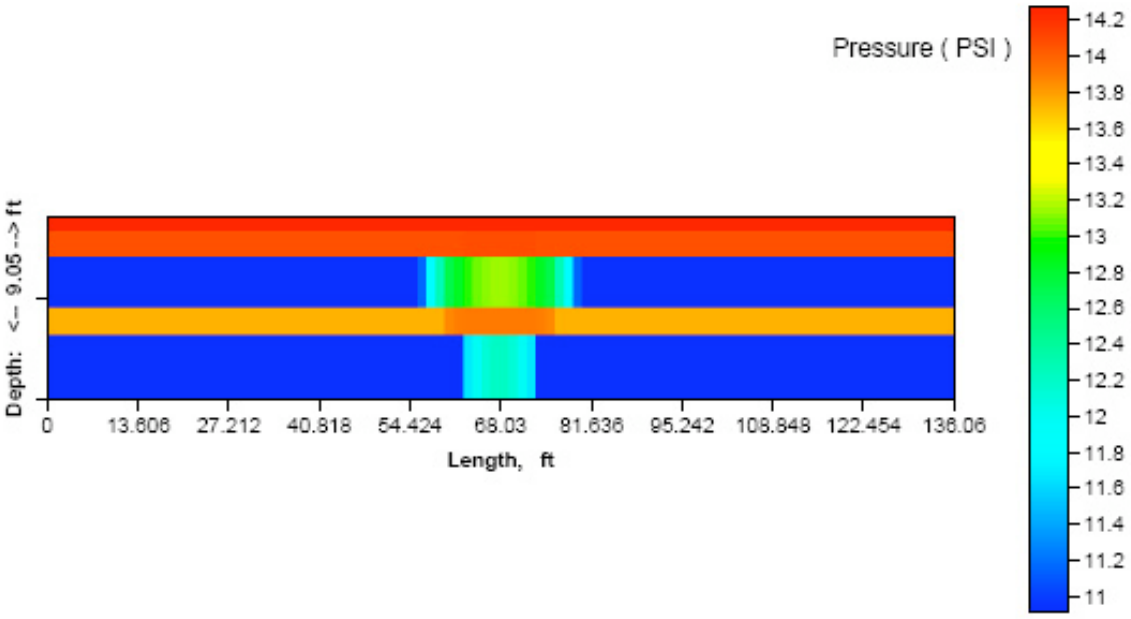

(b) UTCHEM

Figure 5.27 Water Pressure Profiles for Case 4 at 5 Days

(a) IPARS

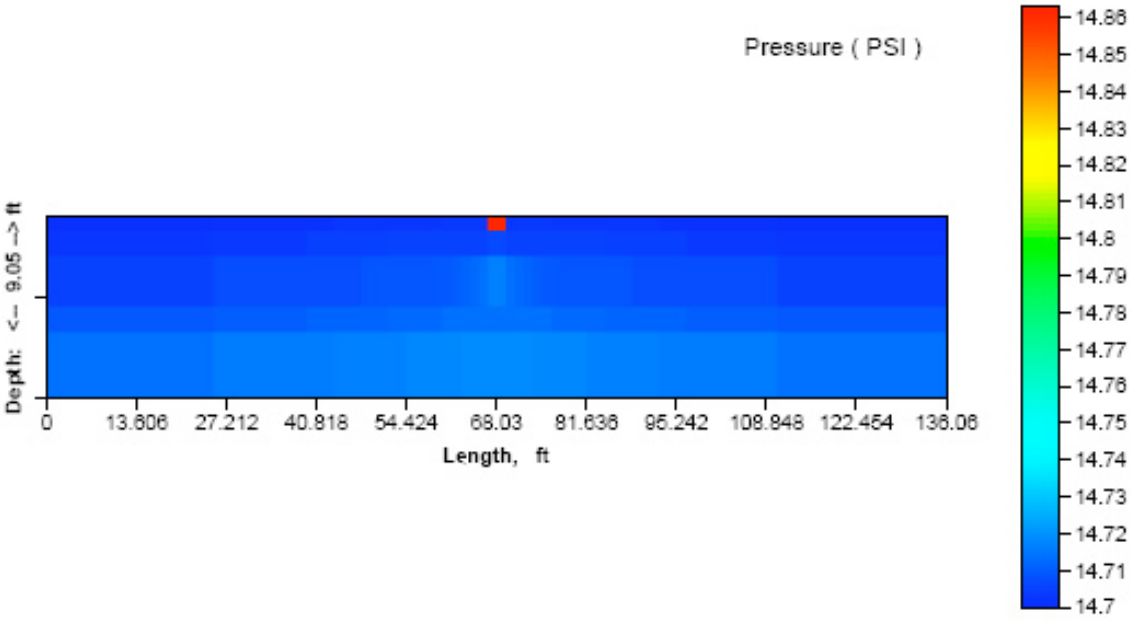

(b) UTCHEM

Figure 5.28 Air Pressure Profiles for Case 4 at 2 Days

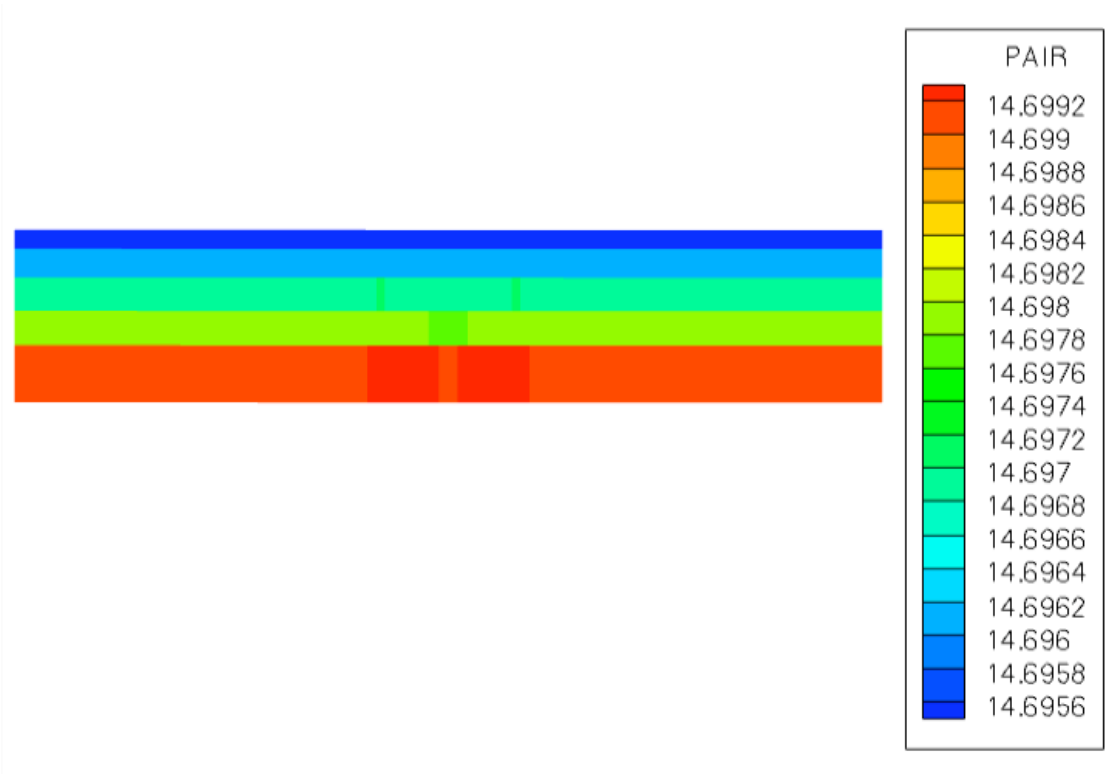

(a) IPARS

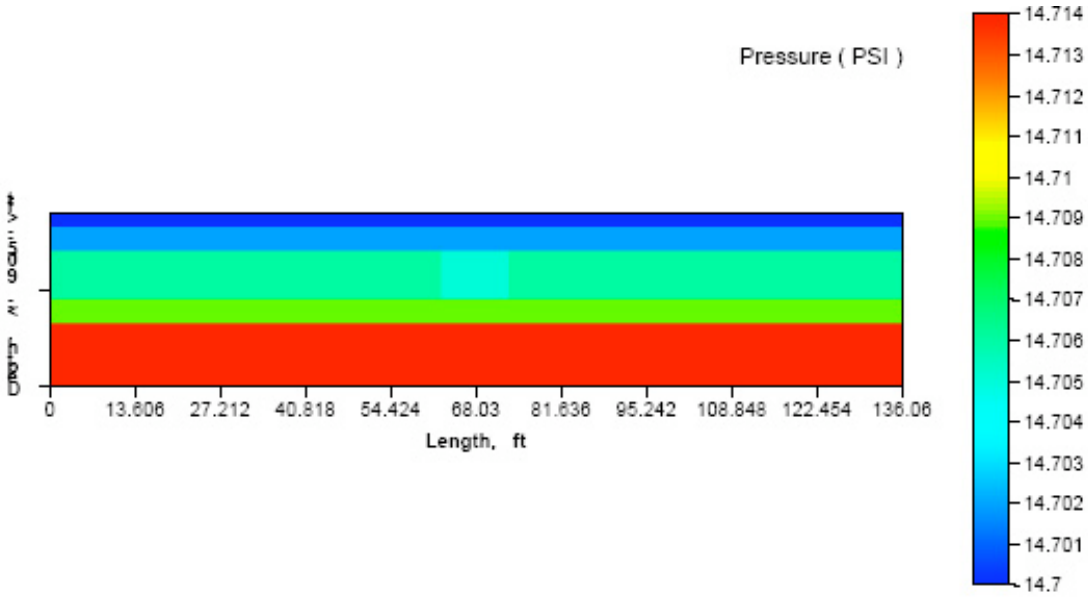

(b) UTCHEM

Figure 5.29 Air Pressure Profiles for Case 4 at 5 Days

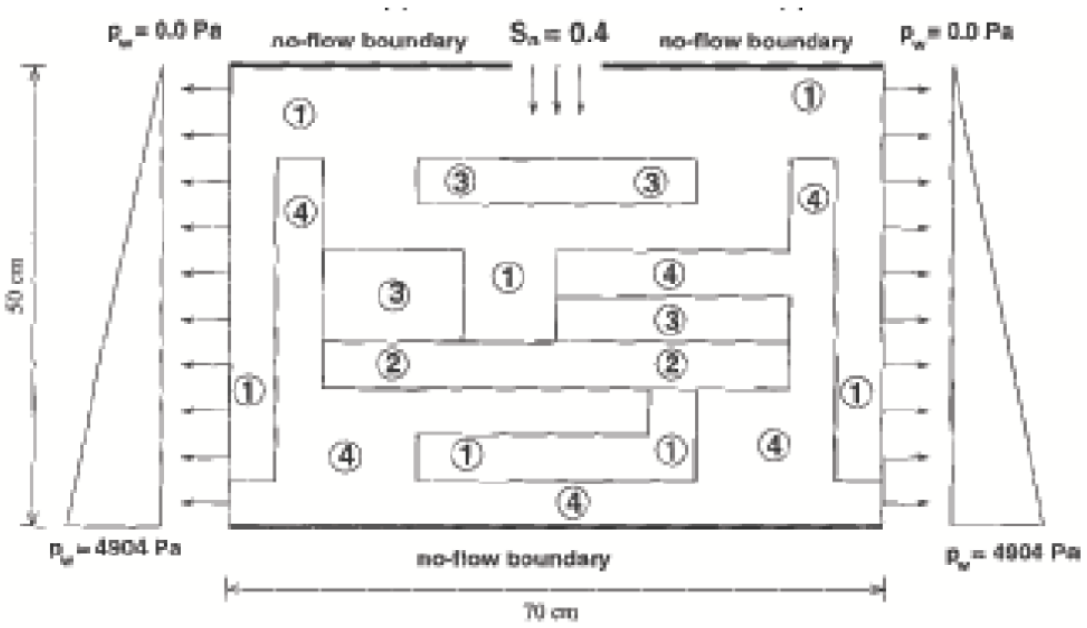

Figure 5.30 Experimental Setup of Kueper (1988) (from Helmig, 1997)

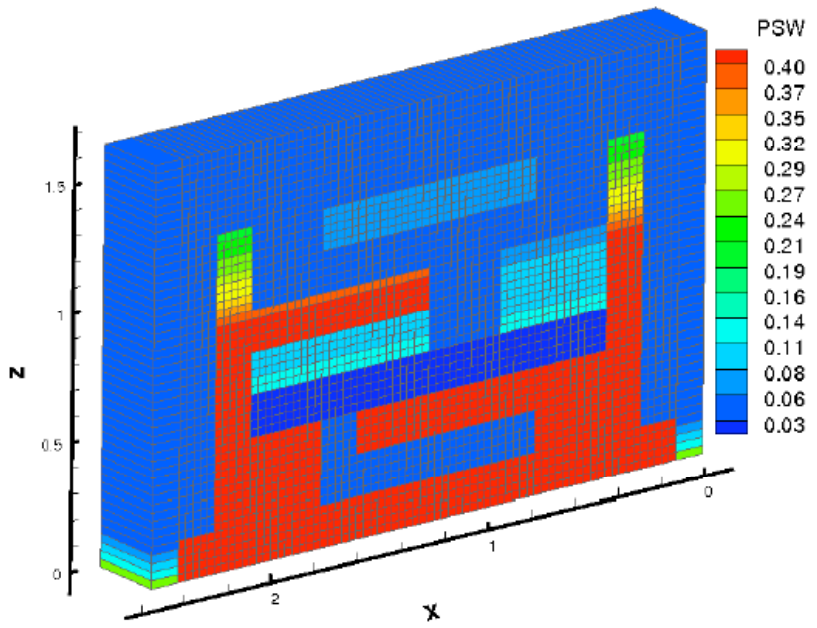

(a) Initial Water Content

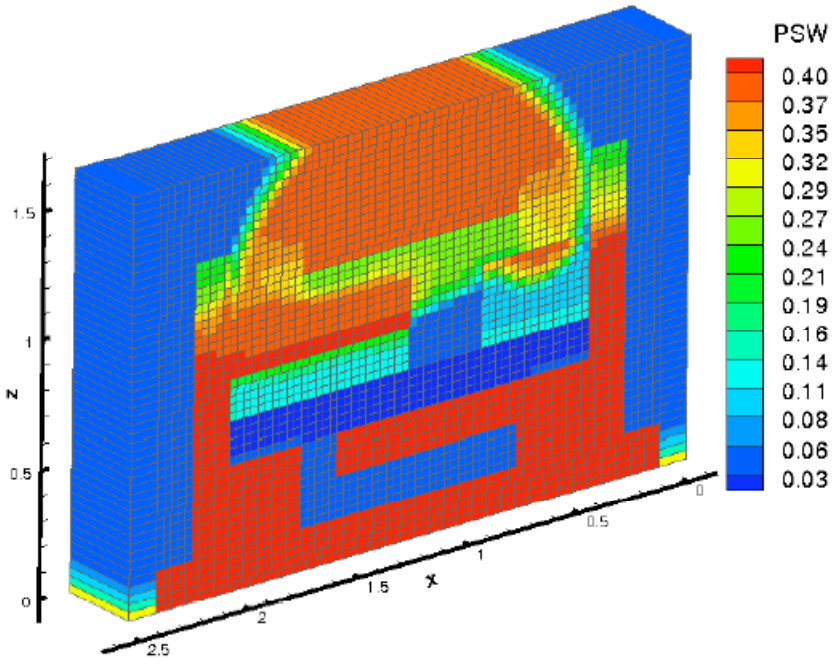

(b) Water Content at 26 sec

Figure 5.31 Water Content for Case 5 from IPARS

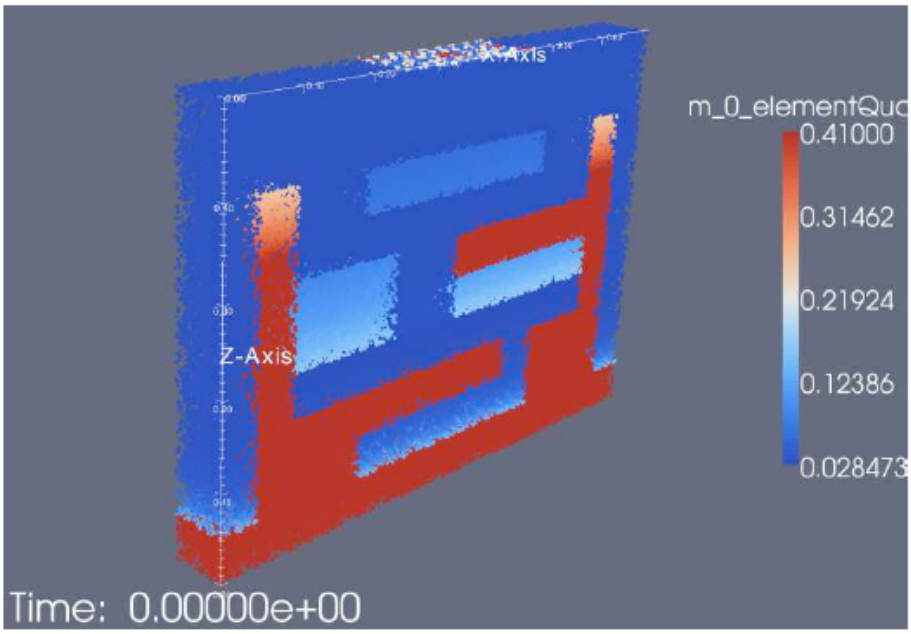

(a) Initial Water Content

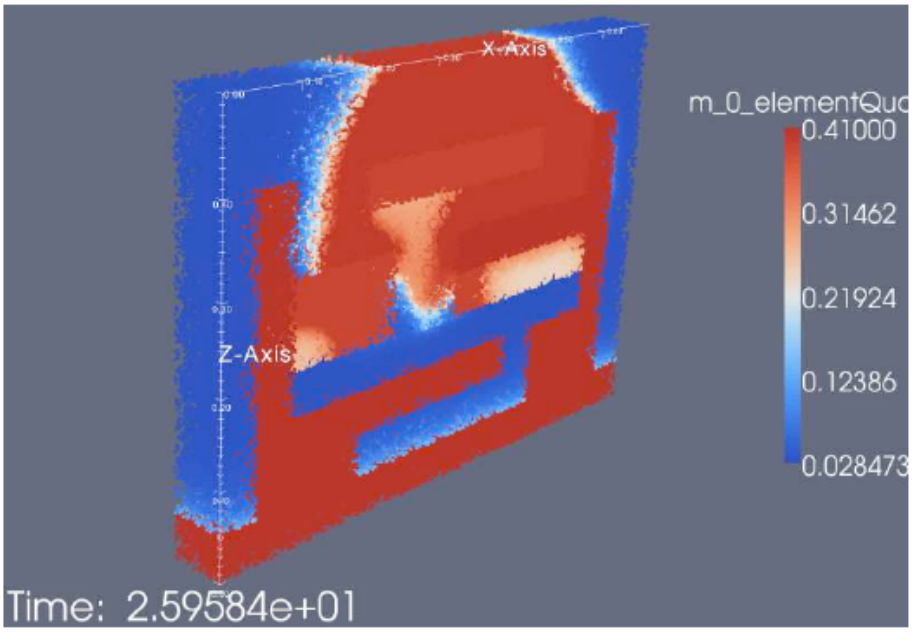

(b) Water Content at 26 sec

Figure 5.32 Water Content for Case 5 from PyAHD

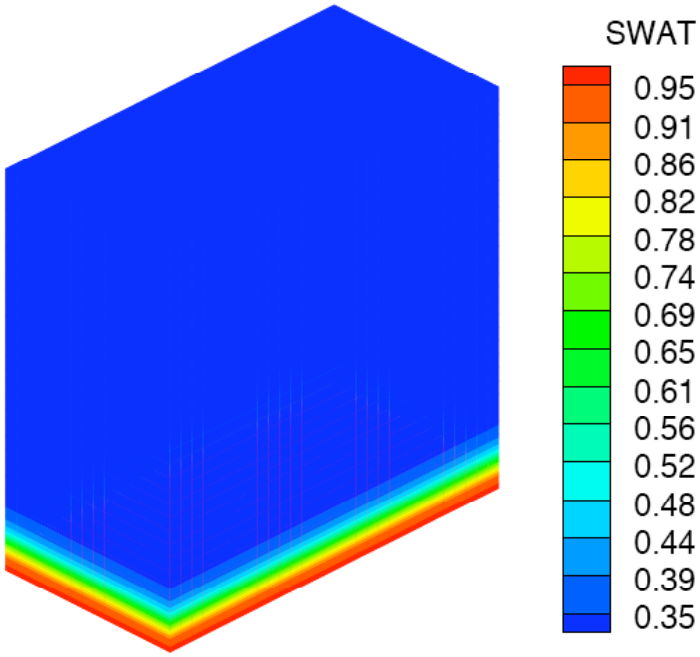

(a) Initial Water Saturation Profile

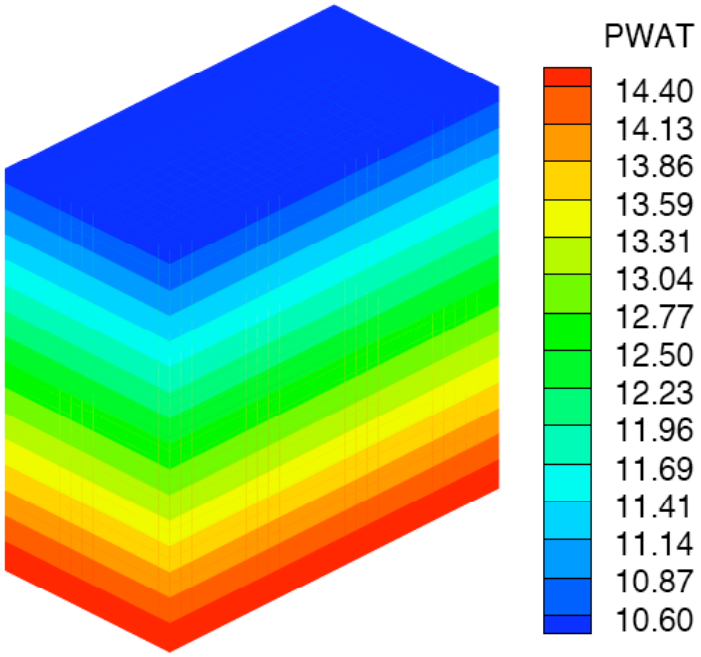

(b) Initial Water Pressure Profile

Figure 5.33 Initial Conditions for Case 6 using IPARS

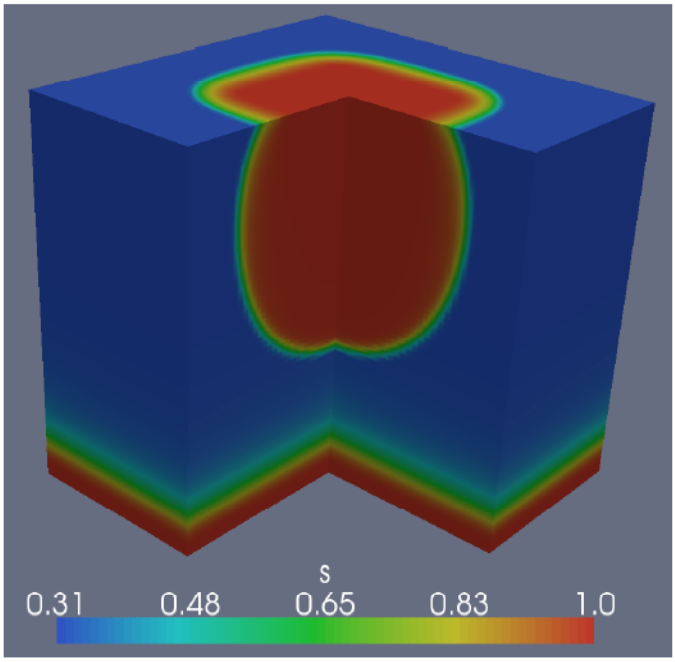

(a) Water Saturation Profile at 0.075 days

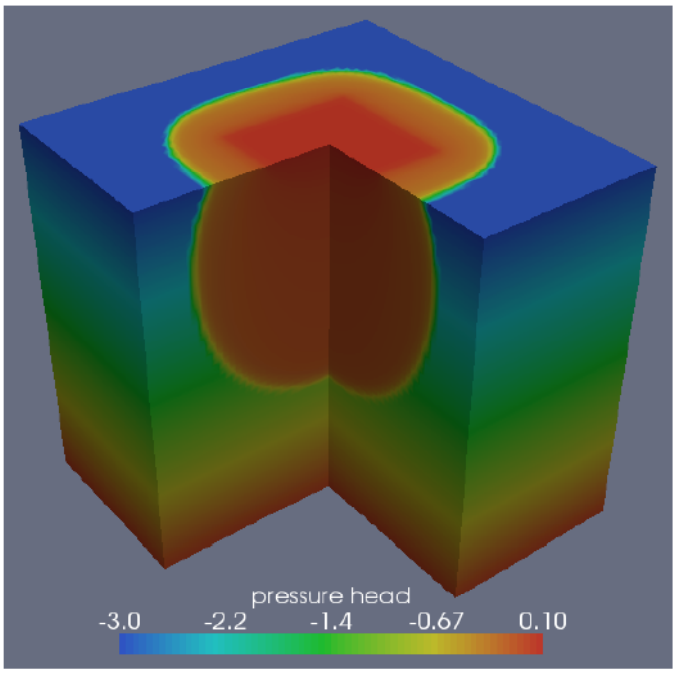

(b) Pressure Head Profile at 0.075 days

Figure 5.34 Solution at 0.075 Days for Case 6 using PyAHD

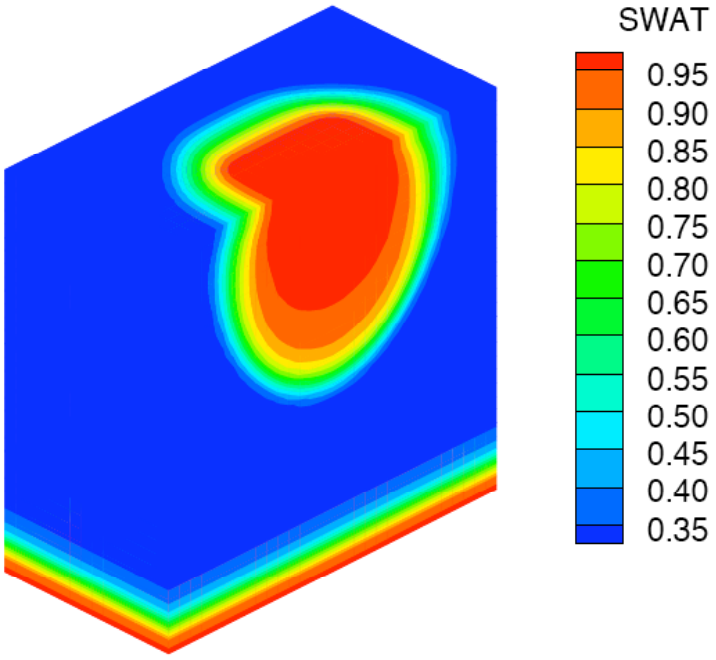

(a) Water Saturation Profile at 0.075 days

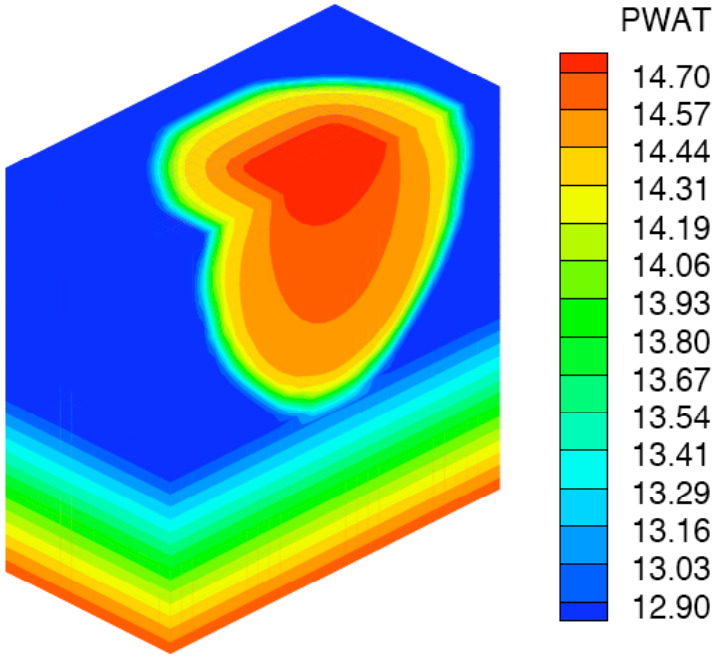

(b) Water Pressure Profile at 0.075 days

Figure 5.35 Solution at 0.075 Days for Case 6 using IPARS

CHAPTER 6

SUMMARY, CONCLUSIONS, AND RECOMMENDATIONS

6.1 POLYMER FLOOD SIMULATIONS

6.1.1 Summary and Conclusions

1. Non-Newtonian polymer flow in porous media has been implemented in a multiphase flow and reactive module of IPARS and solved using efficient time-splitting algorithm to independently solve the advection, diffusion/dispersion, and chemical reactions. To the best of our knowledge, this is the first time that such a comprehensive polymer module is implemented in a fully implicit parallel reservoir simulator with molecular diffusion and physical dispersion included.
2. Polymer properties modeled include power law viscosity, adsorption, inaccessible pore volume, and permeability reduction.
3. Results were verified with an IMPES chemical flood simulator.
4. Fine-scale simulations were performed using up to 24 processors.
5. We observed that the alternative wellblock flux calculation reduces the grid effect caused by shear rate calculation with coarse meshes and yields more accurate injection bottomhole pressure calculation in both homogeneous isotropic and heterogeneous anisotropic reservoirs. The shear rate calculation has no significantly impact on cumulative oil recovery and average reservoir oil saturation but it does affect the performance of individual producers.

6. The grid resolution has very little impact on cumulative oil recovery and average reservoir oil saturation. However it does affect the performance of individual producers, such as oil recovery, oil cut, and effluent polymer concentration for both homogeneous isotropic and heterogeneous anisotropic reservoirs
7. Simulations with finer areal mesh yield higher oil recovery than those using coarser areal mesh but with the same vertical grid resolution. The results indicate that even waterflood results show great sensitivity to the choice of the grid as a result of single phase upscaling procedure for reservoir properties.
8. The cases with fewer vertical layers yield higher oil recovery due to less permeability contrast as a result of property averaging and better vertical equilibrium.

6.1.1 Recommendations

1. A scale up strategy for non-Newtonian fluid behavior needs to be developed for typical grid sizes used in commercial-scale simulations.
2. Viscoelastic polymer behavior, effect of polymer on relative permeability, and polymer degradation need to be studied and implemented in IPARS.
3. The variable time step algorithm need to be optimized to improve the computational efficiency.

6.2 MODELING INFILTRAION IN VADOSE ZONE

The following conclusions are drawn from the simulation of infiltration in the vadose zone:

1. Two-phase model holds for general porous media and conditions and is not limited by several assumptions that must be made for the RE formulations. In particular, RE is applicable only to shallow regions (vadose) that are only several meters in depth and a fully saturated bottom boundary condition may have to be assumed.
2. For RE, drainage capillary pressure and relative permeability relationship is requited.
3. Another disadvantage in using RE instead of two-phase model is that the transport of gas cannot be handled when flow is coupled to a transport model.

References

H.J. Agnew, *Here's how 56 polymer oil-recovery projects shape up*, Oil and Gas J., **70**(1972), 109-112.

T. Arbogast, M.F. Wheeler and I. Yotov, *Mixed finite elements for elliptic problems with tensor coefficients as cell-centered finite differences*, SIAM J. Numerical Analysis, **34**(1997), 828-852.

L. Auvray, J. physique, **42**(1981). 79-95.

P. Barreau, D. Lasseus, H. Bertin, P. Glenat and Z. Zaitoun, *An experimental and numerical study of polymer action on relative permeability and capillary pressure*, Petroleum Geoscience, **5**(1999) 201-206.

R.H. Brooks and A.T. Corey, *Hydraulic properties of porous media*, in "Hydrology Papers", Fort Collins, Colorado State University, 1964.

D. Broseta, F. Medjahed, J. Lecourtier and M. Robin, *Polymer adsorption/retention in porous media: effects of core wettability and residual oil*, SPE Advanced Technology Series, **3**(1995), 103-112.

S.E. Buckley and M.C. Leverett, *Mechanism of fluid displacement in sand*, Trans. AIME, **146**(1942), 107-116.

D. Camilleri, A. Fil, G.A. Pope, B.A. Rouse and K. Sepehrnoori, *Improvements in physical-property models used in micellar/polymer flooding*, SPE Reservoir Engineering, **2**(1988), 433-440.

M. Celia and P. Binning, *A mass conservative numerical solution for two-phase flow in porous media with application to unsaturated flow*, Water resource Research, **28**(1992), 2819-2828.

H.L. Chang, *Polymer flooding technology----yesterday, today, And tomorrow*, J. Pet. Tech., **30**(1978), 1113-1128.

G. Chauveteau, *Molecular interpretation of several different properties of flow of coiled polymer solutions through porous media I oil recovery conditions*, SPE 10060 presented at SPE Annual Technical Conference and Exhibition, 4-7 October 1981, San Antonio, Texas, USA.

G. Chauveteau, *Rodlike polymer solution flows through fine pores: Influence of pore size on rheological behavior*, J. Rheology, **26**(1982), 111-142.

G. Chauveteau and A. Zaitoun, *Basic rheological behaviour of xanthan polysaccharide solutions in porous media: Effects of pore size and polymer concentration*, Proceedings of the First European Symposium on EOR, Bournemouth, England, 1981.

S.K. Choi, M.M. Sharma, S.L. Bryant and C. Huh, *pH-sensitive polymers for novel conformance control and polymerflood applications*, SPE 121686 presented at SPE International Symposium on Oilfield Chemistry, 20-22 April 2009, Woodlands, Texas, USA.

C.N. Dawson and M.F. Wheeler, *An operator-splitting method for advection-diffusion reaction problems*, in "Mathematics of Finite Elements and Applications VI" (ed. J.R. Whiteman), Academic Press, 463-482, 1987.

R. Dawson and R.B. Lantz, *Inaccessible pore volume in polymer flooding*, Soc. Pet. Eng. J. **12**(1972), 448-452.

M. Delshad, G.A. Pope and K. S. Sephehrnoori, *A compositional simulator for modeling surfactant enhanced aquifer remediation 1 formulation*, J. of Contaminant Hydrology, **23**(1996), 303-327.

M. Delshad, G.A. Pope and K. Sepehnoori, "UTCHEM version 9.0 Technical Documentation," Center for Petroleum and Geosystems Engineering, The University of Texas at Austin, 2000.

M. Delshad, G.A. Pope and K. Sepehnoori, "UTCHEM version 9.0 User's Guide," Center for Petroleum and Geosystems Engineering, The University of Texas at Austin, 2002

M. Delshad, D.H. Kim, O.A. Magbagbeola, C. Huh, G.A. Pope and F. Tarahhom, *Mechanistic interpretation and utilization of viscoelastic behavior of polymer solutions for improved polymer-flood efficiency*, SPE 113620 presented at SPE/DOE Symposium on Improved Oil Recovery, 20-23 April 2008, Tulsa, Oklahoma, USA.

J.W. Demmel, S.C. Eisenstat, J.R. Gilbert, X.S. Li and J.W.H. Liu, *A supernodal approach to sparse partial pivoting*, SIAM J. Matrix Analysis and Applications, **20**(1999), 720-755.

J. Douglas, D.W. Peaceman, H.H. Rachford, *A method for calculating multi-dimensional immiscible displacement*, Trans. AIME, **216**(1959), 297-308.

P.A. Domenico and F.W. Schwartz, "Physical and Chemical Hydrogeology", John Wiley and Sons, New York, 1998.

Y. Du and L. Guan, *Field-scale polymer flooding: Lessons learnt and experiences gained during past 40 Years*, SPE 91787 presented at SPE International Petroleum Conference in Mexico, 7-9 November 2004, Puebla Pue, Mexico.

P.J. Flory, "Principles of Polymer Chemistry," Cornell University Press, Ithaca, New York, 1953.

P.A. Forsyth, Y.S. Wu and K. Pruess, *Robust numerical methods for saturated-unsaturated flow with dry initial conditions in heterogeneous media*, Advances in Water Resource, **18**(1995), 25-38.

G. Ghauveteau, *Fundamental criteria in polymer flow through porous media and their relative importance in the performance differences of mobility control buffers*, in "Water-Soluble Polymers" (ed. J.E. Glass), Advances in Chemistry Series of the American Chemical Society, **213**(1986), 227-268.

W.B. Gogarty, G.L. Levy and V.G. Fox, 1972. *Viscoelastic effects in polymer flow through porous media*, SPE 4025 presented at Fall Meeting of the Society of Petroleum Engineers of AIME, 8-11 October 1972, San Antonio, Texas, USA.

C.A. Grattoni, P.F. Luckham, X.D. Jing, L. Norman and R.W. Zimmerman, *Polymers as relative permeability modifiers: adsorption and the dynamic formation of thick polyacrylamide layers*, Journal of Petroleum Science & Engineering, **45**(2004), 233-245.

R. Helmig, "Multiphase Flow and Transport Processes in the Subsurface: A Contribution to the Modeling of Hydrosystems", Springer, Berlin, 1997.

T.J.R. Hughes, *Multiscale phenomena: Greens's functions, the Dirichlet-to-Neumann formulation, subgrid scale models, bubbles and the origins of stabilized methods*, Computer Methods in Applied Mechanics and Engineering, **127**(1995), 387-401.

C. Huh, E.A. Lange and W.J. Cannella, *Polymer retention in porous media*, SPE 20235 presented at SPE/DOE Enhanced Oil Recovery Symposium, 2-25 April 1990, Tulsa, Oklahoma, USA.

C. Huh and G.A. Pope, *Residual oil saturation from polymer floods: Laboratory measurements and theoretical interpretation*, SPE 113417 presented at SPE/DOE Symposium on Improved Oil Recovery, 20-23 April 2008, Tulsa, Oklahoma, USA.

G.J. Hirasaki and G.A. Pope, *Analysis of factors influencing mobility and adsorption in the flow of polymer solution through porous media*, Soc. Pet. Eng. J., **14**(1974), 337-346.

E.W. Jenkins, "The IPARSv2 Air-water Model", Technical Report 02-27, Institute for Computational Engineering and Sciences, The University of Texas at Austin, 2002.

R.L. Jewett and G.F. Schurz, *Polymer flooding - a current appraisal*, J. Pet. Tech., **22**(1970), 675-684.

C.E. Kees and C.T. Miller, *C++ implementation of numerical methods for solving differential-algebraic equations: Design and optimization considerations*, Association for Computing Machinery, Transactions on Mathematical software, **25**(1999), 377-403.

C.E. Kees and C.T. Miller, *Higher order time integration methods for two-phase flow*, Advances in Water Resources, **25**(2002), 159-177.

C.E. Kees, M.W. Farthing and C.N. Dawson, *Locally conservative, stabilized finite element methods for variably saturated flow*, Computer Methods in Applied Mechanics and Engineering, **197**(2008), 4610-4625.

B.H. Kueper and E.O. Frind, *An overview of immiscible fingering in porous media*, Journal of Contaminant Hydrology, **2**(1988), 95-110.

S. Lacroix, Y. Vassilevski, J.A. Wheeler and M.F. Wheeler, *Iterative solution methods for modeling multiphase flow in porous media fully implicitly*, SIAM J. Sci. Comput., **25**(2003), 905-926.

L.W. Lake, "Enhanced Oil Recovery", Prentice-Hall, Inc., Englewood Cliff, NJ, 1989.

E. Lin, "A Study of Micellar/Polymer Flooding Using a Compositional Simulator", Ph.D. dissertation, The University of Texas at Austin, 1981.

Y. Masuda, K.C. Tang, M. Mlyazawa and S. Tanaka, *1D simulation of polymer flooding including the viscoelastic effect of polymer solution*, SPE Reservoir Engineering, **7**(1992), 247-252.

D.M. Meter and R.B. Bird, *Tube flow of non-Newtonian polymer solutions: Parts I and II. Laminar flow and rheological models*, AIChE J., **10**(1964), 878-881, 881-884.

C.T. Miller, G.A. Williams, C.T. Kelley and M.D. Tocci, *Robust solution of Richards' equation for nonuniform porous media*, Water Resour. Res., **34**(1998), 2599-2610.

P.C.A. Milly. *Advances in modeling of water in the unsaturated zone*, in "Groundwater Flow and Quality Modeling" (ed. E. Custodio *et al*.), Dordrecht, Holland Boston, D. Reidel Pub. Co., 489-514, 1988.

H. Morel-SeyToux and J. Billica, *A two-phase numerical model for prediction of infiltration: Applications to a semi-infinite soil column*, Water Resource Research, **21**(1985), 607-615.

G.J. Moridis and D.L. Reddell, *Secondary water recovery by air injection: 1. The concept and the mathematical and numerical model*, Water Resource Research, **27**(1991), 2337-2352.

N. Mungan, *Some aspects of polymer floods*, J. Pet. Tech., **18**(1966), 1143-1150.

D.W. Peaceman, *Interpretation of well-block pressures in numerical reservoir simulation with nonsquare gridblocks and anisotropic permeability*, Soc. Pet. Eng. J. **23**(1983), 531-543.

M. Peszynska, E. Jenkins and M.F. Wheeler, *Boundary conditions for fully implicit two-phase flow models*, Contemporary Mathematics, **306**(2002), 85-106.

M. Peszynska and S. Sun, "Multiphase Reactive Transport Module TRCHEM in IPARS", TICAM01-32, CSM, the University of Texas at Austin, 2001.

A.G. Putz, J.M. Lecourtier and L. Bruckert, *Interpretation of high recovery obtained in a new polymer flood in the Chateaurenard field*, SPE 18093 presented at SPE Annual Technical Conference and Exhibition, 2-5 October 1988, Houston, Texas, USA.

A.G. Putx and R.C. Rivenq, *Commercial polymer injection in the Courtenay field*, J. Pet. Sci. Eng., **7**(1992), 15-23.

D.J. Pye, *Improved secondary recovery by control of water mobility*, J. Pet. Tech., **16**(1964), 911-916.

T.F. Russell and M.F. Wheeler, *Finite element and finite difference methods for continuous flows in porous media*, in "The Mathematics of Reservoir Simulation" (ed. R.E. Ewing), SIAM, Philadelphia, 35-106, 1983.

F. Saaf, "A Study of Reactive Transport Phenomena in Porous Media", Ph.D. dissertation, Rice University, 1996.

B.B. Sandiford, *Laboratory and field studies of water floods using polymer solutions to increase oil recovery*, J. Petro. Tech., **16**(1964), 917-922.

B.A. Schrefler and X.Y. Zhan, *A fully coupled model for water flow and air flow in deformable porous media*, Water Resource Research, **29**(1993), 155-167.

B. Sloat, *Polymer treatment boosts production on four floods*, World Oil, **168**(1969), 44-47.

F.W. Smith, *The behaviour of partially hydrolysed polyacrylamide solutions in porous media*, J. Petro. Tech., **22**(1970), 148-156.

K.S. Sorbie, A. Parker and P.J. Clifford, *Experimental and theoretical study of polymer flow in porous media*, SPE Reservoir Engineering, **2**(1987), 281-304.

K.S. Sorbie, "Polymer –Improved Oil Recovery", CRC Press, Inc., Boca Raton, Florida, 1991.

S. Takaqi, G.A. Pope, K. Sepehrnoori and A.G. Putz, *Simulation of a successful polymer flood in the Chateaurenard field*, SPE 24931 presented at SPE Annual Technical Conference and Exhibition, 4-7 October 1992, Washington, D.C., USA.

M.D. Tocci, C.T. Kelley and C.T. Miller, *Accurate and economical solution of the pressure-head form of Richards' equation by the method of lines*, Advances in Water Resources, **20**(1997), 1-14.

J. Touma and M. Vauclin, *Experimental and numerical analysis of two-phase infiltration on a partially saturated soil*, Transport in Porous Media, **1**(1986), 22-55.

M. Vauclin, *Flow of water and air in soils: Theoretical and experimental aspects*, in "Unsaturated Flow in Hydrologic Modeling Theory and Practice" (ed. Morel-Seytoux), Kluwer Academic Publishers, 53-91, 1989.

S. Verma, B. Adibhatla, R. Kaminsky, C. Wattenbarger, and J. Davidson, *Modeling polymer flood in an unstructured grid simulator*, SPE 118985 presented at SPE Reservoir Simulation Symposium, 2-4 February 2009, Woodlands, Texas, USA.

D.M. Wang, H.Z Dong, C.S. Lv, X.F. Fu and J. Nie, *Review of practical experience of polymer flooding at Daqing*, SPE114342, SPE Reservoir Evaluation & Engineering, **12**(2009), 470-476.

W.W. Weiss and R.W. Baldwin, *Planning and implementing a large-scale polymer flood*, J. Petro. Tech., **37**(1985), 720-730.

J. Wheeler *et al.,* "Integrated Parallel and Accurate Reservoir Simulator User's manual", Center for Subsurface Modeling, The University of Texas at Austin, 2007.

M.F. Wheeler, S. Sun and S.G. Thomas, *Modeling of flow and reactive transport in IPARS*, to appear as a chapter in E-book "Modeling of Reactive Transport in Groundwater", 2009.

G.P. Willhite and J.G. Dominguez, "Improved Oil Recovery by Surfactant and Polymer Flooding" (eds. D.O. Shah and R.S. Shecter), Academic Press Inc. New York, 1977.

D. Wreath, G.A. Pope and K.S. Sepehrnoori. *Dependence of polymer apparent viscosity on the permeable media and flow conditions*, In Situ, **14**(1990), 263-284

G.A. Zeico, *Three dimensional numerical simulation of polymer flooding in homogeneous and heterogeneous systems*, SPE 2186 presented at Fall Meeting of the Society of Petroleum Engineers of AIME, 29 September-2 October, 1968 Houston, Texas, USA.

C.G. Zheng, B.L. Gall, H.W. Gao, A.E. Miller and R.S. Brant, *Effects of polymer adsorption and flow behavoir on two-phase flow in porous dedia*, SPE Reservoir Evaluation & Engineering, **3**(2000), 216-223.

Vita

Changli Yuan was born in Chongqing, P.R. China on July 24, 1973, the daughter of Ms. Guofang Gan and Mr. Ziren Yuan. After completing her high school at Changshou High School, Chongqing, P.R. China in 1990, she entered Beijing Institute of Technology in Beijing, P.R. China. She received a Bachelor of Engineering degree on Chemical Engineering in July 1994. In September 1994, she was admitted to the Graduate School at the Beijing Institute of Technology. She received a Master of Engineering degree on Mechatronic Engineering in April 1997. In August 2005, she entered the Graduate School of The University of Texas at Austin.

Permanent address: 2501 Lake Austin Blvd, Apt D108
Austin, TX 78703

This thesis was typed by the author.